

UCL

Scour and scour protection
around offshore gravity
based foundations

Eng D in Urban Sustainability and Resilience

Mr Nikolas Sokratis Tavouktsoglou

I, Nikolas Sokratis Tavouktsoglou confirm that the work presented in this thesis is my own. Where information has been derived from other sources, confirm that this has been indicated in the thesis.

Signed,

Nikolas Sokratis Tavouktsoglou

Abstract

The prediction of seabed scour around offshore gravity based foundations with complex geometries is currently a significant barrier to optimising and providing cost effective foundation designs. A significant aspect that has the potential to reduce the uncertainty and costs related to the design of these foundations is the understanding of the effect the structural geometry of the foundation has on scour.

This thesis focuses on an experimental investigation of the scour and scour protection around complex structure geometries. The first part of this research considers scour under clear water conditions. During this study different foundation geometries were subjected to a range of different hydrodynamic forcings which enabled a better understanding of the scour process for these foundations. The second part of the research encompasses the design and execution of a series of experiments which investigated stability of the scour protection around such structures. The structures were tested against different combinations of wave and current conditions to determine the bed shear stress required to initiate sediment motion around each structure.

This research has led to a number of novel results. The experimental investigation on scour around complex geometries showed that the scour depth around cylindrical structures (with both uniform and complex cross-sections) is linked to the depth averaged pressure gradient. Following a dimensional analysis, the controlling parameters were found to be the depth averaged Euler number, pile Reynolds number, Froude number, sediment mobility number and the non-dimensional flow depth. Based on this finding a new scour prediction equation was developed which shows good agreement with experimental and prototype scour measurements. The scour protection tests indicated that under wave dominated conditions the amplification of the bed shear stress around these structures does not exceed the value of 2. In the case of current dominated flow conditions the amplification of the bed shear stress is a function of the structure type and the Keulegan–Carpenter number. The results of these experiments were used to develop

a “Shields type” diagram that can guide designers to select the appropriate rock armour size that will be stable for a certain set of flow conditions. The study also revealed that the long term persistence of flow conditions that just lead to incipient motion of the scour protection material can eventually lead to complete failure of the scour protection.

The study provides a set of new design techniques that can allow designers to predict the scour depth around cylindrical and complex foundation geometries and also select the appropriate stone size for their scour protection system. Together, these techniques may allow for the reduction of costs associated with the scour protection of offshore and coastal structures.

Table of Contents

Abstract.....	3
Table of Contents	5
List of Figures.....	13
List of Tables	24
Nomenclature.....	25
List of publications.....	33
Acknowledgments	34

Part I: Overview of scour and scour protection around complex foundations

1 Introduction.....	35
1.1 <i>General overview of the research</i>	35
1.2 <i>Background</i>	35
1.3 <i>Thesis outline</i>	37
2 Literature review	38
2.1 <i>Introduction</i>	38
2.2 <i>Sediment transport and boundary layer theory</i>	38
2.2.1 <i>Steady uniform flow</i>	40
2.2.2 <i>Wave boundary layer</i>	42
2.2.3 <i>Wave current interaction</i>	44
2.2.3.1 <i>Wavelength modification</i>	44

2.2.3.2	Wave current boundary layer.....	45
2.2.4	Incipient motion of sediment particles	47
2.2.5	Threshold current speed.....	54
2.3	<i>Hydrodynamics around cylindrical structures</i>	54
2.3.1	Downflow	56
2.3.2	Horseshoe vortex.....	57
2.3.2.1	Horseshoe vortex in currents.....	57
2.3.2.2	Horseshoe vortex in waves.....	61
2.3.2.3	Horseshoe vortex in combined waves and currents.....	62
2.3.3	Lee-wake vortex.....	64
2.3.3.1	Lee-wake vortex in currents.....	64
2.3.3.2	Lee-wake vortex in waves	67
2.3.4	Streamline contraction	70
2.4	<i>Scour around cylindrical structures</i>	70
2.4.1	Scour types	70
2.4.1.1	General (global) scour	71
2.4.1.2	Local scour.....	72
2.4.2	Sediment transport in local scour	73
2.4.3	Scour in steady unidirectional currents.....	75
2.4.3.1	Influencing parameters	76
2.4.3.1.1	Sediment mobility ratio	77
2.4.3.1.2	Relative flow depth	79
2.4.3.1.3	Sediment gradation.....	81
2.4.3.2	Time evolution of scour.....	81
2.4.3.3	Equilibrium scour depth prediction.....	83
2.4.4	Scour under wave action	86
2.4.4.1	Influencing parameters	86
2.4.4.2	Time evolution of scour.....	87
2.4.4.3	Equilibrium scour prediction.....	87
2.4.5	Scour under the forcing of combined waves and currents	89

2.4.5.1	Influencing parameters.....	89
2.4.5.2	Time evolution of scour	90
2.4.5.3	Equilibrium scour depth prediction	91
2.5	<i>Scour around gravity based foundation</i>	92
2.5.1	Introduction.....	92
2.5.2	Scour in steady unidirectional currents	93
2.5.2.1	Influencing parameters.....	93
2.5.2.2	Time evolution of scour	94
2.5.2.3	Equilibrium scour depth prediction	95
2.5.3	Scour under wave action.....	98
2.5.4	Scour under combined wave and current action.....	99
2.5.5	Discussion on scour prediction around GBFs	100
2.6	<i>Scour protection practice</i>	100
2.6.1	Introduction.....	100
2.6.2	Armour layer	102
2.6.2.1	Stone size.....	102
2.6.2.2	Thickness	106
2.6.2.3	Lateral extent.....	107
2.6.3	Granular filter layer.....	108
2.6.3.1	Geometrically closed filters	108
2.6.3.2	Geometrically open filters.....	109
2.6.4	Discussion on scour protection practice	110
3	Aims and objectives	112

Part II: Scour around complex foundations

4	Methodology	115
4.1	<i>Introduction</i>	115
4.2	<i>General model and scaling considerations</i>	116

4.2.1	Scaling considerations.....	116
4.2.1.1	Hydrodynamic scaling.....	116
4.2.1.2	Sediment scaling	117
4.2.2	Model effects.....	119
4.3	<i>Description of set-up and the models for small scale scour tests</i>	<i>120</i>
4.3.1	Flume and test set-up	120
4.3.1.1	Sand installation and smoothing.....	122
4.3.1.2	Model Structures.....	122
4.3.2	Flow parameters	124
4.3.2.1	Flow velocity	124
4.3.2.2	Flow depth	125
4.3.2.3	Sediment characteristics.....	125
4.3.3	Measurement techniques	126
4.3.3.1	Flow velocity measurements	126
4.3.3.2	Flow and scour depth measurements	129
4.3.4	Experimental programme	130
4.4	<i>Description of set-up and the models for large scale scour experiments.....</i>	<i>132</i>
4.4.1	Flume and test set-up	132
4.4.2	Flow parameters	136
4.4.3	Measuring techniques.....	137
4.4.3.1	Flow velocity measurement	137
4.4.3.2	Flow and water depth measurement	138
4.4.4	Experiment programme	139
4.5	<i>Description of set-up and the models for the pressure and flow measurements near the structure.....</i>	<i>141</i>
4.5.1	Flume and test set-up	141
4.5.2	Measurement techniques	145
4.5.2.1	Pressure measurement	145
4.5.3	Experimental programme	146
4.6	<i>Database compilation for equilibrium scour prediction equation</i>	<i>147</i>

5	Results for scour around complex structures.....	149
5.1	<i>Smaller scale scour results</i>	149
5.1.1	Flow conditions.....	149
5.1.2	Results	150
5.1.2.1	Initiation of scour around complex geometries	150
5.1.2.2	Temporal evolution of scour.....	151
5.1.2.3	Equilibrium scour depth.....	159
5.1.2.4	Repeatability of tests.....	162
5.2	<i>Large scale scour results</i>	165
5.2.1	Flow conditions.....	165
5.2.2	Results	167
5.2.2.1	Temporal evolution of scour.....	167
5.2.2.2	Equilibrium scour depths.....	171
5.2.2.3	Repeatability of tests.....	178
5.3	<i>Pressure and flow measurement</i>	179
5.3.1	Test conditions	180
5.3.2	Pressure Measurements	180
5.3.3	Flow measurements.....	185
5.3.3.1	Monopile.....	185
5.3.3.2	75° conical base structure.....	188
5.3.3.3	60° conical base structure.....	191
5.3.3.4	Cylindrical base.....	192
5.4	<i>Summary of results</i>	194
6	Prediction of equilibrium scour depth around cylindrical structures.....	197
6.1	<i>Introduction</i>	197
6.2	<i>Similitude of scour at complex geometries</i>	197
6.3	<i>Database Description</i>	205
6.4	<i>Equilibrium scour depth prediction equation</i>	208

6.5	<i>Behaviour of scour prediction equation</i>	217
6.5.1	Influence of depth averaged Euler number	217
6.5.2	Influence of pile Reynolds number	221
6.5.3	Influence of Froude number.....	224
6.5.4	Influence of non-dimensional flow depth	226
6.5.5	Influence of the sediment mobility ratio	228

Part III: Scour protection around complex foundations

7	Methodology for scour protection stability tests	230
7.1	<i>Introduction</i>	230
7.2	<i>General model and scaling considerations</i>	230
7.3	<i>Experimental procedure</i>	231
7.4	<i>Description of flume and the models</i>	233
7.5	<i>Flow parameters</i>	238
7.6	<i>Measuring techniques</i>	240
7.6.1	Detection of incipient motion for scour protection.....	240
7.6.2	Flow velocity measurement	242
7.6.3	Measurement of scour protection damage	243
7.6.4	Wave measurements.....	244
7.7	<i>Experiment programme</i>	244
8	Results for scour protection around complex structures	257
8.1	<i>Flow characteristics</i>	257
8.2	<i>Stability of scour protection</i>	260
8.2.1	Choice of wave friction formula.....	260
8.3	<i>Analysis of the results of scour protection stability tests</i>	262

8.3.1	Influence of main variables	263
8.3.1.1	Influence of stone size (D_{50})	263
8.3.1.2	Influence of scour protection level.....	264
8.3.1.3	Influence of bed permeability	265
8.3.1.4	Influence of flow direction.....	266
8.3.1.5	Influence of wavelength	267
8.3.1.6	Influence of the velocity ratio (U_{cw})	268
8.3.1.7	Influence of the KC number: Design diagram for rock cover size selection .	269
8.3.2	Validation of present results.....	274
8.4	<i>Development of scour protection damage</i>	275
8.4.1	Monopile damage pattern	276
8.4.2	75° conical base.....	279
8.4.3	45° conical base.....	282
8.4.4	Cylindrical base structure.....	284
8.4.5	Discussion of results	286

Part IV: Conclusions and recommendations

9	Conclusions and recommendations	287
9.1	<i>Conclusions</i>	287
9.2	<i>Recommendations</i>	290
10	References.....	292

Part V: Appendices

11	Appendix A (correction factors for scour prediction equations).....	312
11.1.1	Sediment gradation ($K\sigma$).....	312
11.1.2	Foundation shape factor (K_s).....	313
11.1.3	Pier orientation factor ($K\omega$)	314
11.1.4	Pier group factor (K_{gr}).....	315

12 Appendix B (scour profiles along the centreline of the structures) 318

List of Figures

Figure 1-1: Breakdown of costs for offshore wind turbines. [Data derived from Blanco (2009)].	36
Figure 2-1: Boundary layer definition sketch	40
Figure 2-2: Definition sketch and zones of turbulence (proposed by Lundgren, 1971).	46
Figure 2-3: Definition sketch of forces acting on a single sediment particle.	47
Figure 2-4: Original Shields curve (Shields, 1936)	50
Figure 2-5: Modified Shields diagram (Miller et al., 1977)	52
Figure 2-6: Updated Shields diagram (Source: Soulsby, 1997)	52
Figure 2-7: Sundborg's modification of the Hjulström diagram. (After Sundborg, 1956.)	53
Figure 2-8: Flow structure interaction definition sketch (source: Roulund et al., 2005)	55
Figure 2-9: Definition sketch of downflow phenomenon (location of the stagnation point is arbitrarily selected in this image)	56
Figure 2-10: Influence of the ReD on the Horseshoe vortex (source: Roulund et al., 2005)	58
Figure 2-11: Influence of the boundary layer thickness on the Horseshoe vortex for $ReD = 2 * 10^2$, line: result of numerical model, x symbol: experimental measurement (source: Roulund et al., 2005).	59
Figure 2-12: Boundary layer separation distance for different cross-sectional shapes (source: Sumer et al., 1997)	60
Figure 2-13: Horseshoe vortex in different phases of wave cycle (Source: Sumer et al., 1997)	62
Figure 2-14: Presence of horseshoe vortex in phase space: influence of superimposed current (Source: Sumer et al., 1997)	63
Figure 2-15: SepaType equation here.ration distance for combined waves and currents (Source: Umeda et al., 2003)	64

Figure 2-16: Lee wake vortex shedding regimes around a cylinder (source: Sumer and Fredsøe, 1997)	65
Figure 2-17: Strouhal number as a function of the pile Reynolds number for smooth and rough cylinders (Data source: Roshko, 1961)	66
Figure 2-18: Effect of cross-flow shape on the Strouhal number (Source: Blevins and Burton, 1976).....	66
Figure 2-19: Regimes of flow separation around cylinders in waves (source: Sumer and Fredsøe, 1997)	67
Figure 2-20: Flow separation regimes for small KC and very small ReD numbers (source: Sumer and Fredsøe, 1997)	68
Figure 2-21: Flow separation regimes for large KC and ReD numbers (source: Sumer and Fredsøe, 1997)	68
Figure 2-22: Definition sketch of steady streaming.....	69
Figure 2-23: Size of steady streaming cell (Reproduced from Wang, 1968).....	69
Figure 2-24: Definition sketch of local scour around monopile in unidirectional flow....	71
Figure 2-25: Scour depth evolution, live bed Vs clear water scour.	73
Figure 2-26: Development of clear-water scour (Derived from: Hoffmans and Verheij, 1997)	74
Figure 2-27: Counter-rotating streamwise phase-averaged vortices (a) streamlines (b) mean vorticity in x- direction (Source: Baykal et al., 2015)	77
Figure 2-28: Influence of flow intensity on scour depth (Derived from: Melville and Sutherland, 1988)	79
Figure 2-29: Effect of flow shallowness on scour depth (Source: Melville, 2008).....	80
Figure 2-30: Examples of GBF foundation geometries.....	92
Figure 2-31: Definition sketch of key structural parameters of composite cylindrical structures.....	94
Figure 2-32: Definition diagram of scour protection design.....	102
Figure 2-33:Types of filters.	108

Figure 4-1: Layout of tidal flume: (a) top view; (b) side view.....	121
Figure 4-2: Structure geometries for scour tests.	123
Figure 4-3: Set-up of the structures for scour tests: (a) Lower part of model (buried under the sand); (b) installation of model foundation on base.	124
Figure 4-4: Grain size distribution for the two sediment types used in the experiments.	126
Figure 4-5: Schematic of LDV working principle.....	127
Figure 4-6: Traverse set-up with LDV	128
Figure 4-7: Flow velocity in the cross-flow direction.	129
Figure 4-8: Layout of costal flume in Mechanical Engineering Department.....	134
Figure 4-9: Image of the flow conditioner.	135
Figure 4-10: Large scale foundation geometries	135
Figure 4-11: Schematic of the flow profiles tested in these tests.	136
Figure 4-12: Acoustic Doppler Velocimetry working principle (source: Sellar et al., 2015).	138
Figure 4-13: (a) Set up of the pressure measurement tests showing the acrylic tubes connecting to the pressure transducer units beneath the flume; (b) Image of 3D model; (c) cut through (from centreline) of model with tubes.	142
Figure 4-14: Location of pressure taps.....	142
Figure 4-15: Side view sketch of the lower part of the pressure measurement apparatus.	143
Figure 4-16: Flow field measurement points in the X-Y plane.	144
Figure 4-17: Flow field measurement points in the X-Z plane.....	144
Figure 4-18: Pressure transducer	145
Figure 5-1: Flow profiles for small scale scour tests: a) h=165mm and b) h=100mm.	150
Figure 5-2: (a) Initiation of scour at 45° conical base structure, (b) bed shear stress amplification contour map for same structure; flow direction from left to right.....	151

Figure 5-3: Time development of scour for tests 1.0-1.5 ($h = 0.165m, d_{50} = 0.6mm$ and $U_c/U_{cr} = 0.73$).....	152
Figure 5-4: Time development of scour for tests 1.6-1.11 ($h = 0.165m, d_{50} = 0.2mm$ and $U_c/U_{cr} = 0.88$).....	153
Figure 5-5: Time development of scour for tests 1.12-1.17 ($h = 0.165m, d_{50} = 0.2mm$ and $U_c/U_{cr} = 0.98$).....	154
Figure 5-6: Time development of scour for tests 1.18-1.23 ($h = 0.165m, d_{50} = 0.6mm$ and $U_c/U_{cr} = 0.88$).....	155
Figure 5-7: Time development of scour for tests 1.24-1.29 ($h = 0.165m, d_{50} = 0.6mm$ and $U_c/U_{cr} = 0.99$).....	155
Figure 5-8: Time development of scour for tests 2.1-2.6 ($h = 0.1m, d_{50} = 0.2mm$ and $U_c/U_{cr} = 0.93$).....	156
Figure 5-9: Time development of scour for tests 2.7-2.12 ($h = 0.1m, d_{50} = 0.6mm$ and $U_c/U_{cr} = 0.78$).....	157
Figure 5-10: Influence of U_c/U_{cr} on scour development for three different structure geometries.....	158
Figure 5-11: Observed scour depth at cylindrical based pier before under-cutting the base cylinder ($h = 0.165m, d_{50} = 0.6mm$ and $U_c/U_{cr} = 0.88$).....	159
Figure 5-12: Influence of water depth on equilibrium scour depth for different structure types (non-dimensionalised by base diameter of the structure).....	162
Figure 5-13: Influence of water depth on equilibrium scour depth for different structure types (non-dimensionalised by equivalent diameter according to Coleman, 2005)....	162
Figure 5-14: Comparison of test 1.5 with Porter (2016) with $D=40mm, U_c = 0.19m/s$ and $d_{50} = 0.6mm$	164
Figure 5-15: Comparison of test 1.11 with Porter (2016) with $D=40mm, U_c = 0.19m/s$ and $d_{50} = 0.2mm$	164
Figure 5-16: Flow profiles for large scale scour tests: a) logarithmic flow profile and b) non-logarithmic flow profiles.....	166

Figure 5-17: Velocity profiles when the wind is opposing the tide (left) and when the wind is following the tide (Source: Holmedal and Myrhaug, 2013).....	166
Figure 5-18: Temporal evolution of scour for a logarithmic flow profile, h=350mm. ...	168
Figure 5-19: Temporal evolution of scour for non-logarithmic flow profile, h=350mm	169
Figure 5-20: Temporal evolution of scour for non-logarithmic flow profile, h=550mm.	170
Figure 5-21: Temporal evolution of scour for the 75deg conical base structure with non-logarithmic flow profile, h=350mm, h=450mm and h=550mm.	170
Figure 5-22: Equilibrium scour depth profiles for Tests 3-1-3.4 at h=350mm and a logarithmic flow profile (flow from bottom): a) Monopile; b) Cylindrical base; c) 45° conical base structure; and d) 75° conical base structure.	172
Figure 5-23: Equilibrium scour depth profiles for Tests 3-5-3.8 at h=350mm and a non-logarithmic flow profile (flow from bottom to up): a) Monopile; b) Cylindrical base; c) 45° conical base structure; and d) 75° conical base structure.....	174
Figure 5-24: Equilibrium scour depth profiles for Tests 3-9-3.12 at h=550mm and a non-logarithmic flow profile (flow from bottom to up): a) Monopile; b) Cylindrical base; c) 45° conical base structure; and d) 75° conical base structure.....	176
Figure 5-25: Equilibrium scour depth profiles 75° conical base structure at three different flow depths and a non-logarithmic flow profile (Tests 3-12-3.14): a) h=550mm; b) h=450mm; and c) h=350mm.....	177
Figure 5-26: Comparison of time development of Test 3.8 and 3.14.	178
Figure 5-27: Comparison of scour contour maps between tests 3.14 and 3.8: a) Test 3.14; b) test 3.8; and c) the difference between 3.8 and 3.14.....	179
Figure 5-28: Flow profile for tests 4.1-4.5.....	180
Figure 5-29: Pressure variation for the cylindrical base structure.	182
Figure 5-30: Pressure variation for the 45° conical base structure.	183
Figure 5-31: Pressure variation for the 60° conical base structure.....	183
Figure 5-32: Pressure variation for the 75° conical base structure.....	184
Figure 5-33: Pressure variation for the monopile structure.....	185

Figure 5-34: Vertical velocity component (w) distribution and u-w velocity vectors along the centreline of the monopile.	186
Figure 5-35: Contours of streamwise velocity component (u) around the monopile at different heights.	187
Figure 5-36: Contours of vertical velocity component (w) around the monopile at different heights.	188
Figure 5-37: Vertical velocity component (w) distribution and u-w velocity vectors along the centreline of the 75° conical base structure.	189
Figure 5-38: Contours of streamwise velocity component (u) around the 75° conical base structure. at different heights.	190
Figure 5-39: Contours of vertical velocity component (w) around the 75° conical base structure. at different heights.	191
Figure 5-40: Vertical velocity component (w) distribution and u-w velocity vectors along the centreline of the 60° conical base structure.	191
Figure 5-41: Vertical velocity component (w) distribution and u-w velocity vectors along the centreline of the cylindrical base structure.	192
Figure 5-42: Contours of streamwise velocity component (u) around the cylindrical base structure at different heights.	193
Figure 5-43: Contours of vertical velocity component (w) around the cylindrical base structure at different heights.	194
Figure 6-1: Definition sketch of main parameters: (a) side view; (b) top view.	198
Figure 6-2: Pressure gradient distribution through the water column [calculated using Eq. (6-8)] for two different structures under the same flow conditions.	204
Figure 6-3: Percentage distribution of non-dimensional quantities in database	206
Figure 6-4: Scour depth as a function of h/D_{base}	210
Figure 6-5: Scour depth as a function of $h/D_{base} Fr$	211
Figure 6-6: Scour depth as a function of $h/D_{base} Fr^{1/\log(ReD)}$	212
Figure 6-7: Scour depth as a function of $h/D_{base} Fr^{1/\log ReD} (U_c/U_{cr})^{0.5}$	212

Figure 6-8: Scour depth as a function of ζ	214
Figure 6-9: Agreement of scour-depth prediction [using Equation (6-17)] and measured scour depths with 10 and 20% confidence bounds	216
Figure 6-10: Comparison of Equation (6-17) with prototype field data.....	217
Figure 6-11: Influence of sediment mobility ratio [$U_c/U_{cr} = 0.74, 0.88$ and 1] on the variation of the equilibrium scour depth as a function of $\langle Eu \rangle$ [Note: Line shows prediction given by Equation (6-17) for each of the three sediment mobility ratios. ...	219
Figure 6-12: Influence of non-dimensional water depth [$h/D_{base} = 3.6$ and 2.2] on the variation of the equilibrium scour depth as a function of $\langle Eu \rangle$ [Note: Line shows prediction given by Equation (6-17) for each of the three sediment mobility ratios. ...	219
Figure 6-13: Influence of vertical flow distribution on the variation of the equilibrium scour depth as a function of $\langle Eu \rangle$ [Note: solid line shows prediction given by Equation (6-17)]	220
Figure 6-14: Influence of ReD on equilibrium scour. Comparison of Equation (6-17) to scour depth data with varying ReD and $Fr = \{0.15 - 0.20\}, U_c/U_{cr} = \{0.7 - 0.85\}, h/D = \{2 - 3\}$ and $\langle Eu \rangle = \{1.7 - 2\}$ (data from dataset collected from current study).....	222
Figure 6-15: Effect of the pile Reynolds number on scour. Comparison of present equation (Equation (6-17)) and the equation of Shen et al, (1969) [Equation 2-54] to the data presented in Breusers et al. (1977) (data source: Sheppard et al., 2011).....	224
Figure 6-16: Definition diagram of the location of the vertical stagnation point.	225
Figure 6-17: Influence of Fr on equilibrium scour. Comparison of Equation (6-17) to scour depth data with varying Fr and $ReD = \{75000 - 150000\}, U_c/U_{cr} = \{0.8 - 1\}, h/D = \{2 - 3\}$ and $\langle Eu \rangle = \{1.7 - 2\}$	226
Figure 6-18: Influence of h/D on equilibrium scour. Comparison of Equation (6-17) to scour depth data with varying h/D and $ReD = 100000 - 300000, U_c/U_{cr} = \{0.8 - 1\}, Fr = \{0.1 - 0.25\}$ and $Eu = \{1.7 - 2\}$	227
Figure 6-19: Effect of boundary layer thickness on scour. Comparison of Equation (6-17) with clearwater scour data compiled from Melville and Sutherland (1988).	228

Figure 6-20: Effect of sediment mobility ratio on scour for monopiles. Comparison of Equation (6-17) to scour depth data with varying U_c/U_{cr} and $ReD = 50000 - 200000, h/D = 3 - 6, Fr = 0.1 - 0.15$ and $Eu = \{1.7 - 2\}$.	229
Figure 7-1: Wave absorber reflection vs incoming wave period (Figure derived from: Edinburgh Designs Ltd, 2005)	231
Figure 7-2: Flow chart of experimental procedure.	233
Figure 7-3: Positions of wave probes (red lines indicate position of the wave probes).	234
Figure 7-4: Layout of scour protection set-up for present tests.	234
Figure 7-5: U-pins used to provide stability to the fabric.	235
Figure 7-6: Rock armour layer set-up: a) first layer of scour protection b) final layout of scour protection with concentric circles.	237
Figure 7-7: Test set-up without the sand pit.	237
Figure 7-8: Large scale foundation geometries	238
Figure 7-9: Comparison of Shields parameter with critical bed shear stress for a range of flow velocities.	239
Figure 7-10: Grain size distribution for the scour protection aggregate used in the experiments.	240
Figure 7-11: Set-up of incipient motion detection method for scour protection stability tests.	241
Figure 7-12: Example of particle tracking recognition: a) image at time frame t ; b) image at time frame $t+1$; and c) result of the subtraction of the two images.	242
Figure 7-13: Working principle of photogrammetry [source: Cuypers et al. ,2009]	243
Figure 8-1: Flow profiles for scour protection stability tests (5.1-5.12 & 6.1-6.16).	258
Figure 8-2: Examples of wave profiles from present tests.	259
Figure 8-3: Distribution of tests as a function of the Ursell number.	259
Figure 8-4: Wave induced Shields parameter (θ) as a function of the non-dimensional stone diameter (D^*): $T=1.5s, H=0.16m$.	261

Figure 8-5: Wave induced Shields parameter (θ) as a function of the non-dimensional wave height (H/h): $T=1.5s$, $D=6.5mm$	261
Figure 8-6: Wave induced Shields parameter (θ) as a function of the non-dimensional wave period (Tg/h): $H=0.16$, $D=6.5mm$	262
Figure 8-7: Influence of non-dimensional stone size on the amplification of the bed shear stress for different geometries (lines are linearly interpolated between points): a) waves only; b) $Uc = 0.18m/s$ and waves and c) $Uc = 0.29m/s$ and waves.....	264
Figure 8-8: Influence of scour protection configuration on the amplification of the bed shear stress for different geometries (lines are linearly interpolated between points): a) waves only, $T=1.4-1.5s$; b) waves only, $T=2s$; c) $Uc = 0.18m/s$ and waves, $T=1.4-1.5s$; d) $Uc = 0.18m/s$ and waves, $T=2s$; e) $Uc = 0.29m/s$ waves, $T=1.4-1.5s$; and f) $Uc = 0.29m/s$ waves, $T=2s$	265
Figure 8-9: Influence of bed permeability on the amplification of the bed shear stress for different geometries: a) waves only, $T=1.2s$ and $D50=3.5mm$; b) waves only, $T=1.4-1.5s$ and $D50=3.5mm$; c) waves only, $T=2s$ and $D50=3.5mm$; d) waves only, $T=1.5s$ and $D50=10.5mm$	266
Figure 8-10: Influence of flow direction on the amplification of the bed shear stress for different geometries: a) $D50=6.5mm$ and $T=1.2s$; b) $D50=10.5mm$ and $T=1.5s$; c) $D50=10.5mm$ and $T=1.5s$; d) $D50=10.5mm$ and $T=2s$; and e) $D50=10.5mm$ and $T=2.5s$	267
Figure 8-11: Influence of wavelength on the amplification of the bed shear stress for different geometries: $D50=6.5mm$, waves only.....	268
Figure 8-12: Influence of velocity ratio (Ucw) on the amplification of the bed shear stress for different geometries: $D50=6.5mm$	269
Figure 8-13: Influence of the Keulegan–Carpenter number (KC) and the amplitude of the wave orbital motion (A) on the amplification of the bed shear stress for different geometries, the colour map shows the velocity ratio and the lines a conservative estimate of the trend of the corresponding data.	271

Figure 8-14: Flow chart for the calculation of the required stone size for scour protections cover layer.	273
Figure 8-15: Comparison of present design curves with published experimental results.	275
Figure 8-16: Damage induced by a cylinder in the following flow regimes: waves only; wave dominated; and current dominated after N number of waves (flow and waves in positive X-direction).	278
Figure 8-17: Damage induced by a cylinder in current only flow conditions after t=1hr and 15min (flow in positive X-direction).	279
Figure 8-18: Damage induced by a 75° conical base structure in the following flow regimes: waves only; wave dominated; and current dominated after N number of waves (flow and waves in positive X-direction).	280
Figure 8-19: Damage induced by a 75° conical base structure in current only flow conditions after t=3hr and 1min (flow in positive X-direction).	281
Figure 8-20: Damage induced by a 45° conical base structure in the following flow regimes: waves only; wave dominated; and current dominated after N number of waves (flow and waves in positive X-direction).	283
Figure 8-21: Damage induced by a 45° conical base structure in current only flow conditions after 3hr and 21min (flow in positive Y-direction).	284
Figure 8-22: Damage induced by a cylindrical base structure in the following flow regimes: waves only; and wave dominated after N number of waves (flow in positive Y-direction and waves in Y-direction).	285
Figure 11-1: K_g as a function of σ_g (Source: Raudkivi and Ettema, 1985).....	313
Figure 11-2: Definition sketch of pile group configurations.	315
Figure 11-3: Pile-group factor for side-by-side pile configuration (configuration (a) in Figure 11-3); (Source: Hannah, 1978).....	316
Figure 11-4: Pile-group factor for tandem pile configuration (configuration (b) in Figure 11-3); (Source: Hannah, 1978).....	316

Figure 11-5: Pile-group factor for staggered pile configuration (configuration (c) in Figure 11-3); (Source: Hannah, 1978).	317
Figure 12-1: Scour profile along the plane of symmetry of the structure for Tests 3-1-3.4 (flow from left to right).	318
Figure 12-2: Scour profile along the plane of symmetry of the structure for Tests 3-5-3.8 (flow from left to right). The black circle highlights the avalanching at the upstream of the scour hole.	318
Figure 12-3: Scour profile along the plane of symmetry of the structure for Tests 3-9-3.12 (flow from left to right).	319
Figure 12-4: Scour profile along the plane of symmetry of the structure for Tests 3-12-3.14 (flow from left to right).	319

List of Tables

Table 2-1: Representative studies on scour around uniform cylinders used in this study.	75
Table 2-2: Summary of scour protection thickness recommendations.....	107
Table 4-1: Wet and dry density for both sediment types.....	126
Table 4-2: Small scale scour experiments programme.....	131
Table 4-3: Large scale scour experiments programme.....	140
Table 4-4: Flow and pressure measurement programme	146
Table 4-5: Sources of data for scour prediction equation.	147
Table 5-1: Equilibrium scour depth for small scale scour experiments.	159
Table 5-2: Equilibrium scour depth for large scale experiments.	171
Table 5-3: Upstream and downstream slopes of the scour slope for tests 3.5-3.8.....	174
Table 6-1: Summary of sources populating the scour database.....	207
Table 7-1: Summary of hydraulic conditions for scour protection stability tests	239
Table 7-2 Values used for determination of incipient motion criterion.....	242
Table 7-3: Experimental programme for scour protection stability tests.....	245
Table 7-4: Summary of scour protection damage progression tests.....	256
Table 8-1: Tested parameters.....	263
Table 11-1: Shape factor for different structure geometries.....	314

Nomenclature

Symbol	Definition
A_0	Non-dimensional quantity for the determination of the separation distance in combined waves and currents
A_{flow}	Cross-sectional area of channel projected to the flow
A_{model}	Cross-sectional area of the structure
A_p	Area of sediment particle exposed to the flow
A_Ω	Area considered in the observation
ADV	Acoustic Doppler Velocimetry
b_0	Coefficient for Equation (2-101)
b_1	Coefficient for Equation (2-101)
C	Chezy coefficient
C_D	Drag coefficient
C_L	Lift coefficient
C_m	Inertia coefficient
C_p	Pressure coefficient
c	Wave celerity
c_1	Fit coefficient for equation (6-17)
c_2	Fit coefficient for equation (6-17)
c_3	Fit coefficient for equation (6-17)
D	Pile diameter
D_{base}	Diameter of base of non-uniform cylindrical structure
D_{eq}	Equivalent diameter of structure
D_{shaft}	Diameter of top shaft of non-uniform cylindrical structure
D_{30}	30th percentile rock size grading

D_{50}	Mean diameter of scour protection rock
D_*	Non-dimensional grain size
d	Constant for Equation (6-20)
$d_{10,b}$	10th percentile of bed material size grading
$d_{15,b}$	15th percentile of bed material size grading
$d_{15,f}$	15th percentile of filter material size grading
d_{16}	16th percentile grain size grading
d_{50}	Mean diameter of sediment
$d_{50,b}$	50th percentile of bed material size grading
$d_{50,f}$	50th percentile of filter material size grading
$d_{60,b}$	60th percentile of bed material size grading
d_{84}	84th percentile grain size grading
$d_{85,b}$	85th percentile of bed material size grading
$d_{85,f}$	85th percentile of filter material size grading
d_{90}	90th percentile grain size grading
Eu	Euler number
e	constant for Equation (6-19)
F_D	Drag force
F_L	Lift force
F_s	Contact force between sediment particles
F_{safe}	Safety factor
Fr	Froude number
f	Weisbach coefficient
$f(t)$	Correction factor for the influence of the time in Equation (2-86)
f_1	Correction factor for the influence of waves in Equation (2-86)

f_2	Correction factor for the influence of combined waves and currents in Equation (2-86)
f_3	Correction factor for the influence of sediment mobility ratio in Equation (2-86)
f_4	Correction factor for the influence of structure height in Equation (2-86)
f_5	Correction factor for the influence of the shape of the structure in Equation (2-86)
f_6	Correction factor for the influence of the flow depth in Equation (2-86)
f_i	Product of all correction factors for scour depth estimation in Equation (2-86)
f_L	Dominant list frequency
f_v	Vortex shedding frequency
f_w	Wave friction factor
f_{wave}	Wave frequency
GBF	Gravity Based Foundation
g	Acceleration of gravity
H	Wave height
h	Flow depth
h_c	Height of the top side of the foundation base taken from original bed level
K_{gr}	Correction factor for the effect of pier group in Equation (2-56)
K_i	Product of all correction factors for scour depth estimation
K_s	Correction factor for the shape of the foundation in Equation (2-56)
K_{shape}	Correction factor for the shape of the foundation in Equations (2-80) and (2-81)
K_σ	Correction factor for the sediment gradation in Equation (2-56)
K_ω	Correction factor for the foundation orientation in Equation (2-56)
KC	Keulegan-Carpenter number

k	Wave number
k_s	Nikuradse roughness length scale
L	Wavelength
L_s	Lateral extend of scour protection
LCRV	Longitudinal Counter-Rotating Vortices
LDV	Laser Doppler Velocimetry
LNG	Liquefied Natural Gas
LPG	Liquefied Petroleum Gas
m	Similarity number of moving sediment particles according to Neil (1968)
N	Dynamic similarity number for sediment grain movement
N_L	Non-dimensional lift frequency
n	Manning number
n_1	constant for scour time development
n_f	Porosity of filter material
n_L	Geometric length scale
n_{ld}	Scale of large sediment particles
n_{sd}	Scale of small sediment particles
n_w	Scale of settling velocity
p	Pressure at the structure at a height z from the bed
p_∞	Freestream pressure at a height z from the bed
R	Radius of cylinder
Re	Reynolds number
Re_*	Grain Reynolds number
Re_D	Reynolds number of structure
r	Distance taken from the centre of cylinder
S	Scour depth

$S_{c,eq}$	Equilibrium scour depth due to current action
$S_{cw,eq}$	Equilibrium scour depth due to combined wave and current action
$S_{w,eq}$	Equilibrium scour depth due to wave action
S_{3D}	Damage number
S_{eq}	Equilibrium scour depth
St	Strouhal number
$Stab$	Stability number for OPTI-PILE method
T	Wave period
T_e	Time scale of scour for Equation (2-86)
T_{rel}	Relative wave period of combined waves and currents
T_{sc}	Time scale of scour process defined as the time required to reach 63% of total scour depth.
T^*	Non-dimensional time scale of scour
t	Time
t_1	Characteristic time scale of scour process
t_c	Thickness of scour protection
t_{eq}	Time required to reach equilibrium scour depth
t_f	Thickness of filter material
U_c	Streamwise depth averaged flow velocity
U_{cr}	Mean threshold velocity of sediment
U_{cw}	Relative flow intensity
U_{des}	Local design velocity in Equation (2-98)
U_f	Friction velocity
U_{lp}	Velocity corresponding to the live bed peak
U_w	near bed wave orbital velocity

Ur	Ursell number
U_{∞}	Freestream velocity corresponding to the frictionless undisturbed flow
u	Streamwise velocity component
u_*	Characteristic bed shear velocity or friction velocity
$u_{*,c}$	Critical friction velocity for given sediment size
V_p	Volume of particle
v	Cross-flow velocity component
W	Weight
W_{scour}	Width of scour hole
w	Vertical velocity component
w_s	Settling velocity of sediment
X	Distance in streamwise direction
x	Distance from leading edge of the plate
x_s	Separation distance in front of structure
Y	Distance in the cross-flow direction
y	vertical location of stagnation point
Z	Distance in the vertical direction
z	Distance from original bed
z_0	Bed roughness length scale
α	Amplification of the bed shear stress
α_{cor}	Correction factor for the shape of the foundation in Equation (2-76)
α_{crit}	Critical amplification of the bed shear stress
α_w	Amplitude of wave
γ	Specific weight of water
γ_1	Constant ranging between 0.2-0.4

γ_s	Specific weight of sediment
Δ	Relative density of sediment
Δ_b	Relative density of bed material
Δ_f	Relative density of filter material
δ	Boundary layer thickness
ε	Similarity number of moving sediment particles according to Yalin (1977)
θ	Shields parameter
θ_{cr}	Critical Shields number for incipient motion
θ_{max}	Maximum Shields parameter for combined waves and currents
κ	Von Karman constant
μ	Dynamic viscosity
ν	Kinematic viscosity
ρ	Density of water
ρ_s	Density of sediment
$\sigma_{Seq/D}$	Standard deviation of scour depth measurements
σ_g	Geometric standard deviation of sediment
τ_0	Undisturbed bed shear stress due to current
τ_b	Bed shear stress at a location near the structure
τ_{cr}	Critical bed shear stress for incipient motion
τ_{max}	Maximum bed shear stress in combined waves and currents
τ_{mean}	Mean bed shear stress in combined waves and currents
τ_w	Undisturbed bed shear stress due to waves
τ_∞	Undisturbed bed shear stress
φ	Angle relative to the flow direction
φ_{dir}	Angle between flow and wave direction

φ_{down}	Downstream scour slope
φ_r	Angle of repose of sediment
φ_{up}	Upstream scour slope
χ_{eff}	Correction factor for the calculation of equilibrium scour depth due to wave action in Equation 2-65
χ_{rel}	Correction factor for the calculation of equilibrium scour depth due to combined wave and current action in Equation 2-70
Ω	Filter material mobility number
ω	Absolute radial frequency of wave

List of publications

Tavouktsoglou, N.S., Harris, J.M., Simons, R.R. and Whitehouse, R.J. (2015). Bed shear stress distribution around offshore gravity foundations. Proceedings of the ASME 2015 34th International Conference on Ocean, Offshore and Arctic Engineering, OMAE2015, St. John's Newfoundland, Canada, May 31 – June 5, Paper No. OMAE2015-41966, American Society of Mechanical Engineers, pp. V007T06A051-V007T06A051.

Tavouktsoglou, N. S., Harris, J. M., Simons, R. R., and Whitehouse, R. J. (2016). Equilibrium scour prediction for uniform and non-uniform cylindrical structures under clear water conditions. Proceedings of the ASME 2016 35th International Conference on Ocean, Offshore and Arctic Engineering, OMAE2016, Busan, South Korea June 5-10, Paper No. OMAE2016-54377, American Society of Mechanical Engineers, pp. V001T10A007-V001T10A007.

Tavouktsoglou, N. S., Harris, J. M., Simons, R. R., and Whitehouse, R. J. S. (2016). Scour development around structures with non-uniform cylindrical geometries. Proceedings of the 8th International Conference on Scour and Erosion, ICSE2016, Oxford, UK, 12-15 September 2016, (p. 355). CRC Press.

Tavouktsoglou, N. S., Harris, J. M., Simons, R. R., & Whitehouse, R. J. S. (2017). Equilibrium Scour-Depth Prediction around Cylindrical Structures. Journal of Waterway, Port, Coastal, and Ocean Engineering, 143(5), 04017017.

Acknowledgments

Firstly, I would like to express my sincere gratitude to my supervisors Professors Richard Simons, Richard Whitehouse and Dr John Harris for the continuous support of my Eng.D study and related research, for their patience, motivation, and immense knowledge. Their guidance helped me in all the time of research and writing of this thesis. I could not have imagined having better advisors and mentors for my Eng.D study.

Special thanks to the Engineering and Physical Sciences Research Council (EPSRC) for funding this research project.

I would like to thank Leslie Ansdell and Keith Harvey for their invaluable help with numerous aspects of the laboratory tests as well as the rest of the technical team for helping me prepare the experiments. Without their precious support it would not be possible to conduct this research.

I thank my fellow researchers and friends Dimitrios Stagonas, Kate Porter and Mohammed Al-Hammadi for the stimulating discussions and for all the fun we have had in the last three years.

Last but not the least, I would like to thank my parents and Maria for supporting me throughout writing this thesis and my life in general. They are the most important people in my world and I dedicate this thesis to them.

Part I: General overview of the project

1 Introduction

1.1 General overview of the research

The present research is motivated by the need for a better understanding of scour around marine and offshore foundations. The project is focused in particular on improving the analysis methods for the scour process and scour protection stability around Gravity Based Foundations (GBFs). To this end, the present work considers the flow-structure-sediment interaction around complex geometries such as the ones possessed by GBFs. As will be shown in Chapter 2 the current literature on scour and scour protection has numerous gaps when it comes to the complex geometries and particularly large foundation such as GBFs. Thus, this thesis aims to address these gaps, through an extensive laboratory investigation. It further aims to provide designers with tools that could lead to the most cost effective design of GBFs through the more accurate estimation of the scour depth and stone size required for scour protection.

1.2 Background

Although concrete GBFs have been used since the beginning of the twentieth century as quay-walls, offshore light houses, bridge piers and breakwaters, the oil and gas industry in the North Sea in the late 1960's has initiated a new era for the use of these types of structure in modern offshore economic development. Since then GBFs have been used as a support system for many offshore structures situated in deep water depths (30m and deeper) which include subsea storage units, and nearshore LNG and LPG terminals. Due to their size these types of structure have only recently been considered as a viable support structure for offshore wind turbines.

Interest in renewable energy on a global level has enabled the offshore wind industry to plan and construct a large number of offshore wind farms in shallow waters (5 to 30m). Due to the increasing demand in offshore wind energy, wind farm locations are being

planned in deeper waters (30 to 60m). These locations are characterized by hydraulic conditions that are similar to those faced by offshore oil platforms where the wave loading on the structure can be large, but the influence of waves on scour may be less pronounced than in shallow water and tidal currents are more dominant. In these locations GBFs become a more cost effective support structure for wind turbines. The challenge introduced by these projects is the considerable increase of the required number of foundations, which has a significant effect on the total cost of the project. It is estimated that 35% (average over all types of foundations) of the total cost of offshore wind turbines is attributed to foundation design (Figure 1-1). This figure accounts for both the construction of the foundation and the measures taken to protect it from erosion.

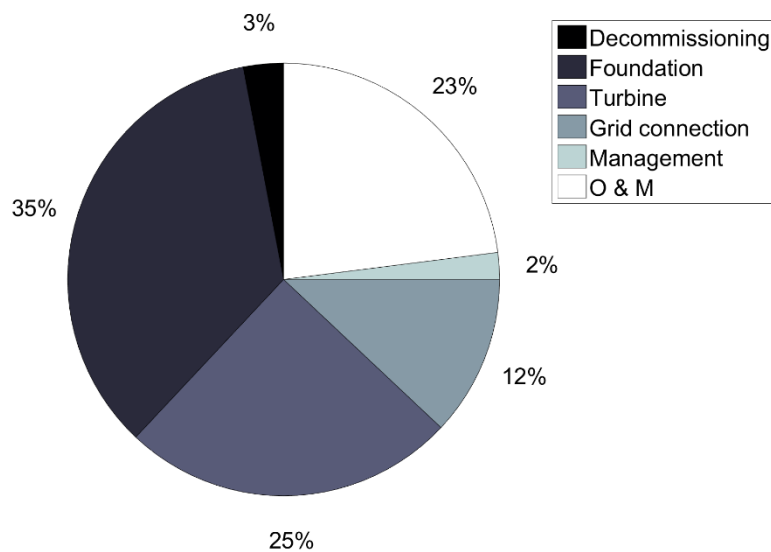


Figure 1-1: Breakdown of costs for offshore wind turbines. [Data derived from Blanco (2009)].

An important step towards reducing the cost of the foundations is by the examination and the in-depth understanding of the hydrodynamic processes around the support structure that lead to scour. Scour here is defined as the erosion of the seabed material around the structure due to the change of the local flow conditions. The reduction of this risk of failure can be achieved through two main methods:

- The close examination of the scour process in order to understand in detail the effect GBFs have on the depth and extent of scour. This can allow the more efficient design of the footing depth which will reduce the need to overdesign the skirt depth to overcome underscour and changes to the bearing area of the foundation.
- The more effective design of scour protection schemes which minimise the effects of scour, thus reducing the installation depth of the footing into the bed.

Scour protection also reduces the variation of the natural frequency of the structure, which leads to a higher efficiency of the wind turbine (Zaaijer, 2004). Therefore, the systematic research of scour and methods to protect wind turbines from it are most important subjects that will lead to a more affordable and efficient provision of sustainable renewable energy.

1.3 Thesis outline

This thesis is structured in four main parts:

- The first part presents a general overview of the key aspects tackled in this work. Chapter 1 begins by presenting the motivation for the present work and the background of the study. The literature review then follows in chapter 2; within this chapter the key gaps and shortcomings in previous research are identified. Having recognised the gaps in literature, chapter 3 details the aims and objectives of the present research.
- The second part of this thesis focuses on scour around Gravity Based Foundations. Chapter 4 presents the methodology followed for the scour experiments and for the scour prediction equation. The results of the experiments are then presented in chapter 5. The next chapter then presents the derivation of the scour prediction equation.
- The third part of the study focuses on the study of scour protection behaviour around GBFs. The methodology for the scour protection tests is explained in chapter 7. Chapter 8 presents the results scour protection results and the discussion of the results obtain by the experiments along with a design diagram that can be used for the selection of the appropriate rock armour size for scour protection systems.
- Finally, chapter 9 presents the conclusions derived from this study and proposals for future research.

2 Literature review

2.1 Introduction

Any structure in a marine and fluvial environment is subject to the prevailing flow conditions which are then altered by the local flow field around the structure. Where this change in the local flow pattern leads to an increase in flow strength or enhanced turbulence, and thus the local sediment transport capacity of the system is increased. Therefore, it is important for any research study that focuses on scour and scour protection to start with a summary of the existing knowledge related to the flow patterns observed around these kind of structures. In order to understand how the flow field is altered by a structure one needs first to understand the behaviour of the undisturbed flow field as well as the effect of the structure. The literature review within this thesis will focus on the following relevant topics:

- Sediment transport and boundary layer theory;
- Flow structure interaction;
- Scour around cylindrical structures; and
- Scour protection around cylindrical structures.

2.2 Sediment transport and boundary layer theory

Sediment transport is caused primarily by the local fluid friction induced by a given hydrodynamic forcing (current, waves or combination of the two). This forcing is expressed through the bed shear stress (τ_0) and can be represented as a characteristic shear velocity (u_*) according to equation (2-1):

$$u_* = \sqrt{\frac{\tau_0}{\rho}} \quad (2-1)$$

where ρ is the density of water.

The shear stress can also be represented in a non-dimensional form (θ) which is named after Shields who first investigated the relationship between bed shear stress and the sediment properties.

$$\theta = \frac{\tau_0}{g(\rho_s - \rho)d_{50}} = \frac{\rho u_*^2}{g(\rho_s - \rho)d_{50}} \quad (2-2)$$

where g is the acceleration of gravity; ρ_s the density of the sediment; and d_{50} the mean diameter of the sediment

When considering sediment transport, the most important section of the flow is the boundary layer. According to Schlichting (1968) the boundary layer is defined as the section (δ) of the flow in which the velocity increases from zero (i.e. a no slip condition) at the boundary to its full value corresponding to that of external frictionless flow (Figure 2-1). According to Schlichting (1968) in the case of a laminar boundary layer this boundary layer length (δ) can be approximated by making use of the von Karman integral equation as:

$$\delta = 5 \sqrt{\frac{\nu x}{U_\infty}} \quad (2-3)$$

where x is the distance from leading edge of the plate (see Figure 2-1); ν is the kinematic viscosity of the fluid; and, U_∞ is the velocity corresponding to the frictionless undisturbed flow (freestream velocity).

For the case of a turbulent boundary layer the boundary layer thickness can be approximated using the von Karman integral equation in conjunction with the Blasius formula which yields:

$$\delta = 0.38x \left(\frac{\nu}{xU_\infty} \right)^{\frac{1}{5}} \quad (2-4)$$

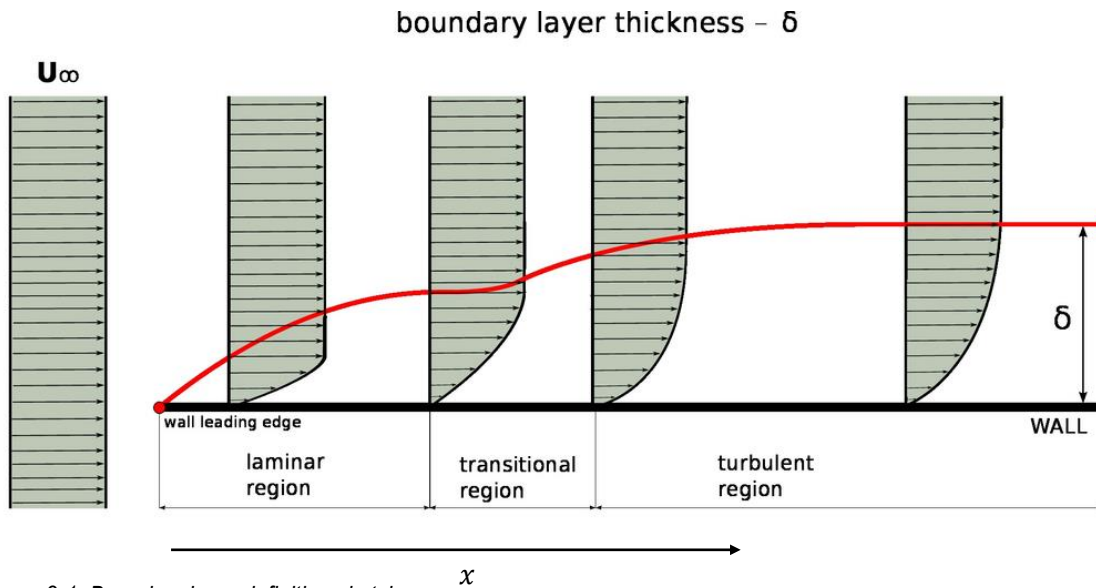


Figure 2-1: Boundary layer definition sketch

The boundary layer and consequently the bed shear stress induced by the flow is treated in a different manner for unidirectional currents, waves and combined waves and currents. This is due to the oscillatory nature of a wave's orbital velocities which do not allow the boundary layer to grow significantly compared to a unidirectional current. This applies also to the case of tides which is periodic flow and results in boundary layer thickness of $O(10)$ cm. Smaller boundary layer thicknesses for the same undisturbed flow velocities along with the acceleration and deceleration are associated with larger amounts of turbulence (Hoffmans, 2012) compared to steady flows, and thus higher sediment transport capacity (see next sections).

2.2.1 Steady uniform flow

As stated previously the bed shear stress is the frictional force exerted by the flow on a unit area of the bed. According to Soulsby (1997) the bed shear stress for a uniform, flat bed of cohesionless sediment is given by:

$$\tau_0 = \rho C_D U_c^2 \quad (2-5)$$

where U_c is the depth-averaged flow velocity; and, C_D is the drag coefficient given by the quadratic friction law.

The value of C_D can be obtained by numerous methods which include the Darcy-Weisbach coefficient (f), Chezy coefficient (C) and the Manning number (n), which relate C_D through the following relationship:

$$C_D = \frac{f}{8} = \frac{g}{C^2} = \frac{gn^2}{h^{\frac{1}{3}}} \quad (2-6)$$

The main methods for determining (C_D) recommended by Soulsby (1997) are given below:

$$C_D = \left[\frac{\kappa}{1 + \ln\left(\frac{z_0}{h}\right)} \right]^2 \quad (2-7)$$

or

$$C_D = \begin{cases} \frac{0.03}{\left(\log\left(\frac{12h}{\frac{3.3\nu}{u_*}}\right)\right)^2}, \text{ for } \frac{u_*k_s}{\nu} \leq 5 \text{ (hydrodynamically smooth flow)} \\ \frac{0.03}{\left(\log\left(\frac{12h}{k_s}\right)\right)^2}, \text{ for } \frac{u_*k_s}{\nu} \geq 70 \text{ (hydrodynamically rough flow)} \end{cases} \quad (2-8)$$

where h is the flow depth;

κ the von Karman constant, taken as 0.4 for an open channel flow; k_s is the Nikuradse roughness length scale, taken as $2.5D_{50}$; and, z_0 is the bed roughness length. The limits of applicability in Equation 2-8 are based on the particle Reynolds number:

$$Re_* = \frac{u_*d_{50}}{\nu} \quad (2-9)$$

The bed roughness length (z_0) is a function of the viscosity, flow velocity and the roughness of the bed, and can be calculated using the Christoffersen and Jonsson (1985) equation which reads:

$$z_0 = \frac{k_s}{30} \left[1 - \exp\left(-\frac{u_* k_s}{27\nu}\right) \right] + \frac{\nu}{9u_*} \quad (2-10)$$

2.2.2 Wave boundary layer

In the case of waves, the boundary layer has an oscillatory behaviour and reverses at every half-cycle of the wave assuming that the water depth is sufficiently small ($\frac{h}{L} < 0.5$).

In this layer the amplitude of the orbital velocity increases from zero at the bed to the value of the near bed orbital velocity (U_w) at the top of the boundary layer. The value of the bed orbital velocity can be determined using linear wave theory as:

$$U_w = \frac{\pi H}{T \tanh(kh)} \quad (2-11)$$

where k is the wave number defined as $k = \frac{2\pi}{L}$; T is the wave period; H is the wave height; and, L is the wavelength which can be determined iteratively using the following expression:

$$L = \frac{gT^2}{2\pi} \tanh\left(\frac{2\pi h}{L}\right) \quad (2-12)$$

For gravity waves the boundary layer does not exceed the thickness of a few centimetres. Compared to steady flows this is $O(100)$ smaller. In the absence of a steady current the turbulence is contained within the boundary layer which in turn yields larger bed shear stresses compared to a steady current. The bed shear stress for such a boundary layer can be determined though the following expression:

$$\tau_w = \frac{1}{2} \rho f_w U_w^2 \quad (2-13)$$

where f_w is the wave friction factor which can be estimated by various methods, the most widely used of which are presented below.

For hydrodynamically smooth boundary layers f_w can be determined analytically via the (Schlichting, 1968) method:

$$f_w = \frac{2\sqrt{\frac{2\pi\nu}{T}}}{U_w} \quad (2-14)$$

For hydraulically rough flows, significantly more methods have been proposed. This is because in most practical applications the boundary layer is rough.

Swart (1974) derived a semi-empirical expression for the determination of the wave friction factor which reads as:

$$f_w = \exp\left\{-5.977 + 5.213\left(\frac{U_w T}{2\pi k_s}\right)^{-0.194}\right\} \quad (2-15)$$

Myrhaug (1989) gives an implicit relationship for the friction factor which is based on Christoffersen and Jonsson (1985) and can be solved iteratively:

$$\frac{0.32}{f_w} = \left\{ \ln\left(6.36 \frac{U_w T}{2\pi k_s} f_w^{\frac{1}{2}}\right) - \ln\left(1 - \exp\left(-0.0262 \frac{U_w k_s}{\nu} f_w^{\frac{1}{2}}\right)\right) \right\} \quad (2-16)$$

Nielsen (1992) suggests the following expression for the wave friction factor:

$$f_w = \exp\left[\left(\frac{5.5U_w T}{2\pi k_s}\right)^{-0.2} - 6.3\right] \quad (2-17)$$

Soulsby (1997) also recommends a formulation of the friction factor which was developed through a best fit analysis from experimental data retrieved from seven different sources. The expression reads:

$$f_w = 1.39\left(\frac{U_w T}{2\pi z_0}\right)^{-0.52} \quad (2-18)$$

Simons et al. (2001) conducted a number of experiments at different scales and recommended the following expression:

$$f_w = 0.33\left(\frac{U_w T}{2\pi k_s}\right)^{-0.82} \quad \text{for } \frac{U_w T}{2\pi k_s} < 30 \quad (2-19)$$

Equation (2-19) also agrees with the findings of Dixen et al (2008) who found that the friction factor is equal to:

$$f_w = 0.32 \left(\frac{U_w T}{2\pi k_s} \right)^{-0.8} \text{ for } 0.2 < \frac{U_w T}{2\pi k_s} < 20 \quad (2-20)$$

Dixen et al. (2008) also noted a phase difference between the free surface elevation and the friction velocity. They recorded a phase difference ranging between 10° and 30° which differs significantly from the laminar solution which yields 45° (Friedrichs and Aubrey, 1994).

2.2.3 Wave current interaction

In most parts of the coastal and offshore environment waves and tidal currents co-exist. The interaction between the two processes is not linear and thus a simple addition of any aspect of their behaviour will not suffice. For the purpose of offshore structures two interactions are of particular interest according to Soulsby (1997):

- Wave current refraction which modifies the wavelength of the wave; and
- Interaction of the boundary layer of waves and currents which leads to an enhancement of the bed shear stress.

2.2.3.1 Wavelength modification

When waves propagate in the presence of a current their wavelength is modified, when viewed from a stationary reference frame. This change is caused by the Doppler effect. Thus by applying the Doppler principle to the dispersion relation for waves the following expression is obtained:

$$(\omega - U_c k \cos(\varphi_{dir}))^2 = gk \tanh(kh) \quad (2-21)$$

Where φ_{dir} is the angle between the flow and the wave direction and ω is the absolute radial frequency defined as:

$$\omega = \frac{2\pi}{T} \quad (2-22)$$

The relative wave period of the combined wave and current (T_{rel}) can thus be estimated by through the Doppler principle, which leads to:

$$T_{rel} = \frac{c + U_c}{c} T \quad (2-23)$$

where c is the wave celerity which is given:

$$c = \frac{L}{T} \quad (2-24)$$

A change in the wavelength implies that the bed orbital velocity is also changed. Therefore, the bed orbital velocity due to the change in the wavelength can be obtained by substituting T_{rel} to Equation (2-11) which leads to the following expression:

$$U_w = \frac{\pi H}{T_{rel} \tanh(kh)} \quad (2-25)$$

2.2.3.2 Wave current boundary layer

The bed shear stress beneath waves and currents is enhanced in a non-linear way. This means that the combined effects of waves and currents in the boundary layer cannot be obtained by a simple superposition of the two. Soulsby (1997) mentions that there are more than twenty models that describe this interaction. In a general case the total shear stress of the flow can be divided into two components τ_s and τ_f , where τ_f is the shear stress contributed by the Reynolds stresses and τ_s is the component attributed to the viscous shear stress. The latter usually contributes only a small amount of the bed shear stress and thus can be neglected.

In a combined wave and current environment, the water column can be divided into three zones according to Lundgren (1971). The first zone (I) located in the viscous sublayer near the bed is dominated by the Reynolds stresses attributed to the wave orbital motion. The thickness of this zone decreases for an increasing magnitude current. The second zone (II) is characterised by the interaction of the viscous stresses attributed to both waves and currents where the magnitudes of these forces are of the same order of magnitude. Finally, the third zone (III) is ruled by the current-induced stresses. The above

characterisation of the water column suggests that the vertical distribution of the flow velocities will also be affected and thus also the bed shear stresses (see Figure 2-2).

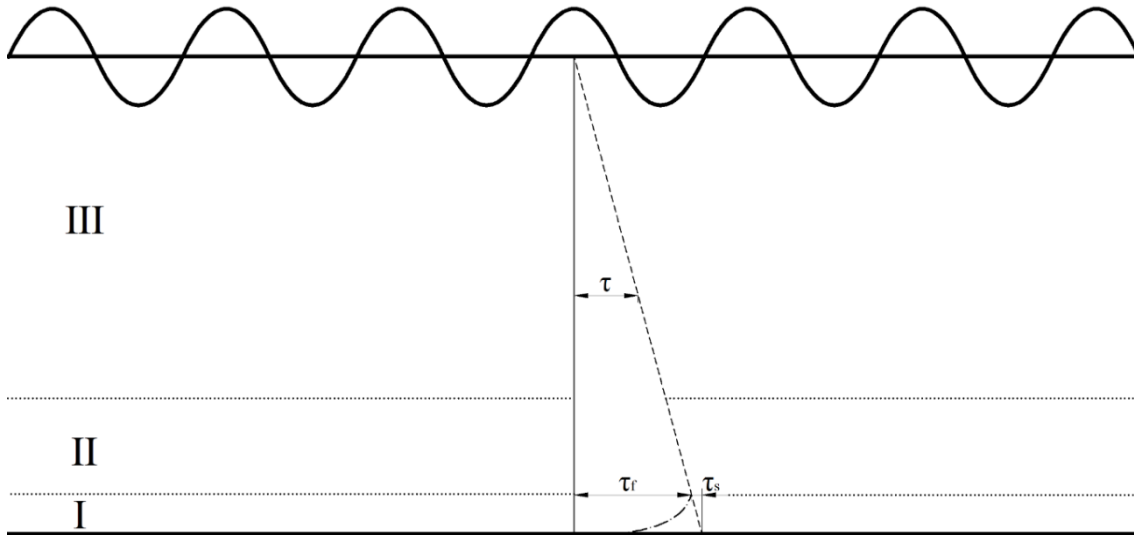


Figure 2-2: Definition sketch and zones of turbulence (proposed by Lundgren, 1971).

As mentioned above, there are different methods for determining the combined effects of waves and currents on the bed shear stress (e.g. Fredsøe and Deigaard, 1992; Soulsby et al., 1993; and Soulsby and Clarke, 2005). In this section only the method proposed by Soulsby et al. (1993) is presented, as it provides an algebraic approximation to most of the models which is accurate to 5% in most cases (Soulsby, 1997).

$$\tau_{mean} = \tau_0 \left(1 + 1.2 \left(\frac{\tau_w}{\tau_0 + \tau_w} \right)^{3.2} \right) \quad (2-26)$$

$$\tau_{max} = ((\tau_{mean} + \tau_w \cos \varphi_{dir})^2 + (\tau_w \sin \varphi_{dir})^2)^{0.5} \quad (2-27)$$

Where φ_{dir} is the angle between the flow and wave direction.

According to Soulsby (1997) the maximum bed shear stress (τ_{max}) should be used for calculations involved in the determination of incipient sediment motion, while the mean

bed shear stress (τ_{mean}) should be used when determining sediment diffusion, both of which are relevant to scour processes.

2.2.4 Incipient motion of sediment particles

It is of importance first to identify and understand the forces that act on a sediment particle in order to study the process of incipient motion. When a stationary sediment particle is in contact with any flow the sum of the forces acting on it need to be in balance; if not in balance the particle will be in motion. Three main forces can be identified: contact forces from other particles F_s , weight (W) and the hydraulic forces which include drag (F_D) and lift (F_L).

F_s and W are related to the weight of the particle acting at its centre of gravity in the vertical direction. It can be determined by multiplying the volume of the particle with the specific weight of the particle. The contact forces are basic reactions exerted by the particles against which the element rests. The magnitudes of these forces are a function of the weight and shape of the particle as well as the resulting fluid force.

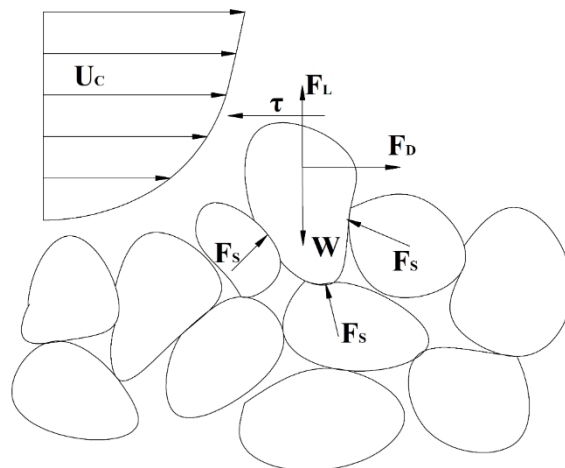


Figure 2-3: Definition sketch of forces acting on a single sediment particle.

The fluid forces acting on the particle are more complicated and will be treated separately below.

For steady currents, the drag force acting on a particle is given by the following expression:

$$F_D = \frac{1}{2} \rho C_D A_p U_c |U_c| \quad (2-28)$$

where C_D is the drag coefficient, which is a function of the particle Reynolds number and varies between 0.5 for wave dominated flow conditions and 1.5 for current dominated conditions (Dixen et al., 2008).

A_p is the area of the particle which is exposed to the flow.

In the case of oscillatory flow, there are two additional contributions to the total fluid force:

$$F_D = \frac{1}{2} \rho C_D A_p u |u| + C_m \rho V_p \frac{du}{dt} + \rho V_p \frac{du}{dt} \quad (2-29)$$

where V_p is the volume of the particle; u could be the orbital velocity, the combined wave-current velocity near the bed or the steady current; C_m is the inertia coefficient which takes the value of 0.5 for the range of the sediment Reynolds number involved in most sediment transport and scour protection problems (Massey and Smith, 1998).

The second term on the right hand side of Equation (2-29) is the hydrodynamic mass force which is caused by the acceleration of the fluid in the surrounding of the body. The third term is known as the Froude-Krylov force, which is produced by the pressure gradient acting on the particle.

The lift force acting on a sediment grain is attributed to four factors according to Vithana (2012):

- Vortex shedding at the lee of the particle;
- The influence of the pressure gradient induced by other stones ahead of the particle;
- Eddies and turbulence induced by other surrounding grains; and
- Quasi steady upward drag induced by the flow alteration created by other particles.

The uplift forces can be determined using a similar Equation to (2-28):

$$F_L = \frac{1}{2} \rho C_L A_p u |u| \quad (2-30)$$

where C_L is the lift coefficient taking a value between 0.1-0.2 for a sphere placed between other particles in both unidirectional and oscillatory flows (Torum et al., 1992).

The approach described above for determining the initiation of sediment movement based on the balance of forces in practical terms is very difficult to achieve, due to the irregularity of the shape of sediment particles. In addition, the continuous movement of sediment and the effects other particles have on the flow cause further uncertainties in the calculation of the forces (Hofland, 2005). This causes the point of application of the forces to change continuously and thus cannot provide a consistent way of determining incipient motion.

Shields (1936) developed a method for determining the incipient motion of sediment based on the bed shear stress exerted by the flow on a flat bed comprised of a homogeneous sediment. In order to make his method dimensionally homogeneous he proposed the non-dimensional form of the critical bed shear stress required to initiate incipient motion (θ_{cr}) as:

$$\theta_{cr} = \frac{\tau_{cr}}{g (\rho_s - \rho) d_{50}} \quad (2-31)$$

where τ_{cr} is the bed shear stress required to initiate sediment motion.

In his original work he proposed that θ_{cr} is a function of the grain Reynolds number (Re_*) (Figure 2-4) which is defined as:

As can be seen in Figure 2-4 u_* is present in both the vertical and horizontal axes. Keeping in mind that u_* and τ_0 are linked to each other with equation (2-1), this makes the estimation of the critical shear stress difficult due to the implicit nature of the Shields graph.

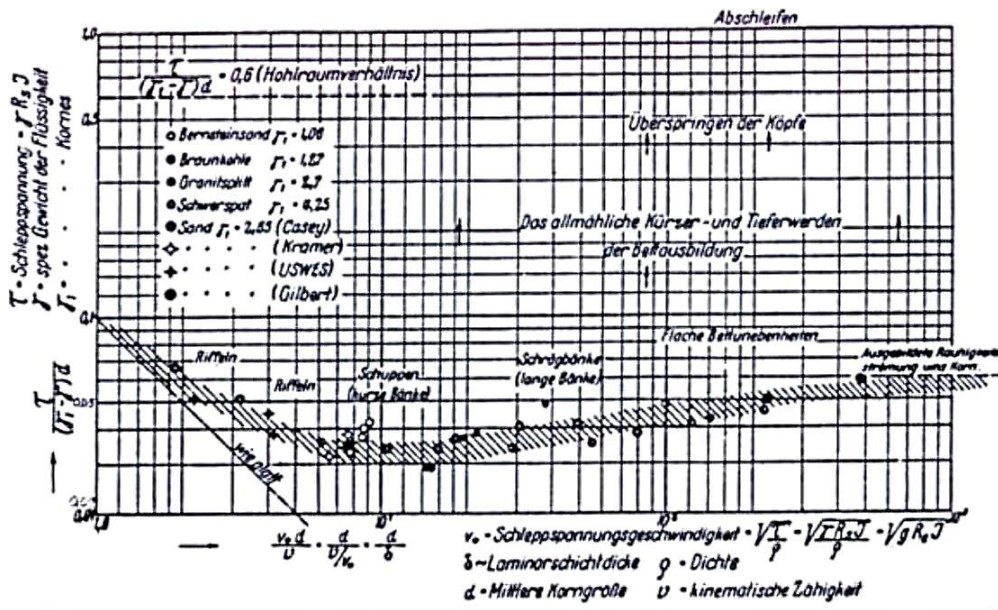


Figure 2-4: Original Shields curve (Shields, 1936)

As can be observed in Figure 2-4 there is some scatter in the data of Shields which is sourced from the irregularities in incipient motion. This is due to the wide grade and irregular shape of sediments, the fact that it is impossible to have a completely flat initial bed, and the inherently turbulent structure of flow that could occasionally cause sediment particles to initiate movement before the others. Thus an interesting question that arises from Shields (1936) is: "How is incipient motion defined?". According to present literature there are two general ways to quantify this threshold condition.

The first method is based on quantifying visual observations of incipient motion. This implies that a general convention as of when and how many sediment particles are required to initiate sediment motion could help reduce the scatter in the plot. Several attempts have been made to quantify this condition with the two most well-known methods being those of Neil (1968) and Yalin (1977).

Neil (1968) suggested that the dynamic similarity of sediment grain movement (N) is a function of the number of particles moving (n) the sediment size (d_{50}) and the bed friction velocity (u_*) and proposed the following formula:

$$N = \frac{md_{50}^3}{u_*} \quad (2-32)$$

Yalin (1977) adopted an analytical approach for quantifying the incipient motion which is based on an assumption that the probability of detachment of a particle from the bed follows a normal distribution. The expression he derived reads as:

$$\varepsilon = \frac{m}{A_\Omega t} \sqrt{\frac{\rho d_{50}}{\gamma_s - \gamma}} \quad (2-33)$$

where A_Ω is the area considered in the observation; t is the time period in which observations are made; and γ_s and γ are the specific weight of the sediment and water respectively.

Yalin (1977) suggests that a practical value of $\varepsilon = 10^{-6}$ in order to be able to compare results from different studies effectively.

The second way of quantifying the threshold condition for sediment motion is by determining the sediment transport rate at which incipient motion occurs. This method involves the arbitrary definition of a small non-dimensional unit transport rate that corresponds more closely to the transport rate observed in most of the existing publications. An example of such work is Whitehouse and Hardisty (1988) who investigated the effect of bed inclination on the threshold of sand transport over submarine slopes.

The Shields diagram was updated with additional data from experiments by Miller et al. (1977) in order to increase its range of validity for a wider range of particle Reynolds numbers (Figure 2-5). The direct conclusion of their work was that the Shields curve shifted to smaller values of θ_{cr} for Re_* values greater than 10.

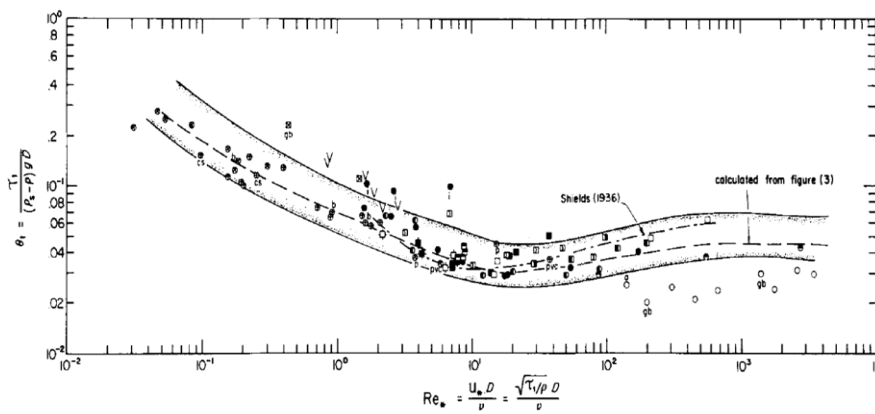


Figure 2-5: Modified Shields diagram (Miller et al., 1977)

Soulsby and Whitehouse (1997) modified the original Shields diagram to make it explicit. In the new method the Shields parameter is plotted against the non-dimensional grain size defined as:

$$D_* = \left[\frac{g \left(\frac{\rho_s}{\rho} - 1 \right)}{\nu^2} \right]^{\frac{1}{3}} d_{50} \quad (2-34)$$

In the same graph additional data from waves, currents and combined waves and currents were plotted, thus extending its range. (Soulsby and Whitehouse, 1997) developed an algebraic expression for the original Shields curve. They further developed a second algebraic expression to account for smaller sediment sizes and found that the original Shields paper overestimated by as much as O(10) the Shields parameter for very small values of D_* (Figure 2-6).

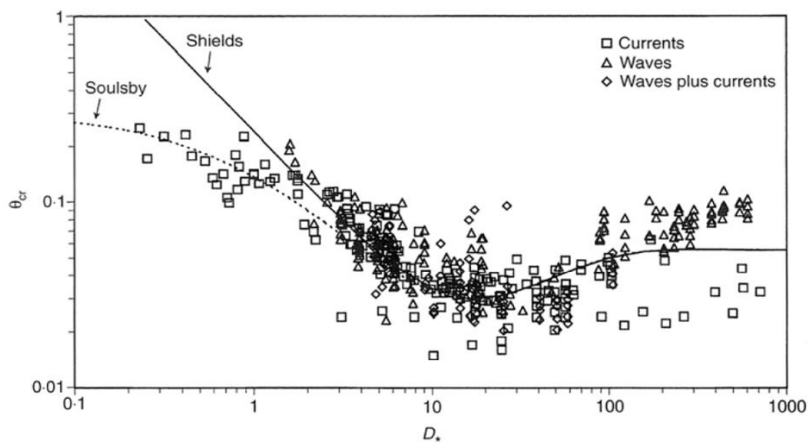


Figure 2-6: Updated Shields diagram (Source: Soulsby, 1997)

The dotted line in Figure 2-6 is given by the following expression:

$$\theta_{cr} = \frac{0.30}{1 + 1.2D_*} + 0.055[1 - \exp(-0.020D_*)] \quad (2-35)$$

Many more studies have been reported where the Shields diagram has been modified or improved by the addition of new data-points. The reader is directed to the publications of (Vanoni, 1964; Buffington and Montgomery, 1997; Hoffmans and Verheij, 1997) who also contributed towards clarifying several aspects of the original Shields diagram.

It is also important to mention the work of (Hjulstrom, 1939) who developed a graph where the different velocities correspond to erosion, transportation and deposition of fluvial sediments (Figure 2-7). The main difference between Hjulstrom and the Shields diagram is that Hjulstrom plots the mean flow velocity against the sediment diameter rather than the non-dimensional bed shear stress and Re_* . This is the reason why multiple lines corresponding to different water depths (0.01 to 10m) are plotted on the graph. This graph is explicit and thus is easy to interpret. But the fact it is dimensional makes it prone to temperature and density changes and thus has not been commonly used by designers.

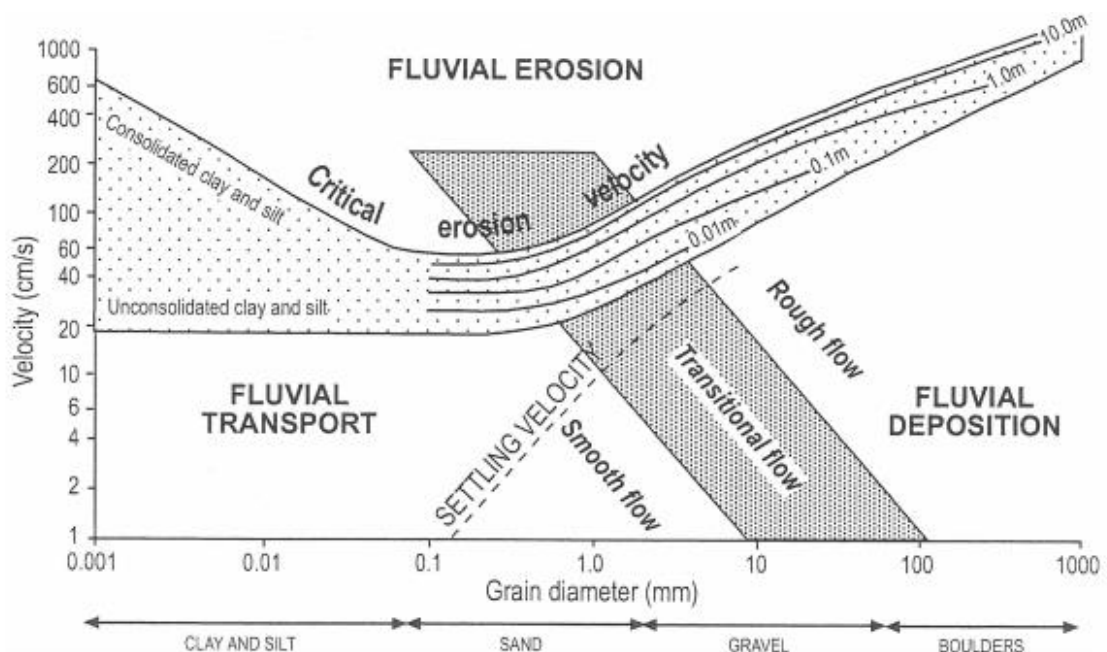


Figure 2-7: Sundborg's modification of the Hjulström diagram. (After Sundborg, 1956.)

2.2.5 Threshold current speed

The threshold of motion speed of sediments (U_{cr}) is an important parameter for any sediment transport process. U_{cr} is the mean flow required to move a sediment particle over a flat bed. It is particularly important for scour and scour protection design and this section will provide an overview of some of the main methods that can be used to determine it.

For a steady current Van Rijn (1984) proposed:

$$U_{cr} = 0.19d_{50}^{0.1} \log\left(\frac{4h}{d_{90}}\right) \text{ with } 100 \leq d_{50} \leq 500\mu m \quad (2-36)$$

$$U_{cr} = 8.5d_{50}^{0.6} \log\left(\frac{4h}{d_{90}}\right) \text{ with } 500 < d_{50} \leq 2000\mu m \quad (2-37)$$

This method is an effective way for determining the threshold velocity but is only valid for non-cohesive sediment up to the size of coarse sand. This provides a limitation with regards to its application to larger grains such as the ones used for scour protection.

A second method proposed by Soulsby (1997) is based on combining the critical Shields parameter and the friction law. This yields a method that is valid throughout the entire range covered by the Shields diagram and reads as:

$$U_{cr} = 7 \left(\frac{h}{d_{50}}\right)^{\frac{1}{7}} [g(s-1)d_{50}\theta_{cr}] \quad (2-38)$$

2.3 Hydrodynamics around cylindrical structures

The local sediment transport around offshore structures is influenced by the flow structure interaction and the resulting changes in the local flow field. Extensive research on the hydrodynamic phenomena around monopiles has been conducted in the past, but much less is known about the hydrodynamic response to more complex structures such as GBFs.

According to (Sumer and Fredsøe, 2002) four phenomena are observed when a flow interacts with a monopile (Figure 2-8):

- The downflow along the face of the structure;
- The horseshoe vortex system that originates at the front of the structure and circles around it;
- The lee-wake vortex shedding which is caused by flow separation along the periphery of the structure; and
- The local contraction of the flow around the structure.

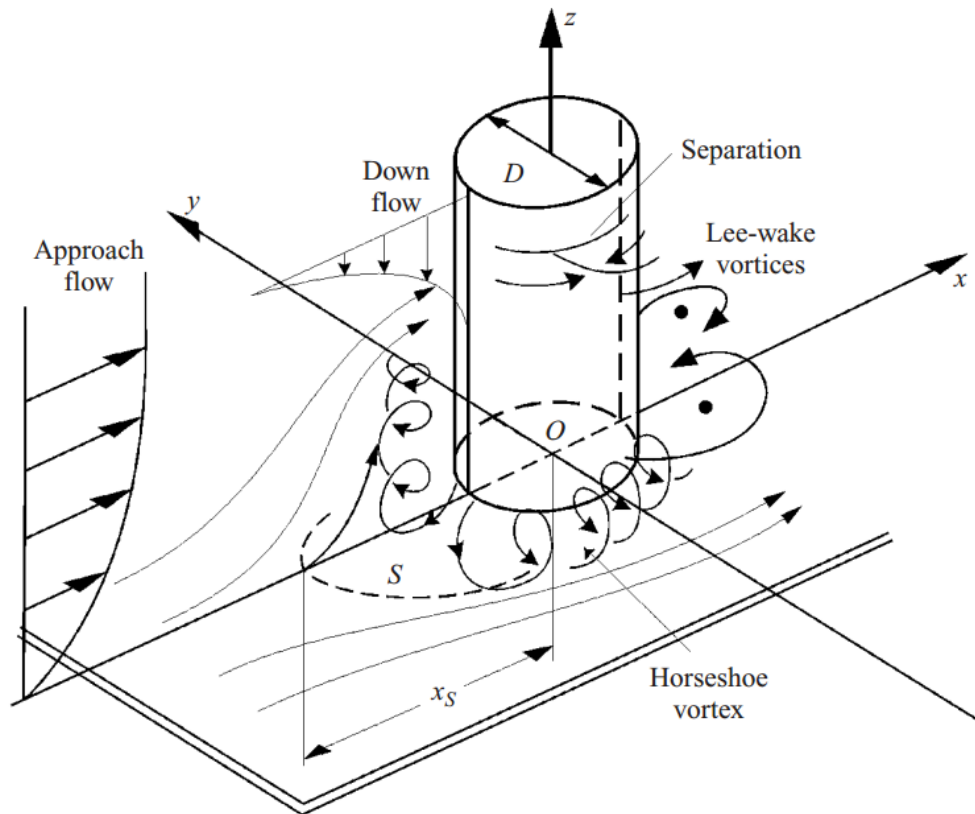


Figure 2-8: Flow structure interaction definition sketch (source: Roulund et al., 2005)

These processes cause a local increase in the bed shear stress. This increase relative to the undisturbed case is described by the bed shear stress amplification factor defined as:

$$a = \frac{\tau_b}{\tau_\infty} \quad (2-39)$$

Here τ_∞ is the undisturbed bed shear stress which can be determined from Equation (2-5) for currents, and Equation (2-12) for waves; τ_b is the local bed shear stress at a location near the structure.

2.3.1 Downflow

The downflow in front of the pile is caused by a stagnation point on the centreline of the face of the structure, which is measured from the original bed (y in Figure 2-9). The stagnation point forces a portion of the flow to move upwards which causes the surface bow wave. The remaining portion of the flow is then directed towards the bed causing a downwards jet (downflow) which feeds into the horseshoe vortex (see Figure 2-9). The energy at the face of the structure is the sum of the kinetic and the static energy components. This means that in shallow waters the hydrostatic component of the total energy is small compared to the kinetic which translates into a stagnation point further away from the bed. Scour under such conditions is called shallow water scour and is highly dependent on the water depth. When the water depth is relatively large compared to the structure's diameter the stagnation point shifts closer to the bed which yields a more evenly distributed downflow and upflow jet. Scour under this condition is named deep water scour and is independent of the water depth.

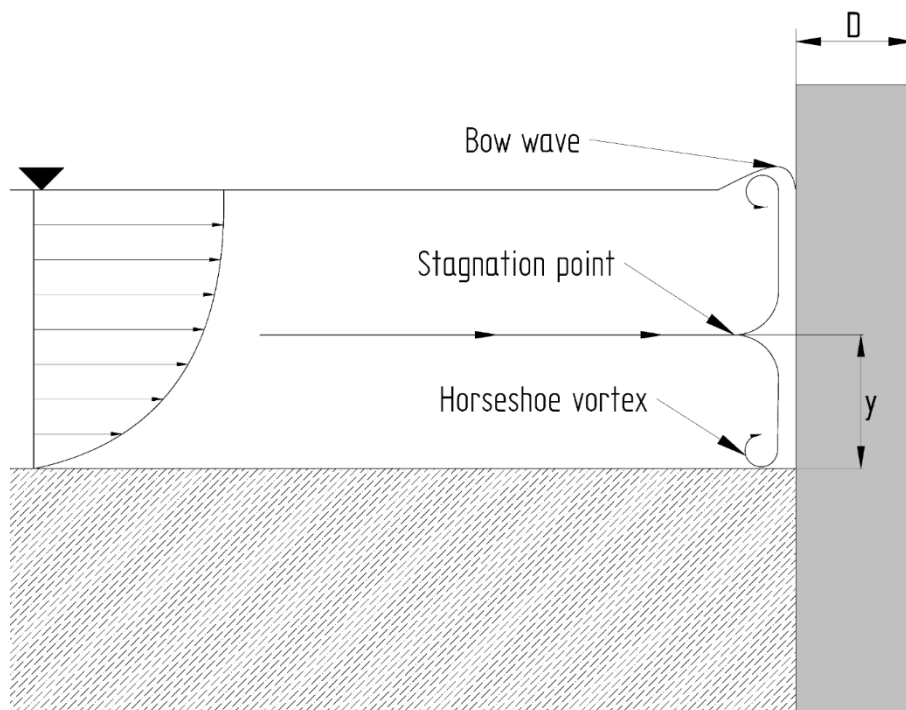


Figure 2-9: Definition sketch of downflow phenomenon (location of the stagnation point is arbitrarily selected in this image)

2.3.2 Horseshoe vortex

The horseshoe vortex plays a significant role in scour development and sediment transport. It is created by the rotation of the incoming flow and is caused by the three-dimensional separation of the incoming flow due to the adverse pressure gradient induced by the structure (Sumer and Fredsøe, 2002). The separated boundary layer then forms a spiral vortex which wraps around the structure and is carried away by the main current forming a horseshoe shape in the plan view (see figure 2-8).

2.3.2.1 Horseshoe vortex in currents

In the case of a unidirectional and steady current the horseshoe vortex has been investigated by numerous authors (see Baker 1978; 1979; 1980; 1985; 1991; Dargahi, 1989; Graf and Yulistiyanto, 1998; and Roulund et al., 2005). The studies of Baker and of Hjiorth (1975) showed that under the forcing of a unidirectional current the amplification of the bed shear stress can be increased up to a factor of 11. The magnitude of this amplification may be challenged, though, due to the methods used to measure the local bed shear stress. Nevertheless, these studies showed that the local bed shear stress experiences significant amplification which drives the sediment transport and is thus an important contributing factor for the scour process.

According to Baker (1978, 1979 and 1980) the horseshoe vortex is characterised by three key non-dimensional quantities:

- The pile Reynolds number (Re_D);
- The relative thickness of the boundary layer (δ/D); and
- The local adverse pressure gradient.

The pile Reynolds number is defined as:

$$Re_D = \frac{U_c D}{\nu} \quad (2-40)$$

where D is the pile diameter.

The pile Reynolds number describes the viscous forces of the flow relative to the inertial forces. This means that if in a specific scenario high viscous forces are anticipated (i.e.

small Re_D) then the boundary layer separation will be delayed, resulting in smaller horseshoe vortex system. Roulund et al. (2005) conducted a series of numerical and experimental investigations and concluded that the size and intensity of the horseshoe vortex increases up to a Re_D value of 500 and then decreases for an increasing value of the pile Reynolds number (Figure 2-10). This decrease in the size of the horseshoe vortex for larger values of Re_D is attributed to the increased momentum exchange between the layers of the fluid in the turbulent boundary layer.

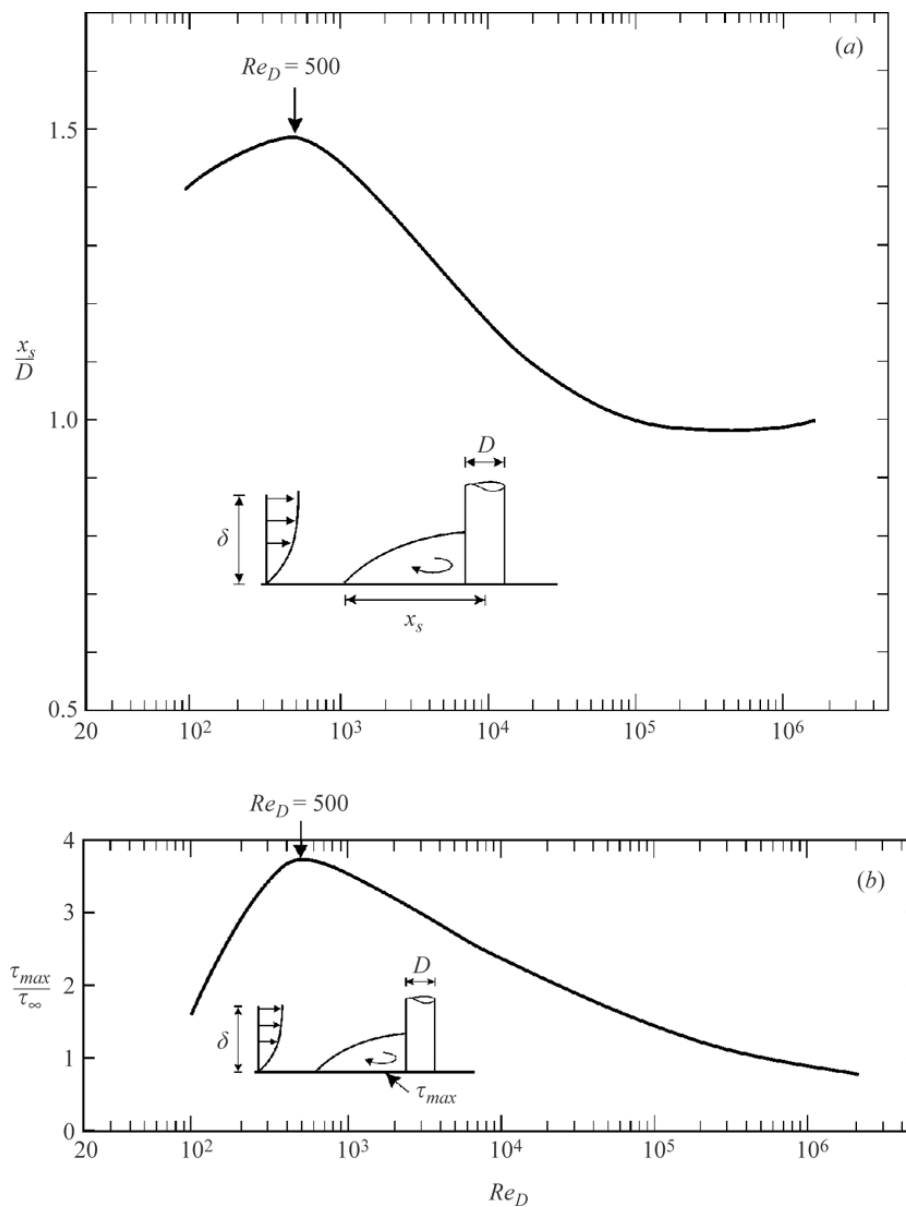


Figure 2-10: Influence of the Re_D on the Horseshoe vortex (source: Roulund et al., 2005)

Similar to the pile Reynolds number the thickness of the undisturbed boundary layer also effects the formation of the boundary layer. It can be understood that the separation of the boundary layer will be delayed (i.e. smaller horseshoe vortex) if the approaching boundary layer is more uniform. This has been verified by Roulund et al. (2005) among other publications (Figure 2-11), they predicted accurately the separation distance of the horseshoe vortex but not as well the amplification of the bed shear stress, which is most probably linked to the choice of turbulence model in the study. The study concluded that the horseshoe vortex increases in size and intensity up to certain point and then reaches a plateau which is dependent on the pile Reynolds number.

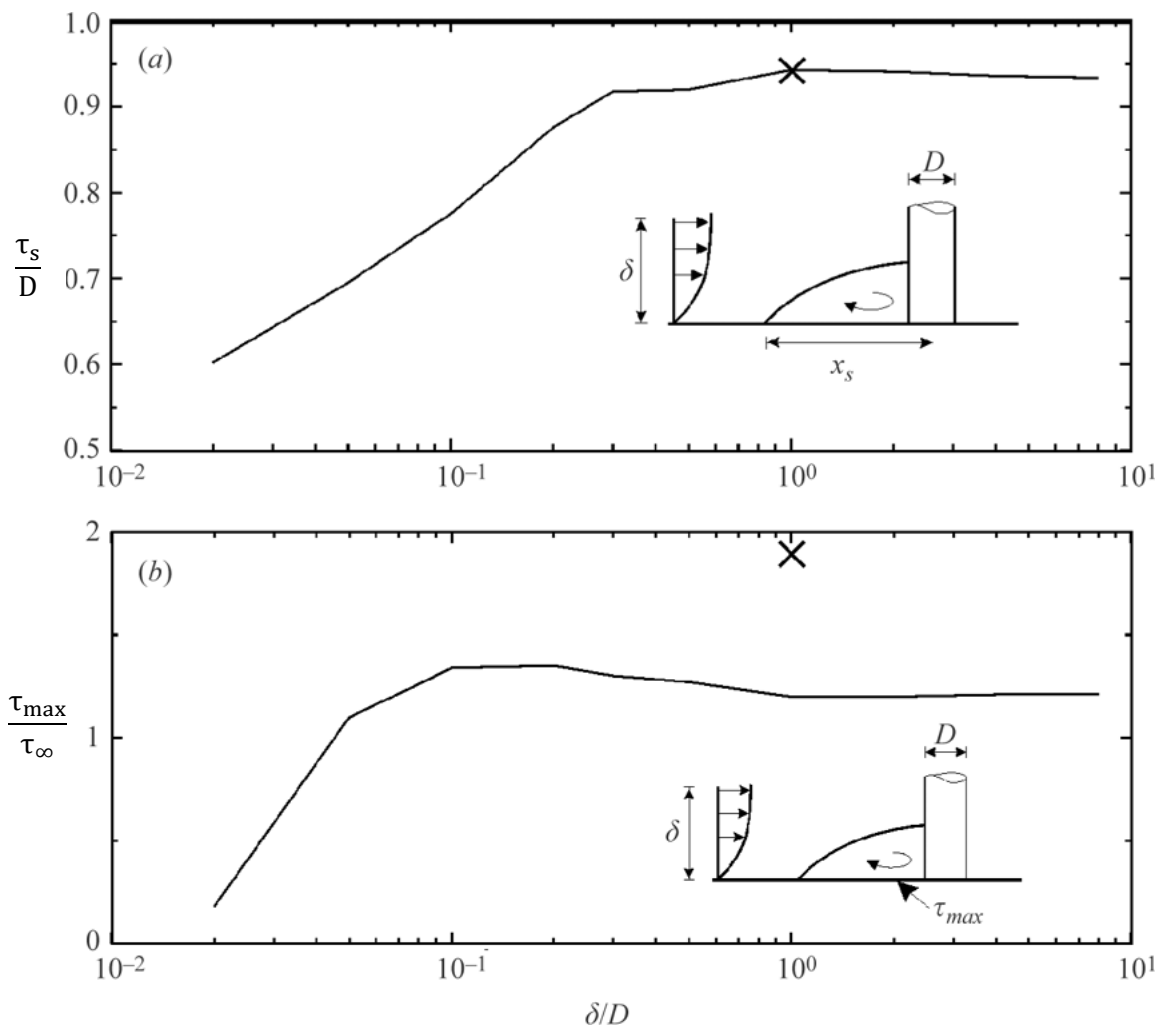


Figure 2-11: Influence of the boundary layer thickness on the Horseshoe vortex for $Re_D = 2 * 10^2$, line: result of numerical model, x symbol: experimental measurement (source: Roulund et al., 2005).

The final factor influencing the horseshoe vortex in the case of a unidirectional current is the adverse pressure gradient. When the flow profile does not change, the pressure

gradient is a direct function of the shape of the structure. This means that a more streamlined structure geometry will result in a smaller horseshoe vortex compared to a uniform cylinder. Sumer et al. (1997) reported values of the separation point along the centreline of different cross-sectional shapes (taken in the planar view point) the results of which are shown in Figure 2-12. The study showed that the orientation of a rectangular foundation can result in a reduction in the size of the horseshoe vortex by a factor of 15%.

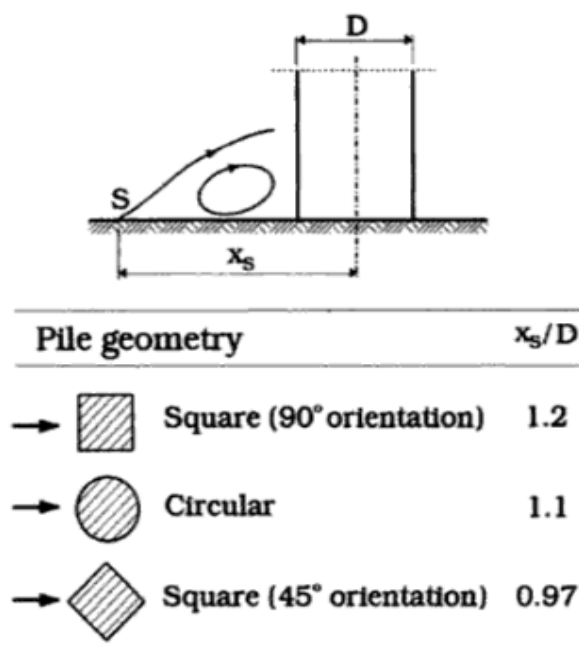


Figure 2-12: Boundary layer separation distance for different cross-sectional shapes (source: Sumer et al., 1997)

In addition, the lateral shape and dimension of the structure significantly influences the horseshoe vortex size. Chou and Chao (2000) investigated the characteristics of the horseshoe vortex around non surface piercing rectangular foundations. Their study showed that the horseshoe vortex system breaks up into a series of smaller regularly shaped vortices when the aspect ratio of the foundation (W/h_c) exceeded the value of 10. More regular vortices yield a smaller amplification of the bed shear stress and thus smaller sediment transport capacity. Here W is the cross flow width of the foundation and h_c is the height of the foundation. Further studies on the effects of conical based foundation on the amplification of the bed shear stress conducted by Sumer et al. (1994)

revealed that the amplification of the bed shear stress increases as the side slope of the conical based structures increases. This finding was also supported by the findings of Tavouktsoglou et al. (2015) who reported the amplification of the bed shear stress around cones.

2.3.2.2 Horseshoe vortex in waves

According to Sumer and Fredsøe (2002) the presence of waves introduces one additional non-dimensional quantity, the Keulegan-Carpenter number (KC). The Keulegan-Carpenter number is a non-dimensional quantity which describes the relative importance of the drag over the inertial forces and is defined as:

$$KC = \frac{U_w T}{D} = \frac{2\pi a_w}{D} \quad (2-41)$$

Here U_w is the amplitude of the bed orbital velocity, T the wave period, D the diameter of the cylinder and a is the amplitude of the wave.

The expression in equation (2-41) implies that when the KC is small (i.e. smaller than 6) the stroke of the wave is small relative to the diameter of the pile and thus a horseshoe vortex is not expected to develop. On the other hand if KC is large (greater than 60) then the orbital motion is much greater than the diameter of the structure which means that the horseshoe vortex in this case should resemble the vortex system induced by a unidirectional current (Sumer and Fredsøe, 2002).

The horseshoe vortex in waves is not present at all phases of the wave cycle. It emerges sometime after the flow reverses and it ceases of existence before the flow reverses again (Sumer et al., 1997). The life span of the horseshoe vortex is also dependent on the KC number according to same study (Figure 2-13). Figure 2-13 also shows that the crest of the wave has the tendency to induce larger horseshoe vortices compared to the trough. This difference is attributed to the asymmetry in the wave itself which tends to follow Stokes' wave theory in most flume tests.

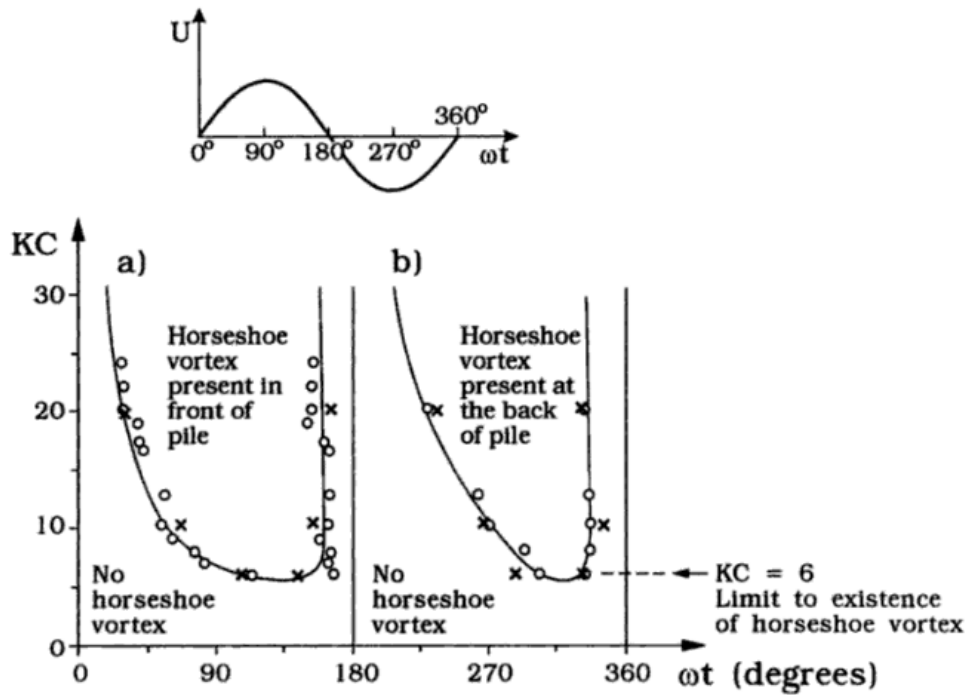


Figure 2-13: Horseshoe vortex in different phases of wave cycle (Source: Sumer et al., 1997)

The horseshoe vortex in waves for non-uniform cross section structures is a subject which has not been investigated in the literature. This is a clear gap in the knowledge which needs to be filled in order to understand in more depth the scour process around such structures in waves.

2.3.2.3 Horseshoe vortex in combined waves and currents

According to Sumer et al. (1997) the lifespan of the horseshoe vortex increases as the ratio of the current velocity to the bed orbital velocity (U_c/U_w) increases. Figure 2-14 shows that the horseshoe vortex is created for smaller values of the KC number, and below the critical value of 6 in waves alone, as the current flow speed increases when the current is following the wave.

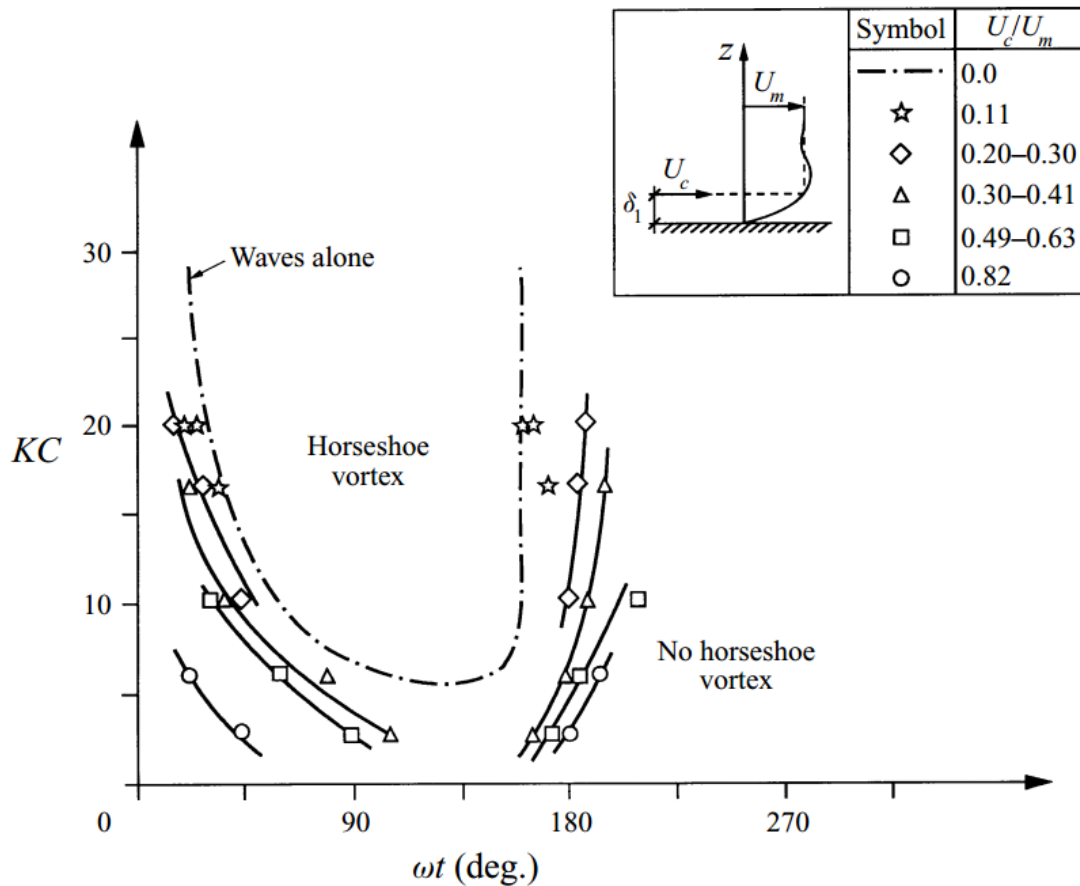


Figure 2-14: Presence of horseshoe vortex in phase space: influence of superimposed current (Source: Sumer et al., 1997)

Further to the study of Sumer et al. (1997); Umeda et al. (2003) conducted a series of computational simulations where the horseshoe vortex was measured around cylinders for combined waves and currents, with waves that were following and opposing the current. Their study showed that in the case where the waves followed the main current a strong horseshoe vortex developed at the leading edge of the structure. In the case where the waves were opposing the current a smaller horseshoe vortex developed at the leading edge of the structure and no vortex system developed on the lee side. Their results showed that the horseshoe vortex system increases in size for an increasing value of KC or $V_t = U_c/U_w$, which agrees with the general findings of Sumer et al. (1997). Further to this they proposed an empirical equation that relates the flow separation distance (x_s) in front of the structure to the non-dimensional quantity A_0 , which is shown in figure 2-15. A_0 is defined as:

$$A_0 = KC \frac{2 + \pi \frac{U_c}{U_w}}{4\pi} \quad (2-42)$$

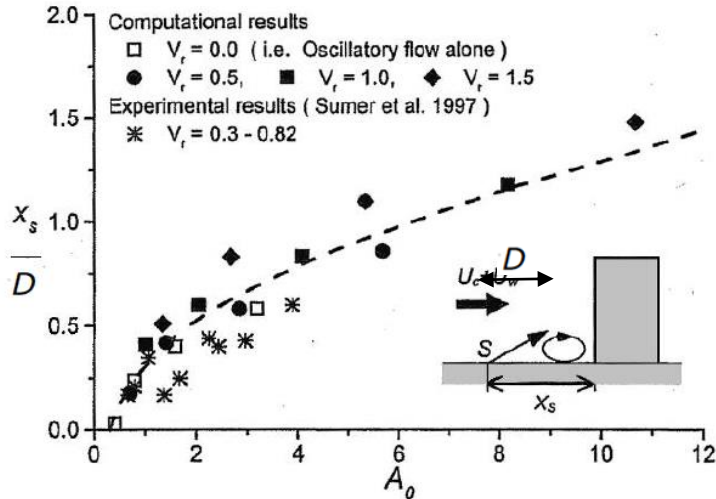


Figure 2-15: Separation distance for combined waves and currents (Source: Umeda et al., 2003)

2.3.3 Lee-wake vortex

2.3.3.1 Lee-wake vortex in currents

Sumer and Fredsøe (1997) provide a comprehensive review of the lee-wake phenomenon around cylindrical structures which is important for scour in currents. The lee-wake vortex is a function of the pile Reynolds number with the main regimes summarised in Figure 2-16. The most important phenomenon in the lee-wake region is named vortex shedding, which occurs for $Re_D > 40$. In this range of Reynolds number, the boundary layer on the outer face of the cylinder separates due to the adverse pressure gradient. The vorticity in the boundary layer is then fed into the shear layer at the lee of the structure creating a streak of asymmetric vortices that are carried downstream with the main current. The vortex shedding phenomenon continues to occur for as long as the two shear layers occurring on each side of the cylinder interact.

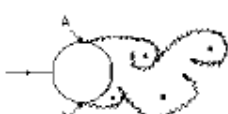
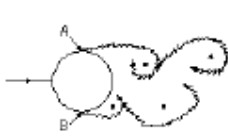
a)		No separation. Creeping flow	$Re_D < 5$
b)		A fixed pair of symmetric vortices	$5 < Re_D < 40$
c)		Laminar vortex street	$40 < Re_D < 200$
d)		Transition to turbulence in the wake	$200 < Re_D < 300$
e)		Wake completely turbulent A: Laminar boundary layer separation	$300 < Re_D < 3 \times 10^5$ Subcritical
f)		A: Laminar boundary layer separation B: Turbulent boundary layer separation: but boundary layer turbulent	$3 \times 10^5 < Re_D < 3.5 \times 10^5$ Critical (Lower transition)
g)		B: Turbulent boundary layer separation: boundary layer partly laminar partly turbulent	$3.5 \times 10^5 < Re_D < 1.5 \times 10^6$ Supercritical
h)		C: boundary layer completely turbulent at one side	$1.5 \times 10^6 < Re_D < 4 \times 10^6$ Upper transition
i)		C: boundary layer completely turbulent at two sides	$4 \times 10^6 < Re_D$ Transcritical

Figure 2-16: Lee wake vortex shedding regimes around a cylinder (source: Sumer and Fredsøe, 1997)

The non-dimensional form of the vortex shedding frequency is known as the Strouhal number (St) defined as:

$$St = \frac{f_v D}{U_c} \quad (2-43)$$

St and thus the turbulence level at the lee of the structure has been found to be a function of the pile Reynolds number and is shown in the following figure (Figure 2-17).

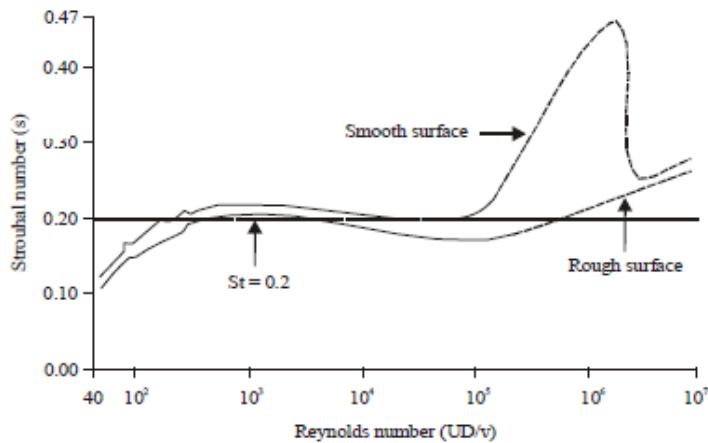


Figure 2-17: Strouhal number as a function of the pile Reynolds number for smooth and rough cylinders (Data source: Roshko, 1961)

As well as the roughness of the body the cross-flow shape of the structure also effects the Strouhal number due to the change of the pressure gradient induced by the structure. The relationship of the Reynolds number with different 2D uniform geometries is given by Blevins and Burton (1976) and is shown in figure 2-18. For non-cylindrical geometries with $Re_D > 10^4$ the Strouhal number is not expected to undergo any further variations as the separation point is fixed.

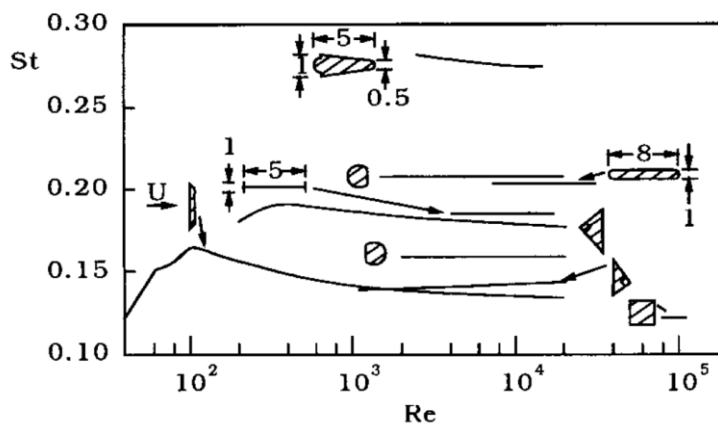


Figure 2-18: Effect of cross-flow shape on the Strouhal number (Source: Blevins and Burton, 1976)

In addition to the factors mentioned in the preceding paragraphs Sumer and Fredsøe (1997) suggest that an increasing level of incoming turbulence would result in an overall increase in the Strouhal number for the entire range of Reynolds numbers. The same effect also occurs when the shear gradient in the approach flow increases according to Kiya et al. (1980).

2.3.3.2 Lee-wake vortex in waves

In the case of waves the lee-wake process has a secondary role with regards to scour, with the horseshoe vortex governing the scour process (Sumer and Fredsøe, 2002). For waves, KC becomes an influencing parameter in the lee-wake process. The six main flow separation regimes around a cylinder are summarised in Figure 2-19. The KC ranges in the following figure were derived for a pile Reynolds number of 10^3 . Sumer and Fredsøe (1997) provide two additional graphs based on a compilation of experimental studies to describe the dependence of these regimes on both the KC and Re_D (Figures 2-20 and 2-21).

As can be understood from the figures, in the case of waves it is difficult to define the vortex shedding frequency (f_v). One way of defining the vortex shedding frequency is by calculating the lift frequency power spectrum and then determining the dominant lift frequency (f_L). The non-dimensional form of the lift frequency is then defined by Equation (2-44):

$$N_L = \frac{f_L}{f_{wave}} \quad (2-44)$$

Here f_{wave} is the wave frequency.

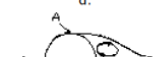
	No separation. Creeping (laminar) flow	$KC < 1.1$
	Separation with Honji vortices	$1.1 < KC < 1.6$
	A pair of symmetric vortices.	$1.6 < KC < 2.1$
	A pair of symmetric vortices. Turbulence over the cylinder surface (A)	$2.1 < KC < 4$
	A pair of asymmetric vortices	$4 < KC < 7$
	Vortex shedding	$7 < KC$ Shedding regimes

Figure 2-19: Regimes of flow separation around cylinders in waves (source: Sumer and Fredsøe, 1997)

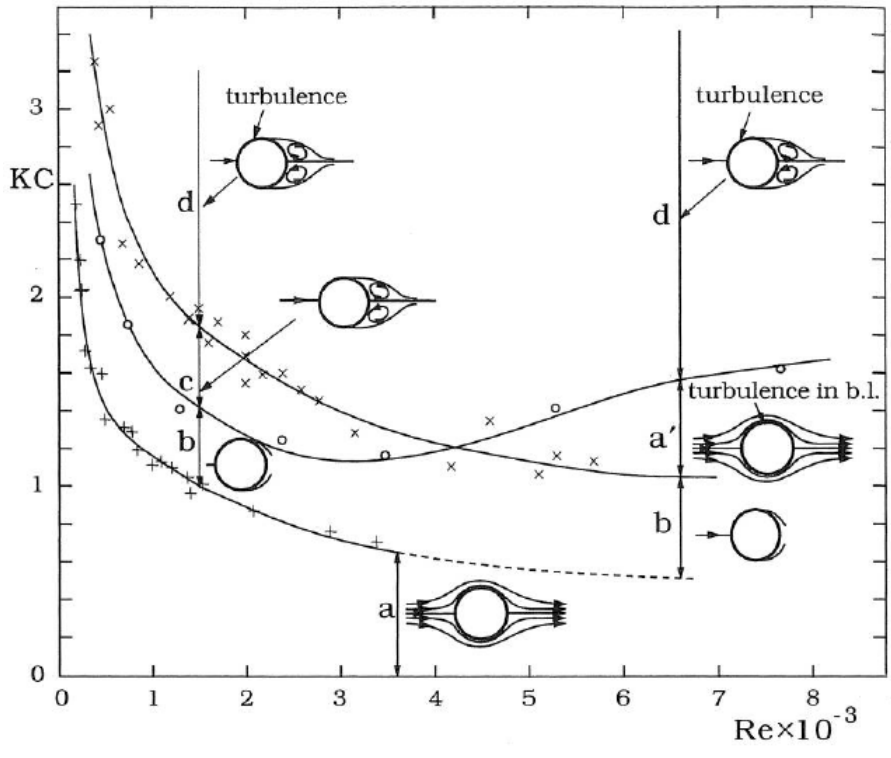


Figure 2-20: Flow separation regimes for small KC and very small Re_D numbers (source: Sumer and Fredsøe, 1997)

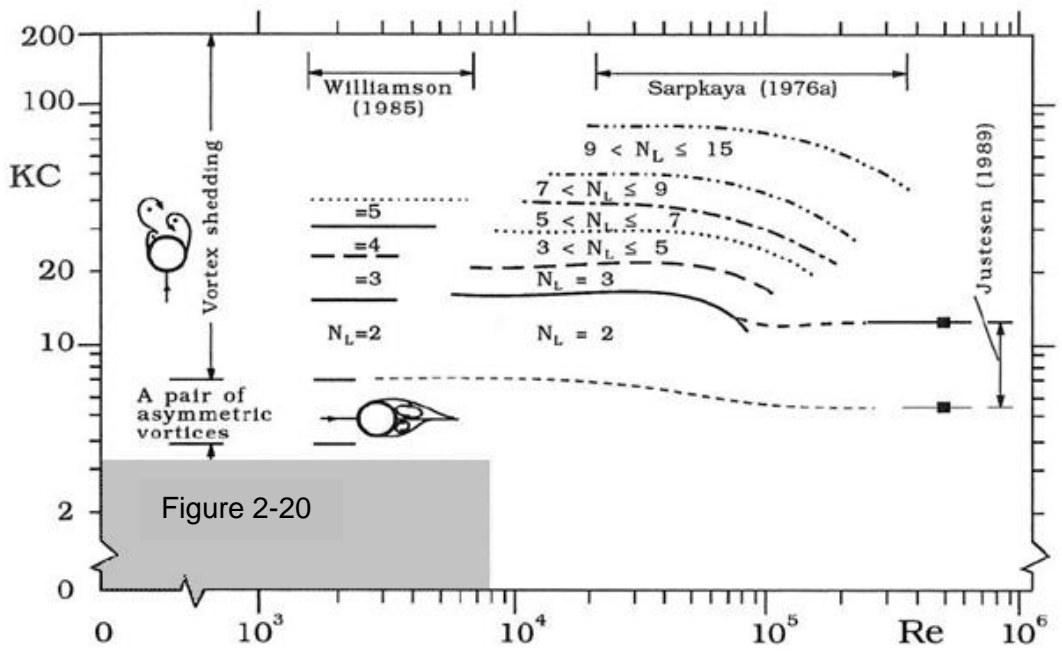


Figure 2-21: Flow separation regimes for large KC and Re_D numbers (source: Sumer and Fredsøe, 1997)

One more important consequence of the lee-wake phenomenon that particularly concerns large diameter structures is steady streaming. In this case four recirculating

flow cells (one in each quadrant) are created (Figure 2-22) due to the unseparated oscillatory flow.

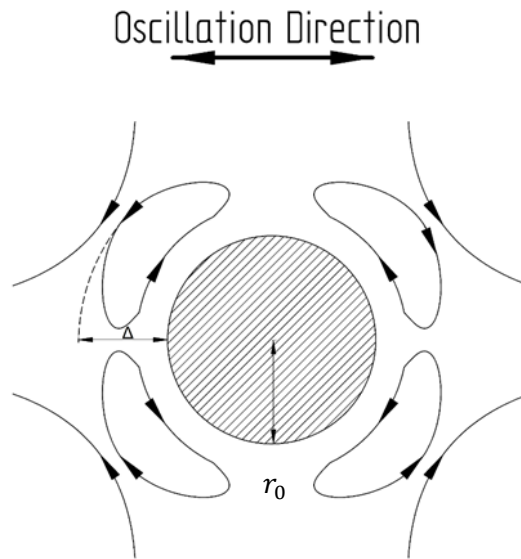


Figure 2-22: Definition sketch of steady streaming

Wang (1968) developed a semi-analytic theory that predicts the size of the recirculating cell (Δ in Figure 2-22) for small values of Reynolds number. The solution shows that the largest recirculating cells occur for a combination of large KC and small Re which is in accordance with potential flow theory.

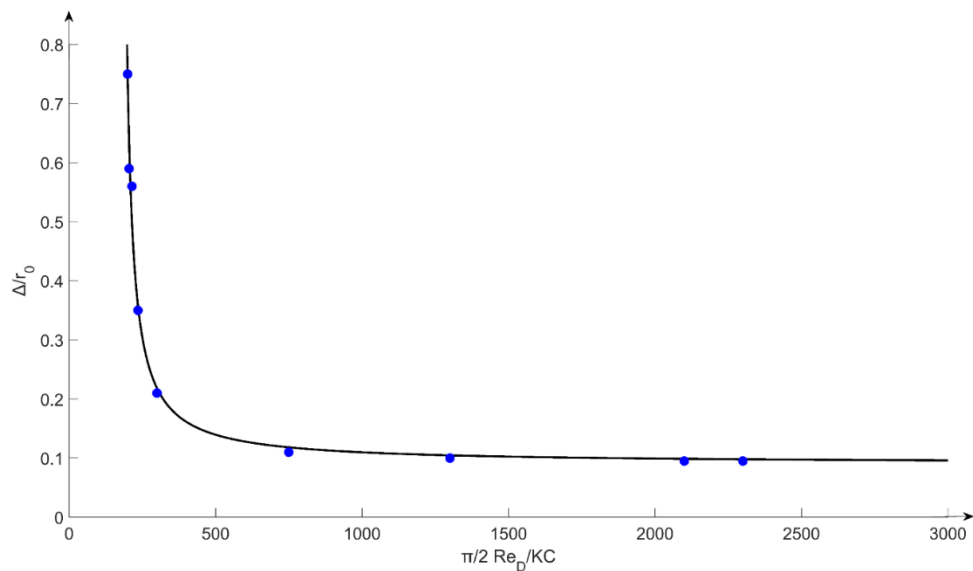


Figure 2-23: Size of steady streaming cell (Reproduced from Wang, 1968)

2.3.4 Streamline contraction

According to classical hydrodynamics streamline contraction is caused by the presence of the structure which reduces the cross-sectional area through which the flow passes, and this causes a local acceleration of the flow, which in turn causes the amplification of the bed shear stress to increase significantly. According to Hjorth (1975) the combined effect of the horseshoe vortex with streamline contraction can result in amplifications of the bed shear stress up to a factor of 10.

2.4 Scour around cylindrical structures

Changes in the flow pattern around lead to an increase in the local velocities and turbulence, which increase the sediment transport capacity of the flow. An equilibrium condition may then be achieved as the local hydraulic conditions are adjusted through the scour process. Here scour is defined as the erosion of sediment around a structure. This section provides an overview of the key literature and physics that are associated with the scour around both uniform and non-uniform cylindrical structures.

2.4.1 Scour types

Scour around structures can be divided into two main types of scour, general (or global) scour and local scour. These two scour processes have different time and length scales. The total scour can then be determined as the sum of the two components (local and global). Figure 2-24 present a diagram of the basic variables involved in the scour process for monopiles in unidirectional currents. Here h is the flow depth; D the diameter of the pile; $U(z)$ the velocity profile S the scour depth takes as the local change in depth near the structure from the original bed level; φ_{up} and φ_{down} the upstream and downstream slope of the scour hole; and W_{scour} the total width of the scour hole.

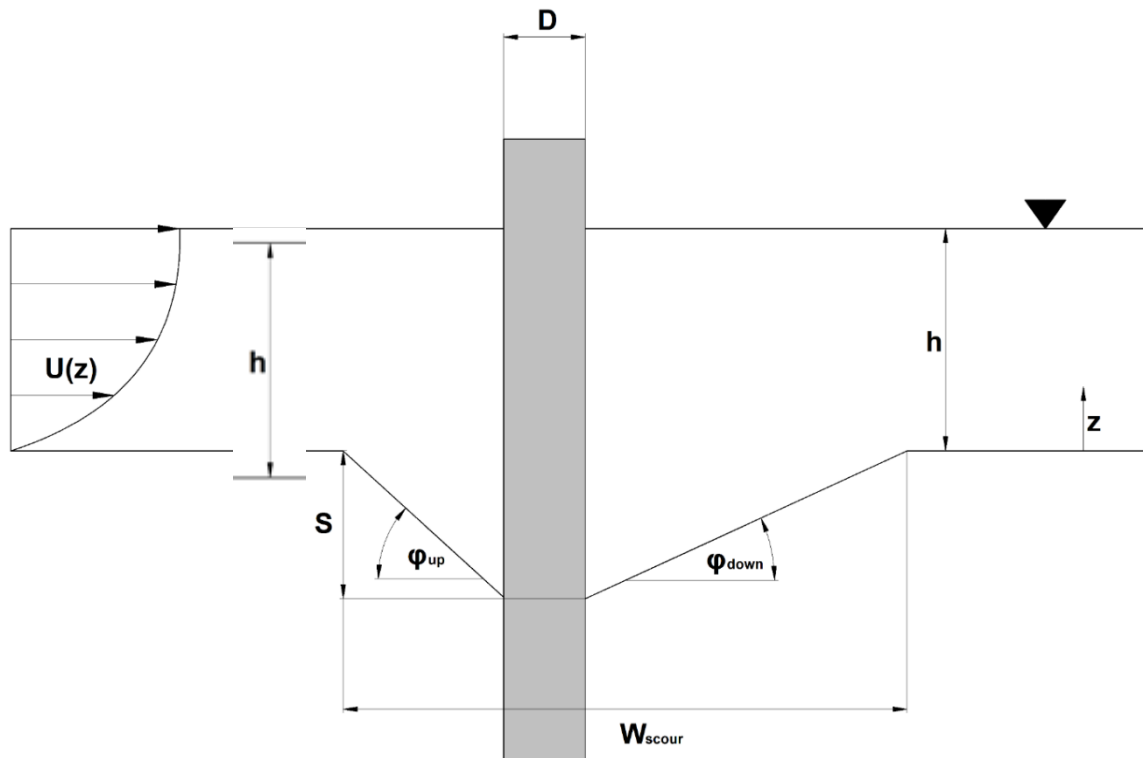


Figure 2-24: Definition sketch of local scour around monopile in unidirectional flow.

2.4.1.1 General (global) scour

The time-scale of global scour tends to be longer compared to the corresponding for local scour. General scour can be attributed to two physical phenomena (Hoffmans and Verheij, 1997):

- Overall degradation of the bed; and,
- Contraction scour.

Overall Degradation

Overall degradation results from the inherent flow conditions at a given location or from the modification of the stable flow regime. Examples of features that result in such degradation are:

- Storm surges in coastal waters;
- Dredging and land reclamation in coastal waters;
- Sand waves; and,
- Flood events in rivers and estuaries.

The result of the overall degradation at foundations will be the lowering of the bed which introduce additional failure risks that may lead to the complete failure of the foundation. It should be noted that human interventions may also lead to aggradation which may result in the reduction of scour risk.

Contraction scour

Contraction scour occurs due to the reduction of the cross-sectional area where the flow naturally passes, which causes a local increase in the flow velocities. This results in the general lowering of the bed across the entire width of the control volume. Examples of contraction scour are:

- The scour by blockage induced by a composite structure such as a jacket foundation;
- Closure works and multiple bridge footings; and,
- River bridge embankments.

2.4.1.2 Local scour

Local scour is the result of the impact the structure or a structural element (when considering composite structures) has on the local hydrodynamics. Given that global scour is very site specific (Hansen and Gislason, 2005) local scour is the most researched scour type. Physical and prototype model testing can be used for the development of scour prediction equations for different types of structure. When considering more unusual structures, physical modelling results can be used for obtaining the appropriate information required for the design. When considering local scour problems, the equilibrium scour depth is the most relevant parameter, especially when isolated structures (bridge piers, offshore foundations etc.) are considered (Hoffmans and Verheij, 1997). The time development of scour is of importance in some cases, examples of which are post-installation monitoring, closure works, and temporary installations such as cofferdams among other hydraulic engineering applications.

2.4.2 Sediment transport in local scour

Local scour around structures can be distinguished into two categories based on the upstream sediment transport:

- Clear water scour (black line in Figure 2-25), occurs when the bed material upstream of the structure is not in motion. The sediment transported into the contracted section is essentially zero. Generally, under clear-water scour, no refilling of the scour hole occurs lack of sediment supply. With regards to scour evolution the equilibrium scour depth is reached asymptotically with time; and,
- Live bed scour (blue line in Figure 2-25), which is where sediment transport exists throughout the domain. Sediment particles are transported from upstream of the structure into the scour hole. This forces the equilibrium scour hole to be smaller compared to the clear water mode. In this case the scour depth increases rapidly with time and then fluctuates about an average equilibrium scour depth.

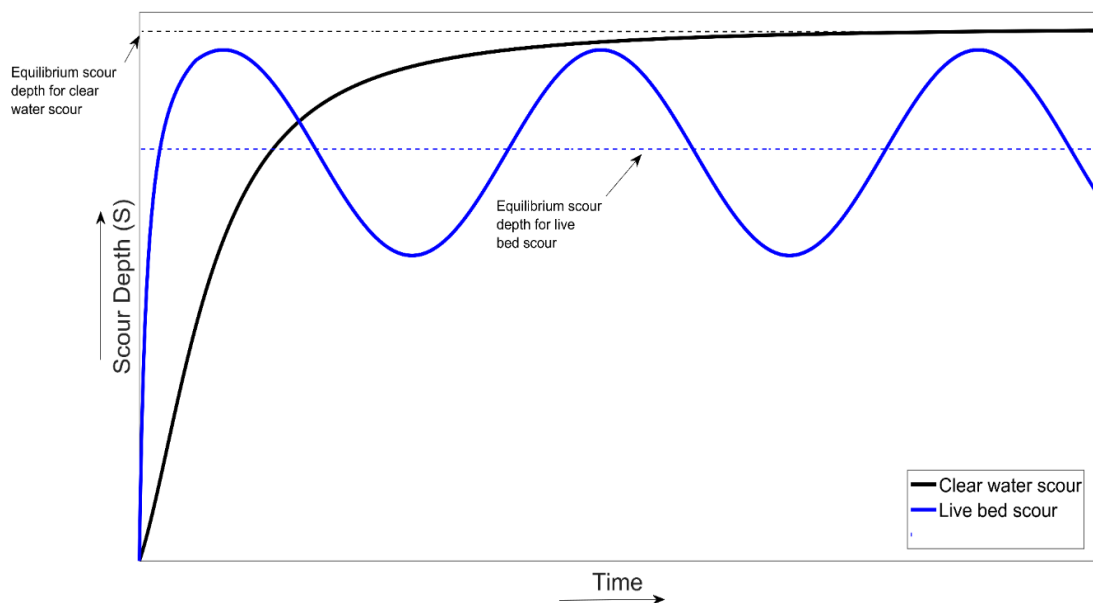


Figure 2-25: Scour depth evolution, live bed Vs clear water scour.

In clear water scour four scour evolution phases have been identified according to Breusers (1965) (see Figure 2-26).

In the initial phase the flow in the scour hole is nearly uniform in the streamwise direction. During this phase the scour process is the most rapid with sediment being eroded

quickly, and in some cases suspended into the water column. Some of the suspended sediment particles are transported with the main flow and the lee wake vortex shedding and deposited at the lee of the structure. In addition, sediment is eroded in the form of bed load. In this phase the scour hole width and length increase considerably.

The second phase of the scour process is the development phase. During this phase the scour hole geometric shape does not change considerably. The depth and width of the scour hole continue to grow at a constant rate according to observations reported by Hoffmans (1990), while the lower part of the scour hole (near the structure) continues to change due the turbulent bursts induced by the horseshoe vortex. Furthermore, the suspended sediment load decreases considerably and the main part of the erosion is carried through bed-load transport.

The third phase is the stabilization. In this phase the rate of scour decreases in time. The erosion potential within the scour hole is small, with the width of the scour hole increasing more relative to the scour depth. Finally, equilibrium (phase 4) is achieved when the dimensions of the scour hole do not change significantly with time.

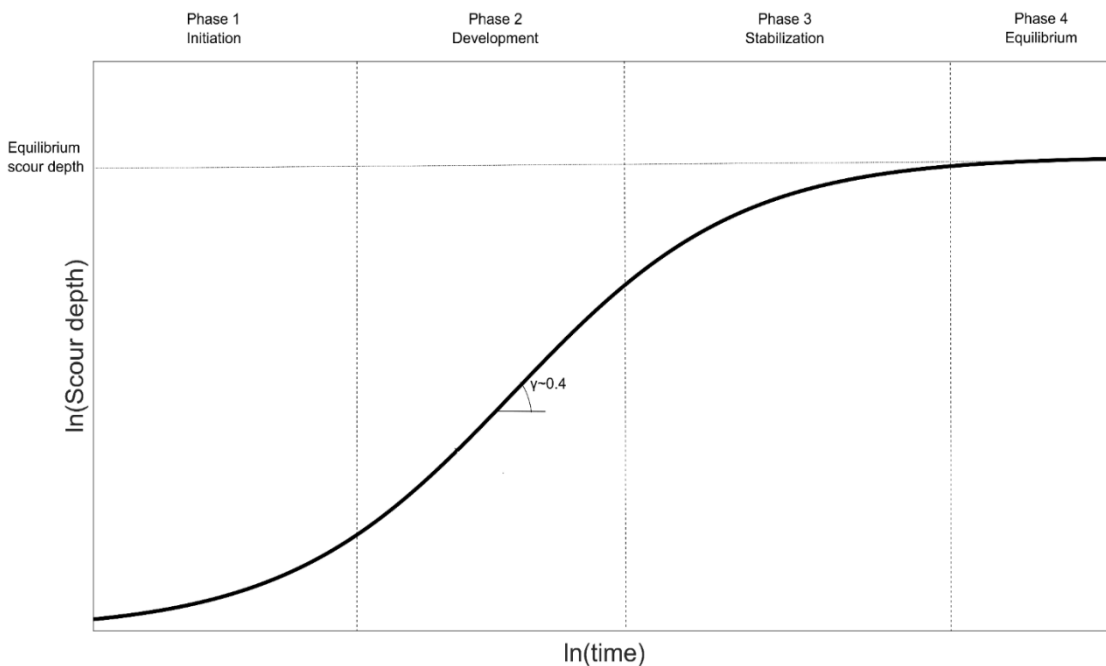


Figure 2-26: Development of clear-water scour (Derived from: Hoffmans and Verheij, 1997)

2.4.3 Scour in steady unidirectional currents

Many studies have been conducted to investigate the scour around cylindrical structures, particularly in the context of scour around bridge piers. Some key studies include Hjorth (1975), Melville (1975), Breusers et al. (1977), Ettema (1980), Melville and Sutherland (1988) and Melville and Raudkivi (1996). Extensive reviews on the topic can also be found in Hoffmans and Verheij (1997), Whitehouse (1998), Melville and Coleman (2000) and Sumer and Fredsøe (2002).

Table 2-1 presents additional publications that were used in this study for the derivation of a new scour prediction equation.

Table 2-1: Representative studies on scour around uniform cylinders used in this study.

Study	Key findings.
Shen et al (1969)	Investigated the influence of the pile Reynolds number.
Jain and Fischer (1979)	Investigated scour at high Froude numbers which typical of river environments.
Ettema (1980)	Found that variations in scour depth around monopiles is a function are related to the comparative pier and particle diameters, approach flow depths and the particle size distribution of a sediment.
Yanmaz and Altinbilek (1991)	The study found that the shape of the scour hole around bridge piers remains almost unchanged with respect to time.
Dey et al (1995)	Studied the dependence of the scour hole shape with the horseshoe vortex.
Melville, B. W. (1997)	Presented a large number of experimental results on scour around bridge piers and developed correction factors for the prediction of the equilibrium scour depth around them.
Melville and Chiew (1999)	Investigated the effect of the flow duration on the shape and depth of the scour hole.
Sheppard et al (2004)	Investigated large scale scour around monopiles and found that the equilibrium scour depths were found to depend on the wash load concentration.
Ettema et al (2006)	Presented the effect of large scale turbulence on scour behaviour.
Sheppard and Miller (2006)	Conducted a number of large scale experiments and compared the accuracy of predictive equations.
Mututano et al (2013)	Compiled a database of equilibrium scour depths in the North sea and evaluated the predictive ability of existing design equations.

2.4.3.1 Influencing parameters

In steady currents, the governing hydrodynamic process has been identified to be the horseshoe vortex (Whitehouse, 1998). Thus the scour process around uniform cylinders has mainly been researched with respect of the behaviour of the horseshoe vortex and the effect the different flow conditions have on it. According to Dargahi (1989) the size of the horseshoe vortex is independent of the flow condition and depends only on the diameter of the structure. More specifically, Muzzammil and Gangadhariah (2003) showed the diameter of the primary vortex is equal to about 20% of the pile diameter. After the formation of the horseshoe vortex sediment starts to be transported once the locally induced pressure gradient is high enough to mobilise the sediment, which creates a scour hole. The size of the horseshoe vortex increases linearly for an increasing scour hole depth (Dey and Raikar, 2007; Muzzammil and Gangadhariah, 2003), while the intensity of the horseshoe vortex decreases (Dey and Raikar, 2007). A weaker horseshoe vortex means that the sediment transport capacity of the local flow decreases while it also has a steep slope to travel in order to exit the scour hole. Therefore, this can explain the decreasing scour rate in the scour development curve (see Figure 2-25).

More recently a secondary mechanism that effects the scour phenomenon in unidirectional steady currents has been identified, namely, the counter-rotating streamwise phase-averaged vortices (LSCSVs) (see Figure 2-27). The LSCSVs are mainly driven by the longitudinal counter-rotating vortices which are created partly by the horseshoe vortex and the variation of the shedding frequency over the height of the structure (Baykal et al., 2015). These vortices effectively pickup sediment (in the form of suspended load) from the lee of the structure and transport it further away, thus increasing the scour potential. It should be noted that the effectiveness of the LSCSV in transporting material away from the structure should also be affected by the ability of the flow to keep it suspended while it is advected by the mean flow and this vortex system. Thus, for a certain set of flow conditions, sediments with a larger settling velocity (w_s)

would be deposited closer to the structure, while sediments with a lower w_s would be advected further away.

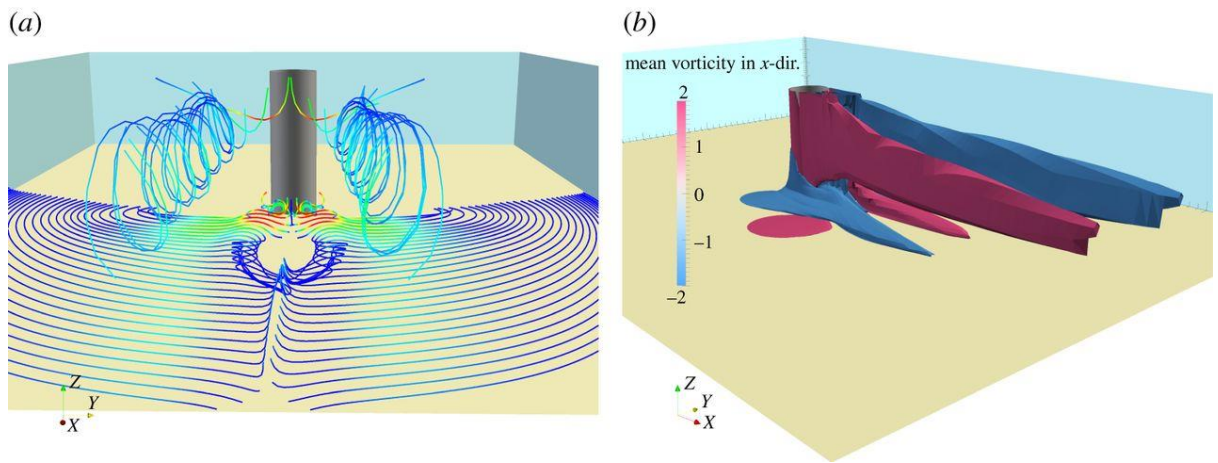


Figure 2-27: Counter-rotating streamwise phase-averaged vortices (a) streamlines (b) mean vorticity in x -direction (Source: Baykal et al., 2015)

The previous paragraphs show that the scour around a cylinder is dependent on the horseshoe vortex and on the lee wake vortex shedding. Therefore, the scour process should be influenced by the physical quantities that describe these processes and the quantities that describe the sediment's ability to resist these processes. Based on existing knowledge the following quantities have been identified as the most influencing and have been extensively researched:

- The sediment mobility ratio;
- Relative flow depth; and,
- Sediment gradation.

The following paragraphs explain the influence these parameters have on the scour process.

2.4.3.1.1 Sediment mobility ratio

The sediment mobility ratio or flow intensity (U_c/U_{cr}) describes the undisturbed flow velocity relative to the critical velocity for mobilisation of the bed material. This non-dimensional quantity is important as it distinguishes if the scour process is in the clearwater ($U_c/U_{cr} \leq 1$) or live bed regime ($U_c/U_{cr} > 1$) (Section 2.4.2) Breusers et al. (1977) and Melville and Sutherland (1988), among others have investigated the influence

an increasing sediment mobility has on the equilibrium scour depth and showed that for an increasing ratio the scour depth increases almost linearly up to a value of $U_c/U_{cr} = 1$ at which point the scour depth reaches its peak value for a constant flow depth and structure diameter. As the ratio increases further (i.e. live bed scour regime) the normalised scour depth starts to decrease. This decreasing trend is attributed to the backfilling of the scour hole due to the incoming sediment flux from upstream. However, as the flow intensity continues to increase the magnitude of scour increases again reaching a second peak value which is known as the live bed peak (see live bed peak in Figure 2-28). This peak coincides with the point where the undisturbed sediment transport changes from bed load to sheet flow (Sumer et al., 1996). In addition, the value of the threshold and the live bed peak (see Figure 2-28) are also effected by the sediment gradation which is linked to the armouring effect (see section 2.4.3.1.3 for more details). With wider graded sediments (i.e. a larger fraction of larger soil particles) leading to a smaller volume of sediment being transported by the local flow forcing. This leads to smaller scour depths with the corresponding threshold peak being shifted to larger values of U_c/U_{cr} . This effect explains the shift of the curve shown in Figure 2-28 for an increasing sediment gradation.

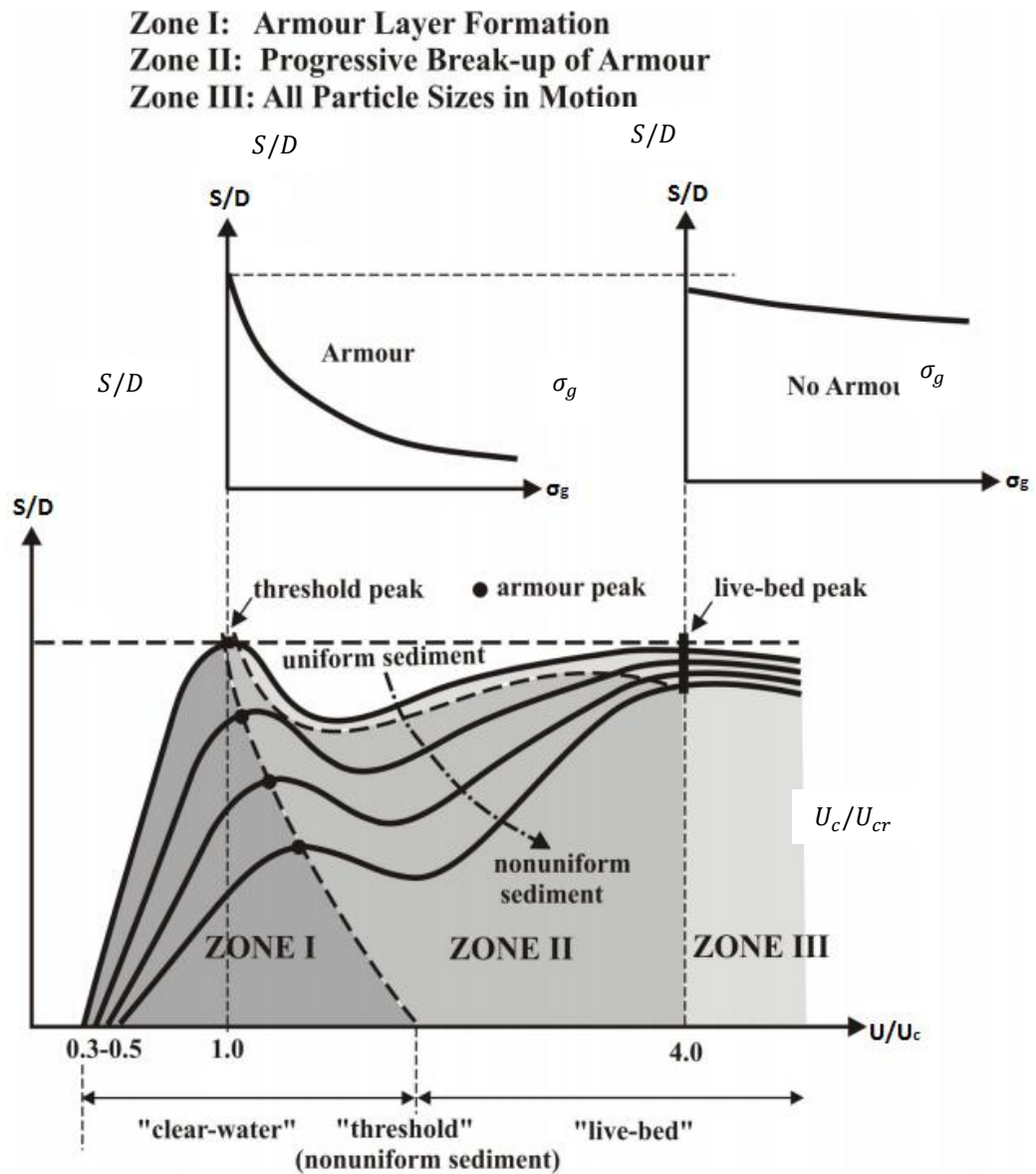


Figure 2-28: Influence of flow intensity on scour depth (Derived from: Melville and Sutherland, 1988)

2.4.3.1.2 Relative flow depth

The relative flow depth or flow shallowness is the non-dimensional parameter that describes the effect the flow depth has on the equilibrium scour depth. According to numerous authors (Laursen, 1963; Breusers et al., 1977; Chee, 1982; Raudkivi, 1986) an increasing flow depth results in an increase of the scour potential of a cylinder. Figure 2-29 show a conceptual graph of this effect according to Melville (2008).

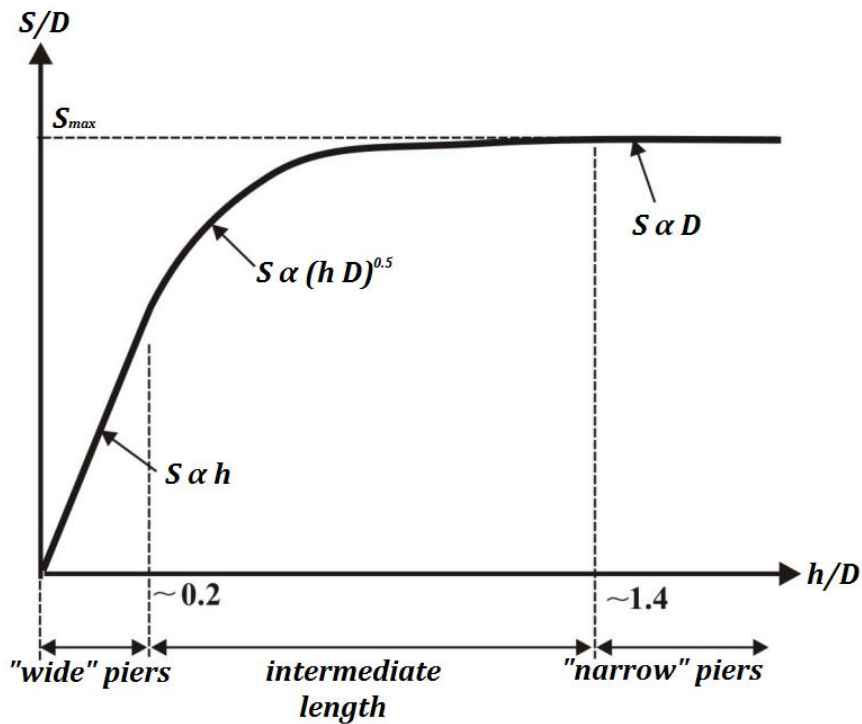


Figure 2-29: Effect of flow shallowness on scour depth (Source: Melville, 2008)

In deep flows (i.e. narrow pier regime) the scour depth is proportional to the pile diameter. This is because in deep flows the horseshoe vortex intensity is only dependant on the cylinder's diameter. For a decreasing flow depth, the surface roller (or bow wave) starts to interact more with the horseshoe vortex resulting in weaker amplification of the bed shear stress near the structure and thus smaller scour depths. For this reason, the scour depth in intermediate depths is a function of both the flow depth and the pile diameter. As the flow depth further decreases the scour process becomes independent of the horseshoe vortex and thus depends only on the flow depth because the bow wave cancels out the effect of the horseshoe vortex. This results in a zone of slow moving fluid in front of the structure, and scour depths that are significantly smaller compared to the narrow pier zone (Melville, 2008). These water depths are called the shallow water scour regime (or wide pier scour regime). It should be mentioned that different studies show that the narrow pier regime occurs for values of h/D ranging from 2 to 4. This shows that the effect of the water depth on scour is not completely clear and that most probably other physical quantities also influence the scour process.

2.4.3.1.3 Sediment gradation

Sediment gradation or the sediment uniformity is a measure of the spread of the distribution of the size of the sand particles comprising the bed. The sediment gradation is traditionally defined by the geometric standard deviation of the sediment:

$$\sigma_g = \frac{d_{84}}{d_{50}} \simeq \sqrt{\frac{d_{84}}{d_{16}}} \quad (2-45)$$

where d_{84} , d_{50} and d_{16} are the 84th, 50th and 16th percentile grain size gradings, respectively.

The most systematic investigations of the effect of sediment gradation have been carried out by Ettema (1976 and 1980) and Baker (1986). These studies revealed that the scour depth did not change drastically for $1 < \sigma_g < 1.3$. Significant reductions in the scour depths have been recorded for σ_g increasing further from the value of 1.3. This reduction is attributed to the bed armouring by a layer of coarser sediment particles that are left behind because the local flow conditions are not strong enough to remove them. Figure 2-28 shows the effect of the sediment non-uniformity on scour in live bed and clear-water conditions. It can be observed that the effect of the sediment gradation reduces as the flow intensity increases. This is due to the ability of the flow to break up the armour layer as well as to transport larger particles as the flow intensity increases.

2.4.3.2 Time evolution of scour

After the pile is installed the scour depth develops rapidly; however, it is important to predict the time evolution of scour for several reasons:

- To determine the scour development during a storm or extreme flood event; and,
- To calculate the time window available to install scour protection after the foundation is installed.
- To evaluate the total scour depth in layered and mixed sediments.

Numerous methods for predicting the time evolution of scour around monopiles have been developed. This section will provide an overview of the key equations.

For slender piles the method proposed by Breusers (1972) allows the determination of the scour depth as a function of time ($S(t)$) under the forcing of a unidirectional current:

$$\frac{S(t)}{S_{c,eq}} = 1 - \exp\left(\ln\left(1 - \frac{D}{S_{c,eq}}\right)\left(\frac{t}{t_1}\right)^{\gamma_1}\right) \quad (2-46)$$

in which D is the diameter of the cylinder; t is time in (s); t_1 is the characteristic time-scale at which the scour depth ($S(t)$) is equal to D ; and, γ is a constant that ranges between 0.2 and 0.4.

According to Nakagawa and Suzuki (1976) the value of t_1 can be determined through the following expression.

$$t_1 = \frac{29.2D}{\sqrt{2}U_c} \left(\frac{\sqrt{\Delta g d_{50}}}{\sqrt{2}U_c - U_{cr}}\right)^3 \left(\frac{D}{d_{50}}\right)^{1.9} \quad (2-47)$$

in which D_{50} is the mean particle diameter; g is the acceleration of gravity; U is the mean flow velocity; U_{cr} is the critical velocity for incipient motion (see Section 2.2.5); and,

$\Delta = (\rho_s - \rho) / \rho$) is the relative density of the sediment.

The most widely used time development scour equation is the one proposed by Whitehouse (1998) and Sumer and Fredsøe (2002), which is given by:

$$\frac{S(t)}{S_{eq}} = \left(1 - \exp\left(-\frac{t}{T_{sc}}\right)^{n_1}\right) \quad (2-48)$$

in which n is a constant and T is the time-scale of the scour process which according to Whitehouse (1998) is the value required to reach 63% of the equilibrium scour depth and is given by:

$$T_{sc} = \frac{D^2}{\sqrt{g(s-1)d_{50}^3}} T^* \quad (2-49)$$

with T^* given by:

$$T^* = \frac{1}{2000} \frac{h}{D} \theta^{-2.2} \quad \text{for currents} \quad (2-50)$$

Subsequently Melville and Chiew (1999) developed an equation for the prediction of the time evolution of scour.

$$\frac{S(t)}{S_{c,eq}} = \exp \left[-0.03 \left| \frac{U_{cr}}{U_c} \ln \left(\frac{t}{t_{eq}} \right) \right|^{1.6} \right] \quad (2-51)$$

in which t_{eq} is the time to the equilibrium scour depth (in days) and is given by:

$$t_{eq}(days) = \frac{48.26D}{U_c} \left(\frac{U_c}{U_{cr}} - 0.4 \right) \quad \text{for } \frac{h}{D} > 6 \quad (2-52)$$

$$t_{eq}(days) = \frac{30.89D}{U_c} \left(\frac{U_c}{U_{cr}} - 0.4 \right) \left(\frac{h}{D} \right)^{0.25} \quad \text{for } \frac{h}{D} < 6 \quad (2-53)$$

where h is the flow depth

2.4.3.3 Equilibrium scour depth prediction

The most important parameter when considering scour around cylindrical structures is the equilibrium scour depth ($S_{c,eq}$). In the context of clear water scour the equilibrium scour depth as described in the previous sections is the maximum scour depth that is expected to be experienced by a structure over its lifetime. While in the case of live bed scour the equilibrium scour depth may be defined as the mean value of the scour depth after a net sediment transport of zero has been achieved near the structure.

It is important to predict the equilibrium scour depth around such structures in order to design an effective scour protection scheme and other structural components (e.g. the burial length of the pile). This section will provide an overview of the scour prediction methods that have been developed for the prediction of the equilibrium scour depth for monopiles. Many of the published scour predictors have been based on modifications of previous versions. This section will present a selection of the most popular and well tested equations. The reader is referred to Sheppard et al. (2013) who provides a comprehensive list of scour prediction equations.

One of the first scour predictors was proposed by Shen et al. (1969). In their method scour is described in terms of the pile Reynolds number (Re_D). The expression yields an estimation of the scour depth in metres and reads as:

$$S_{c,eq} = 0.000223Re_D^{0.619} \quad (2-54)$$

here $S_{c,eq}$ is the equilibrium scour depth induced by an unidirectional current.

This equation provides a best fit to specific laboratory data and does not capture the effects of flow shallowness or, flow intensity for example.

On the basis of experimental data obtained through their study, Breusers et al. (1977) proposed the following two equations for the calculation of S_{eq} :

$$\frac{S_{c,eq}}{D} = 2K_i \left(\frac{2U_c}{U_{cr}} - 1 \right) \tanh \left(\frac{h}{D} \right) \text{ for clear water scour} \quad (2-55)$$

$$\frac{S_{c,eq}}{D} = 1.5K_i \tanh \left(\frac{h}{D} \right) \text{ for live bed scour} \quad (2-56)$$

Here K_i is the product of all correction factors for the sediment gradation (K_σ), foundation shape (K_s), pier orientation (K_ω) and pier group interaction (K_{gr}) which are presented in appendix A. It is worth noting that in this approach it is implied that no scour occurs for flow velocities which are smaller than half of the critical velocity of the sediment.

Zanke (1982) developed a semi-analytical implicit formula based on the balance of sediment transport for the prediction of the equilibrium scour around cylinders. The method requires a number of iterations in order to be solved. An explicit approximation of his solution is also presented in the same work and reads as:

$$\frac{S_{c,eq}}{D} \simeq 2.5 \left(1 - \frac{0.5U_{cr}}{U_c} \right) \quad (2-57)$$

Another predictive method is described in Sumer et al. (1992). The method was based on statistical analysis of the scour data published by Breusers et al. (1977). Their results

showed that the mean non-dimensional scour depth was 1.3 and the standard deviation 0.7 and thus for practical considerations the scour depth should be given by:

$$\frac{S_{c,eq}}{D} = 1.3 + \sigma_{S_{eq}/D}, \text{ with } \sigma_{S_{eq}/D} = 0.7 \quad (2-58)$$

One of the most common scour prediction equations used in the field of river engineering is that of the Colorado State University (Johnson, 1992). This method was based on a dimensional analysis of the scour around piers and on new experimental data. It was designed to be conservative and provide an envelope curve to all of the data. The relation reads as:

$$\frac{S_{c,eq}}{h} = 2K_i Fr^{0.43} \left(\frac{D}{h}\right)^{0.65} \quad (2-59)$$

It is of interest to see that this method has selected the flow depth as the non-dimensionalising variable for the scour depth. This means that the scour depth scales with the depth rather with the diameter of the structure.

A similar method to Johnson (1992) has also been proposed by numerous other authors with the difference that the non dimensionalising variable of the scour depth is the diameter of the pile. The most well-known methods are those of Richardson and Davis (2001) (i.e. HEC 18); Guo et al. (2012) which is a less conservative method; Melville and Sutherland (1988) and Raudkivi (1991).

More recently Sheppard (2003a and 2003b) developed a scour prediction method which is based on the best fit of large scale scour data. The method is applicable to both clear water (Equation (2-60)) and live bed (Equation (2-60)) scour.

Clear water scour ($0.45 < U_c/U_{cr} < 1$):

$$\frac{S_{c,eq}}{D} = 2.5 \left\{ \tanh\left(\frac{h}{D}\right)^{0.4} \right\} \left\{ 1 - 1.75 \left[\ln\left(\frac{U_c}{U_{cr}}\right) \right]^2 \right\} \left\{ \frac{\frac{D}{d_{50}}}{0.4 \left(\frac{D}{d_{50}}\right)^{1.2} + 10.6 \left(\frac{D}{d_{50}}\right)^{-0.13}} \right\} \quad (2-60)$$

Live bed scour ($1 \leq U_c/U_{cr} < U_{lp}/U_{cr}$) :

$$\frac{S_{c,eq}}{D} = \left\{ \tanh\left(\frac{h}{D}\right)^{0.4} \right\} \left\{ 2.2 \left(\frac{\frac{U_c}{U_{cr}} - 1}{\frac{U_{lp}}{U_{cr}} - 1} \right) + 2.5 \left(1 - 1.75 \left[\ln\left(\frac{U_c}{U_{cr}}\right) \right]^2 \right) \left(\frac{\frac{U_{lp}}{U_{cr}} - \frac{U_c}{U_{cr}}}{\frac{U_{lp}}{U_{cr}} - 1} \right) \right\} \quad (2-61)$$

Here U_{lp} is the velocity corresponding to the live bed scour peak which can be determined using the Sutherland and Melville (1998) plot that describes scour depth as a function of the sediment mobility ratio (Figure 2-28).

2.4.4 Scour under wave action

2.4.4.1 Influencing parameters

In the presence of waves the flow processes governing scour change significantly. Due to the reversing nature of the orbital velocities (over a short period of time), the boundary layer in front of the monopile does not develop significantly and therefore does not form a strong horseshoe vortex system. At the same time the vortex shedding process takes up a more significant role, thus becoming the dominant mechanism contributing towards scouring (Sumer et al., 1992). According to Kobayashi and Oda (1995) the effect of the wave action on the scour around a cylinder is best described through the KC number (see Equation ((2-41))).

It is worth mentioning that for piles with small KCs (i.e. $KC < 6$) the scour process differs to that with larger KCs (i.e. $KC > 6$). Scour under such conditions is caused by the steady streaming process (see section 1.3.3.2). Scour under low KC values has not been examined as thoroughly as for slender piles. The research of Rance (1980), Toue et al. (1993) and Khalfin (2007) showed that an additional parameter to KC also influences the scour process around large diameter cylinders. This is the ratio of the pile diameter to

wavelength ratio (D/L). It can be argued though that the KC number inherently includes the effects of D/L as $KC = f(H, T, D)$.

2.4.4.2 Time evolution of scour

The most well-known method for the prediction of the time development of scour around slender piles has been presented in (2-48). Sumer and Fredsøe (2002) propose that the effects of waves can be captured by adjusting the time-scale of scour (T^*) as follows:

$$T^* = 10^{-6} \left(\frac{KC}{\theta} \right)^3 \quad \text{for waves} \quad (2-62)$$

The present method is conservative and tends to yield scour evolution time-series which are faster than what are observed both in the field and the laboratory. Current literature suggests that there are no other equations for predicting the time evolution of scour under the forcing of waves. In addition, the literature to date does not report any prediction methodologies for the time development prediction of scour induced by waves on large cylinders.

2.4.4.3 Equilibrium scour prediction

As mentioned before the most important parameter when considering scour is the equilibrium scour depth. Literature reports a number of predictive equations. This section will provide a summary of the most important.

For scour around slender piles under the action of waves Sumer et al. (1992) proposed the following formula:

$$\frac{S_{w,eq}}{S_{c,eq}} = \{1 - \exp[-0.03(KC - 6)]\}; \quad KC \geq 6 \quad (2-63)$$

where:

$S_{w,eq}$ is the equilibrium scour depth induced by waves only; and $S_{c,eq}$ is the scour depth predicted for a current alone case.

By substituting the finding of Sumer et al. (1992) (i.e. $S_{c,eq}/D = 1.3$) into Equation (2-63).

The following explicit relation can be derived:

$$\frac{S_{w,eq}}{D} = 1.3\{1 - \exp[-0.03(KC - 6)]\}; KC \geq 6 \quad 2-64$$

This formula is valid for live bed scour. Sumer et al. (1992) argue that for waves in the clear water regime the local hydrodynamics do not get amplified sufficiently in order to induce scour and thus a scour prediction formula is not required.

More recently Zanke et al. (2011) presented a semi-empirical scour prediction equation which was based on an extensive database of scour experiments. The equation has a very similar format to that presented by Sumer et al. (1992). The method is valid for $KC > 6$ and for both clear and live bed scour regimes.

$$\frac{\left(\frac{S_{w,eq}}{D}\right)}{\left(\frac{S_{c,eq}}{D}\right)} = x_{eff} \quad (2-65)$$

where

$$x_{eff} = 0.03(KC - 6); KC > 6 \quad (2-66)$$

For $KC < 6$ Khalfin (2007) developed an empirical formula on the basis of a multi-regression analysis of large scale experiments.

$$\frac{S_{w,eq}}{D} = 0.0753 \left(\sqrt{\frac{\theta}{\theta_{cr}}} - 0.5 \right)^{0.69} KC^{0.68} \quad (2-67)$$

This equation is valid for $KC \in [0.1, 3.5]$ and $D/L \in [0.06, 0.8]$ because for values of D/L larger than 0.8 the diffraction effects become dominant.

2.4.5 Scour under the forcing of combined waves and currents

2.4.5.1 Influencing parameters

Scour around cylinders under the forcing of combined waves and currents has been investigated by numerous authors. General observations suggest that the scour depth in the case where currents co-exist with waves is smaller than that for corresponding currents alone (Sumer and Fredsøe, 2002; Rudolph and Bos, 2006; Chen et al., 2012). However, Eadie and Herbich (1986), Kawata and Yoshito (1988) and Whitehouse et al. (2006) found that the superposition of waves on a current may yield scour depths which are comparable to the scour depths produced by currents only (i.e. $S/D \sim 1.5$). This difference may be attributed to the different scour regimes at which the tests were conducted. Existing research suggests that the scour depth around cylinders in such conditions is a function of both the KC number and the relative flow intensity (U_{cw})

$$U_{cw} = \frac{U_c}{U_c + U_w} \quad (2-68)$$

where U_c and U_w is the mean current velocity and the bed orbital velocity of the waves respectively.

Based on the results of Sumer and Fredsøe (2002), Rudolph and Bos (2006) and Chen et al. (2012) it can be deduced that:

- As the relative flow intensity (U_{cw}) tends to zero (i.e. wave dominated case) the scour depth approaches the values of waves only and as $U_{cw} \rightarrow 1$ (i.e. current dominated case) the scour depth reaches the maximum value equivalent to the corresponding scour depth of produced by currents only;
- For cases with low KC values even the superposition of a weak current can increase the scour potential significantly due to the presence of a horseshoe vortex; and,
- For $U_{cw} > 0.7$ the scour process is dominated by the presence of the horseshoe vortex and thus the corresponding scour depths are similar to scour depths of current alone scenarios.

Scour under the forcing of breaking waves has not been studied extensively. Bijker and de Bruyn (1988) concluded that the scour depth in such scenarios is larger than the corresponding current only situation, but their tests were conducted in the live bed scour regime and thus the larger scouring may also be attributed to the migration of bed forms. More recently Nielsen et al. (2012) showed that scour under similar conditions to the tests of Bijker and de Bruyn (1988) produced scour depths which were smaller than those corresponding to current alone but larger than those induced by non-breaking waves imposed on a current.

2.4.5.2 Time evolution of scour

Petersen et al. (2012) conducted a series of tests to investigate the effect combined waves and currents have on the time development of scour. They concluded that the time-scale of scour (T^*) is a function of U_{cw} , KC and the Shields number (θ). They further deduced that the time-scale is significantly affected when a small current is superimposed on waves with a small KC . The KC number effects the time-scale of the scour process for values of U_{cw} up to 0.4. Finally, their research showed that an increasing Shields number decreases T^* . Sumer et al. (2013) investigated the time evolution of the backfilling process in combined waves and currents. They define backfilling as the process by which the waves fill the scour hole (which was created by the current) with sediment thus reducing the scour depth. Based on the time-scale of the backfilling process one could thus derive an estimate of the time evolution of scour in combined waves and currents. They suggested that the time-scale of the backfilling process is given by the following equation which can be used in conjunction with Equation (2-49).

$$T^* = -\frac{15.15}{KC^{2.38}}(U_{cw} - 0.7) \text{ for } KC \in [0.7, 1.5] \text{ and } 0 \leq U_{cw} < 0.7 \quad (2-69)$$

Sumer et al. (2013) further suggests that the backfilling process is triggered under three conditions:

- The flow climate changes from steady current to wave dominated;

- The flow climate changes from steady current to combined waves and currents; and,
- When the wave height changes.

2.4.5.3 *Equilibrium scour depth prediction*

This section provides a summary of the scour prediction equations found in the literature. Both equations presented in this section are modified versions of the equations presented in section 2.4.4.3.

For scour around slender piles under the forcing of waves and currents Sumer and Fredsøe (2002) proposed the following expression:

$$\frac{S_{wc,eq}}{S_{c,eq}} = \left[1 - \exp \left\{ - \left(0.03 + \frac{3}{4} U_{cw}^{2.6} \right) (KC - (6 \exp(-4.7 U_{cw}))) \right\} \right]; KC \geq 4 \quad (2-70)$$

where S_{wc} is the equilibrium scour depth induced by the combined action of waves and currents.

The expression is a version of Equation (2-63) modified to fit the data for combined waves and currents. This equation was derived for the live bed scour regime and should be used with caution in the clear water scour case.

Zanke et al., 2011 propose a scour prediction equation for slender piles which is valid in both the live and clear water scour regimes.

$$\frac{S_{wc,eq}}{D} = 2.5 \left(1 - \frac{0.5 U_c}{U_{cr}} \right) x_{rel} \quad (2-71)$$

with

$$x_{rel} = \frac{x_{eff}}{x_{eff} + 1} \quad (2-72)$$

and

$$x_{eff} = 0.03 \left(1 - \frac{0.035 U_{cr}}{U_c} \right) (KC - 6); KC \geq 6 \quad (2-73)$$

The present review shows that there is not an extensive study on the scour around cylinders under the forcing of waves and currents. The few predictive equations that are

found are valid for $KC > 6$ which on practical grounds does not cover the entire range of flow conditions experienced by offshore foundations. In addition, there has not been systematic research of the effect combined waves and currents have on large diameter cylinders.

2.5 Scour around gravity based foundation

2.5.1 Introduction

As in the case of uniform cylinders, more complex structures (such as GBFs) also cause an alteration in the local flow conditions which leads to an imbalance in the net sediment transport near the structure and hence causes scour.

GBFs have geometries which are more complex than a uniform cylinder (see Figure 2-30). In addition, these structures may also be truncated and not be surface piercing. These types of structure may also induce local hydrodynamic phenomena that differ from the corresponding phenomena experienced by a uniform cylinder. This may also lead to different scour behaviour with respect to both the time and spatial development of scour.

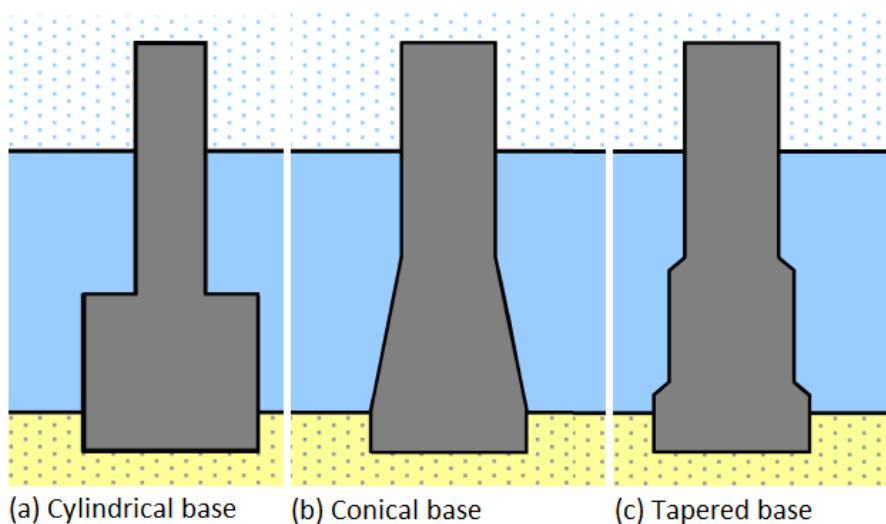


Figure 2-30: Examples of GBF foundation geometries.

Research into scour around offshore foundations has been focused mainly on the impacts different hydrodynamic conditions have on the bed when they interact with a monopile. A systematic review is given section 2.4. While a considerable amount of

research has been conducted for the fluid-structure-soil interaction around monopiles, extensive research for more complex structures such as Gravity Base Foundations (GBFs) has not been conducted, although the resulting scour has been analysed by Whitehouse et al. (2011).

This section will provide a comprehensive review of scour around gravity based foundations and other complex structure geometries focusing on the effect the geometry has on the equilibrium and time development of scour.

2.5.2 Scour in steady unidirectional currents

2.5.2.1 Influencing parameters

The influence of the structural geometry of non-uniform cylindrical structures was first investigated in the context of river scour around composite structures which in their general form are comprised of a wider cylindrical base near the bed and a narrower shaft on top. Chabert and Engeldinger (1956) first investigated scour around such structures and found that the resulting scour was mainly a function of the diameter of the base (D_{base}) and the height of the cylindrical base (h_c) (see Figure 2-31). Investigations on scour around similar geometries in fluvial environments by Jones et al. (1992), Parola et al. (1996) and Melville and Raudkivi (1996) yielded similar conclusions.

Further to scour around cylindrical based structures Fredsøe and Sumer (1997) investigated the effect conical shaped foundations have on scour. The objective of the study was to investigate the effect of the side slope of breakwater heads on scour. The results showed that a decreasing side slope of a cone yielded smaller scour depths. Simons et al (2009) investigated the effect h_c and the burial depth of the foundation has on the scour potential of truncated cylinders. Whitehouse et al. (2011) evaluated scour at marine gravity foundations and concluded that it should be possible to make more streamlined GBFs by modifying structural components (e.g. rounding off corners at scour critical areas). But they highlighted that more research is required in order to understand the scour potential of such structures. More recently, Jennaty et al. (2015) compiled a

dataset of scour around prototype complex foundations in rivers and evaluated prediction methods. Finally, Moreno et al. (2015) investigate experimentally the effect h_c and D_{shaft}/D_{base} have on the scour process.

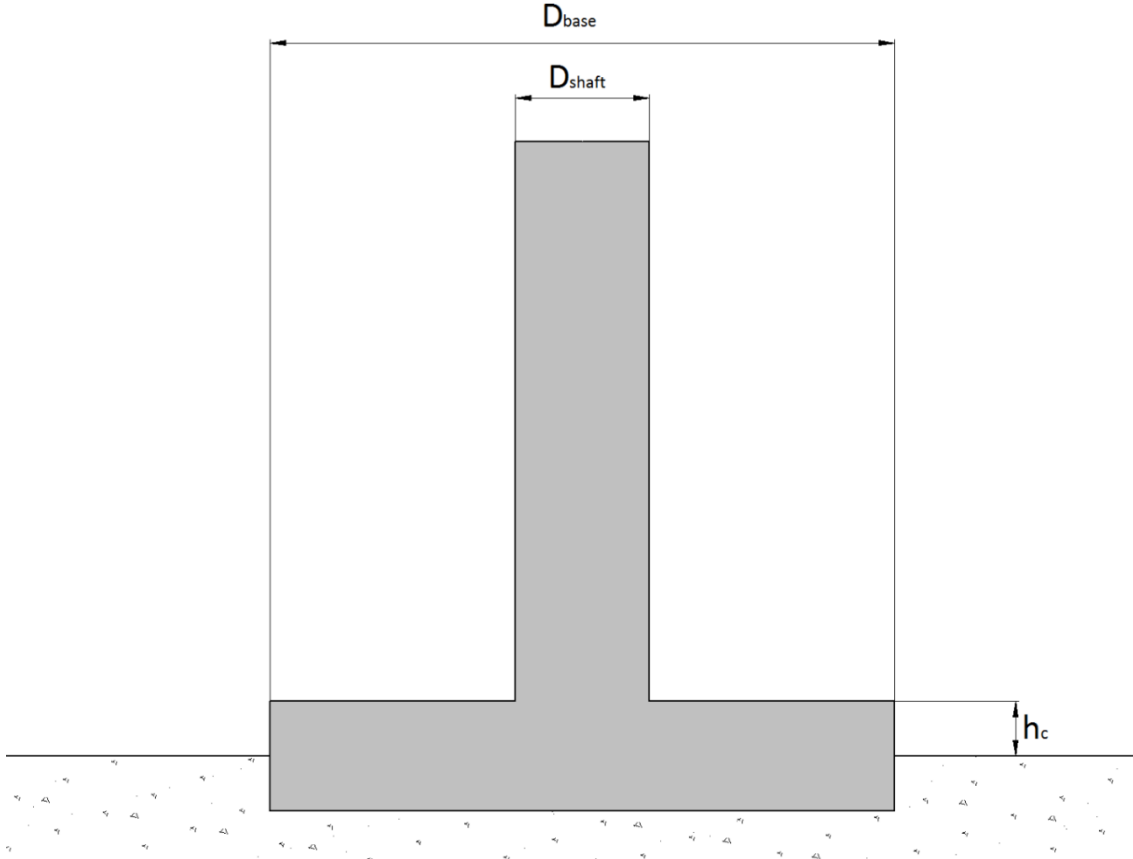


Figure 2-31: Definition sketch of key structural parameters of composite cylindrical structures.

2.5.2.2 Time evolution of scour

The only known equation for the prediction of the time development of scour around gravity based foundations was proposed by Teramoto et al. (1973) and reads as:

$$S(t) = 0.072h \left(\frac{u_*}{u_{*,c}} \right)^{2.75} \left(\frac{Fr^2 U_c t}{h} \right)^{0.364} \quad \text{for } u_* < u_{*,c} \quad (2-74)$$

The equation above is an empirical relation derived by a best fit analysis to a number of experimental tests on truncated structures in the clear water scour regime. The

expression does not include a length scale of the structure and thus implies that the scour development for any type of geometry is only a function of the flow conditions. In addition, the function does not have a cut-off limit with respect to time which suggests that the scour development will continue indefinitely, which is certainly an oversimplification. For these reasons the expression should be used with caution when applied to practical problems.

2.5.2.3 *Equilibrium scour depth prediction*

This section will provide an overview of the main equilibrium scour prediction methods for complex structural geometries in both river and marine environments.

The first equation for scour around gravity based foundations was proposed by Khalfin (1983) and was derived from a number of physical model tests around conical and cylindrical structures under the forcing of a unidirectional current. The equation reads as:

$$\frac{S_{c,eq}}{D} = 8.96 \left(\frac{2U_c}{U_{cr}} - 1 \right) \left(\frac{h}{D} \right)^{1.43} Fr \left(\frac{0.83h}{D} \right)^{0.34} \quad (2-75)$$

The expression above was further modified by Hoffmans and Verheij (1997) in order to predict scour depths around non-cylindrical geometries such as structures with a rectangular footprint and truncated structures.

$$\frac{S_{c,eq}}{D_{eq}} = 8.96 \left(\frac{\alpha_{cor} U_c}{U_{cr}} - 1 \right) \left(\frac{h_c}{D_{eq}} \right)^{1.43} \left(\frac{(\alpha_{cor} U_c)^2}{4gh_c} \right)^{\left(\frac{0.83h_c}{D_{eq}} \right)^{0.34}} \quad (2-76)$$

In this expression the pile diameter (D) was replaced by an equivalent pile diameter (D_{eq}) taken as the average length and breadth of the structure and the depth of the flow (h) was replaced by the height of the structure (h_c). Finally, a flow intensity modification factor (α_{cor}) was introduced to account for additional turbulence induced by the corners of rectangular structures. α takes a value of 2 for cylindrical footprints and 2.3 for rectangular. The two aforementioned expressions are valid in the range $0.1 < Fr < 1$ which corresponds to relatively shallow water conditions in a marine environment.

Whitehouse (2004) conducted physical model tests of scour around a range of different GBF geometries. The study showed that under the forcing of currents the expected scour depth around a cylindrical base GBF is approximately $0.18D_{base}$.

Further to the Khalfin formula additional methods for the prediction of the scour depth around composite structures were developed for alluvial environments. Melville and Raudkivi (1996) developed a method for predicting the equilibrium scour depth around composite cylindrical structures (see Figure 2-31). The method distinguishes two main scenarios: when the footing is buried under the bed (i.e. $h_c < 0$);

$$\frac{S_{c,eq}}{D_{shaft}} = 2.4 \left(\frac{D_{shaft}}{D_{base}} \right)^{0.4+0.5 \left(\frac{D_{shaft}}{D_{base}} \right)} \quad (2-77)$$

and, the case where the bottom footing is protruding from the original bed level (i.e. $h_c > 0$).

$$\frac{S_{c,eq}}{D_{shaft}} = 2.4 \left(\frac{D_{shaft}}{D_{base}} \right)^{\left(\frac{D_{shaft}}{D_{base}} \right)^{+0.1-0.47} \sqrt{0.75 - \frac{h_s}{D_{shaft}}}} \quad (2-78)$$

In addition, an approach for determining an equivalent structural diameter for the prediction of the scour depth is also given in the same study:

$$D_{eq} = D_{shaft} \left(\frac{h + h_c}{h + D_{base}} \right) + D_{base} \left(\frac{D_{base} - h_c}{h + D_{base}} \right) \quad (2-79)$$

The above length scale of the structure can be used with the scour prediction methods for cylinders shown in section 2.4.3.

Parola et al. (1996) also developed a similar method. They assume two main configurations of the structure when the base is buried under the original bed:

$$\frac{S_{c,eq}}{D_{base}} = 1.872 \left(K_{shape} \left(\frac{h_c}{D_{base}} \right)^{0.255} \right) \quad (2-80)$$

and when the footing is above the bed:

$$\frac{S_{c,eq}}{S_{shaft}} = 2.4K_s \quad (2-81)$$

S_{shaft} is the theoretical scour depth induced by the shaft of the structure assuming that no footing is present and K_s can be found in Appendix A. This can be calculated with the expressions presented earlier in section 2.4.3.

The aforementioned method provides an envelope curve which encloses most of the data under it. Thus it is a conservative design method.

Richardson and Davis (2001) (i.e. HEC-18 method) and Sheppard and Glasser (2004) proposed a superposition method for predicting the equilibrium scour depth around composite structures. In this method the structure is split into components with the same geometry and then the scour depth attributed to each component is calculated separately and then added. This method provides an alternative to the methods shown above but does assume that there is no interaction between each component which may be regarded as an oversimplification.

Finally, Coleman (2005) proposed a method for calculating the equivalent pile diameter for cylindrical based structures. He distinguishes five main structure configurations in his study which are summarized below:

Case I, the pile cap is installed under the original bed and not affected by scour:

$$D_{eq} = D_{shaft} \quad (2-82)$$

Case II, the pile cap is at least partially installed under the original bed and is effected by scour:

$$D_{eq} = D_{shaft} \left\{ \left(\frac{D_{shaft}}{D_{base}} \right)^3 + 0.1 - \left[0.47 \left(0.75 - \frac{h_c}{D_{shaft}} \right) \right] \right\} \quad (2-83)$$

Cases III to V correspond to configurations where the supporting piles of the structure are exposed. These are out of the scope of the present research. For further information, the reader is recommended to read Coleman (2005).

2.5.3 Scour under wave action

Scour under the forcing of waves has not been studied extensively. Khalfin (1983) examined the scour due to wave action around large cylinders and cones and concluded that the main influencing parameters are the relative orbital velocity (U_w/U_c), the relative wavelength (D/L) and the Ursell number (Ur) which is a measure of the non-linearity of the wave. This is defined as:

$$Ur = \frac{HL^2}{h^3} \quad (2-84)$$

Subsequently, Khalfin (1988) proposed a scour prediction equation for cones and cylinders under the forcing of waves, which was derived by a multiple regression analysis on a set of 55 scour experiment results. The equation reads as:

$$\frac{S_{w,eq}}{D} = 0.013 \left(\frac{U_w}{U_c} - 0.5 \right)^{0.4} \left(\frac{D}{L} \right)^{-0.43} Ur^{0.39} \quad (2-85)$$

Bos et al., 2002a investigated the effects of waves on a truncated structure (F3 Offshore GBF Platform). They compared empirical formulations for the prediction of the equilibrium scour depth with physical model tests and survey measurements from the actual platform. They concluded that the existing empirical equations over-predict the scour depth by approximately 50%.

Whitehouse (2004) conducted a study on scour around conical and cylindrical based structures. The study showed that scour around such structures in random wave action was $0.04D_{base}$ (i.e. four time smaller than for currents alone).

Though several examples of offshore gravity based foundations exist (e.g. Nysted, Denmark), GBFs have only recently become a more appealing foundation option for offshore wind farms. For this reason, no significant research into the time development of scour around such structures has been conducted yet.

2.5.4 Scour under combined wave and current action

As is the case for scour around GBFs under the forcing of waves, scour in combined waves and currents has not been researched extensively. The only information available on scour around large structures in combined waves and currents comes from the results presented in Rance (1980) and Whitehouse (2004) who present a limited number of experimental results on scour around GBFs.

Bos et al., (2002b) presented a method for predicting the equilibrium scour depth around sit-on GBFs (i.e. large truncated structures) under the combined forcing of waves and currents. Their method is based on that presented by Breusers et al. (1977) which describes scour as the product of a number of different influencing factors (f_i). The general form of the equation is presented here:

$$\frac{S_{cw,eq}}{h} = \prod_{i=1}^6 f_i \quad (2-86)$$

in which f_1 is the wave coefficient:

$$f_1 = 0.044KC \quad (2-87)$$

f_2 is the effect of combined waves and currents:

$$f_2 = \frac{A \tanh(3.5(U_{cw} - B)) + 1.9 - A}{A \tanh(-3.5B) + 1.9 - A} \quad (2-88)$$

with: $A = 0.95/(1 + 0.005KC)$ and $B = 0.8/(1 + 0.005KC^2)$

f_3 is the effect of the relative sediment mobility:

$$f_3 = \frac{U_c}{U_{cr}} \quad (2-89)$$

f_4 represents the effect of the structural height:

$$f_4 = \tanh \left[3.5U_{cw} \left(\frac{h_c}{h} - 1.4 \right) \right] + 1 \quad (2-90)$$

$f_5 = K_s$ is the shape factor of the structure which can be found in Appendix A.

f_6 is the effect of the relative flow depth:

$$f_6 = 1.5 \tanh\left(\frac{D_{base}}{h}\right) \quad (2-91)$$

Bos et al., 2002b suggests that the time evolution of scour can also be predicted by multiplying the right hand side of Equation (2-86) with a time factor:

$$f(t) = 1 - \exp\left(-\frac{t}{T_e}\right) \text{ with } T_e = 0.2 + 60d_{50} \quad (2-92)$$

The present time factor was derived using measurements that were made in the later stages (where the rate of scouring is small) of the scour development and thus caution is advised when applying it to the earlier stages of the scour process. In addition, the tests were conducted with coarse sediments and rocks with large geometric standard deviations and thus its applicability on fine and uniform sands may be questioned.

2.5.5 Discussion on scour prediction around GBFs

In contrast with scour around slender cylindrical piles, scour around more complex geometries like GBFs is far less investigated. Most of the equations derived for the prediction of scour around GBFs have been based on a limited number of experimental studies and do not account for all the different possible geometries. This shows that there is no existing method that links key hydraulic processes around both uniform cylinders and more complex geometries. This leaves a significant gap in the literature especially regarding GBF scour.

2.6 Scour protection practice

2.6.1 Introduction

Scour protection may be defined as protection of the local bed around a hydraulic structure against the local amplified flow forces. The purpose of scour protection is to stabilise the soil near the structure and thus ensure that the functionality of the structure remains intact. There are a number of different criteria for the design of scour protection systems. The majority of these have been developed for the protection of bridge piers in rivers. Examples are presented by Chiew (1995) and Hoffmans and Verheij (1997). The

design of scour protection systems in the marine environment is a relatively new field. Key studies on this topic are Den Boon et al. (2004), Grune et al. (2006), Whitehouse et al. (2006), De Vos et al. (2011 and 2012), Petersen et al. (2014) and Nielsen et al. (2013 and 2015).

As mentioned previously, the main purpose of scour protection is to provide an effective and efficient means of maintaining the bed around a structure to a level which ensures that the structure will fulfil its full functionality. The most common type of scour protection is rip rap (i.e. loose rock). Rip rap is generally the widest used scour countermeasure as it is readily available and economic in most areas. In addition to rip rap several other methods of scour protections are available such us:

- Mattresses: This type of protection consists of a fabric (usually a geotextile or a flexible concrete mattress) which is weighted down with the use of heavy materials such as concrete blocks, rocks or steel slabs. There are no design guidelines for the use of mattresses as a form of scour protection. Their design and installation is usually based on case-specific physical model tests; and,
- Flow inhibitors: The purpose of these types of scour countermeasure is to reduce the effects of the downflow, horseshoe vortex and vortex shedding on the bed. This also does not have any design guide-lines.

Melville and Coleman (2000) recommend that any scour protection system to prevent scour of depth S should consider the following two components (see Figure 2-32 for definitions):

- Armour layer, which is the part of the scour protection system which provides the required resistance; and,
- The filter layer, which ensures that the bed material does get removed through the top armour layer.

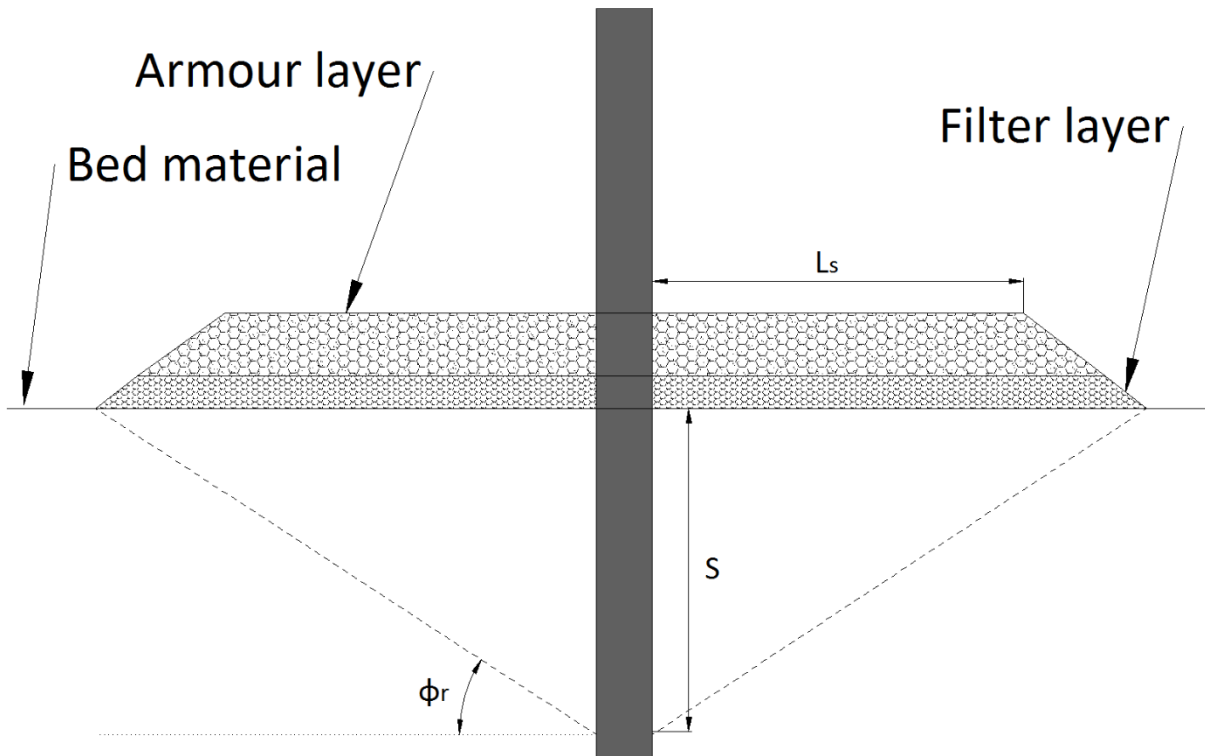


Figure 2-32: Definition diagram of scour protection design.

More recently in the offshore industry, scour protection systems comprised of one thicker layer of widely graded rock have been successfully installed and are now the most common way of protecting offshore wind turbine foundations against scour.

The key issues that need to be addressed when designing scour protection systems are the size of rock, lateral extent, thickness of the scour protection layer and whether or not a filter layer is required.

The following sections will provide a summary of existing scour protection design codes and practice for rip rap given the lack of information for the other scour mitigation methods (e.g. mattresses).

2.6.2 Armour layer

2.6.2.1 Stone size

The most common method for selecting the required stone size of the armour layer is based on the potential flow solution of a unidirectional current interacting with a circular cylinder (Hoffmans and Verheij, 1997 and Whitehouse, 1998). According to potential flow the following criterion arises:

$$\tau_{cr} > 4\tau_{\infty} \quad (2-93)$$

In this expression τ_{crit} is the critical bed shear stress of the armour layer which can be calculated using Equations (2-31),(2-34) and (2-35). And τ_{∞} is the undisturbed bed shear stress which can be determined using the methods outlined in section 2.2.

Breusers and Raudkivi (1991) propose that the median size of the rock riprap (D_{50}) can be determined using the expression:

$$D_{50} = \left(\frac{U_c}{4.8\sqrt{\Delta h^{\frac{1}{3}}}} \right)^3 \quad (2-94)$$

Here Δ is defined as the relative density of the stone $\Delta = (\rho_s - \rho_w)/\rho_w$.

Equation (2-94) is valid for unidirectional currents and was derived under the hypothesis that the critical Shields parameter is constant at 0.04. This may yield conservative results in practice.

May and Escarameia (1992) propose the following expression for determining the required stone size for the rip rap.

$$D_{50} = \frac{3.1U_c^2}{2g(s-1)} \quad (2-95)$$

This expression was derived based on the Isbash (1935) method and fitted to a wide range of experimental tests under the forcing of unidirectional currents and included tests on rip rap, gabions and stone mattresses.

The US Army Corps of Engineers (2010) river analysis manual recommends the method of Maynard (1995) for the prediction of the required rock size. The method was developed based on prototype measurements at bridge piers in rivers and reads as:

$$D_{30} = S_f C_s h \left(\frac{U_c}{(s-1)\sqrt{K_1 g h}} \right)^{2.5} \quad (2-96)$$

Here D_{30} is the 30% finer stone size; S_f is a safety factor; C_s is a stability coefficient taken as 0.3 for angular rocks; and K_1 is the slope correction factor which is taken as 1 for flat beds.

Chiew (1995) developed an iterative approach for determining the required stone size for rip rap at cylindrical bridge piers:

$$D_{50} > \frac{1}{5.956\sqrt{h}} \left\{ \frac{U_c}{\left(\left(\frac{U_c}{U_{cr}} \right) \sqrt{(s-1)g} \right)} \right\}^3 \quad (2-97)$$

in which U_c can be determined based on Equations (2-31),(2-34) and (2-35).

HEC-23 further recommends that the Isbash (1935) formula should be used to determine the required median stone size:

$$D_{50} = \frac{0.692U_{des}^2}{\Delta 2g} \quad (2-98)$$

in which U_{des} is defined as the local design velocity found from potential flow theory and taken as: $U_{des} = 2U_c$.

Den Boon et al. (2004) and Whitehouse (2006) present a summary of the OPTI-PILE scour protection design tool. In this method the stability of rip rap around offshore monopiles is assessed using the following equation:

$$Stab = \frac{\theta_{max}}{\theta_{cr}} \quad (2-99)$$

in which θ_{max} is the maximum Shields parameter from the combined effect of waves and currents. Which can be calculated in accordance with equation (2-27); θ_{cr} is the critical Shields parameter for the rip rap determined from equation (2-35). According to the OPTI-PILE method the scour protection behaviour can be classified into three categories:

- Statically stable: No movement of scour protection is allowed. This occurs for $Stab < 0.415$;

- Dynamically stable: In which some movement is allowed in the armour layer but the movement does not lead to the failure of the scour protection. This occurs in the range of $0.415 \leq Stab < 0.460$; and,
- Failed: This means that the filter layer has been exposed over a total area of at least $4D_{50}^2$. This is defined as the range of $Stab \geq 0.460$.

More recently De Vos et al. (2011) proposed an empirical method for evaluating the stability of a given scour protection system around monopiles in combined waves and currents, which is based on a linear regression analysis of a number of physical model experiments. The equation is derived for a statically stable scour protection cover layer (i.e. no movement of stones):

$$\frac{\tau_{cr}}{\rho_w \Delta g D_{50}} > 0.001 + 3.303 \frac{\tau_0}{\rho_w \Delta g D_{50}} + 1.015 \frac{\tau_w}{\rho_w \Delta g D_{50}} \quad (2-100)$$

De Vos et al. (2012) proposed a second method for the prediction of the required stone size for a dynamically stable scour protection layer. This method is based on the Van der Meer (1988) method for quantifying damage in rubble mound breakwaters:

$$\begin{aligned} \frac{S_{3D}}{N^{0.24}} = & \frac{0.0008 U_w^3 T^2}{\sqrt{gh}(s-1)^2 D_{50}^2} + \\ & + b_0 \left(-0.02 + 0.008 \frac{\left(\frac{U_c}{w_s}\right)^2 (U_c + b_1 U_w)^2 \sqrt{h}}{g D_{50}^{\frac{3}{2}}} \right) \end{aligned} \quad (2-101)$$

in which w_s is the settling velocity of a sediment particle;

$$b_0 = \begin{cases} 0; & \text{for waves following currents and } \frac{U}{\sqrt{gD_{50}}} < 0.92 \\ 1; & \text{for waves opposing currents and } \frac{U}{\sqrt{gD_{50}}} \geq 0.92 \end{cases}$$

$$b_1 = \begin{cases} 1; & \text{for waves following currents} \\ \frac{Ur}{6.4}; & \text{for waves opposing currents} \end{cases}$$

and the damage number (S_{3D}) is defined as:

$$S_{3D} = \frac{V_s}{D_{50}^2} \quad (2-102)$$

in which S_{3D} is the non-dimensional damage in the scour protection which is classified as:

- $S_{3D} < 0.25$ corresponds to a statically stable configuration;
- $0.25 \leq S_{3D} < 1$ corresponds to a dynamically stable scour protection armour layer; and,
- $S_{3D} \geq 1$ corresponds to the complete failure of the scour protection.

and V_s is the volume of scoured material.

This method provides an option to the designer to quantify the allowable damage depending on the requirements of their design and to select the appropriate stone size. The method is based on 85 physical model tests which were conducted at a relatively large KC numbers (i.e. $KC > 6$). This range of KC is representative of slender structures and thus the application of this method to GBFs (with typical $KC < 6$) should be done with caution.

It should be noted that in practice designers do not select a specific D_{50} for the design of the scour protection cover layer but rather select a rock grade that satisfies the minimum D_{50} .

2.6.2.2 Thickness

The thickness of the armour layer (t_c) is also an important factor in the design of scour protection. The thickness determines the damage the scour protection can withstand without exposing the underlying filter layer or bed. Several rules for the required thickness exist all of which have been derived for scour protection around uniform cylinders under the forcing of unidirectional currents. The following table provides a summary of the existing rules:

Table 2-2: Summary of scour protection thickness recommendations

Author	Minimum thickness	Maximum thickness	Comments
US Army Corps of Eng. (2010)	$1.5D_{50}$	-	The thickness of the cover layer should be increased by 50% if installed underwater.
Breusers and Raudkivi (1991)	$2D_{50}$	-	-
Hoffmans and Verheij (1997)	$2D_{50}$	-	-
Whitehouse (1998)	$2D_{50}$	-	-
May et al. (2002)	$2.5D_{50}$	$1.5D_{100}$	-

2.6.2.3 Lateral extent

Several suggestions have been made for the required lateral extent of scour protection around monopiles. The majority of these have been developed for the case of unidirectional currents. The lateral extent of the scour protection (L_s) is defined as the length of the scour protection from the perimeter of the structure (see Figure 2-32).

Bonasoundas (1973) proposed that the extent of the scour protection in a unidirectional current should have a minimum length of $2.5D$ in the front but should extend at least $4.5D$ at the lee.

Hjorth (1975) suggested that the length of the scour protection in front of the pile should be $0.75D$ and the length at the lee should extend to $5D$ in order to accommodate the large turbulence levels attributed to the lee wake vortex shedding.

Carstens (1976) suggested that the extent of the scour protection should be equal to the length of the scour hole at the equilibrium phase and proposed the following formula:

$$L_s = F_{safe} S \cot(\phi_r) \quad (2-103)$$

in which F_s is a safety factor taken as 1.5; S the equilibrium scour depth due to any combination of waves and currents; and ϕ_r is the angle of repose of the bed material (see Figure 2-32)

Other authors such as Breusers and Raudkivi (1991) and Schiereck (2003) recommend that the extent of the protection should be at least $3D$ around the entire periphery of the structure.

Gökçe et al. (1994) suggested that the lateral extent of the scour protection around a breakwater for the case of waves should be 3-4 times the diameter of the head of the breakwater. This rule of thumb could also be used in the case of monopiles and GBFs.

In practice the lateral extent of the scour protection is usually determined through numerical and physical modelling tests to determine the maximum area around the structure where the local flow forcing is amplified by the presence of the structure. The extent of the scour protection is then selected in order to cover this area. In addition, the lateral extent may be further extended to accommodate loss of scour protection due to edge scour.

2.6.3 Granular filter layer

The purpose of a filter layer in a scour protection system is to minimize the loss of finer sediment coming from the bed while maintaining it permeable enough for the water to flow through it. Granular filters can be divided into two categories (also see Figure 2-33):

- Geometrically Closed: The pores between the filter material are small enough not to allow material from the base layer to pass through; and,
- Geometrically Open: The flow velocity through the filter layer is not strong enough to transport sediment through it.

This section will provide a summary of the key design equations for these two types of filter.

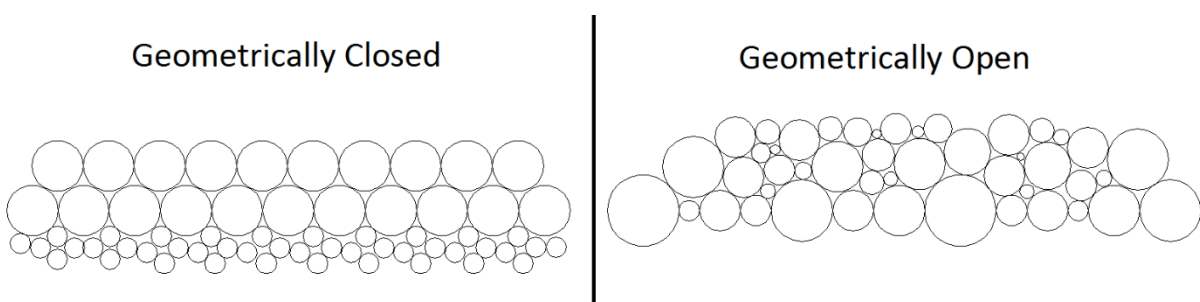


Figure 2-33: Types of filters.

2.6.3.1 Geometrically closed filters

These filters follow the filter design rules formulated originally by Terzaghi (1939). The method suggests that a filter can be functional under three conditions:

- a) The filter layer blocks the movement of the particles through it which is achieved when:

$$\frac{d_{15,f}}{d_{85,b}} < 5 \quad (2-104)$$

- b) The permeability of the filter layer is larger than the permeability of the base layer. This ensures that no pressure build-up occurs:

$$\frac{d_{15,f}}{d_{15,b}} > 5 \quad (2-105)$$

- c) The base layer is internally stable which means that the size of the larger particles is not big enough to allow the movement of the smaller particles in the soil:

$$\frac{d_{60,b}}{d_{10,b}} < 10 \quad (2-106)$$

where d_i i^{th} percentile of bed material size grading; and the subscripts refer to the filter layer f and the base layer b .

Similar design criteria with slightly different formulations for geometrically closed filters are also proposed by other sources such as US Army Corps of Engineers (2010), Whitehouse (1998) and Schiereck (2003).

2.6.3.2 Geometrically open filters

The basic principle of operation of a geometrically open filter is that the flow passing through it is damped due to friction and thus is not capable of transporting base material through it. In general, these types of filter are associated with larger uncertainties and larger thicknesses compared to closed filters. On the other hand, they tend to be cheaper and easier to install than geometrically closed filters. For this reason, they are usually chosen for the protection of most offshore and coastal structures. This section will provide a summary of the main design methods for such filters.

Wörman (1989) investigated the granular filters around bridge piers in rivers and derived the following empirical relation for the required thickness of a geometrically open filter (t_f):

$$\frac{t_f}{d_{50,f}} = 0.16 \frac{n_f d_{85,f} \Delta_f}{1 - n_f d_{85,b} \Delta_b} \quad (2-107)$$

in which n_f is the % porosity of the filter; Δ_f and Δ_b are the relative density of the filter and base material respectively.

A similar equation is proposed by Hoffmans (2012). The equation is based on turbulence theory and empirical data. The method also gives a relation between the required thickness and the size of median size of the filter material and reads as:

$$\frac{t_f}{d_{50,f}} = 1.2 \ln \left(\frac{d_{50,f}}{d_{50,b}} \right) \quad (2-108)$$

Finally, Nielsen et al. (2013) recommend that the required stone size for a filter layer installed around a pile under the forcing of a unidirectional current can be determined using the following expression:

$$\Omega = \frac{U_c^2}{g(s-1)h} \frac{d_{50,f}}{D} \frac{n_f}{1 - n_f} \quad (2-109)$$

Here Ω is a sediment mobility parameter similar to the Shields parameter that can be used to determine when sediment will be mobilised underneath a scour protection or a filter layer. In the same study Nielsen et al. (2013) reports that a thin filter layer of coarser stones and a scour protection with a similar thickness and no filter layer behaved in the same manner with regards to bed sediment movement. It should be noted though that every design situation will need to be evaluated on a case by case basis.

2.6.4 Discussion on scour protection practice

In this section the current practice in the field of scour protection around uniform cylinders has been presented. The literature review showed that the majority of methods for determining the required stone size in the armour layer have been developed based on experimental tests. The method of Whitehouse (1998) which suggests that the stone size should be based on the local amplification of the bed shear stress proves an effective method. However, at this point there is uncertainty as to whether or not a universal amplification factor of 4 could be applied to all combinations of structure and

hydrodynamic conditions. With regards to the lateral extent and thickness of the scour protection it seems that there is general agreement with most studies agreeing on $L_s > 2D - 3D$ and $t_s > 2D$. One significant gap in existing literature is the complete lack of information on scour protection specifications around more complex structures such as GBFs.

With regards to the filter layer design criteria, geometrically closed filters often are a more reliable solution. All of the design methods rely on the original method of Terzaghi (1939) and all show good results. A more economical solution, though associated with more uncertainty, involves geometrically open filters. There is not a significant amount of knowledge on the subject but a number of design criteria are also available for such solutions. Again, as was the case for the cover layer, there has not been any significant research into the stability of the filter layer around GBFs.

3 Aims and objectives

This chapter will present the aims and objectives of this study which were determined based on the gaps in the literature identified in the previous chapter.

The main aim of this thesis is to provide a better understanding on the subject of scour and scour protection around Gravity Based Foundations. The present work focuses on the effect the structural geometry has on scour and on the stability of the rock armour cover layer used for scour protection. As was shown in the literature review the effect of the foundation geometry has mostly been looked at by examining the scour induced by individual components of a composite structure. This approach overlooks the interaction the geometry has as a whole with the incoming flow. And in terms of scour protection there have not been any studies examining the effect of the foundation geometry on the stability of the cover layer. The present work aims to fill the following gaps in literature:

- With respect to scour:
 - Understand the effect the structural geometry has on the equilibrium scour depth and on the shape of the scour hole.
 - Determine which length scale is the most appropriate to non-dimensionalise scour around complex geometries.
 - Obtain a better understanding of the local flow field near the structure and link flow mechanisms to scour behaviour.
 - Gain insight on how several flow parameters such as the flow depth, flow velocity and sediment size affect the equilibrium scour depth of complex structures.
 - Link the pressure gradient which is induced by the interaction of the flow with a complex structure to the equilibrium scour depth.
 - Develop a scour prediction method that can predict the equilibrium scour depth around both complex and uniform cylindrical structures by taking into account the interaction the structure has with the incoming flow conditions.

- With respect to scour protection:
 - Create an objective method for determining the incipient motion of rocks without relying on the visual observation which introduces a significant amount of error.
 - Better understand how properties of the scour protection (e.g. position relative to the bed, permeability of bed, rock size) effect the stability of the rock cover.
 - Determine how different combinations of waves and currents (including waves opposing current) influence the stability of the rip-rap.
 - Develop a method for determining the required stone size for the scour protection rock that can be used for both monopiles and complex geometries.
 - Obtain a better understanding of the affect different flow conditions have on the damage pattern around the foundations considered in this study.
 - Determine whether or not flow conditions that just lead to the incipient motion of rocks around GBFs and persist for a sufficiently long period of time lead to the failure of the scour protection.

To meet the aims and objectives detailed above an extensive series of experiments has been designed and conducted. The details of the experimental design are detailed in Chapters 4 and 7 and the scope of the experiments is further detailed below:

- Scour experiments:
 - The study focused on six foundation geometries.
 - The tests were conducted using non-cohesive sediments. Two different sediments were used to examine the effect of sediment size. All sediments were well graded to avoid gradation effects.
 - Tests were conducted at two different structural scales with the geometries maintaining the same proportions.
 - The tests were conducted in the clear water regime under the forcing of a unidirectional current for the following reasons:
 - To avoid rippling of the sediment bed. In the live bed scour regime sediment transport occurs through the entire sediment bed. This means that sediment will move into the scour hole reducing the scour depth.

- To measure the scour depth more accurately. Due to the varying incoming flux of sediment into the scour hole the measurement of the exact scour depth becomes more difficult. In addition, the bed forms that are created under live bed scour are strongly affected by the flume scale and the size of the sediment. Given that the equilibrium scour depth in live bed scour is a function of the sediment transported into the scour hole the resulting equilibrium scour depth would also be strongly affected by these factors. Thus, the resulting scour depths would be hard to be compared with prototype measurements.
 - To obtain conservative results with regards to the measured scour depth, as near critical flow velocities yield the deepest scour (Melville and Sutherland, 2000); and
 - The existing facilities did not have the capacity of providing a constant recirculating sediment flux.
 - The pressure and flow measurements were conducted under the forcing of a similar unidirectional current. The measurements were conducted over a fixed bed to avoid having discrepancies in the measurement due to the different scour rates associated with each structure type.
 - Pressure measurements were made up to an angle of 140° relative to flow direction due to equipment limitations.
- Scour protection experiments:
 - The work was constrained to testing the stability of the cover layer of scour protection. This means that the effects by the other processes such as edge scour and infiltration of sediment were not allowed in the design of the physical models.
 - The study examined four foundation geometries at one structural scale due to the difficulty of scaling down the scour protection rock.
 - The effect of rock grading was not examined in the tests. For this reason, only well graded rocks were used as scour protection material.
 - The effect of the thickness of the scour protection will not be considered.
 - The effect of flow direction and different combinations of waves and currents was examined.
 - The effect of the scour protection configuration was tested.

Part II: Scour prediction around complex structures

4 Methodology

4.1 Introduction

The purpose of this section is to explain the methodology followed during the scour experiments and to provide a description of the methods followed for the development of the scour prediction equation. In this study an extensive series of scour experiments around uniform and non-uniform cylinders were carried out over a range of different hydraulic conditions. In addition, experiments were carried out at different scales in order to investigate scale effects. The purposes of these tests was threefold:

- To investigate the effect, the structural geometry has on the equilibrium scour depth for different flow conditions.
- To study the pressure field around complex structures.
- To develop an equation capable of predicting the scour depth around cylindrical structures with uniform and non-uniform cross-sections.

For this reason, three different experimental series were derived. First small scale scour experiments were conducted to get a preliminary understanding of the effects the geometry of structures have on scour. Then a series of larger scale experiments were run to investigate scour at a different scale. Finally, the pressure and flow field around these structures were measured. The outcome from these experiments was then used in conjunction with a database of equilibrium scour depth data to develop a new scour prediction equation. This equation provides a method for predicting the scour depth around uniform cylinders and complex structures.

This chapter describes the set-up of the experimental facilities used for these tests, the choice of parameters for the hydraulic models, the equipment used during the tests and the experimental programme for each test series. Finally, it describes the methodology

followed for compilation of the database of equilibrium scour results used for the development of the equilibrium scour depth prediction equation.

4.2 General model and scaling considerations

Hydraulic engineering relies on three main techniques for the design and study of hydraulic phenomena:

- Physical modelling;
- Field measurements; and,
- Numerical modelling.

According to Hughes (2003) physical modelling is a reliable tool for the investigation of hydraulic phenomena. This is because to date the capabilities of conventional computers are quite limited. The need for physical modelling becomes even more apparent in the case of scour and scour protection since existing computational models cannot simulate effectively the sediment transport around structures. Finally, even though field studies have their merits especially because they are not subject to scale effects they also have a number of shortcomings, which among others are:

- High costs;
- Field measurements tend to have time-varying flows which make it difficult to determine if a given scour hole has reached the equilibrium phase;
- Unknown historical effects such as long term morphological changes may affect the accuracy of the measurements; and,
- In most cases it is hard to monitor systematically due to the environmental conditions.

4.2.1 Scaling considerations

4.2.1.1 Hydrodynamic scaling

Hughes (1993) suggests that successful physical models must have similitude between the main non-dimensional quantities governing the processes. These quantities are the Reynolds (Re), Froude (Fr), Strouhal (St), Euler (Eu), Ursell (Ur), Keulegan–Carpenter (KC), Cauchy (Ca) and Weber (We) numbers. In most practical cases it not possible to achieve similitude of both the Reynolds and Froude number. For this reason, in practice

the most influencing parameters are identified and scaled accordingly. Sutherland and Whitehouse (1998) discuss Reynolds number similarity is usually not achieved. This is because the turbulent shear stresses do not scale with the Froude number because gravity and the viscosity are usually constant in both experiments and prototype conditions. However they state that the Reynolds number is important for values reaching 2×10^5 for flow around piles.

The experiments conducted in this study do not set out to model prototype conditions. Rather they aim to investigate basic processes. The influence of scale effects on the scour process are examined by conducting tests at different scales.

4.2.1.2 Sediment scaling

When considering scour and scour protection experiments another important aspect is the scaling of the sediment. Sutherland and Whitehouse (1998) provide a comprehensive discussion on the subject of sediment scaling. They distinguish three main methods for scaling sediment.

Small size sediment scaling

For small diameter sediments ($D_* < 2.4$) the sediment can be scaled by applying Froude scaling to the settling velocity. Assuming that the sediment density is the same in both prototype and model cases this yields:

$$n_{sd} = \sqrt{n_w} = n_L^{\frac{1}{4}} \quad (4-1)$$

Here n_{sd} is the scale of small sediment particles, n_w the scale for the settling velocity and n_L the geometric length scale.

Large size sediment scaling

For larger sized sediments (i.e. $D_* > 25.9$) the quadratic bluff-body fall speed can be used for the Froude scaling of the sediment. This yields:

$$n_{ld} = n_w^2 = n_L \quad (4-2)$$

Here n_{ld} is the scale for large sediments.

It should be noted that sediment scaling can be done using the Soulsby (1997) equation for the settling velocity (w_s) in conjunction with the Froude scaling. The benefit of the Soulsby equation is that it is valid for the entire range of sediment sizes and does not have discontinuities. The equation reads as:

$$w_s = \frac{v}{d_{50}} \left(\sqrt{10.36^2 + 1.049D_*^3} - 10.36 \right) \quad (4-3)$$

Shields parameter scaling

One more way of scaling the sediment is by ensuring that the ratio θ/θ_{crit} is the same between the prototype and model. This ensures that the mode of sediment transport (e.g. sheet flow or suspended load) is going to be the same, but the time scale of the sediment transport may be affected.

An additional scaling consideration is the relative size of the sediment to structure diameter. According to Chiew (1984) and Sheppard (2004) when the sediment size is large relative to the structure the local pressure gradient induced by the structure on the sediment particle decreases thus resulting in smaller scour depths. In clear water scour this effect becomes negligible when:

$$\frac{d_{50}}{D} < \frac{1}{50} \quad (4-4)$$

An additional consideration regarding the sediment is the formation of ripples on the bed. In laboratory conditions ripples tend to be relatively larger than in prototype conditions. This problem arises because the spacing between the ripples is proportional to the sediment size and sediments are not geometrically scaled in many physical models (Sutherland and Whitehouse, 1998). There are two main concerns when ripples (i.e. live bed scour regime) are formed in scour experiments:

- a. Scour depths tend to be smaller. This is mainly because the ripples migrate through the scour hole (incoming sediment flux) thus replenishing the local sediment transport demand. This behaviour has been reported by numerous authors among which are Melville (1984), Kawata and Tsuchiya (1988) and Khalfin (2007).
- b. The measurement of the scour depth becomes difficult as the ripples migrate through the scour hole. This can introduce an error in the scour measurement in the order of magnitude of the ripple height.

Given that the present study does not aim to model specific prototype conditions the sediment was scaled according to the Shields method. The tests were conducted in the clear water regime to minimize ripple effects which could make it difficult to determine the equilibrium scour depth. In addition the size of the sand and structure were selected in order to comply with Equation (4-4). This also avoids having large suspended sediment quantities in the flow that could possibly damage the pumps.

4.2.2 Model effects

One of the most important model effects in flume experiments is the blockage effect. Blockage effects arise when the width of the model is large relative to the flume width, thus forcing the flow to accelerate. This is an important problem especially in scour tests because it can potentially lead to deeper scour holes than what would be expected in reality. Whitehouse (1998) suggests that blockage effects become negligible as long as the following condition is met:

$$\frac{A_{model}}{A_{flow}} < \frac{1}{6} \quad (4-5)$$

Here A_{model} and A_{flow} are the cross-sectional area of the structure and the channel projected to the flow. For the experiments conducted in this study the dimensions of the structures were all selected in order to fulfill the above criterion.

An additional modelling consideration which arises when conducting scour experiments is the time required to run an experiment in order to reach the equilibrium scour depth. Defining in a consistent way the time to equilibrium scour is important for scour

experiments as it provides a method for stopping the test in a consistent manner thus providing results that are comparable. Different approaches exist for stopping scour tests (e.g. Melville and Chiew, 1999; Link, 2006; Fael et al, 2006) most of which are formulated in a similar manner to the Melville and Chiew (1999) criterion:

$$\frac{\Delta S}{\Delta t} < \frac{0.05(D \text{ or } D_{base})}{\Delta t} \quad (4-6)$$

Here ΔS is the scour depth achieved over a time period Δt . These criteria have been derived based on experimental studies that were conducted at different scales and thus must be used with caution. In addition, they do not take into account possible effects the geometry of a structure might have. Another way of defining the equilibrium scour depth is proposed by Hoffmans and Verheij (1997) and Cardoso and Bettess (1999) which suggest that the equilibrium scour depth can be assumed to be achieved once the slope of the scour development curve has reached a value tending to zero when plotted in a logarithmic plot. This definition is independent of scale effects and structure properties. For these reasons this criterion was used to determine when to stop the scour tests conducted in this study.

4.3 Description of set-up and the models for small scale scour tests

4.3.1 Flume and test set-up

The small scale scour experiments were conducted in the tidal flume in the Pat Kemp Fluids Laboratory at University College London. The flume is 10m long, 0.3m in width and 0.35m in height (see Figure 4-1). The flume operates as follows:

- i. A pump delivers water from an underground sump to a constant head tank above the flume.
- ii. Water from the overhead tank delivers water to the flume inlet. The discharge is then controlled through a series of valves.
- iii. Water leaving the flume passes over a weir gate and then returns back to the sump.

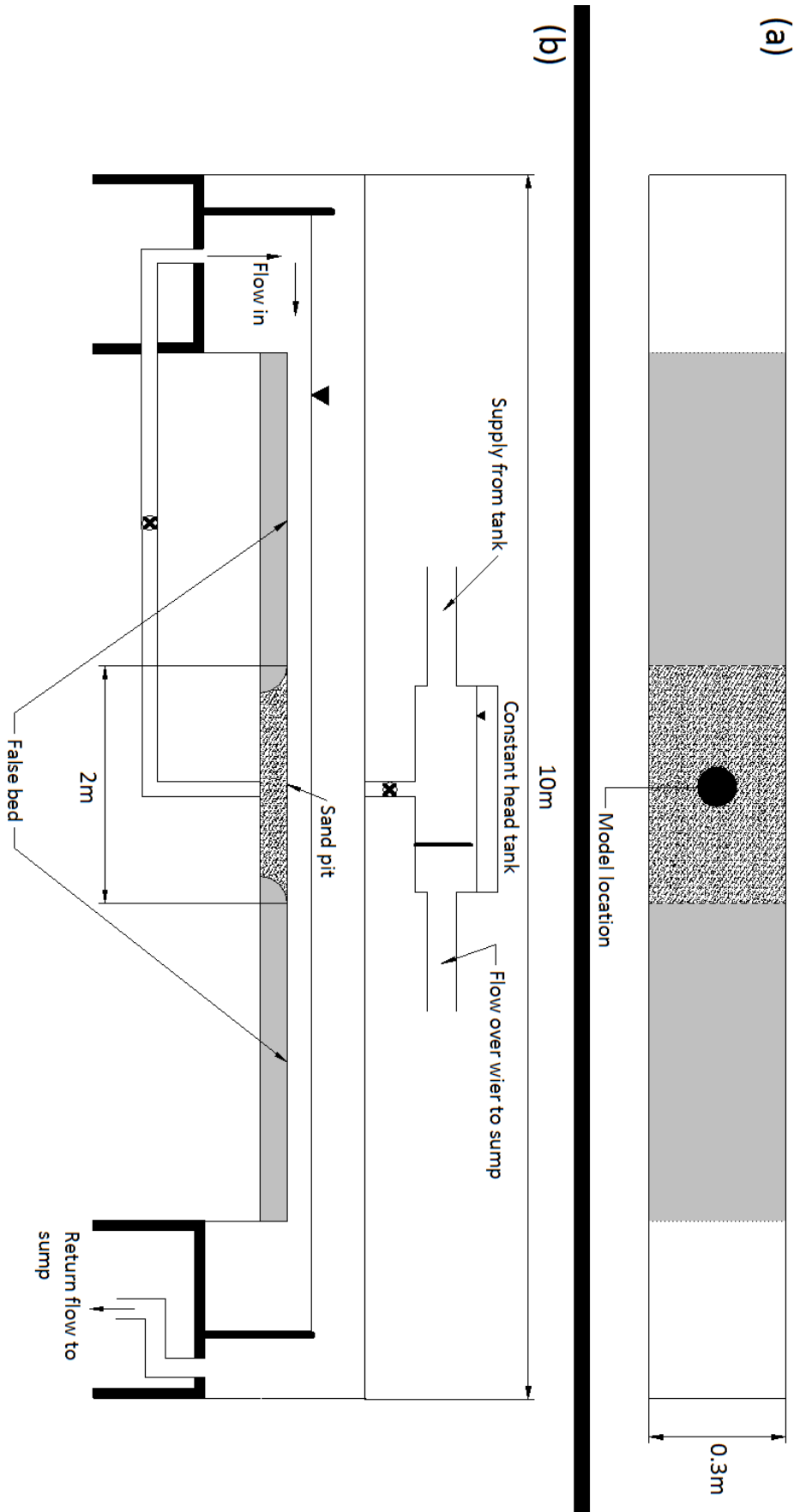


Figure 4-1: Layout of tidal flume: (a) top view; (b) side view.

The false bed was installed throughout the length of the flume in order to raise the bed and enable the installation of a sand pit in the mid-section of the flume which would allow the undertaking of scour experiments. In all tests the same type of sand used in the sand pit section was glued on the false bed in order to minimize any additional turbulence induced by the transition from one bed roughness to the other. In addition, the sand pit was smoothed flush with the top of the false bed to ensure an easy transition of the flow between the two sections. The roughened false bed also contributed to “tripping” the boundary layer and ensuring that a rough boundary layer was present at the test section.

4.3.1.1 Sand installation and smoothing

The sand used for the experiments was pre-soaked in water for at least 10 days prior to use in order to reduce the effects of air entrained within the sediment’s pores. The sand was then carefully placed in the sand pit after the lower part of the foundation was installed. Extra care was taken when the sand was placed in order to minimise air being trapped. The following steps were followed each time the sand was introduced to the sand pit:

1. The flume was filled 10-20mm above the false bed.
2. Sand was carefully placed in the sand pit with the use of a small trowel. Even though the sand used in the tests was fairly uniform it was gently mixed when it was placed in the sand pit. This allowed to have a more uniformly distributed sand particles in the test section.
3. The sand bed was then flattened and smoothed with the use of a scraper which was supported by a trolley system on levelled rails.
4. Excess sand was scraped to the false bed and then taken out of the flume.

4.3.1.2 Model Structures

The model structures were installed in the middle of the sand pit at a distance of 1m from the end of the false bed and 0.15m from the side walls. A range of different geometries were investigated in this test programme. These were; a monopile 45mm in diameter, three conical based structures with side slopes of 45°, 60° and 75°, a cylindrical base

structure and a truncated cylinder. The dimensions of the geometries are given in Figure 4-2.

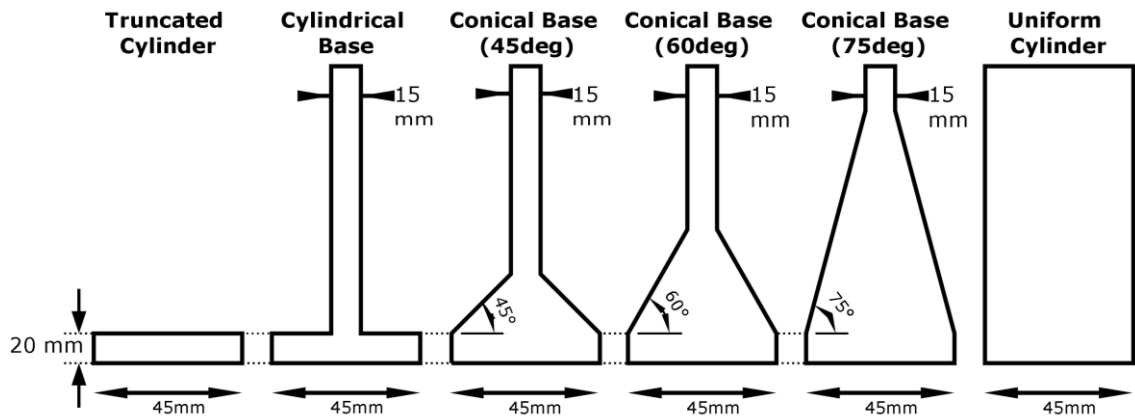


Figure 4-2: Structure geometries for scour tests.

All structures were selected to have a base diameter of 45mm which is also the diameter of the monopile to provide a basis for comparison. In addition, the stick-up height of the base for the non-uniform cylindrical structures was also selected to have the same height (i.e. 20mm) to provide a comparison of the effect this structural property has.

All models were made from black Polyvinyl Chloride (PVC) Rods which were trimmed and then polished in order to obtain the required shape and to minimise possible roughness effects. The models consisted of two parts:

- A cylindrical foundation which had a diameter of 45mm (same diameter as the base of the models) the top side of which was flush with the false bed. This component was screwed to the base board of the flume and positioned in the middle of the test section (see Figure 4-3 (a)). Then the sand was placed in the sand pit and smoothed flush with the top of the cylindrical foundation.
- The main part of the structure which was screwed to the foundation mentioned above (see Figure 4-3 (b)). This enabled the initiation of the experiments after the desired flow conditions were achieved.

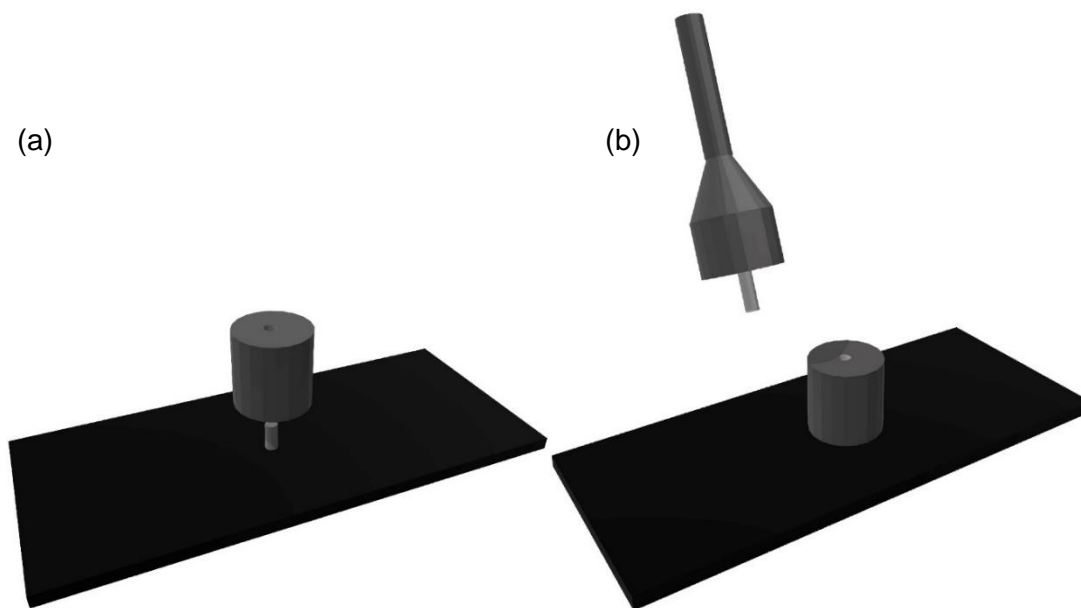


Figure 4-3: Set-up of the structures for scour tests: (a) Lower part of model (buried under the sand); (b) installation of model foundation on base.

4.3.2 Flow parameters

The purpose of the small scale experiments was to investigate the influence of different hydraulic parameters on the scour around the structures presented in Figure 4-2. More specifically the flow parameters tested in these experiments include the water depth, the flow velocity, the sediment size and the structure geometry. This section provides the rationale behind selecting the hydrodynamic forcing conditions for this test series.

4.3.2.1 Flow velocity

For this test series all velocities were designed to be in the clear water scour regime. Experiments were conducted for different sediment mobility ratios (U_c/U_{cr}) to investigate the influence this parameter has on scour around complex structures in the clear water regime. The critical flow velocity for the sediments used in the tests was determined in accordance with both the Soulsby (1997) and Van Rijn (1984) methods, both of which gave the same answer within two decimal points. Furthermore, prior to the scour tests the critical velocity for the incipient motion of the sand was also determined experimentally and found to be within 10% of the result given by the empirical equations. The majority of the tests were conducted at a sediment mobility in the range of 0.73-1.

This is because for these conditions scour depths tend to be the deepest for both live and clear water scour regimes.

4.3.2.2 Flow depth

Two flow depths were examined in this test series. The first flow depth was selected as 165mm in order to yield a non-dimensional flow depth (h/D) of 3.7 which is above the critical value of 3 after which the effects of the water depth become negligible according Melville (2008). The second water depth was taken as 100mm in order to examine the effect shallower flow depths have on the scour potential around complex structures. The corresponding non-dimensional flow depth for these tests was 2.2 which is closer to the corresponding value a GBF for a wind turbine would have in the North Sea which corresponds to a flow depth of 35-40m approximately.

4.3.2.3 Sediment characteristics

Two types of sediments were used in the experiments. Given that the purpose of the tests was to investigate the effect of the pressure gradient on scour the coarser sand tests were conducted to investigate if the sand coarseness has an effect on the local pressure field and thus on scour around complex structures. All existing knowledge regarding the effect of d_{50}/D has been conducted for scour around uniform cylinders, which is not necessarily applicable for more complex structures. These were selected in order to avoid cohesion effects (i.e. $d_{50} > 100\mu\text{m}$). The two sands had a median size of 0.2mm (hereafter fine sand) and 0.6mm (hereafter coarse sand). The size of the sediment was determined from sieving tests that were conducted on samples of the two sediments in UCL's Geotechnical laboratory (see Figure 4-4). Both sediments were fairly uniformly graded with a geometrical standard deviation of 1.5 for the fine sand and 1.3 for the coarse sand.

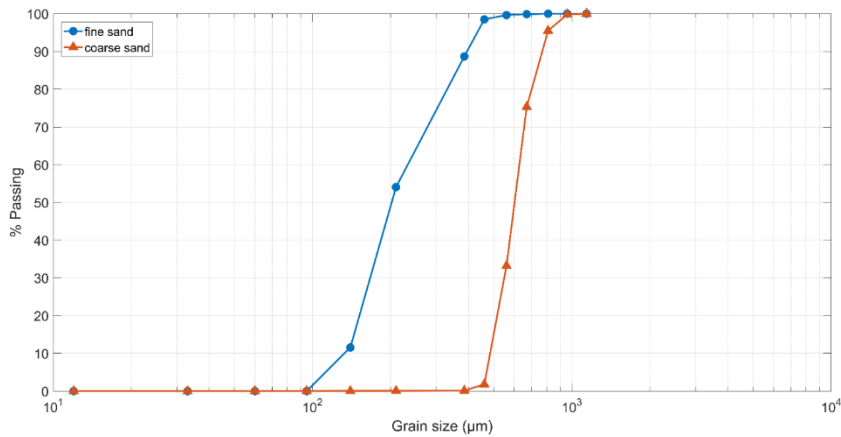


Figure 4-4: Grain size distribution for the two sediment types used in the experiments.

The density of the sediment under wet and dry conditions was also determined for two samples of the sand and are presented in the following table.

Table 4-1: Wet and dry density for both sediment types.

Sand type	d_{50} (mm)	Wet density (Kg/m^3)	Dry density (Kg/m^3)
Fine sand	0.2	1601	1585
Coarse sand	0.6	1468	1490

As can be seen from Table 4-1 there is a small difference between the dry and wet densities for each sand type which suggests that the sediments do not absorb significant amount of water. The data also shows that the densities of the two sands differ by approximately 5%.

4.3.3 Measurement techniques

This section provides a description of the measurement techniques used in the small scale scour experiments. These include the measurement of the undisturbed flow velocity and scour depth measurements.

4.3.3.1 Flow velocity measurements

As discussed in sections 1.3, 1.4 and 1.5 the undisturbed flow velocity is an important influencing parameter for the scour potential around any structure. For this reason, the

velocity profile was measured at the location of the pile before it was screwed into place prior to each set of experiments. The flow velocities for the scour experiments were measured using Laser Doppler Velocimetry (LDV). The basic principle of operation of an LDV uses two light beams to measure the flow velocity within a given control volume. The two beams are obtained by splitting one beam in order to ensure coherence between the two light sources. A transmitting optics lens focuses the beams at a specific location at which they superpose (i.e. form a pattern of fringes). As particles in the water pass through the fringes light is scattered. This scattered light is then collected by a photodetector. The light received (which has a different frequency compared to the original beam) is then analysed to determine the Doppler shift which is directly related to the flow velocity of the passing particle (see Figure 4-5). The present LDV device was capable of measuring the two orthogonal components of the flow velocity (u and w), i.e. horizontal and vertical components respectively.

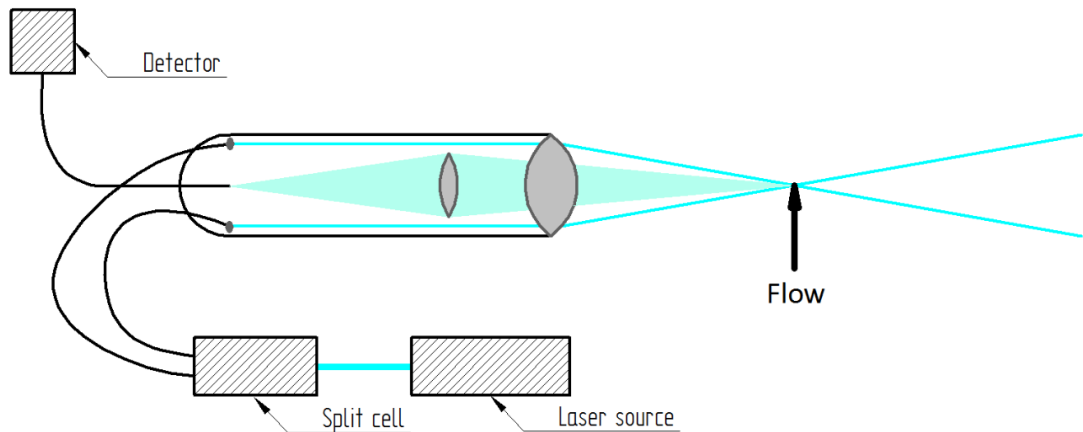


Figure 4-5: Schematic of LDV working principle

In order to measure the flow profile, the LDV was mounted on a traverse system capable of moving in three dimensions outside the flume (see Figure 4-6). This allowed to make precise point measurements of the flow without intruding the flow. The mean flow velocity was then determined in accordance with the Soulsby (1997) method.



Figure 4-6: Traverse set-up with LDV

Further to the flow velocity for the scour experiments a set of flow measurements was made in order to investigate the influence of the side walls on the flow across the channel width. The test conditions for this preliminary experiment were:

- Mean flow velocity (U_c): 0.25m/s;
- Flow depth (h): 165mm; and,
- Nominal diameter of the sand comprising the bed: 0.6mm.

The mean velocity was selected to have relatively high magnitude in order to accentuate any flow asymmetry across the channel width. The symmetry of the flow was then checked by making detailed streamwise velocity measurements through the depth and at positions across the channel. Flow measurements near the wall were not possible due to the low concentration of seeding particles near the walls. Figure 4-7 shows the results of these measurements.

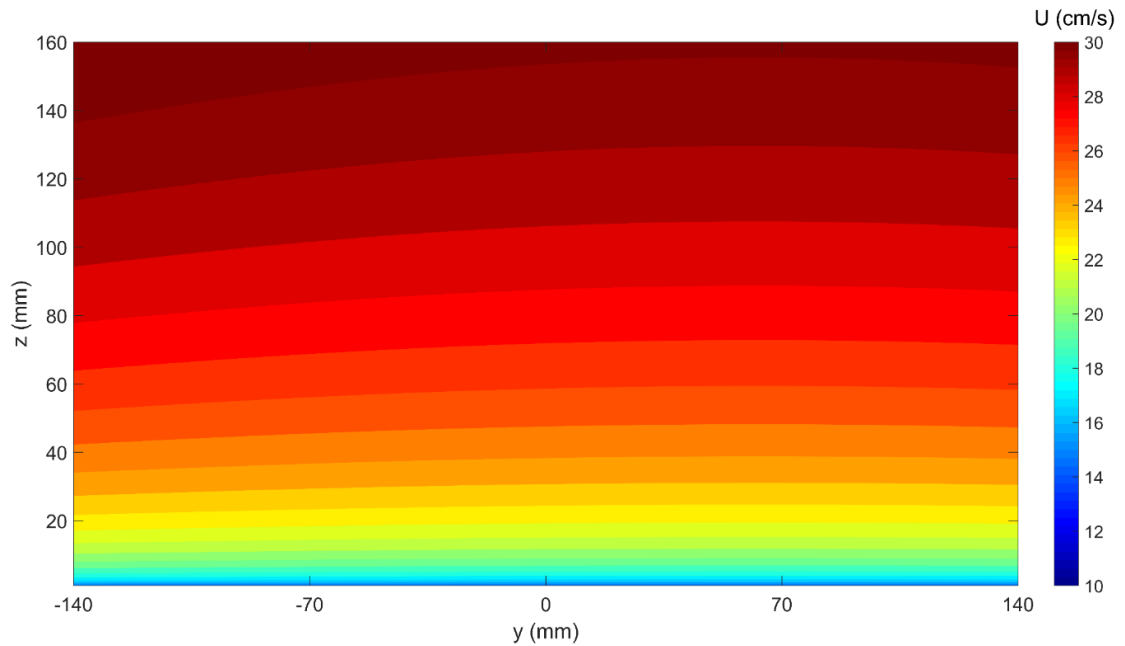


Figure 4-7: Flow velocity in the cross-flow direction.

In this figure the vertical axis shows vertical distance from the bed, the horizontal axis the distance across the flume (with negative values being closest to the far side of the flume) and the colour map the flow velocity (u). It can be seen that the streamwise velocity across the width of the test section is fairly uniform with a tendency to accelerate along the far-side of the flume. The maximum variation near the water surface at the far-side of the flume is 5% of the streamwise velocity at the centre. From the results of this preliminary test it can be concluded that the flow is fairly homogeneous along the cross-flow direction. Thus the mean flow along the centreline of the flume can be used to characterise the flow in the channel.

4.3.3.2 Flow and scour depth measurements

The water depth for the experiments was determined using rulers which were attached to the glass side-wall of the flume at different locations. The lower part of the rulers was carefully positioned at the top of the sand bed and an average from all the rulers was taken to determine the flow depth. This was done to account for the small flow changes in the water depth due to the hydraulic gradient.

Several methods for the measurement of scour depth around structures are recorded in the literature; Porter et al. (2014) provides a comprehensive review of the advantages and disadvantages of each method. Because the main goal of these tests was to obtain preliminary insights into the scour process for complex structures only the time series of scour and the equilibrium scour depth were recorded.

For these tests the foundation (under the initial bed level) of the structure was marked at 5mm intervals. The scour depth readings were determined by visual observations and through the use of time-lapse photography. At the initial stages of the scouring process the scour depth was recorded every 10s. The frequency of measurements then reduced as the scour hole developed and the scour rate reduced. The initial readings were verified later through the time-lapse photographs which were acquired at intervals of 10s. For these tests only the deepest scour point was recorded. This was located at an angle ranging between 0° and 90° relative to flow direction.

4.3.4 Experimental programme

The purpose of the small scale experiments was to investigate the influence of the structural geometry on the scour process around complex structural geometries (listed in Figure 4-2). These structures were subjected to a series of different flow conditions to investigate the influence they have on the scour potential.

All tests in this series were subject to a unidirectional current and were conducted in the clear water scour regime. The influence of the bed material was investigated by conducting tests with two types of sediment while keeping constant the sediment mobility ratio (U_c/U_{cr}). The effect of the flow depth on scour around such structures was also investigated by conducting tests at two water depths which correspond to deep and medium water depths.

All of the structures were subject to the same flow conditions in order to determine the differences in the scour potential induced by each type. Given that the purpose of the tests was to determine the maximum scour potential of the structures, the foundation

extended to the bottom of the sand pit. **Error! Reference source not found.** presents the summary of the small scale scour experimental test programme.

Table 4-2: Small scale scour experiments programme.

No.	Structure Type	U_c	Flow Profile	h	D or D_{base}	d_{50}	U_{cr}	h/D_{base}^*	U_c/U_{cr}
(-)	(-)	(m/s)	(-)	(m)	(mm)	(mm)	(m/s)	(-)	(-)
1.0	Truncated	0.195	Logarithmic	0.165	45	0.6	0.267	3.67	0.73
1.1	Cylindrical base	0.195	Logarithmic	0.165	45	0.6	0.267	3.67	0.73
1.2	45° conical base	0.195	Logarithmic	0.165	45	0.6	0.267	3.67	0.73
1.3	60° conical base	0.195	Logarithmic	0.165	45	0.6	0.267	3.67	0.73
1.4	75° conical base	0.195	Logarithmic	0.165	45	0.6	0.267	3.67	0.73
1.5	Uniform cylinder	0.195	Logarithmic	0.165	45	0.6	0.267	3.67	0.73
1.6	Truncated	0.2	Logarithmic	0.165	45	0.2	0.227	3.67	0.88
1.7	Cylindrical base	0.2	Logarithmic	0.165	45	0.2	0.227	3.67	0.88
1.8	45° conical base	0.2	Logarithmic	0.165	45	0.2	0.227	3.67	0.88
1.9	60° conical base	0.2	Logarithmic	0.165	45	0.2	0.227	3.67	0.88
1.10	75° conical base	0.2	Logarithmic	0.165	45	0.2	0.227	3.67	0.88
1.11	Uniform cylinder	0.2	Logarithmic	0.165	45	0.2	0.227	3.67	0.88
1.12	Truncated	0.237	Logarithmic	0.165	45	0.2	0.237	3.67	0.98
1.13	Cylindrical base	0.237	Logarithmic	0.165	45	0.2	0.237	3.67	0.98
1.14	45° conical base	0.237	Logarithmic	0.165	45	0.2	0.237	3.67	0.98
1.15	60° conical base	0.237	Logarithmic	0.165	45	0.2	0.237	3.67	0.98
1.16	75° conical base	0.237	Logarithmic	0.165	45	0.2	0.237	3.67	0.98
1.17	Uniform cylinder	0.237	Logarithmic	0.165	45	0.2	0.237	3.67	0.98
1.18	Truncated	0.235	Logarithmic	0.165	45	0.6	0.267	3.67	0.88
1.19	Cylindrical base	0.235	Logarithmic	0.165	45	0.6	0.267	3.67	0.88
1.20	45° conical base	0.235	Logarithmic	0.165	45	0.6	0.267	3.67	0.88
1.21	60° conical base	0.235	Logarithmic	0.165	45	0.6	0.267	3.67	0.88
1.22	75° conical base	0.235	Logarithmic	0.165	45	0.6	0.267	3.67	0.88
1.23	Uniform cylinder	0.235	Logarithmic	0.165	45	0.6	0.267	3.67	0.88
1.24	Truncated	0.264	Logarithmic	0.165	45	0.6	0.267	3.67	0.99
1.25	Cylindrical base	0.264	Logarithmic	0.165	45	0.6	0.267	3.67	0.99
1.26	45° conical base	0.264	Logarithmic	0.165	45	0.6	0.267	3.67	0.99
1.27	60° conical base	0.264	Logarithmic	0.165	45	0.6	0.267	3.67	0.99
1.28	75° conical base	0.264	Logarithmic	0.165	45	0.6	0.267	3.67	0.99
1.29	Uniform cylinder	0.264	Logarithmic	0.165	45	0.6	0.267	3.67	0.99
2.1	Truncated	0.196	Logarithmic	0.100	45	0.2	0.211	2.22	0.93
2.2	Cylindrical base	0.196	Logarithmic	0.100	45	0.2	0.211	2.22	0.93
2.3	45° conical base	0.196	Logarithmic	0.100	45	0.2	0.211	2.22	0.93
2.4	60° conical base	0.196	Logarithmic	0.100	45	0.2	0.211	2.22	0.93
2.5	75° conical base	0.196	Logarithmic	0.100	45	0.2	0.211	2.22	0.93
2.6	Uniform cylinder	0.196	Logarithmic	0.100	45	0.2	0.211	2.22	0.93
2.7	Truncated	0.193	Logarithmic	0.100	45	0.6	0.248	2.22	0.78
2.8	Cylindrical base	0.193	Logarithmic	0.100	45	0.6	0.248	2.22	0.78
2.9	45° conical base	0.193	Logarithmic	0.100	45	0.6	0.248	2.22	0.78
2.10	60° conical base	0.193	Logarithmic	0.100	45	0.6	0.248	2.22	0.78
2.11	75° conical base	0.193	Logarithmic	0.100	45	0.6	0.248	2.22	0.78
2.12	Uniform cylinder	0.193	Logarithmic	0.100	45	0.6	0.248	2.22	0.78

*For tests with uniform cylinders $D_{base} = D$.

4.4 Description of set-up and the models for large scale scour experiments

Scour experiments were conducted in a larger facility in order to:

- Investigate scale effects on the scour process.
- Examine the effect different flow profiles have on the scour process around complex foundation geometries.
- To collect data that can be used to develop a scour predictor.

This section will provide an overview of the set-up of the flume, the procedures followed during the experiments, the measurement techniques and the list of experiments conducted.

4.4.1 Flume and test set-up

The large scale scour tests were conducted in the coastal flume which is located in the Department of Mechanical Engineering at University College London. The flume has dimensions of 20m × 1.2m × 1m (length × width × depth). The side walls and the base of the flume were made of glass to allow visual observation and to facilitate non-intrusive measurement equipment (e.g. Particle Image Velocimetry (PIV) and Laser Doppler Velocimetry (LDV)). The flume is equipped with a set of active absorption piston wave makers both ends, which allows the generation of waves from one end while the other actively absorbs wave energy thus reducing wave reflections. Currents are generated via recirculating pumps which are situated under the flume. The pumps are capable of generating currents in two directions (forward and backward). The inlets and outlets of the flow are located in front of each wave maker. Figure 4-8 provides a schematic of the flume used in these experiments.

The large scale scour tests were conducted in the clear water scour regime under the forcing of a unidirectional current. Due to the configuration of the flume it was not possible to construct a false bed throughout the length of the flume. For this reason, the bed was raised by means of a marine plywood ramp which hosted a sand pit in the centre of it. The ramp consisted of the following components:

- Sand pit in the centre of the flume. The sand pit had a depth of 25cm and was filled with sand flush to the top of the apparatus.
- False bed extending 2.2m on either side of the sand pit. The false bed was roughened by gluing fine sand (same type of sand as used in the sand pit) on the surface of the wooden surface. This was done to assist the development of the turbulent boundary layer and to reduce the amount of turbulence induced by the transition between the false bed and the sand pit surface.
- Sand traps, to protect the pumps from the sediment. The sand traps were 30cm gaps at the end of the false bed which were covered by perforated plates. This allowed the majority of the sediment to settle into the trap and avoid getting sucked into the pumps.
- Ramps on either side of the false bed with a side slope of 1:6 (H : L). The slope of the ramp was limited by the size of the flume and the location of flow inlet/outlet.

The entire apparatus described above was held in place by gluing the bottom parts to the glass bed of the flume using silicone.

Flow straighteners (conditioners) were installed in front of the flow inlet. The purpose of the conditioners was twofold:

- To minimise the lateral and transverse turbulent velocity components induced by the pump and inlet geometry.
- To modify the flow velocity profile by changing the friction at different levels of the flow.

The flow conditioner consisted of a number of rolled wire meshes which were installed parallel to each other immediately after the flow inlet (see Figure 4-9). The configuration of the meshes was then adjusted to achieve the desired flow profile.

The sand used in the experiments was placed in the sand pit and flattened following the same procedure described in the section 4.3.1.1. Due to the size of the flume it was not

possible to have a trolley system to support the sand scraper. For this reason, the sand bed surface was smoothed by the author who needed to be located in the flume.

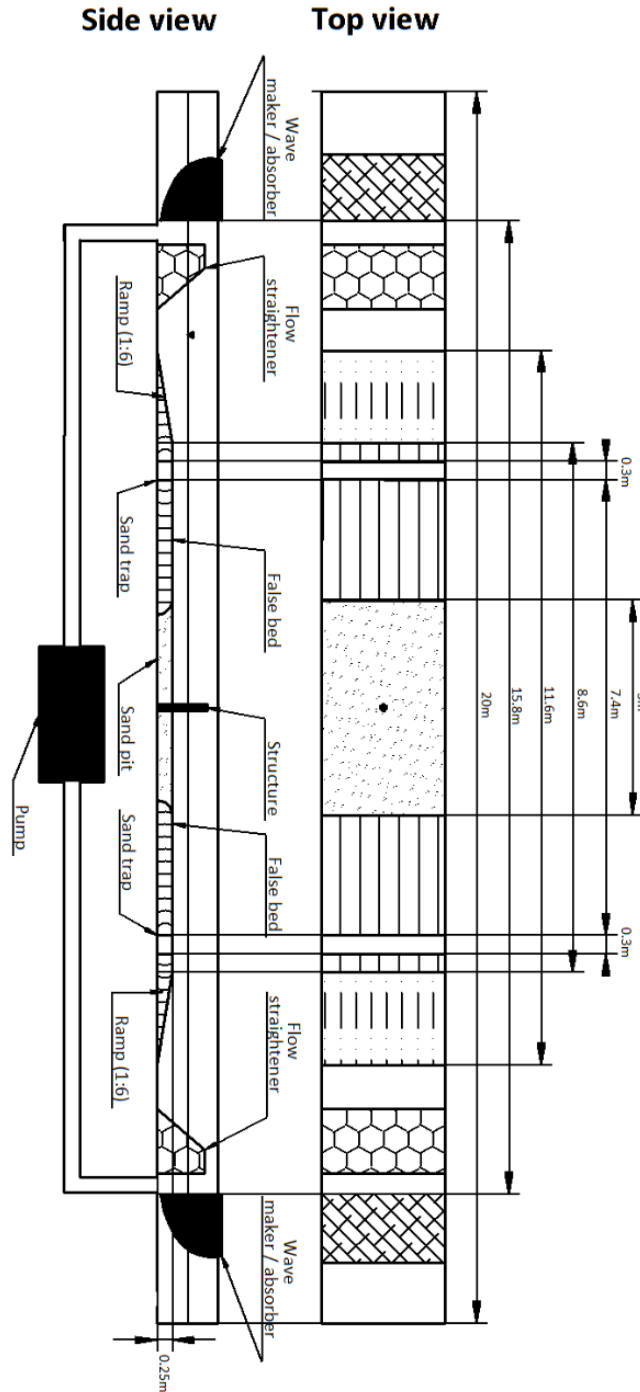


Figure 4-8: Layout of costal flume in Mechanical Engineering Department



Figure 4-9: Image of the flow conditioner.

The foundation geometries tested in this flume were scaled-up models of the structures used in the small scale tests. Given that scour tests at this scale had an expected duration which was much larger than at the smaller scale, it was decided not to include the 60° conical base structure and the truncated cylinder in these tests. Figure 4-10 shows the dimensions of the structures used in these tests.

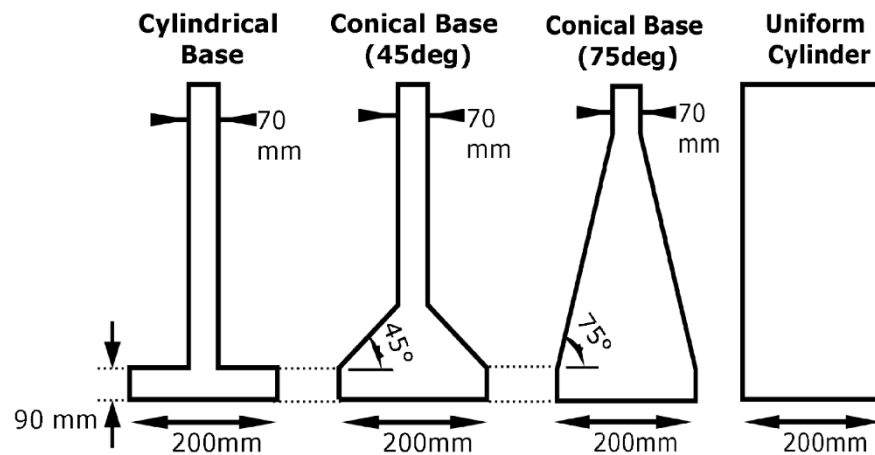


Figure 4-10: Large scale foundation geometries

The structures referred to in Figure 4-10 were then screwed onto the base component which was already installed in the sand pit in a similar way to that shown in Figure 4-3 and described in section 4.3.1.2.

4.4.2 Flow parameters

All tests were conducted in the clear water scour regime with a sediment mobility ratio (U_c/U_{cr}) between 0.90 and 1. This flow condition (i.e. near critical flow velocity) was selected because it was expected to induce the most severe scour depth. In addition, two different flow profiles were tested:

- a logarithmic flow profile, in order to examine possible scale effects compared to the smaller scale experiments (Figure 4-11 a); and,
- a non-logarithmic flow profile with the same flow flux as in the first set, for the purpose of examining the possible effects of non-logarithmic flow profiles on the scour process. The flow profile was altered through changes in the flow straightener configuration in order to achieve a flow profile resembling one subject to a wind stress at the surface (Figure 4-11 b).

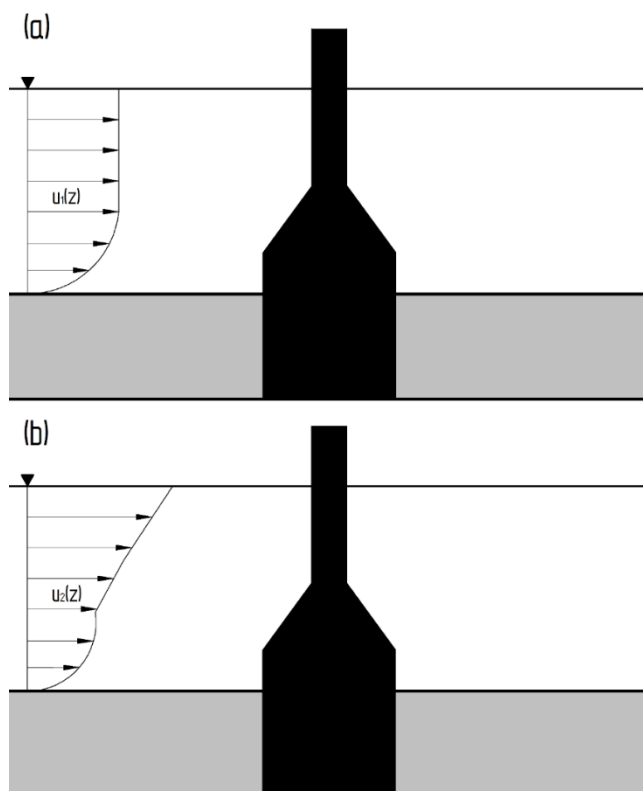


Figure 4-11: Schematic of the flow profiles tested in these tests.

Three flow depths were tested in this set of experiments. The four geometries were subjected to both logarithmic and non-logarithmic flow profiles with a depth of 350mm. The purpose of these tests was to investigate the influence different profiles have on the structures for a constant flow flux. To investigate the effect water depth has on complex geometries in non-logarithmic flow profiles the 75° conical base structure was further tested at water depths of 350, 450 and 550mm. Finally, four structures were subjected to a non-logarithmic flow profile at a depth of 550mm to further investigate the effect of varying depth on the structures in such flow profiles.

The fine sediment used in these experiments was the same as the one used in the small scale flume. The reader is referred to section 4.3.2.3 for further details regarding the sediment distribution and density.

4.4.3 Measuring techniques

This section provides a description of the measurement techniques used in the large scale experiments. The quantities measured during these tests include the flow velocity and the scour depth around the structures.

4.4.3.1 Flow velocity measurement

For the large scale experiments the flow velocity was measured at the location of the pile after the sand bed was smoothed and before the upper part of the pile was screwed into place. Due to the width of the flume it was not possible to use the LDV to measure the velocity at the centre of the flume due to the limited focal length of the LDV. For this reason, the flow profile in the larger flume was measured using Acoustic Doppler Velocimetry (ADV). For this test series a Vetrino+ ADV was used. As for the LDV the ADV operates by the principle of the Doppler shift. The device sends out acoustic waves with a specific frequency from the transmitter. These waves then reflect from the seeding particles which are distributed in the flow and the acoustic receivers detect the change in the frequency of the echoes. The Doppler shift detected by each sensor is proportional to one of the three flow velocity components. Figure 4-12 provides a schematic of the

working principle of the ADV. Given that the ADV is an intrusive measuring instruments the flow velocity was only measured prior to the initiation of the experiments to avoid it interfering with flow.

The ADV was mounted on a vertical bar at the centre of the flume. The bar had holes at 1cm intervals which allowed precise vertical positioning within the water column. The point measurements of the velocity were conducted for 3min in order to average out effects of turbulence. The average flow velocity was then computed using the trapezoidal rule described in Soulsby (1997).

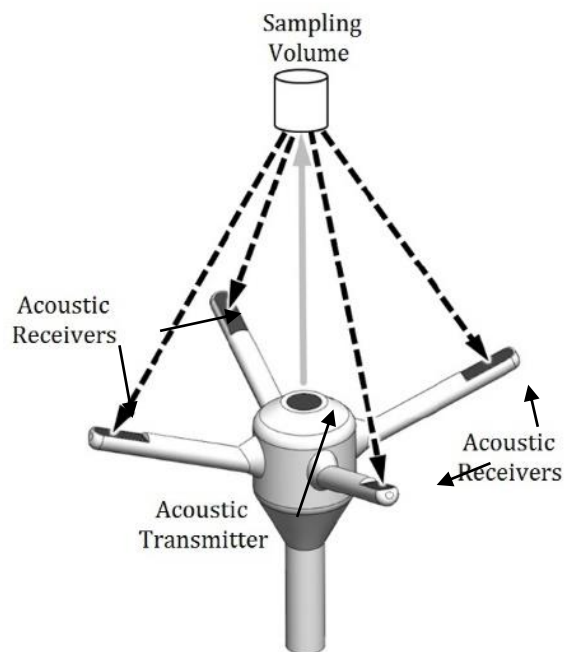


Figure 4-12: Acoustic Doppler Velocimetry working principle (source: Sellar et al., 2015).

4.4.3.2 Flow and water depth measurement

In addition to measuring the time development and the equilibrium scour depth the large scale experiments were intended to investigate the three dimensional characteristics of the scour hole developed by the complex geometries. In these test the flow depth and the time development of the scour was measured using time lapse photography in the same manner outlined in section 4.3.3.2. The 3D shape of the equilibrium scour hole was then measured using an echosounder device. The following paragraphs will

describe the principles of operation of the echosounder along with the general set-up of the device used in the experiments.

The echosounder used in this study was a General Acoustics Ultralab UWS echosounder which is capable of making point measurements. The device consisted of a sensor 30mm in diameter and 50mm in height which needed to be in contact with the water surface in order to make the measurements. The measuring frequency of the echosounder was 1MHz capable of measuring the water depth with a 1% accuracy with a maximum error of 1mm. The operational range of the sensor is 1mm to 10m and the echo beam angle was less than 3°.

To measure the morphology of the equilibrium scour hole, the echosounder was mounted on a traverse system which was installed above the flume. This allowed the sensor to move in the x (streamwise direction) and y (cross-flow direction) direction. For the present tests the profiler was set-up to measure an area 700mm (x-direction) × 690mm (y-direction) around the pile. The scour depth was then measured by taking point measurements at 5mm intervals in the x and y direction. In order to reduce noise in the depth measurements due to reflections of the echo beam off the structure the equilibrium scour profile was taken after the structure was unscrewed from the base. For these measurements the datum was taken as the bed elevation in front of the structure before the initiation of the experiment. The scour depth was then determined by subtracting the depth measurement of the echosounder from the datum level.

4.4.4 Experiment programme

The purpose of the large scale experiments was to gain insight to the effect the structural scale and different flow profiles have on the scour development around complex geometries. They were also designed to further investigate the effect of the water depth has on the scour depth.

All tests were conducted under the forcing of a unidirectional current and were all in the clear water flow regime. The sediment mobility number was selected to be between 0.9

and 1 as for these flow conditions the most severe scour depth is expected. Tests 3.1 to 3.4 were conducted under the forcing of a logarithmic flow profile and their main purpose was to provide a dataset that would be compared to the small scale results from tests 2.2 to 2.6 which have similar non-dimensional values. Tests 3.5 to 3.8 were conducted under the forcing of a non-logarithmic flow profile with the same flow flux and flow depth as in tests 3.1 to 3.4. The purpose of these tests was to investigate the effect a different flow profile has on the scour process. Tests 3.9 to 3.12 were conducted with a non-logarithmic profile and a similar flow speed as in tests 3.5-3.8 but at a different flow depth. This subset was designed to investigate the effect a change in flow depth has on the scour process in non-logarithmic flow profiles. Finally, tests 3.12 to 3.14 were conducted to investigate further the effect of the depth in such conditions. It should be noted that test 3.14 was also conducted to investigate the repeatability of test 3.8. Table 4-3 presents a summary of the key flow parameters adopted in these tests.

Table 4-3: Large scale scour experiments programme.

No.	Structure Type	U_c	Flow Profile	h	D or D_{base}	d_{50}	U_{cr}	h/D_{base}^*	U_c/U_{cr}
(-)	(-)	(m/s)	(-)	(m)	(mm)	(mm)	(m/s)	(-)	(-)
3.1	Monopile	0.245	logarithmic	0.35	200	0.2	0.253	1.75	0.97
3.2	Cylindrical base	0.245	logarithmic	0.35	200	0.2	0.253	1.75	0.97
3.3	45° conical base	0.245	Logarithmic	0.35	200	0.2	0.253	1.75	0.97
3.4	75° conical base	0.245	Logarithmic	0.35	200	0.2	0.253	1.75	0.97
3.5	Monopile	0.245	non-logarithmic	0.35	200	0.2	0.253	1.75	0.97
3.6	Cylindrical base	0.245	non-logarithmic	0.35	200	0.2	0.253	1.75	0.97
3.7	45° conical base	0.245	non-logarithmic	0.35	200	0.2	0.253	1.75	0.97
3.8	75° conical base	0.245	non-logarithmic	0.35	200	0.2	0.253	1.75	0.97
3.9	Monopile	0.254	non-logarithmic	0.55	200	0.2	0.270	2.75	0.94
3.10	Cylindrical base	0.254	non-logarithmic	0.55	200	0.2	0.270	2.75	0.94
3.11	45° conical base	0.254	non-logarithmic	0.55	200	0.2	0.270	2.75	0.94
3.12	75° conical base	0.254	non-logarithmic	0.55	200	0.2	0.270	2.75	0.94
3.13	75° conical base	0.246	non-logarithmic	0.45	200	0.2	0.262	2.25	0.95
3.14	75° conical base	0.246	non-logarithmic	0.35	200	0.2	0.253	1.75	0.97

*For tests with Monopiles i.e. uniform cylinders, $D_{base} = D$.

4.5 Description of set-up and the models for the pressure and flow measurements near the structure

4.5.1 Flume and test set-up

A number of small scale experiments were conducted in the flume described in section 4.3.1. In these tests the pressure distribution around a number of structures with both uniform and non-uniform cylindrical geometries was measured using pressure transducers. In addition, the flow field around each structure was measured for the same conditions for which the pressure measurements were conducted. The setup of the flume was similar to that of Figure 4-1 with the difference that the sand pit was removed and replaced by a false bed. Figure 4-13 (a) shows the setup of the flume. For these experiments, models of the structures shown in Figure 4-2 were generated using 3D printing. In order to reduce costs, it was decided not to print the truncated cylinder. The printed models of the structures were designed with tapping holes at different heights along their face (see Figure 4-14), each of which led through internal tubes to the base of the structure (Figure 4-13 and Figure 4-15). This allowed water through the structure to the tubes connected to the pressure transducer at the bottom of the structure. The internal tubes in the structures extended 10mm from the bottom of the model foundation in order to allow enough space to connect them to acrylic tubes. The acrylic tubes were then passed out of the flume via specially designed exit glands (Figure 4-13 (a) and Figure 4-15) which finally connected to the transducer system.

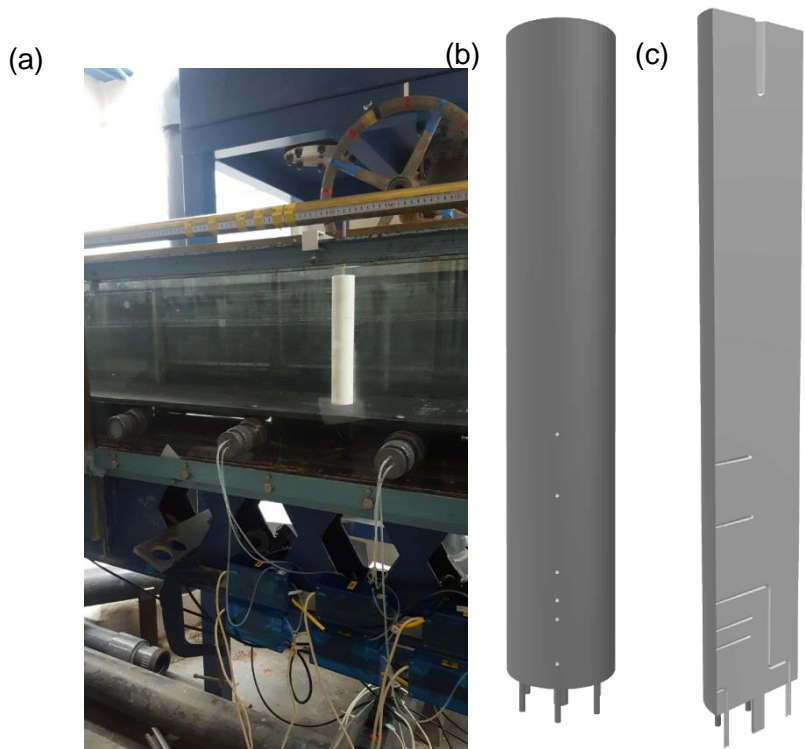


Figure 4-13: (a) Set up of the pressure measurement tests showing the acrylic tubes connecting to the pressure transducer units beneath the flume; (b) Image of 3D model; (c) cut through (from centreline) of model with tubes.

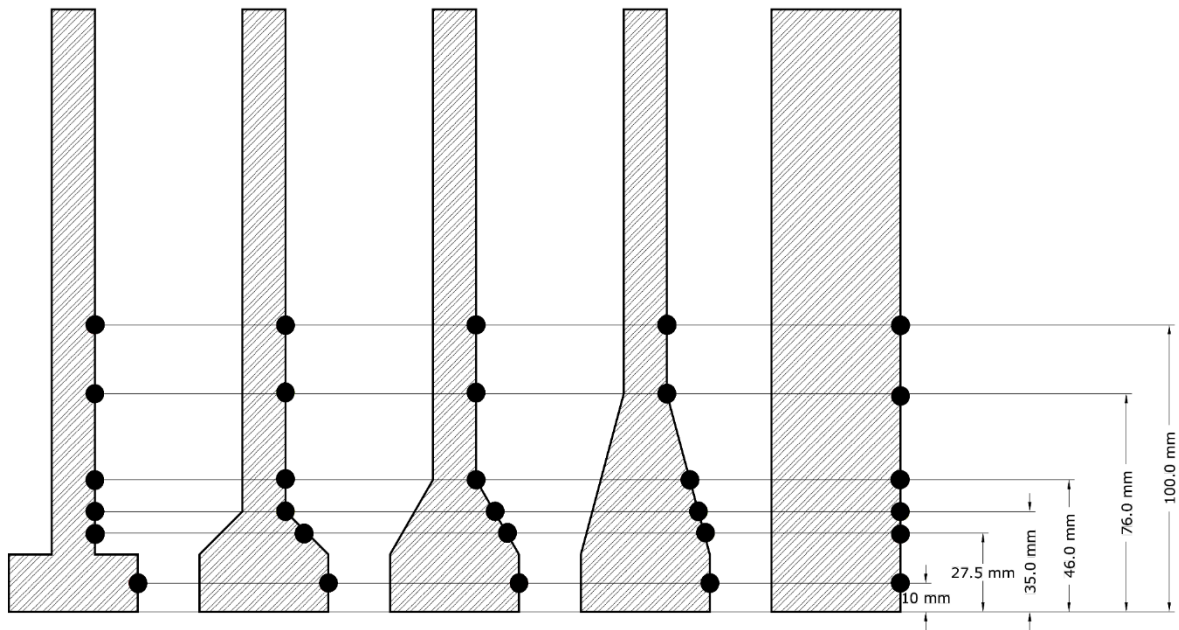


Figure 4-14: Location of pressure taps.

In order to allow the rotation of the structure which would enable the measurement of the pressure field around it, a 45mm hole was opened through the false bed of the flume at the mid-point of the test area. This allowed the structures to slip into the gap (all

structures have a base diameter of 45mm) and provided stability with respect to the overturning moments created by the flow and structure interaction. In addition, a watertight seal was installed around the periphery of the hole in order to avoid flow seeping through potential gaps which may be created between the structure and the edge of the hole. The structures were then supported from the top via a support pin which was held by an anchor clamp. The support system allowed the rotation of the entire structure without the need to stop the flow.

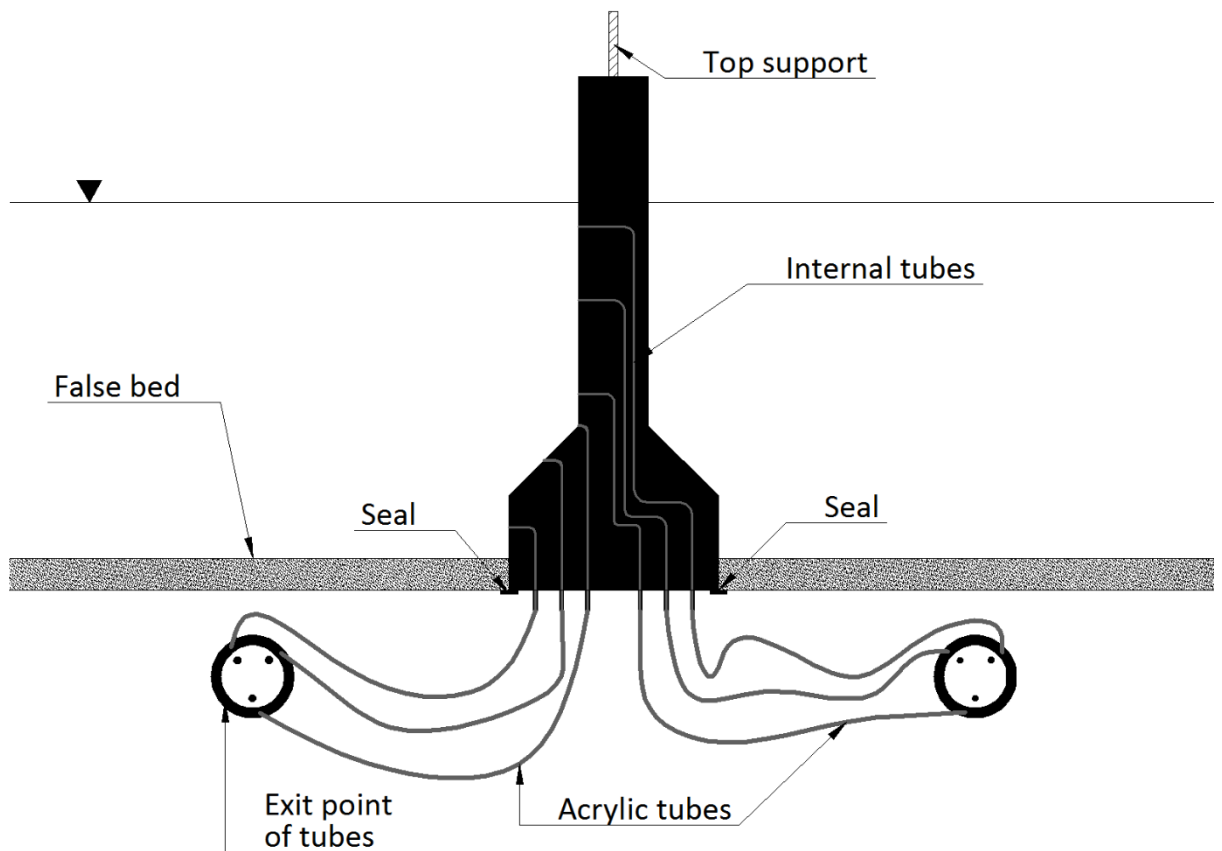


Figure 4-15: Side view sketch of the lower part of the pressure measurement apparatus.

The present tests were designed to measure the pressure field around the GBF foundation geometries tested in the scour experiments. The main objective of the tests was to establish the range of validity of potential flow theory around these structures. For this reason, only one flow condition was tested. For the present tests the false bed was roughened by gluing 0.2mm sand across the surface of the flume's bed. The undisturbed flow velocity was measured at the location of the structure using an LDV.

Two types of flow measurements were conducted using the LDV for the same flow conditions as for the pressure measurements:

- Measurement of the two components of the flow velocity (u and w) along the plane of symmetry of the structure.
- Measurement of the two components of the flow velocity (u and w) in the volume surrounding half of the structure (hereafter volumetric flow measurements). Figures 2-10 and 2-11 show the points where the measurements were made in the X-Y and X-Z planes respectively.

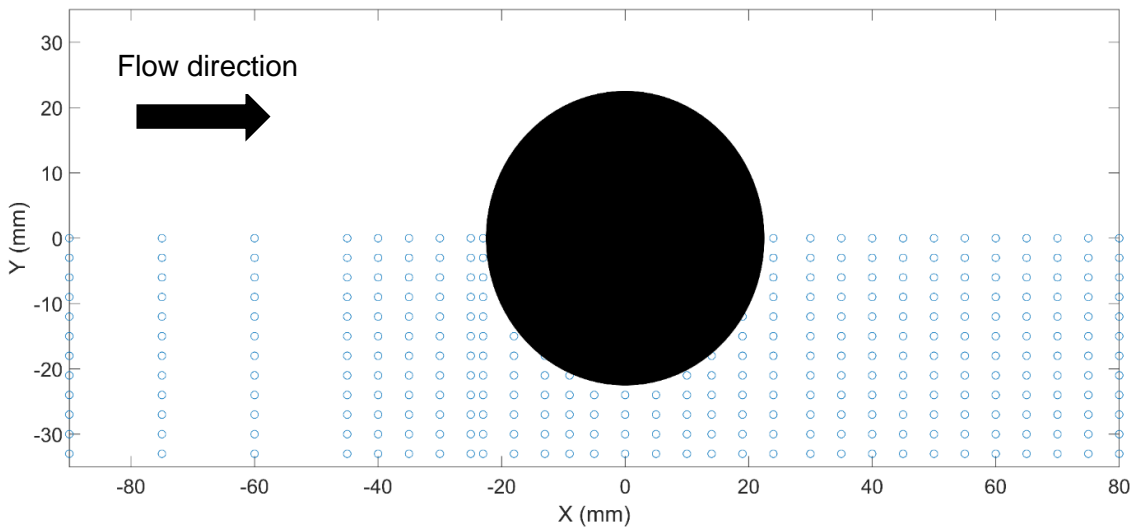


Figure 4-16: Flow field measurement points in the X-Y plane.

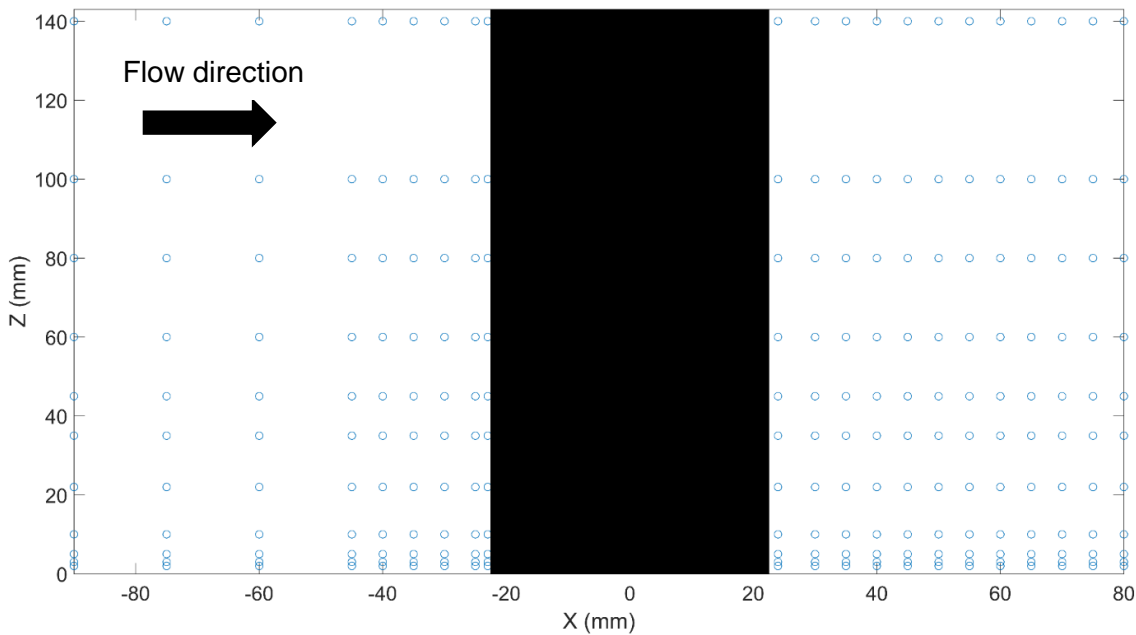


Figure 4-17: Flow field measurement points in the X-Z plane.

4.5.2 Measurement techniques

This section provides a description of the measuring equipment used for the current tests. Given that all depth and velocity measurements were conducted using the same equipment as for the small scale scour experiments the reader is redirected to section 4.3.3 for details about the set-up and working principles of the equipment. The present section will therefore focus on the description of the pressure measurements.

4.5.2.1 Pressure measurement

The pressure transducer used for measuring the pressure around the structure was a Honeywell 40PC001B2A series (see Figure 4-18). The present transducer is temperature compensated and is regulated by its own internal amplifier. The transducer has a sensor element of constant area which reacts to the pressure applied by the fluid in the silicon tubes. The pressure of the fluid deflects the diaphragm inside the pressure transducer which is then translated into a voltage output which is recorded by a data logging system. The analogue voltage output is then translated into a pressure through a linear calibration which was conducted prior to the experiments.

The tubes leading to the transducer were bled before the initiation of each test in order to remove any air bubbles that may have been trapped in the tubing. In addition, the connection of the transducer to the data-logger was conducted via coaxial cables instead of regular copper cables. This provided a significant improvement in the signal quality and sensitivity to the pressure forces.

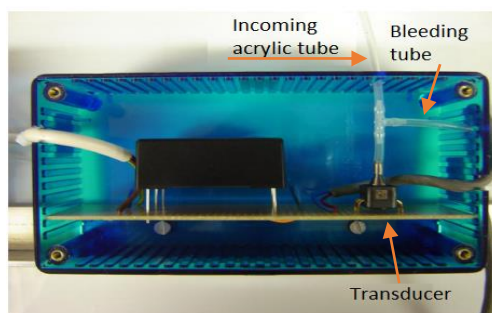


Figure 4-18: Pressure transducer

4.5.3 Experimental programme

The present test programme was carried out under the forcing of a unidirectional current with a mean flow velocity of 0.33m/s. This velocity was higher than the velocities tested in the scour experiments listed in Tables **Error! Reference source not found.** Table 4-3 because they were below the operation range of the pressure sensor.

After the completion of the pressure measurements flow measurements were conducted for the same undisturbed mean flow velocity. No flow measurements were conducted for the 45° conical base structure because it broke while being removed from the flume after the pressure measurements. In addition, due to time constraints it was not possible to conduct flow measurement around all the structures due to the time required for the tests. For that reason, complete flow measurements were conducted only for the cylindrical base, 75° conical base and monopile. These structures represent the three different types of geometries investigated in this study. Table 4-4 shows the experimental programme for the flow conditions and the types of measurements conducted for this test series.

Table 4-4: Flow and pressure measurement programme

Test	Structure	U_c	d_{50}	h	Pressure measurement	Flow measurement (plane of symmetry)	Flow measurement (around structure)
(-)	(-)	(m/s)	(mm)	(m)	(-)	(-)	(-)
4.1	Cylindrical base	0.33	0.2	0.165	✓	✓	✓
4.2	45° conical base	0.33	0.2	0.165	✓	✗	✗
4.3	60° conical base	0.33	0.2	0.165	✓	✓	✗
4.4	75° conical base	0.33	0.2	0.165	✓	✓	✓
4.5	Uniform cylinder	0.33	0.2	0.165	✓	✓	✓

4.6 Database compilation for equilibrium scour prediction equation

A significant amount of equilibrium scour data has been published in the past. In this study published data on equilibrium scour depths around both uniform and complex cylindrical structures were selected in order to create an equilibrium scour prediction equation for clearwater scour conditions. The decision to focus on the clearwater regime was made in order to avoid data that were influenced by ripple formation upstream of the structure, which would introduce additional sediment transport scale effects. A summary of the sources and quantities of scour data is given in Table 4-5.

Table 4-5: Sources of data for scour prediction equation.

Data Source	Number of data points
Complex geometries	
Amini (2014)	6
Ataie-Ashtiani et al (2010)	8
Ferraro et al (2013)	10
Hoffmans and Verheij (1997)	1
Jannati et al (2015)	2
Melville and Raudkivi (1996)	7
Moreno et al (2015)	8
Parola et al (1996)	13
Simons et al (2009)	4
Whitehouse (2011)	2
Total complex geometries	61
Uniform Cylinders	
Chabert and Engeldinger (1956)	85
Dey et al (1995)	18
Ettema (1980)	70
Ettema et al (2006)	5
Jain and Fischer (1979)	26
Melville (1997)	5
Melville and Chiew (1999)	12
Matutano et al (2013)	10
Shen et al (1969)	16
Sheppard and Miller (2006)	4
Sheppard et al (2004)	4
Yanmaz and Altinbilek (1991)	14
Total uniform cylinders	269

The data presented include scour tests that were conducted in the clearwater regime for cohesionless sediments only. Data were included only if all relevant parameters were presented in the publication. The aforementioned parameters include the median sediment size, average flow velocity, the sediment geometric standard deviation, water depth, structural dimensions and the time to equilibrium scour. Tests were discarded if:

- They were not run for a sufficiently long period to achieve equilibrium scour. According to Melville and Chiew (1999) this is the time required to reach a scour depth in which the scour rate does not exceed 5% of the structure diameter in 24 hours; and,
- The sediment geometric standard deviation (σ_g) was greater than 1.5. This was done to avoid the effects of bed armouring.

In addition, for a limited number of structures that did not have a circular footprint the equivalent diameter was determined and used. Only one field study is included in this dataset (Matutano et al, 2013) even though there have been a large number of field studies published. The majority of field studies were excluded for three reasons:

- Field measurements tend to have time-varying flows which make it difficult to determine if a given scour hole has reached the equilibrium phase;
- In most cases, naturally occurring flows in tidal or alluvial environments are high, thus forcing scour to occur in the live bed regime for at least part of the time. The extensive bed formations developed upstream of the structure and the general lowering of the bed would provide additional difficulty in generalising any information; and,
- In most cases it is not possible to monitor the scour development systematically and, therefore, it is not possible to determine if the scour hole is fully developed.

5 Results for scour around complex structures

This chapter will present the results of the experimental study on scour around uniform and non-uniform cylindrical structures. It will start with the results for the small scale scour tests, then the large scale scour results followed by the pressure and flow measurements around the same geometries.

5.1 Smaller scale scour results

This section will provide the results of tests listed in section (4.3.4). First the flow conditions will be presented followed by the results for the time development of scour and the equilibrium scour depths.

5.1.1 Flow conditions

For the small scale scour experiments. Flow profiles were measured at the location of the pile before it was installed. Figure 5-1 (a) and (b) show the flow profiles for the 165mm and 100mm water depth scour tests. The symbols correspond to the flow conditions outlined in Table (4.1) and the lines show profile approximation for tidal currents proposed by Soulsby (1990) and applied for the corresponding mean flow velocity. It can be observed that the flow profiles for tests conducted with similar mean flow velocities but with different bed roughness show good agreement. This behaviour may be attributed to the fact that the flow has been developed at the location of the measurement. Furthermore, it can be observed that all the measurements show a good agreement with the prediction given by the Soulsby (1990) method. Therefore, it can be safely stated that the present flow conditions resemble that of tidal currents.

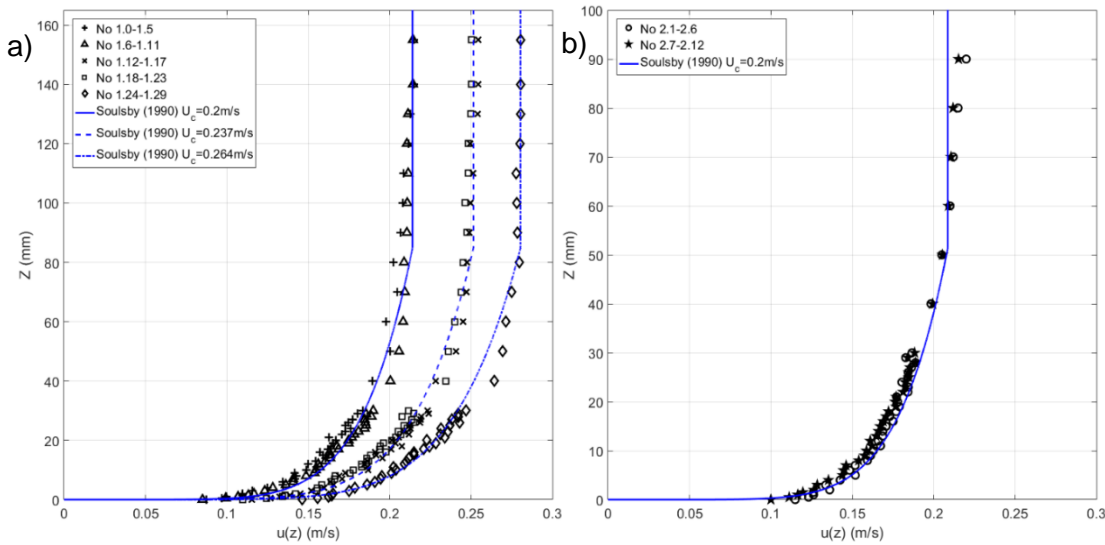


Figure 5-1: Flow profiles for small scale scour tests: a) $h=165\text{mm}$ and b) $h=100\text{mm}$.

5.1.2 Results

In this section the results from the small scale scour experiments will be presented.

5.1.2.1 Initiation of scour around complex geometries

During the initial stages of the scouring process the uniform cylinders showed a different behaviour compared to the conical based structures. For the conical base structures, the scour process initiates at the lee of the structure at an angle approximately 120° relative to flow direction (see Figure 5-2). The deepest scour then gradually propagates towards the upstream of the structure and reaches the leading face of the structure; the deepest scour point then stabilizes at a location adjacent to the structure at an angle approximately 45° relative to the flow direction. This point of initiation of scour agrees with the findings of Tavouktsoglou et al. (2015) who found that the maximum amplification of the bed shear stress occurs at the same location for all conical based structures. This is consistent with the observations of Khalfin et al. (1983) who observed that the maximum scour for some conical structures occurred at the lee of the structure. This behaviour is also reported in Petersen (2014) who examined the behaviour of edge scour around protected piles with the difference that the maximum scour depth did not move towards the front of the scour protection scheme.

This behaviour can be explained by the presence of the conical base (which is composed of a cone imposed onto a cylinder) which effectively weakens the horseshoe vortex at the initial stages of the scour process (as will be shown in section 5.3.3), thus making the scour process vortex-shedding dominated. Once the scour reaches the leading face of the structure then the horseshoe vortex gains more strength as a result of the greater depth over which it has to act, therefore making it a horseshoe vortex-dominated process which explains the shift of the maximum depth of scour to the same location where it occurs for a monopile.

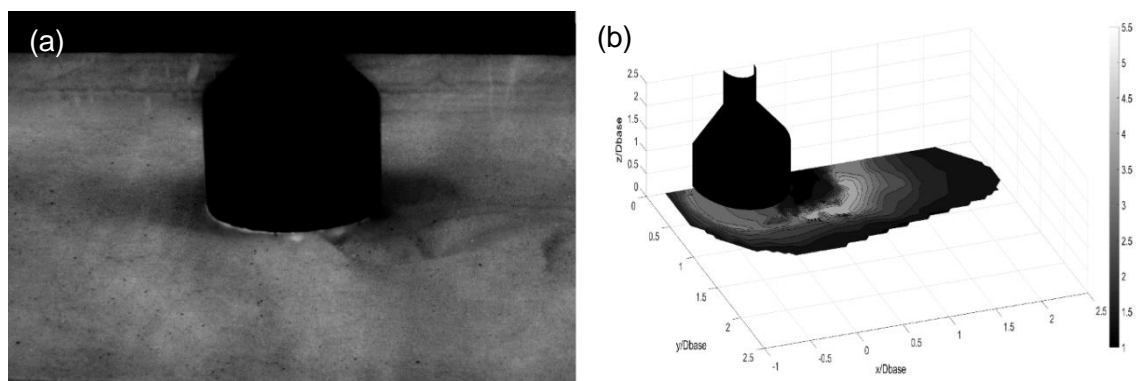


Figure 5-2: (a) Initiation of scour at 45° conical base structure, (b) bed shear stress amplification contour map for same structure; flow direction from left to right.

5.1.2.2 Temporal evolution of scour

In this section the scour development around the structures detailed in section (4.3.4) are presented. The results for each flow condition will be presented in one graph to demonstrate the effects of geometry on the scour development.

Figure 5-3 presents the results for tests 1.0-1.5. The tests were conducted at a flow depth of 165mm with a sediment mobility ratio of 0.73 with $D_{50} = 0.6\text{mm}$. The value of U/U_c is relatively small but the purpose of this test was to examine the behaviour of the scour development when the current strength is not large. In general, the scour development follows a similar trend to that expected when plotting the data on a log scale (Figure 2-26). The monopile structure tends to start off with a scour rate similar to the other structures then log scale gradient increases. This behaviour might be attributed to the increasing strength of the horseshoe vortex as the scour hole deepens. The 75° and 60°

conical based structures follow the expected scour development trend as they reach the development phase (steeper slope in the graph) early in the tests. The behaviour for the 45° conical base structure and the cylindrical base structure is different to the aforementioned structures. More specifically, the data show that it takes some time for the scour to enter the development phase. This behaviour might be attributed to the limited effect the shaft of the structure has on the scour process due to sheltering of the bed provided by base of the structure. Finally, the truncated cylinder shows minimal scouring due to the limited effect it has on the flow.

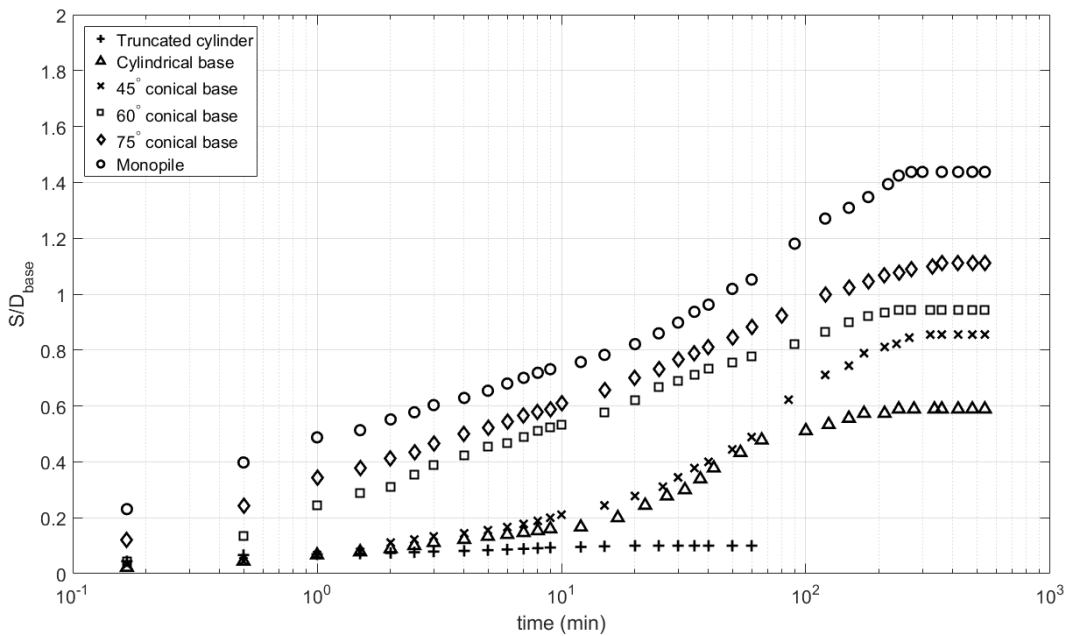


Figure 5-3: Time development of scour for tests 1.0-1.5 ($h = 0.165\text{m}$, $d_{50} = 0.6\text{mm}$ and $U_c/U_{cr} = 0.73$).

Figure 5-4 shows the results for tests 1.6-1.11. The present tests were conducted for the same flow depth as in the previous case and $U_c/U_{cr} = 0.88$ over a bed comprised of sediment with $d_{50} = 0.2\text{mm}$. It can be observed that the development trends for all the structures with the exception of the truncated cylinder follow a more linear behaviour (in the log-scale) with the structures entering the development phase early on in the experiment. In the case of the truncated cylinder the scour rate is considerably smaller compared to the other structures in the initial stages. The scour rate for this structure starts to increase for a scour depth $\gtrsim 0.2S/D_{base}$, which is the same non-dimensional

depth at which the cylindrical and 45° conical as seen in Figure 5-3. Furthermore, it can be observed that the rate of scour (i.e. slope of the graph) is the same for all the structures except for the truncated cylinder.

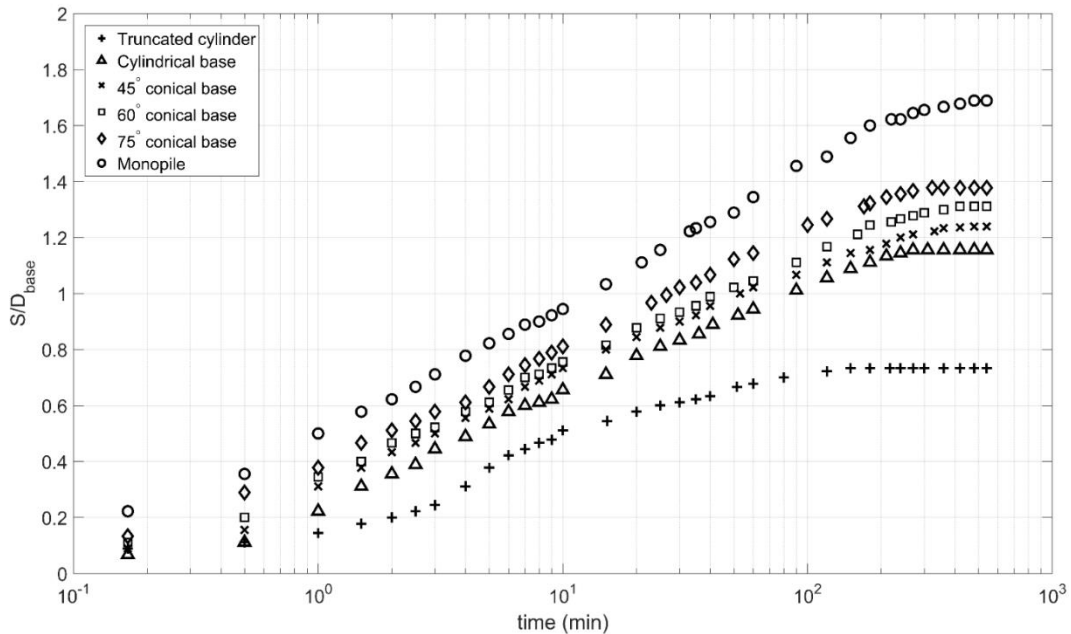


Figure 5-4: Time development of scour for tests 1.6-1.11 ($h = 0.165m$, $d_{50} = 0.2mm$ and $U_c/U_{cr} = 0.88$).

Figure 5-5 shows the results for tests 1.12-1.17 which were conducted for a flow depth of 165mm, sediment mobility ratio of 0.98 and a sediment median size of 0.2mm. In these tests all of the structures tend to follow a straight trend in the logarithmic plot. There is a clear increase in the scour rate for all structures compared to the previous set of tests (tests 1.6-1.11). This increase is in the order of 10%. Interestingly, for this flow condition the scour development for the 45° and 60° conical base structures is almost identical to each other.

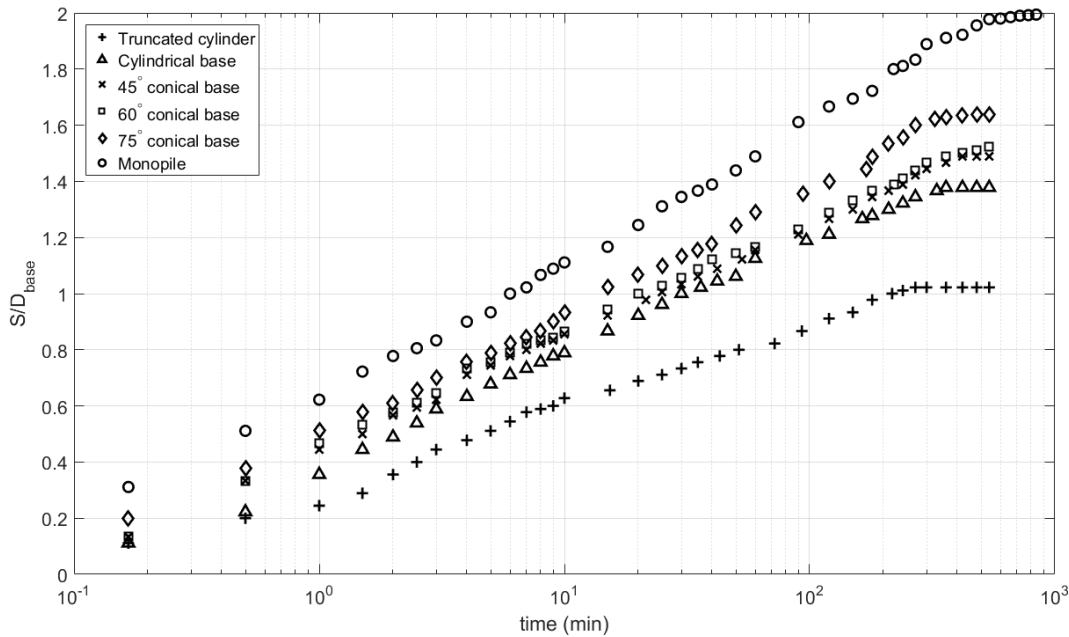


Figure 5-5: Time development of scour for tests 1.12-1.17 ($h = 0.165m$, $d_{50} = 0.2mm$ and $U_c/U_{cr} = 0.98$).

The following graph (Figure 5-6) shows the results for tests 1.18-1.21. These tests were conducted for similar flow conditions as in 1.6-1.11 with the exception of the bed material which in these tests had $D_{50} = 0.6mm$. The purpose of these tests was to examine the effect the sediment size has on the scour process. As can be seen in the figure the scour development follows the same trend for all the structures as the ones in Figure 5-4. An exception to this observation is the truncated cylinder which has a slower scouring rate under the same flow conditions. This behaviour might be effected by d_{50}/D scaling effects as described in section (4.2). Considering that this rule has been derived for monopiles extending to the water surface it can be expect that scaling issues would arise for an even smaller ratio of d_{50}/D in the case of truncated cylinders because the pressure field around it is weaker and thus any scaling issue would be more pronounced. This could explain the smaller scour rate and equilibrium depths observed for this test.

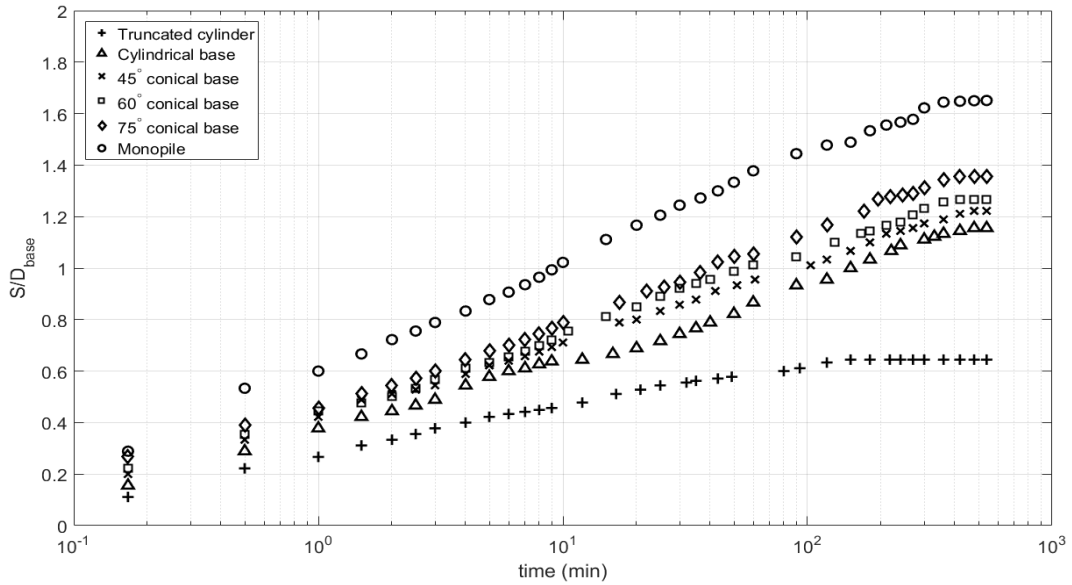


Figure 5-6: Time development of scour for tests 1.18-1.23 ($h = 0.165m, d_{50} = 0.6mm$ and $U_c/U_{cr} = 0.88$).

The last set of tests conducted at a depth of 165mm were tests 1.24-1.29 and the results are presented in Figure 5-7. In these tests $U_c/U_{cr} = 0.99$ and $d_{50} = 0.6mm$. For this flow condition the time development of scour behaves in similar manner to that observed in Figure 5-5 which was conducted under a similar mobility ratio and depth but with a finer sediment. The trend lines for all the structures have generally the same slope and lead to the same equilibrium depths as the ones depicted in Figure 5-5.

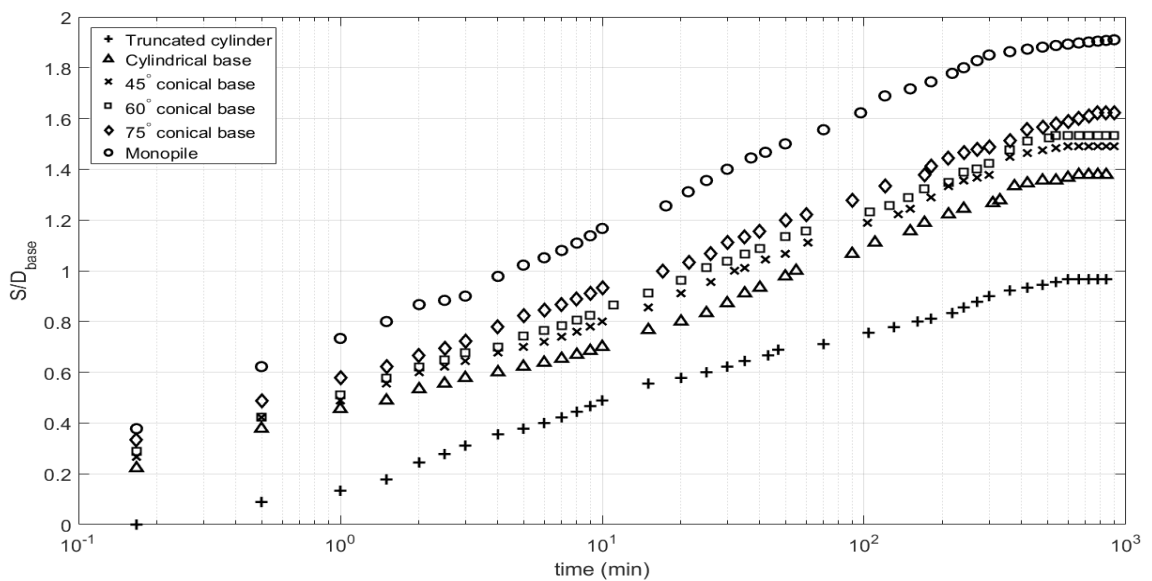


Figure 5-7: Time development of scour for tests 1.24-1.29 ($h = 0.165m, d_{50} = 0.6mm$ and $U_c/U_{cr} = 0.99$).

Two sets of scour experiments were conducted at a smaller water depth ($h=100\text{mm}$) to investigate the effect this parameter has on scour. Tests 2.1-2.6 (Figure 5-8) were conducted for a flow velocity of 0.2m/s with a sediment size of 0.2mm which leads to a sediment mobility ratio of 0.93 . Tests 2.7-2.12 (Figure 5-9) were undertaken at flow a velocity of 0.19m/s with $d_{50} = 0.6\text{mm}$ which yields a $U_c/U_{cr} = 0.78$. In both graphs it can be observed that the scour rate and equilibrium scour depths for all structures except for the monopile are larger than the ones produced for the same sediment mobility ratio at a larger depth. At first glance this contradicts the generally accepted rule for cylinders which suggests that a decreasing flow depth yields smaller scour depths. In the case of the non-uniform cylindrical structures a smaller flow depth forces a larger portion of the flow to interact with the lower part of the structure which in the case of these tests is wider. This phenomenon is linked to the local increase in the pressure gradient due to the flow and structure interaction and will be further discussed in the next chapter. This process may explain this increase in the scour rate and equilibrium depth.

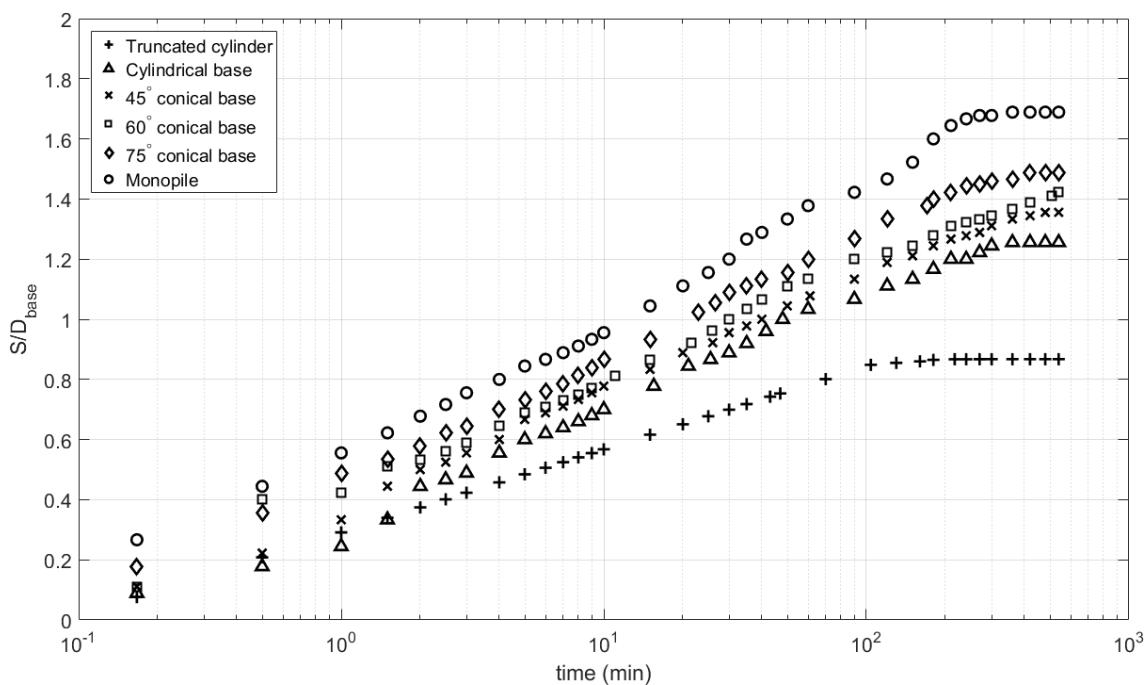


Figure 5-8: Time development of scour for tests 2.1-2.6 ($h = 0.1\text{m}$, $d_{50} = 0.2\text{mm}$ and $U_c/U_{cr} = 0.93$).

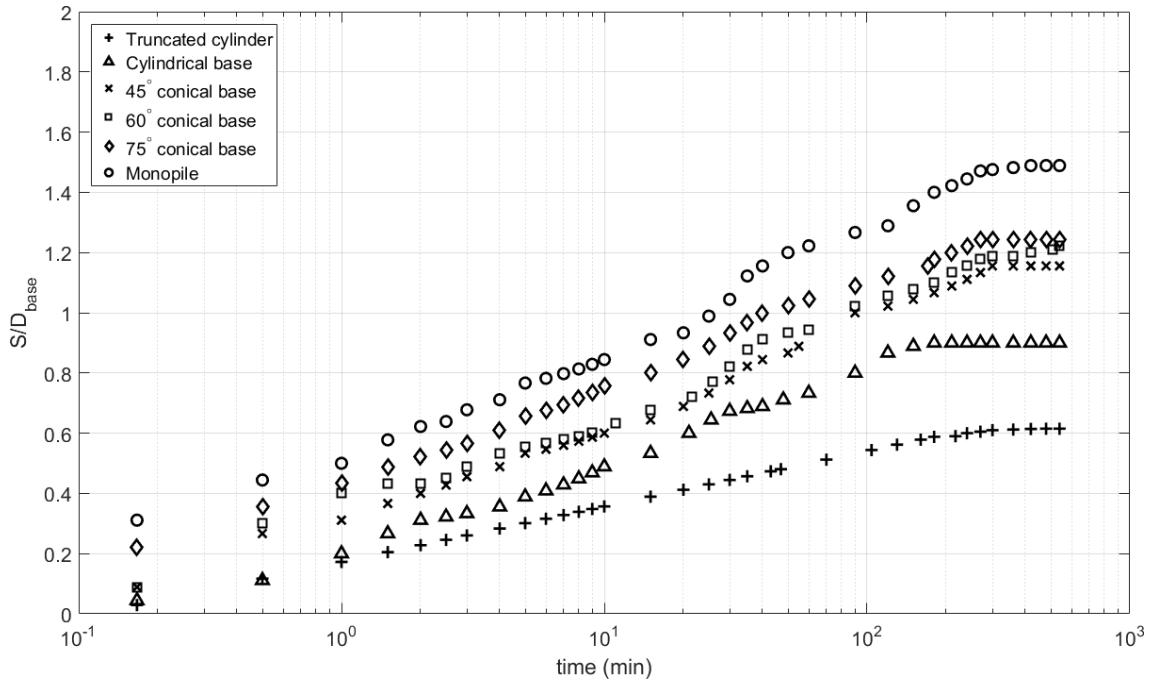


Figure 5-9: Time development of scour for tests 2.7-2.12 ($h = 0.1m$, $d_{50} = 0.6mm$ and $U_c/U_{cr} = 0.78$).

Figure 5-10 demonstrates the influence of the ratio U_c/U_{cr} on the scour development for three representative structures tested in this study (cylindrical base, 60° conical base and uniform cylinder). It can be observed that an increase in the mobility ratio yields an increase in the rate of scour and equilibrium scour depth which is in accordance with the findings of Breusers et al., (1977) for uniform cylinders.

The present data also show that for the cases where U_c/U_{cr} is constant (or has a similar value) an apparent deceleration in the scour rate is observed as it approaches its equilibrium stage for the cases where the coarser bed material is used. This deceleration effect is reduced as the blockage induced by the structure increases and as the mobility ratio increases. It is noted that according to Raudkivi and Ettema (1983) the effects of bed armouring are minimal as the geometric standard deviation of the sediments presented here are minimal since the σ_g for both the sands is smaller than 1.5.

Figure 5-10 also shows the effect the side slope of the structure has on the development of scour. It can be observed that as the side slope of a structure increases, the rate of

scour also increases which is a result of the local amplification of the pressure gradient due to the increased obstruction.

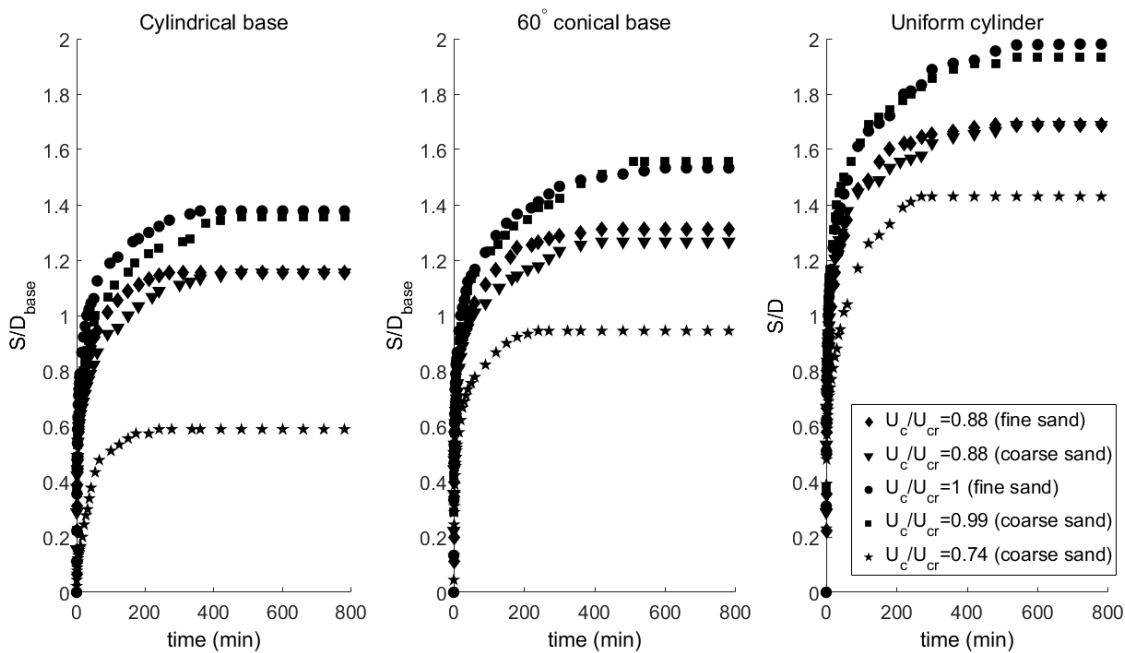


Figure 5-10: Influence of U_c/U_{cr} on scour development for three different structure geometries.

The present experiments also suggest that the geometry of the foundation plays an important role with regards to the shape of the scour hole. Figure 5-11 shows that for a cylindrical base structure at low mobility ratios ($U_c/U_{cr} < 0.8$) the scour hole did not extend around the periphery of the structure. The scour process eroded sediment from the upstream face of the structure and deposited it at the lee. This behaviour has also been reported by Briaud et al. (2004) and Ataie-Ashtiani et al. (2010) and is further supported by the flow measurements that will be presented in section 5.3.3.4. The flow measurements show that a clockwise circulation cell is present at the lee of the structure which brings sediment from further downstream near the edge of the base. Consequently, it can be stated that the shape of the footing plays an important role which should be considered when investigating scour phenomena and particularly scour protection schemes.

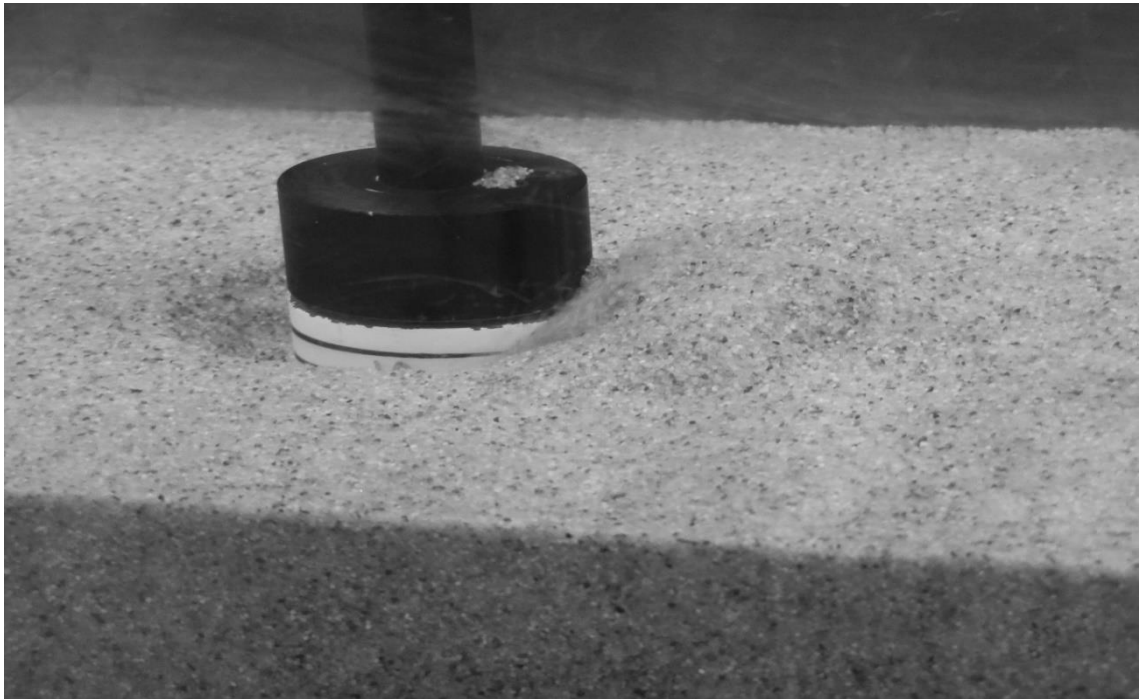


Figure 5-11: Observed scour depth at cylindrical based pier before under-cutting the base cylinder ($h = 0.165m$, $d_{50} = 0.6mm$ and $U_c/U_{cr} = 0.88$).

5.1.2.3 Equilibrium scour depth

This section will present the results for the equilibrium scour depths for the small scale (i.e. smaller than 1:100) experiments. First will be discussed the importance of the non-dimensionalising parameter, then the influence of the geometry and the water depth on the equilibrium scour depth. Table 5-1 presents the scour depths for each tests.

Table 5-1: Equilibrium scour depth for small scale scour experiments.

Test No	S/D_{base}						
1.0	0.1	1.11	1.69	1.22	1.36	2.4	1.42
1.1	0.59	1.12	1.02	1.23	1.65	2.5	1.49
1.2	0.87	1.13	1.38	1.24	0.97	2.6	1.69
1.3	0.95	1.14	1.49	1.25	1.38	2.7	0.62
1.4	1.12	1.15	1.52	1.26	1.49	2.8	0.9
1.5	1.43	1.16	1.64	1.27	1.53	2.9	1.16
1.6	0.73	1.17	2	1.28	1.62	2.10	1.22
1.7	1.16	1.18	0.64	1.29	1.93	2.11	1.25
1.8	1.23	1.19	1.16	2.1	0.87	2.12	1.49
1.9	1.31	1.2	1.22	2.2	1.26		
1.10	1.38	1.21	1.27	2.3	1.36		

The results of this study show that the equilibrium scour depth around non-uniform cylindrical geometries is strongly affected by the flow depth. Figure 5-12 demonstrates this effect for two different flow conditions with a mobility ratio of 0.88-0.90 (top) and 0.73-0.75 (bottom). Both figures show an increase in the equilibrium scour depth for all non-uniform cylindrical geometries while for the range of conditions tested in this study the uniform cylinders do not seem to be affected by the water depth which agrees with the findings of Melville and Sutherland (1988) for monopiles.

In the case of cylindrical base structures and given that the diameter of the top shaft is small relative to the diameter of the base the scour depth would increase as the stick-up height increases. Up to the point where the velocity profile switches from a logarithmic to a uniform profile. After this stick-up height the scour would be independent of the h_c . In the case of conical structures, the scour depth increases as the side slope of the cone increases and then reaches the equilibrium scour depth of a monopile with the same base diameter as the cone (for more details refer to Chapter 6).

The behaviour of both types of structure can be explained in terms of the local change in the pressure gradient as follows:

- In the case of non-uniform cylindrical structures, a decreasing flow depth while the mean flow velocity remains constant results in a larger portion of the flow interacting with the wider diameter base of the structure. This translates into an increase in the local pressure field induced by the structure which is responsible for the amplification of the bed shear stress which is the driver of the scour phenomenon.
- For the uniform cylinder, the effect of a decreasing flow depth is not as apparent because the total flow interacting with the cylinder remains very similar thus not effecting the scour process significantly. This is true as long as the water depth is not in the “shallow water scour” regime Guo et al. (2012).

Figure 5-12 also shows that an increasing side slope of a structure results in deeper equilibrium scour depths. In addition, it can be concluded, that for the cylindrical based structures tested in these experiments the equilibrium scour depth is not solely driven by

the cylindrical footing. Comparison between the values of equilibrium scour depth of the truncated cylinder and cylindrical based structure show that the latter structure type yields equilibrium scour depths which are 7 % and 36% greater than that of the truncated cylinder with the same height of emergence, depending on the given flow conditions and sediment type. The data suggest that the difference between the equilibrium scour of the two structures increases as the water depth increases, which is in line with the notion of increased pressure gradients. These points suggest that the scouring process is not solely dependent on the horseshoe vortex formed by the footing of the structure, but is also influenced by the shaft of the structure which contributes to the increase of the pressure gradient and therefore increases the equilibrium scour depth.

The results also demonstrate that the equivalent diameter is not effective in describing the equilibrium scour depth for the structure geometries tested in this study. Figure 5-12 and Figure 5-13 present the same results with the difference being that in the first the scour depth is non-dimensionalised by the diameter of the base (D_{base}) and in the second by the equivalent diameter as proposed by Coleman (2005). It can be seen that non-dimensionalising the equilibrium scour depth with the equivalent diameter yields unrealistically high non-dimensional scour depths in most cases and particularly in the case of submerged/truncated cylinders.

Given that the scale at which these experiments have been conducted is small, it is expected that the non-dimensional scour depths included in this study may be subject to scale effects. According to Schlichting (1968) the size of the boundary layer is proportional to $1/\ln(\text{Re})$ which means that the overall turbulence induced by the flow structure interaction would decrease as the Reynolds number increases. In addition, Achenbach (1968) showed that an increasing Re_D forces the separation point on the face of the structure to shift further to lee of the pile which would also result in a decrease in the sediment transport capacity of the lee wake vortices and thus decrease the overall

scour potential. This shows that Re_D could account for some scale effects that result in smaller scour depths for larger scale structures.

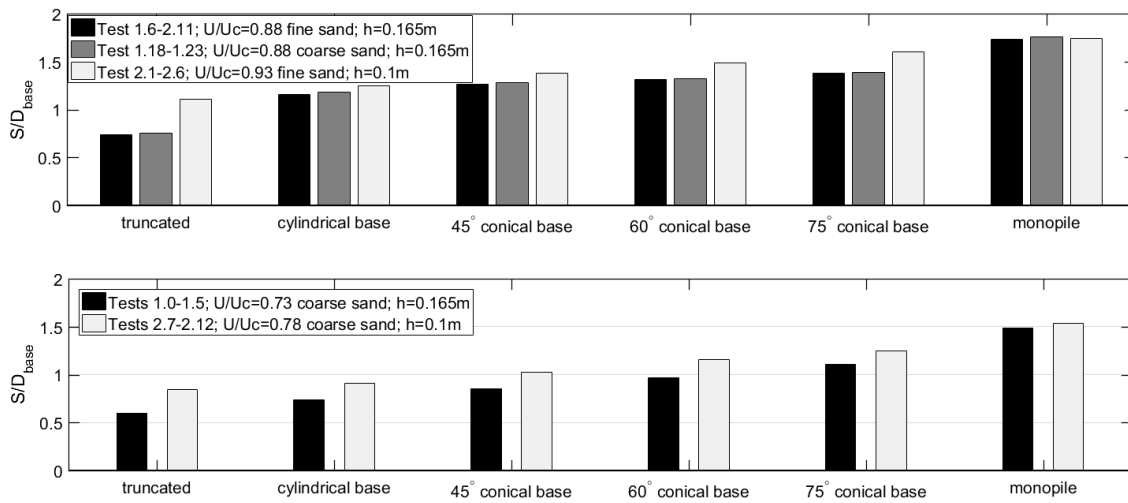


Figure 5-12: Influence of water depth on equilibrium scour depth for different structure types (non-dimensionalised by base diameter of the structure).

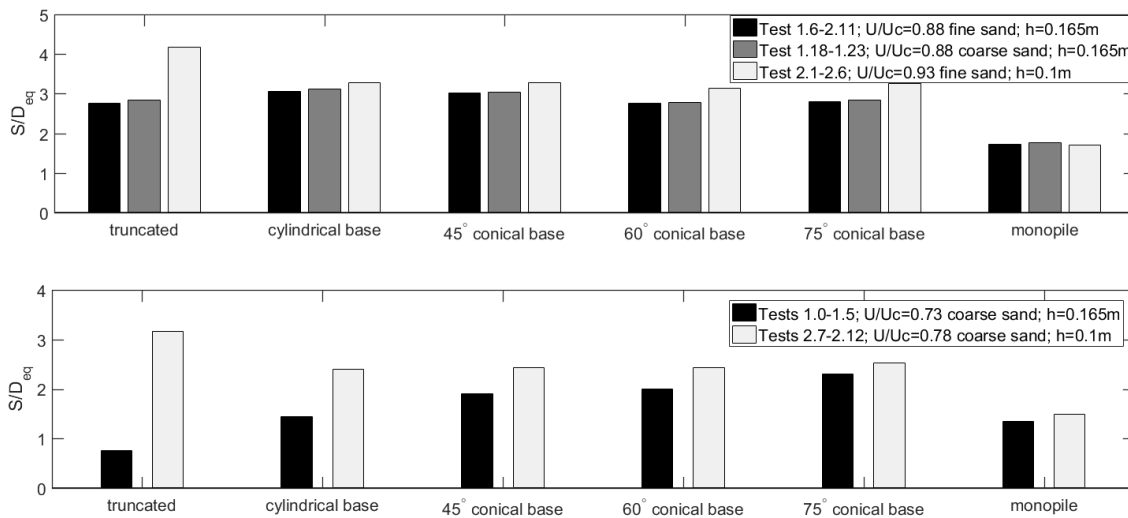


Figure 5-13: Influence of water depth on equilibrium scour depth for different structure types (non-dimensionalised by equivalent diameter according to Coleman, 2005).

5.1.2.4 Repeatability of tests

This section will deal with the repeatability of the small scale scour experiments. The repeatability of a physical tests is important for two reasons:

- It demonstrates that the test conditions can be repeated and that the outcome of the tests is not subject to large variations

- It can provide a measure of the error in the measurement.

Due to the long duration of the tests, in this study it was decided not to repeat certain tests. Instead some tests are compared with the results of another author who conducted scour experiments in the same flume using the same sediments. The advantage of this practice is that the data used for the comparison are independent of errors that may occur due to the procedures and measuring techniques used in the current study.

Test 1.5 which was conducted for a uniform cylinder of $D=45\text{mm}$ at a flow velocity of 0.2m/s , a flow depth of 0.165m and a sediment size of $d_{50}=0.6\text{mm}$. This test was compared with results from Porter (2016) who conducted scour tests in the same flume with the same sediment for a uniform cylinder of $D=40\text{mm}$, a flow velocity of 0.19m/s and the same flow depth. Figure 5-14 provides the comparison between the two tests. As can be observed, the scour evolution curves for the tests show good agreement. The largest discrepancy between the two tests is $5\% S/D$. This occurs as the scour process reaches the equilibrium stage. Given the slight differences in pile diameter and flow velocity this is reasonable.

Figure 5-15 presents the results from the second comparison between the test 1.11 which corresponds to the monopile with $D=45\text{mm}$, $U_c = 0.20\text{m/s}$ and $d_{50} = 0.2\text{mm}$ and an equivalent test of Porter (2016) which was conducted for $D=40\text{mm}$, $U_c = 0.19\text{m/s}$ and $d_{50} = 0.2\text{mm}$. The comparison between the two time development curves is similar to that shown in Figure 5-14. The maximum error between the two data sets is $5.5\% S/D$. The maximum error occurs at the equilibrium phase of the scour process which coincides with the finding of the previous figure. Given that the velocity and the pile diameter are slightly smaller in the experiment of Porter (2016) this behaviour is expected.

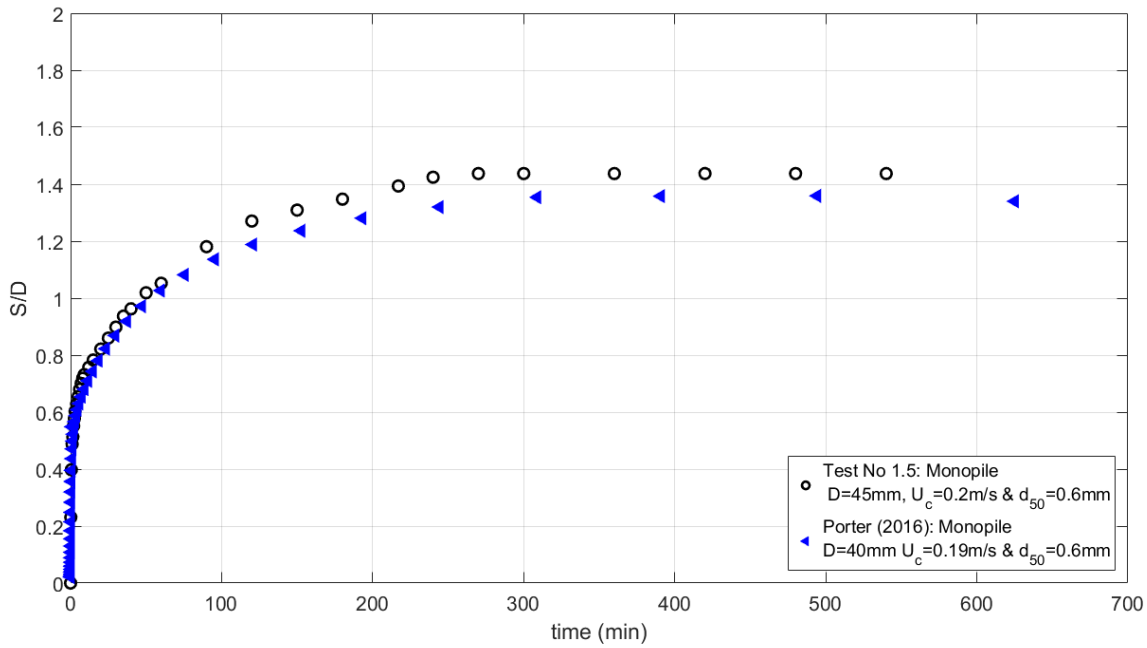


Figure 5-14: Comparison of test 1.5 with Porter (2016) with $D=40\text{mm}$, $U_c = 0.19\text{m/s}$ and $d_{50} = 0.6\text{mm}$.

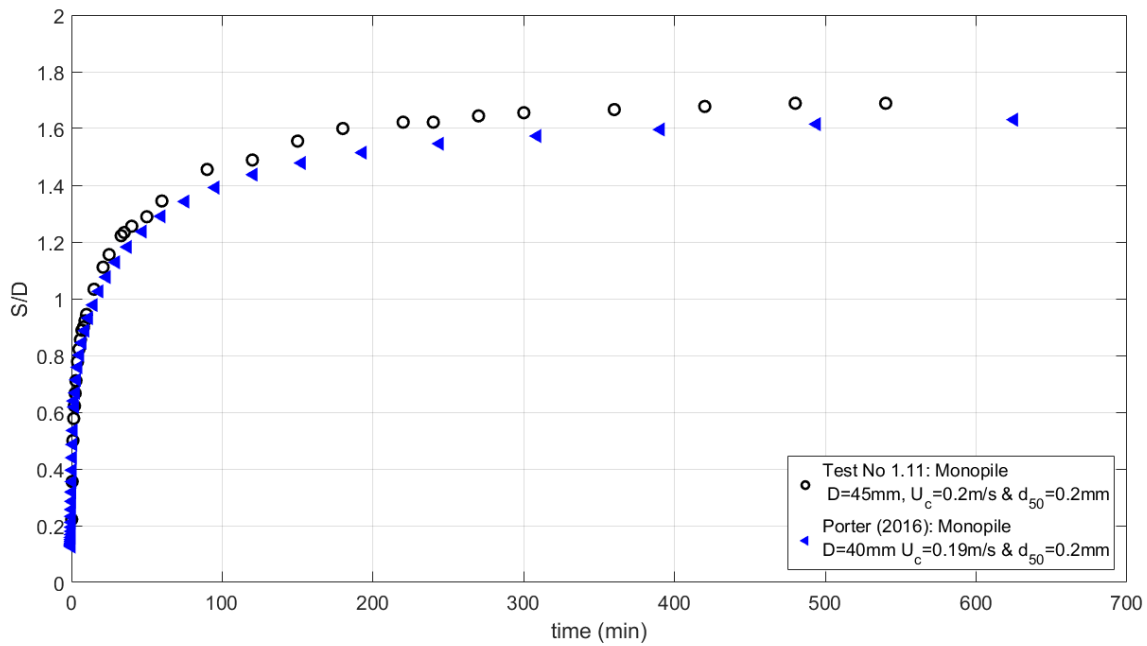


Figure 5-15: Comparison of test 1.11 with Porter (2016) with $D=40\text{mm}$, $U_c = 0.19\text{m/s}$ and $d_{50} = 0.2\text{mm}$.

Concluding, the comparisons reveal that the maximum difference between the two pairs of tests is $0.055 S/D$ which can be taken as the uncertainty of the tests. The comparisons also show that the rate of scour in the present study follows the same behaviour as in

Porter (2016) which can lead to the conclusion that the tests in this study can be repeated by other researchers.

5.2 Large scale scour results

This section will provide the results for the tests detailed in the section (4.4.4). First the flow conditions will be presented followed by the results for the time development of scour and the equilibrium scour depths. Finally, the section will conclude with a discussion on the repeatability of the tests.

5.2.1 Flow conditions

This section presents the unidirectional flow conditions under which the large scale scour tests were carried out. One of the main aims of these tests was to investigate the effect of non-logarithmic flow profiles on the scour process. Such flow profiles may be present in locations where large lateral wind loads are expected such as the locations where offshore wind farms are situated. In these locations the wind load effectively produces a wind driven shear flow on top of the existing logarithmic flow (Davies and Lawrence, 1994) creating a flow profile similar to that of Figure 2-11 (b). To create these flow profiles, flow straighteners were used to alter the flow profiles and the resulting flow profiles are presented in Figure 5-16 (a) and (b). Figure 5-16 (a) shows the measured logarithmic profile and the tidal flow prediction of Soulsby (1990) for the same mean flow velocity. Figure 5-16 (b) shows the measured flow profiles for the non-logarithmic flow profiles which were conducted at 3 different flow depths. All four flow profiles yielded a mean flow velocity of 0.25m/s which allowed the comparison of the results while keeping the flow flux constant.

The measured flow profile in Figure 5-16 (a) and the prediction of Soulsby (1990) shows good agreement which can allow us to conclude that the present flow condition is representative of a tidal flow. The measurements shown in Figure 5-16 (b) for non-logarithmic profiles also show a resemblance to the behaviour captured by the model of

Holmedal and Myrhaug (2013) who calculated and verified the flow profile of a combined tidal and wind driven flow in the Celtic Sea (given in Figure 5-17).

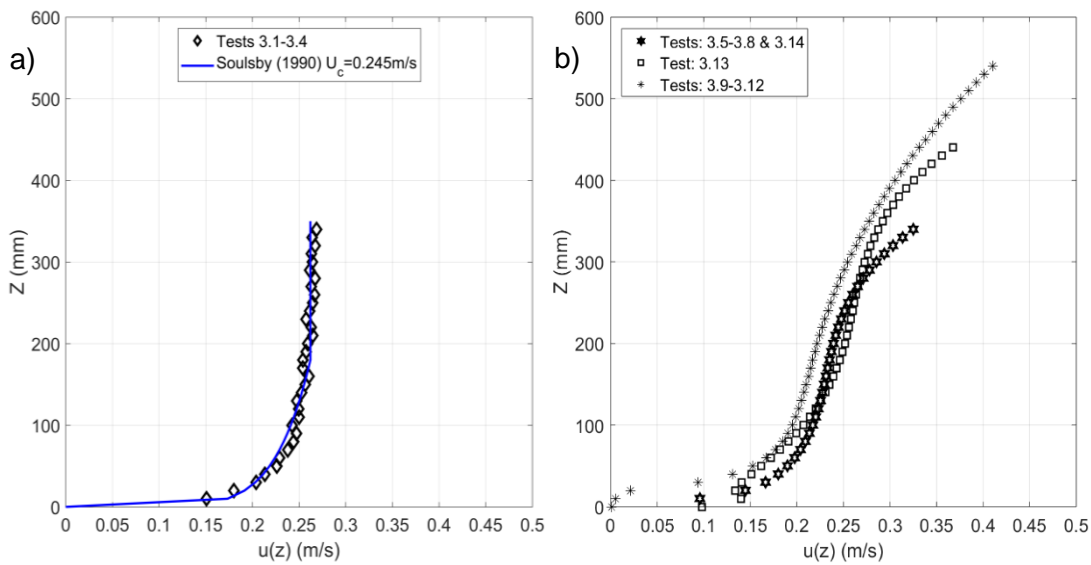


Figure 5-16: Flow profiles for large scale scour tests: a) logarithmic flow profile and b) non-logarithmic flow profiles.

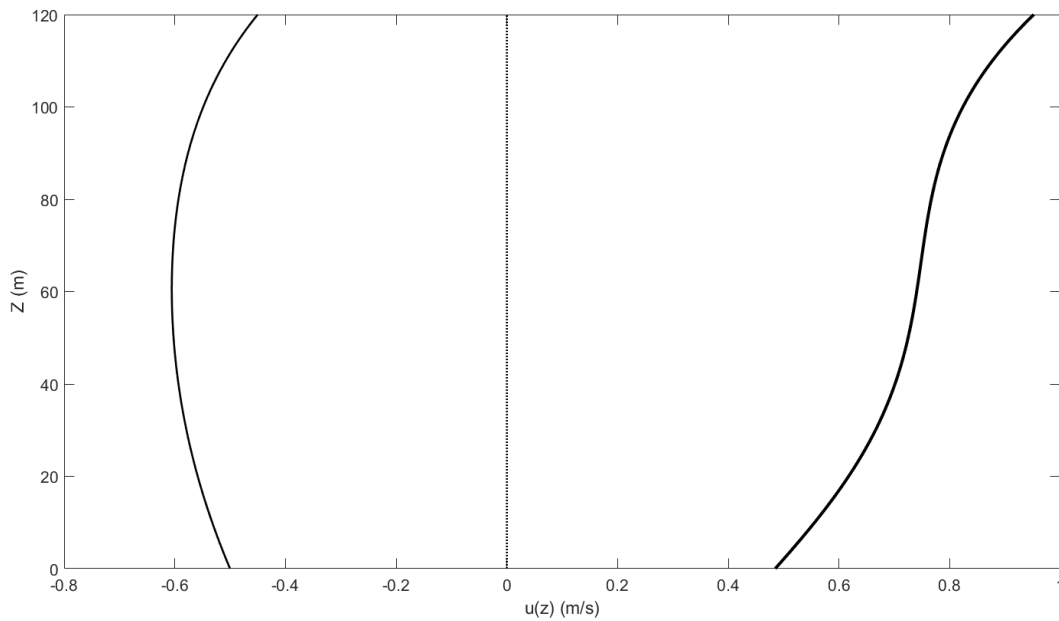


Figure 5-17: Velocity profiles when the wind is opposing the tide (left) and when the wind is following the tide (Source: Holmedal and Myrhaug, 2013).

5.2.2 Results

This section will present the results of the larger scale experiments. The section will first present the findings regarding the temporal evolution of scour around the structures and then the equilibrium scour depths. The section will then conclude with a discussion on the repeatability of the tests.

5.2.2.1 Temporal evolution of scour

Figure 5-18 presents the results for tests 3.1-3.4 which correspond to a logarithmic flow profile at a water depth of 350mm and $U_c/U_{cr}=0.94$. As was the case for the small scale test the data behave in accordance with the time development profile described in Hoffmans and Verheij (1997), with the scour developing rapidly at the initial stages and then slowing down later into the tests. The scour rates for the three complex geometries (i.e. cylindrical base, 45° and 75° conical base structures) are similar at the initial stages of the scour process. The time development then decelerates in the later stages of the tests with the smaller structures reaching the equilibrium stage sooner than the larger ones. Interestingly, the scour process for the monopile starts off much more rapidly than the other cases and then decelerates, reaching a scour rate similar to the other structures (at $t=1$ min). The scour then accelerates once again approximately at $t=20$ min. This behaviour is also recorded in the smaller scale tests and is attributed to the gain in strength of the horseshoe vortex with an increasing local depth. When comparing the results of these experiments with those of small scale tests it can be observed that the time scale of the scour process is approximately 3-4 times slower for the larger scale experiments. This is in accordance with the scour evolution equation presented in Equation (2-48). According to equations (2-49) and (2-50) the time scale of scour around a cylinder in a unidirectional current is $T \propto D$. Given that the scale of the structures has increased by a factor of 4 between the two sets of experiments this increase in the time scale of scour is reasonable. The present data also show that the same time scaling also applies to the complex geometries.

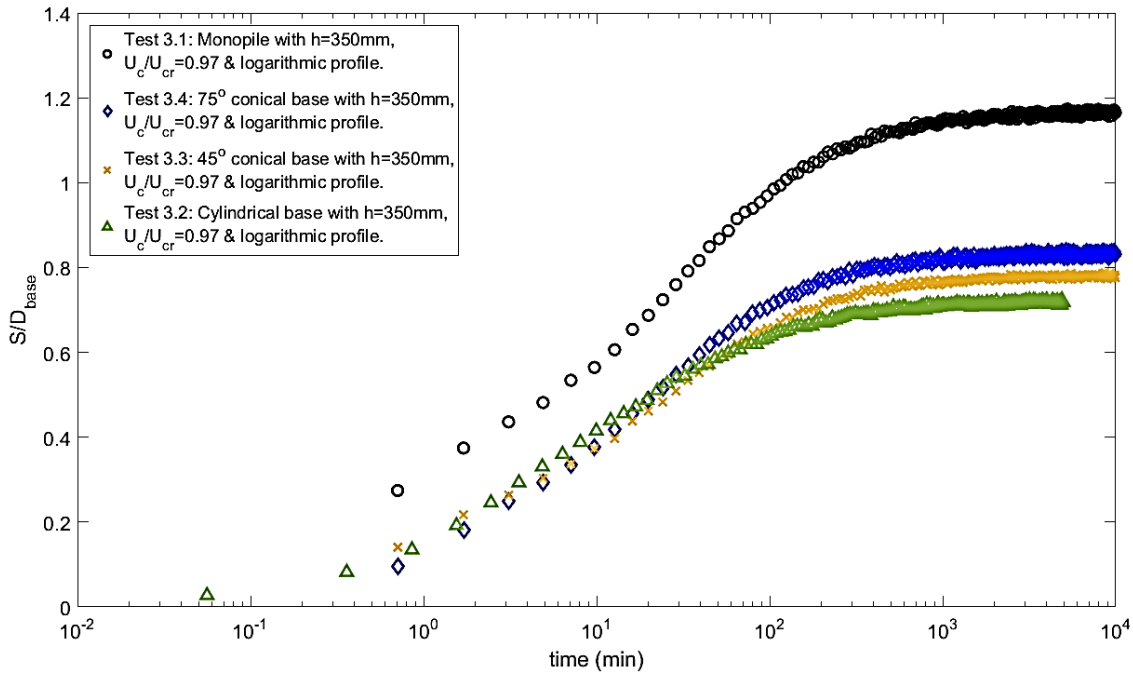


Figure 5-18: Temporal evolution of scour for a logarithmic flow profile, $h=350\text{mm}$.

Figure 5-19 presents the results for tests 3.5 to 3.8 which were conducted under the forcing of a non-logarithmic profile and for similar flow conditions as the results presented in Figure 5-18. The results reveal that the scour development for the monopile follows very similar path to the logarithmic case (see Figure 5-18). In the case on the non-uniform structure geometries (i.e. cylindrical base, 45° and 75° conical base structures) the rate of scour is significantly reduced, by a factor of 50% approximately. This behaviour can be explained by the change in the spatial distribution of the flow velocity through the water column. With the non-logarithmic profile smaller flow velocities are present near to the bed where the structure has the largest diameter. This leads to the local amplification in the adverse pressure gradient being smaller.

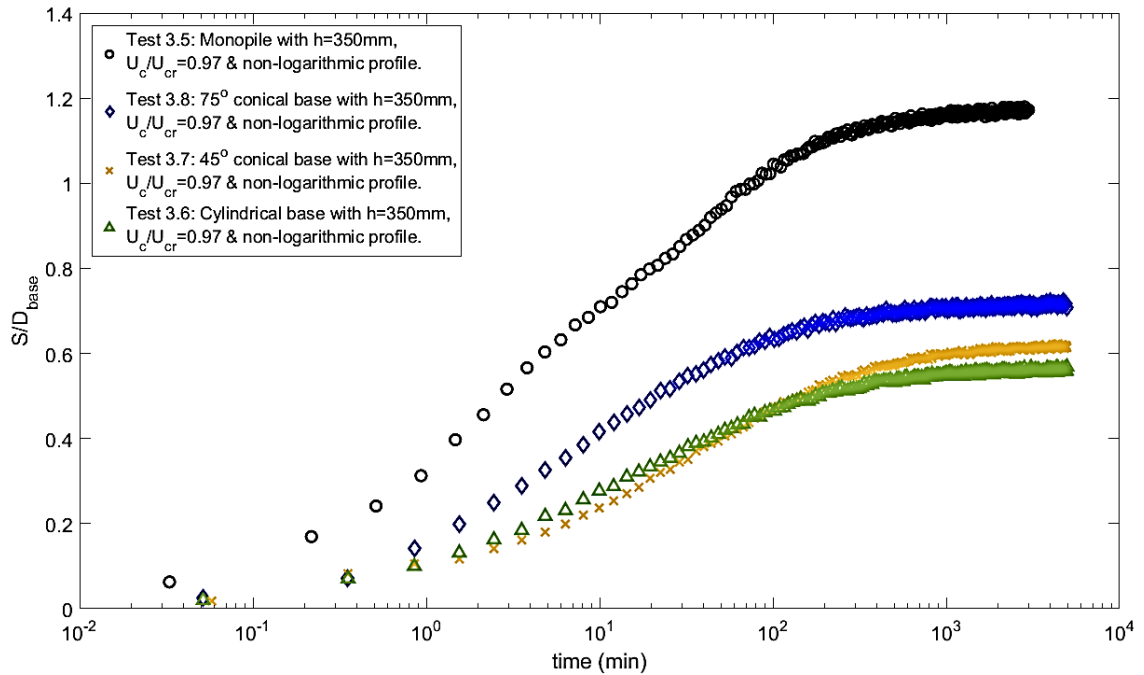


Figure 5-19: Temporal evolution of scour for non-logarithmic flow profile, $h=350\text{mm}$

Figure 5-20 shows the results for the scour development for the four geometries under the forcing of a non-logarithmic flow profile for a flow flux similar to tests 3.5-3.8 with the difference that the flow depth has been increased to 550mm. The behavior of the monopile structure follows a similar trend to the two previously presented results. This behavior is expected as the total flow flux is constant and the change in the adverse pressure gradient is not very great compared to the other cases. Observing the behaviour of the remaining non-uniform geometries it can be seen that the overall scour rate is further reduced compared to Figure 5-19. This can also be explained by the increase in the water depth. The flow profile in this case shows that there is a reduction of the velocity near the bed compared to the previous case (Tests: 3.5-3.8) which means that the local amplification of the pressure field near the bed will be smaller; thus the scour rate should also be smaller.

To further examine the effect water depth has on the scour process the 75° conical base structure was tested under similar velocities (i.e. $U_c/U_{cr} \sim 0.94$) at water depths of 350mm, 450mm and 550mm. The results reveal that the scour rate and equilibrium scour

depth reduce as the depth increases which is in line with the finding of tests 3.5-3.12. These findings show that there is an apparent link between scour rate, the flow profile and the shape of the structure which will be examined in chapter 6.

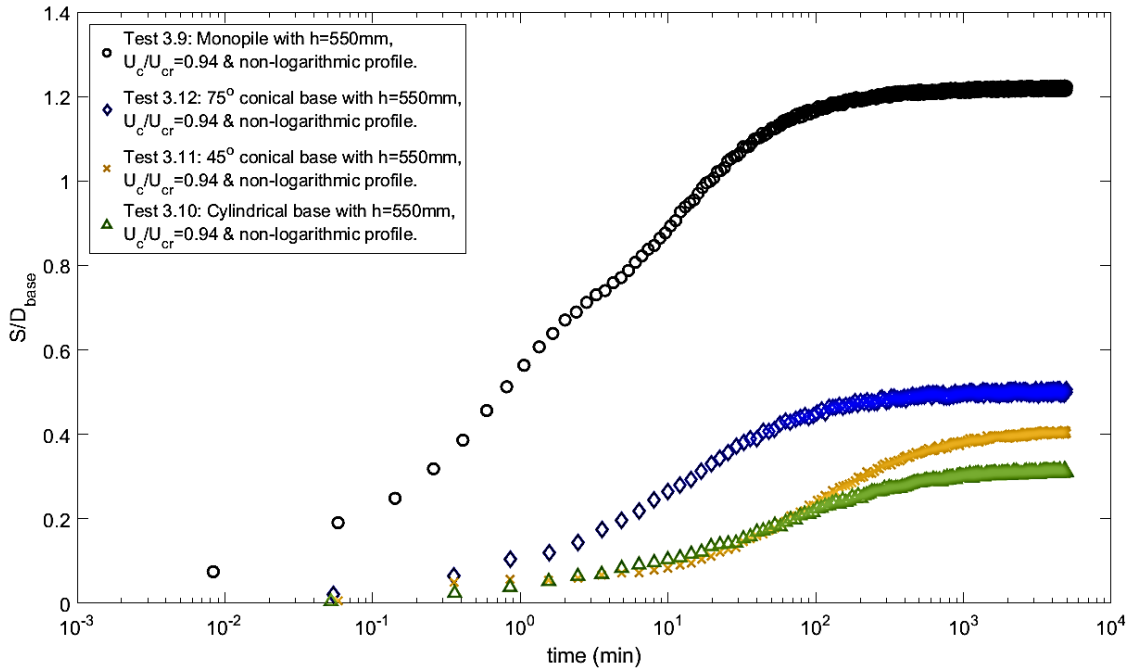


Figure 5-20: Temporal evolution of scour for non-logarithmic flow profile, $h=550\text{mm}$.

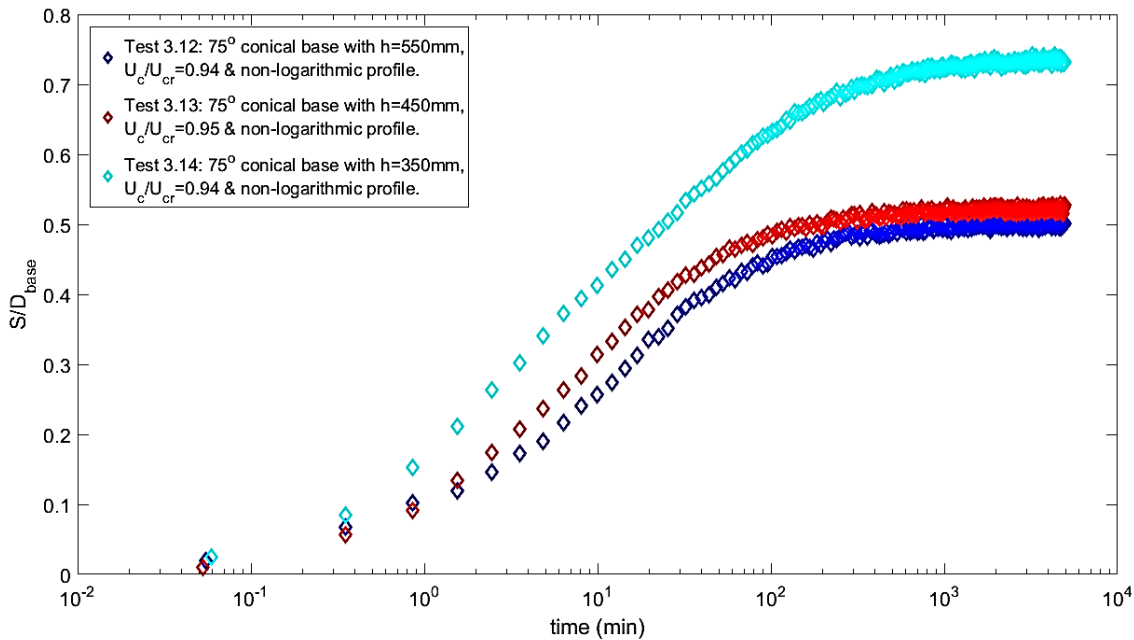


Figure 5-21: Temporal evolution of scour for the 75deg conical base structure with non-logarithmic flow profile, $h=350\text{mm}$, $h=450\text{mm}$ and $h=550\text{mm}$.

5.2.2.2 Equilibrium scour depths

This section will present the equilibrium scour depths for the large scale experiments. For these tests full profile measurements of the scour hole were taken using the echosounder. This made it possible to show contour maps of the equilibrium scour hole. Table 5-1 presents the equilibrium scour depth for each test which is taken as the deepest point of scour at the time at which the test was stopped.

Table 5-2: Equilibrium scour depth for large scale experiments.

Test No	S/D_{base}						
3.1	1.17	3.5	1.17	3.9	1.22	3.13	0.54
3.2	0.72	3.6	0.57	3.10	0.32	3.14	0.72
3.3	0.78	3.7	0.61	3.11	0.41		
3.4	0.84	3.8	0.71	3.12	0.51		

Figure 5-22 presents the contour maps of the equilibrium scour depth for Tests 3.1-3.4 where scour below the initial bed level is given as negative values. These show that the maximum scour occurs at an angle 45°-90° relative to flow direction. This coincides with numerous studies on scour (Hjorth, 1975 and Sumer et al., 1994) and with potential flow theory which suggests that the maximum amplification of the pressure gradient occurs at 45°. An interesting observation is that in the case of the monopile the scour hole becomes significantly shallower at the downstream side of the scour hole which is a common scour pattern in shallow water scour according to (Amini et al., 2011). In the case of the complex structures though, the scour hole tends to become shallower at an angle of 130° relative to the flow direction and deepens once again as we approach an angle of 180°. This effect may be explained by the non-uniform cross-sectional shape of the structure which effectively reduces the size of the horseshoe vortex. The reduced size of the horseshoe vortex makes the interaction of the contracted flow with the lee wake vortices stronger and thus the scour deeper at this location. Furthermore, it can be observed that the extent of the scour hole increases as the cross-sectional area of the

structure increases. The monopile induces the widest scour hole and the cylindrical base structure the narrowest.

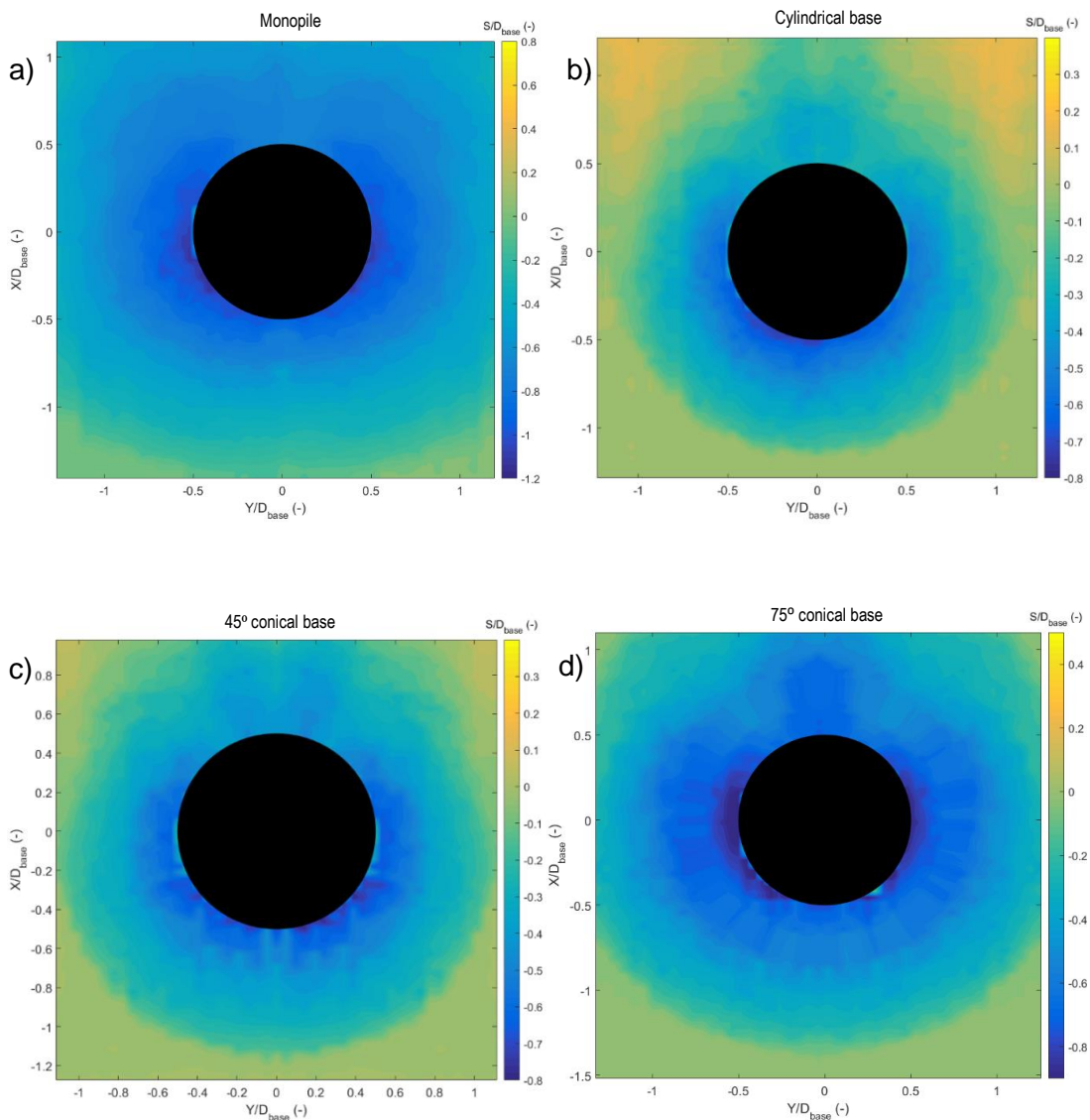


Figure 5-22: Equilibrium scour depth profiles for Tests 3-1-3.4 at $h=350\text{mm}$ and a logarithmic flow profile (flow from bottom): a) Monopile; b) Cylindrical base; c) 45° conical base structure; and d) 75° conical base structure.

Another interesting observation is the slope of the scour hole upstream and downstream of the structures (see Appendix B for figure). The upstream slope of the scour hole for all structures ranges between 38° and 40° which for the specific sediment falls within the expected values of the angle of repose for submerged sediments (Miedema, 2014) but is higher than the angle of repose of loose sand reported by Sumer and Fredsøe (2002). The steep slopes may also be explained by the presence of a strong horseshoe vortex in the scour hole which effectively helps the steep slope not to collapse. There is a

significant change in the behavior of the downstream slope of the scour hole with recorded slopes ranging between 9° and 15° which are significantly smaller than those reported in literature (Sumer and Fredsøe, 2002). There is no clear correlation between the downstream slope and the structure type.

The scour pattern for tests 3.5-3.8 are presented in Figure 5-23. The flow conditions are the same as in Figure 5-22 with the difference that for these tests the profile is non-logarithmic. Comparison between the two sets of figures (Figure 5-22 and Figure 5-23) shows that the scour patterns for each structure have qualitative similarities. The scour hole becomes shallower at the downstream end of the monopile, while for the complex structures there is a secondary depression behind the structure. Under the forcing of the non-logarithmic flow profile it can be observed that the point of deepest scour shifts further to the lee in the case of the monopile. This behaviour may be attributed:

- To the weaker horseshoe vortex due to the smaller flow velocities near the bed which reduces the amplification upstream of the pile.
- To the stronger vortex shedding induced by the higher velocity near the surface of the flow.

Further comparison between the two figures reveals that the maximum scour depth in the case of the non-logarithmic flow profile is significantly reduced for the complex structures. This agrees with the notion of reduced pressure gradients due to the change in the flow profile.

For this flow condition there is evidence that there is a link between the structure and the average slope upstream and downstream of the structure (also see Appendix B). Table 5-3 shows that as the size of the structure decreases both the upstream and downstream slopes of the scour hole become milder. This finding might be linked to the intensity of the horseshoe vortex which weakens as the structures decrease in size and thus is not able to maintain the steep slopes. This can also explain the evidence of avalanching upstream of the complex structure that can be seen in Appendix B.

Table 5-3: Upstream and downstream slopes of the scour slope for tests 3.5-3.8.

Test	Structure	φ_{up} ($^{\circ}$)	φ_{down} ($^{\circ}$)
3.5	Monopile	45	42
3.8	75 $^{\circ}$ conical base	40	24
3.7	45 $^{\circ}$ conical base	36	15
3.6	Cylindrical base	30	12

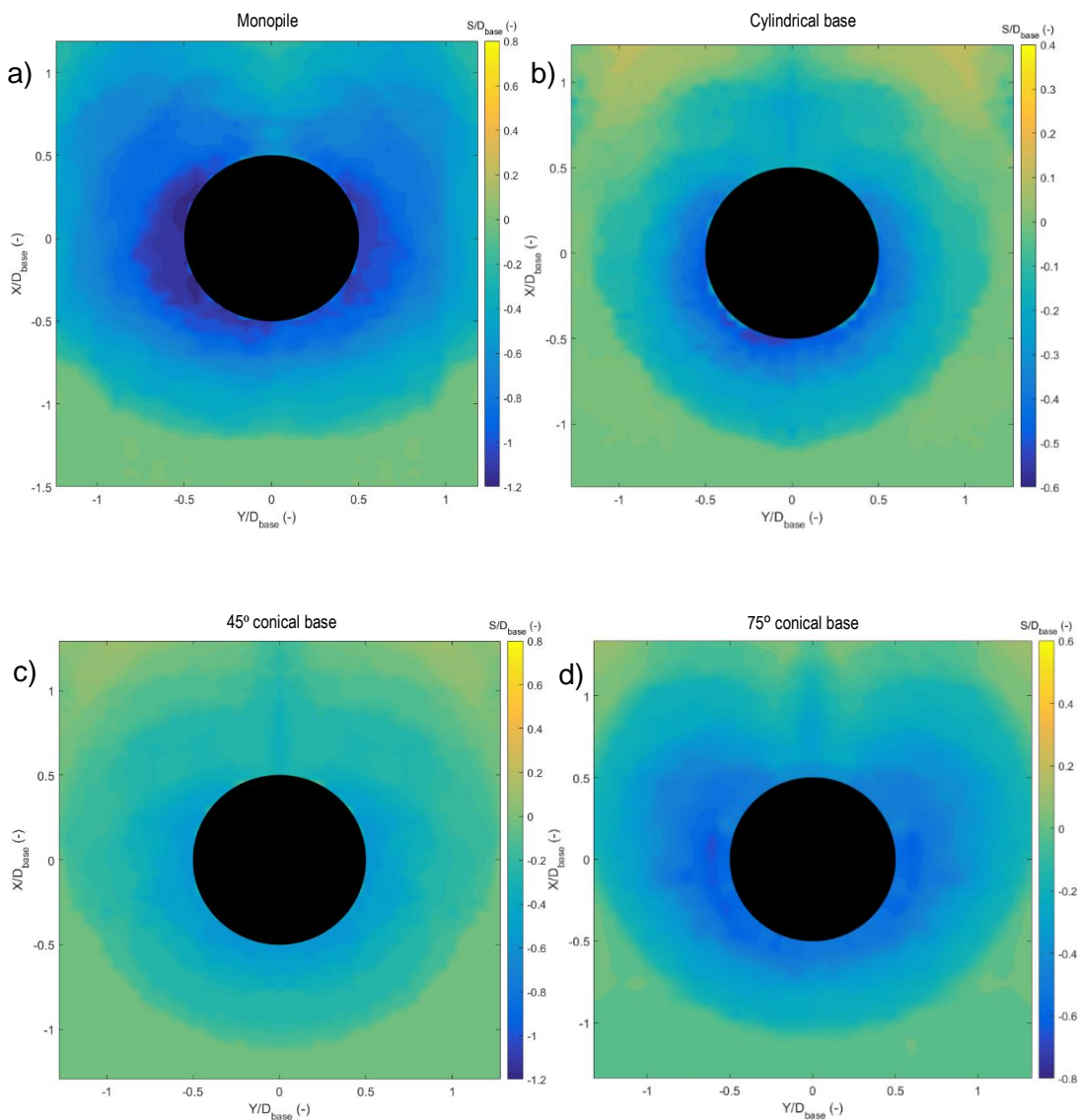


Figure 5-23: Equilibrium scour depth profiles for Tests 3-5-3.8 at $h=350\text{mm}$ and a non-logarithmic flow profile (flow from bottom to up): a) Monopile; b) Cylindrical base; c) 45 $^{\circ}$ conical base structure; and d) 75 $^{\circ}$ conical base structure.

The 3D scour profiles for tests 3.9-3.12 with a deeper flow depth are presented in Figure 5-24. The small lateral extent of the scour hole in front of the structures allowed the measurement of the deposition pattern behind them. It can be observed that although

the scour pattern is qualitatively similar to the other cases the width of the scour holes is significantly smaller. This behaviour may be linked to the non-logarithmic flow profile which has even lower near-bed velocity compared to the two previous cases. This can translate to a weaker horseshoe vortex and thus scour depths. An exception to this observation is the 45° conical base structure which has a very asymmetric scour pattern. This deviation to the scour pattern may be attributed to the lateral seiche which was observed during the specific test. The causes of this are not clear but a possible explanation might be the interaction between the water surface disturbance caused by the lee wake vortices and the sidewalls of the flume. The figures also reveal that there are secondary scour holes radiating away from the structure at an angle of 135° to 150° relative to the flow direction which are a consequence of the lee wake vortex shedding. These secondary scour holes become larger in diameter for structures with a larger cross-sectional area. This is because the diameter of the structure near the bed becomes increasingly larger thus generating larger vortices at the lee.

For these tests the upstream slope of the scour hole for the monopile and cylindrical base structure have an angle approximately 45° while for the 75° conical base a slope of 37° (see Appendix B). At the downstream end of the structure the slope of the scour hole becomes steeper as the structure becomes larger, with the cylindrical base structure having a slope of 0°, the 75° conical base structure 18° and the monopile a slope of 45°.

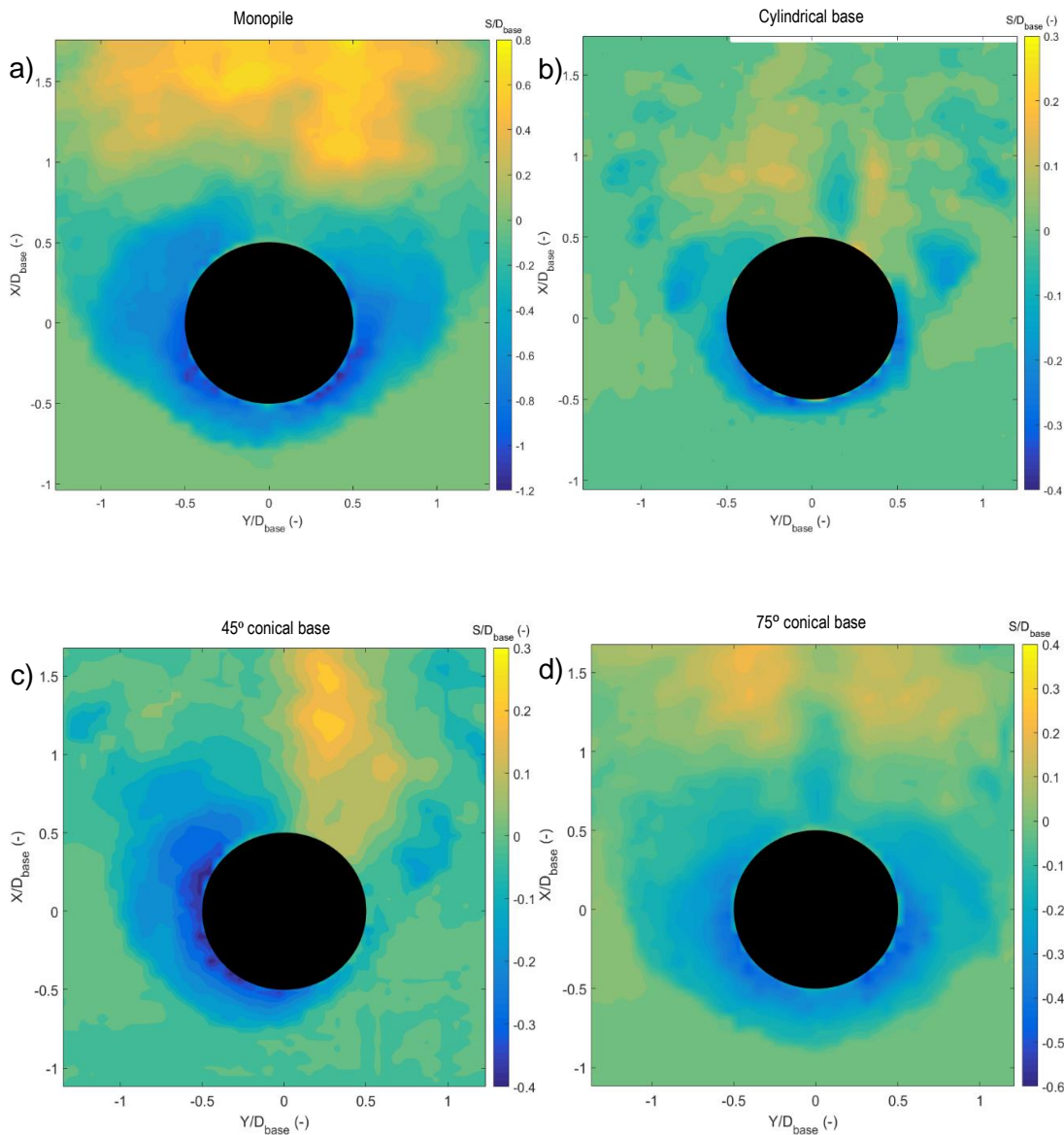


Figure 5-24: Equilibrium scour depth profiles for Tests 3-9-3.12 at $h=550\text{mm}$ and a non-logarithmic flow profile (flow from bottom to up): a) Monopile; b) Cylindrical base; c) 45° conical base structure; and d) 75° conical base structure.

Figure 5-25 presents the results for scour tests 3.12-3.14 which show the effect of changes to water depth on the equilibrium scour depth profile for the 75° conical base structure. It can be observed that as the water depth decreases both the lateral extent and maximum depth of the scour hole decreases. As stated earlier in this section this may be linked to the reduction of the pressure gradient around the structure. The qualitative characteristics of the scour hole remain the same between the three water depths depicted in the figure. For the water depth of 450mm two distinct depressions are formed in the lee of the scour hole while for the other two flow depths only one is present.

This difference may be linked to the deflection of the incoming flow by the slopes of the cone which is sensitive to the incoming flow characteristics which change with the depth. The location of maximum scour occurs between 45° and 90° relative to the flow direction which agrees with the majority of the observation so far and the potential flow theory as well. Finally, the upstream scour slope for the three cases fall between 37° - 42° while the downstream slopes are relatively less steep with values ranging from 18° to 20° (see appendix B).

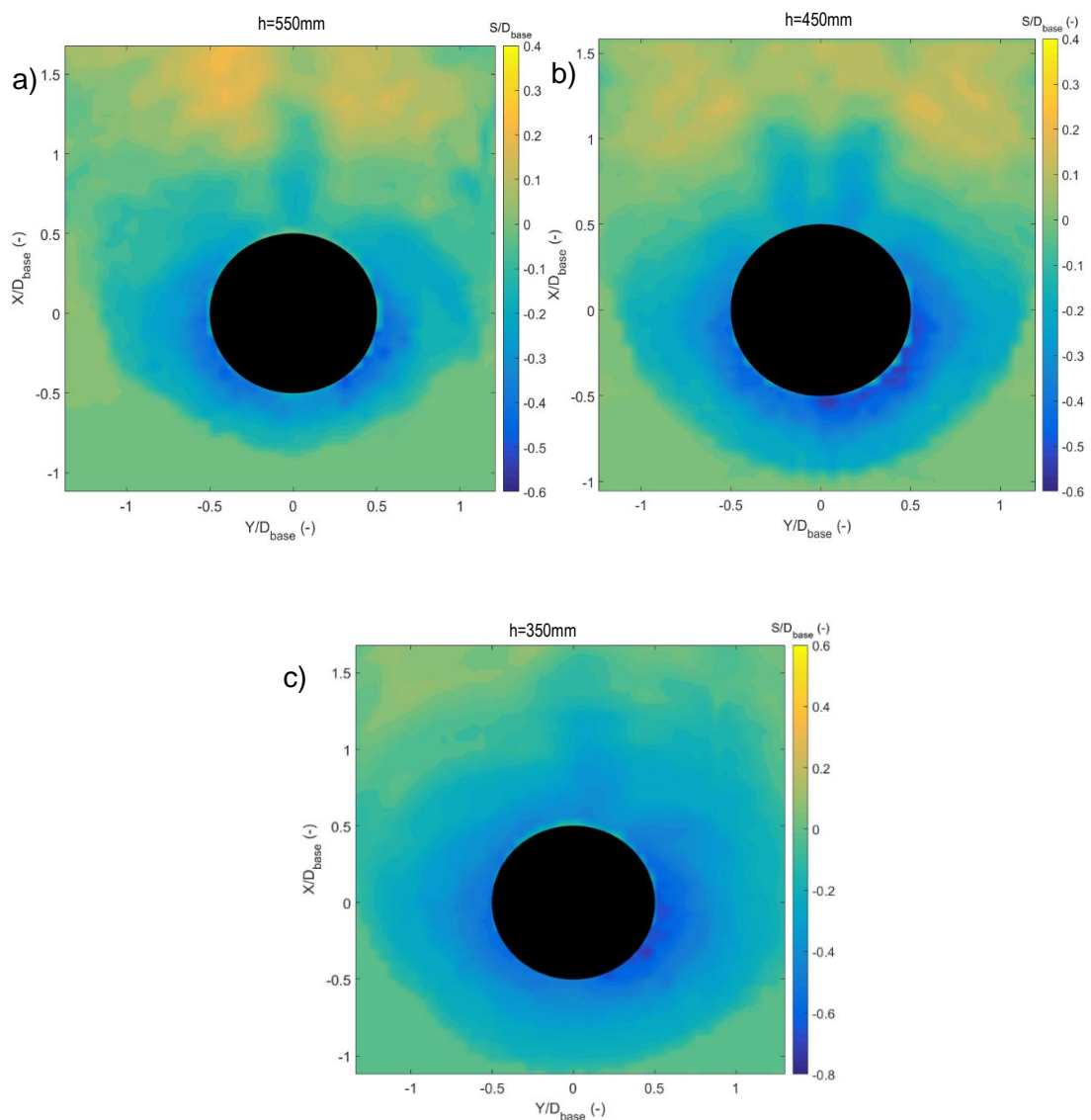


Figure 5-25: Equilibrium scour depth profiles 75° conical base structure at three different flow depths and a non-logarithmic flow profile (Tests 3-12-3.14): a) $h=550\text{mm}$; b) $h=450\text{mm}$; and c) $h=350\text{mm}$.

5.2.2.3 Repeatability of tests

For the purpose of examining the repeatability tests 3.14 and 3.8 were conducted under the same conditions. As for the small scale tests this allowed to estimate the error associated with the measurement of the scour depth and also allowed the examination of the repeatability of several qualitative characteristics of the scour hole profile. Given that the present tests have not been performed before it was not possible to use information from other authors to evaluate the repeatability of the tests. For this reason, tests 3.8 and 3.14 were designed with the same flow conditions.

Figure 5-26 presents the time development plots between tests 3.8 and 3.14. The figure shows that there is very good agreement between the two curves. The overall rate of scour in the two experiments is the same and there is a slight discrepancy between the two curves at the equilibrium phase. The maximum difference between the tests is $2\%S/D_{base}$ which is acceptable given the uncertainty associated with measuring the scour depth and slight differences with the sediment distribution.

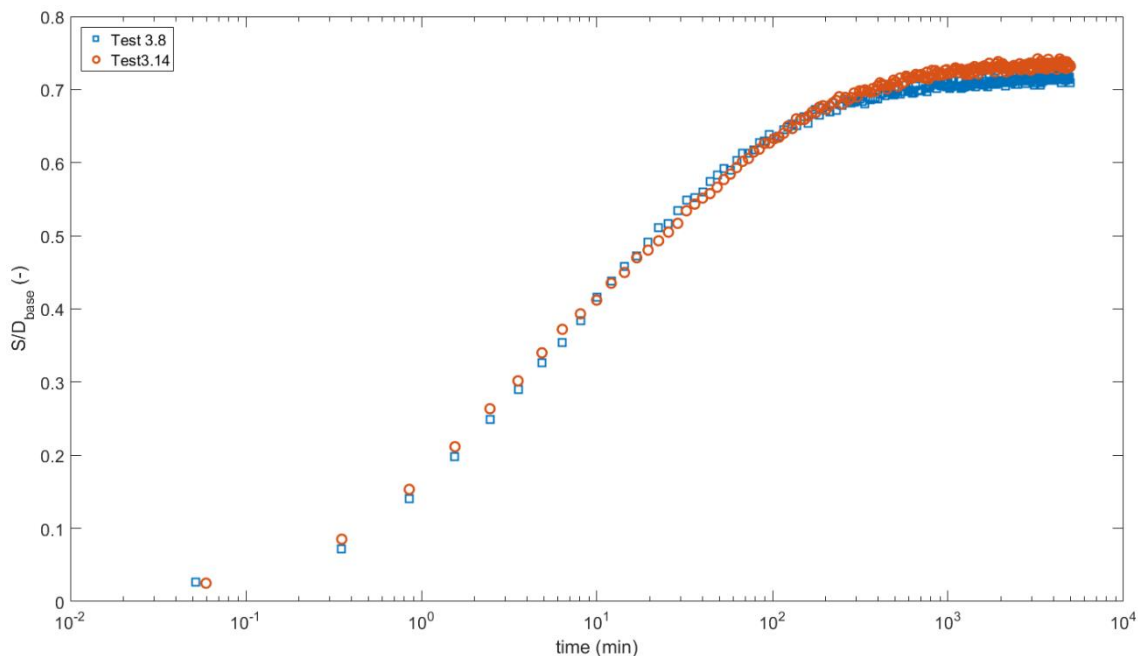


Figure 5-26: Comparison of time development of Test 3.8 and 3.14.

Figure 5-27 (a) and (b) depict the scour profiles for the two tests while (c) shows the difference between the two tests. In addition to the agreement of the maximum scour depth which was observed in the previous figure, Figure 5-27 shows that the dimensions of the scour hole are also in agreement. Qualitative comparison between the contour plots of the scour depth between the two tests also show that the small depression at the lee of the structure is present in both cases though the location of it is slightly skewed in the case of test 3.14. In addition, it can be observed that the location of maximum scour also occurs at $\pm 90^\circ$ relative to flow direction. Figure 5-27 (c) shows that the maximum difference throughout the entire scour hole is smaller than $0.2S/D_{base}$. There is a tendency the scour hole in test 3.8 being shallower in $0 < \frac{X}{D_{base}} < 1.5$ and deeper in $-1.5 < X/D_{base} < 0$. This apparent asymmetry is attributed to the non-uniform installation of the flow straighteners which may have caused a slight asymmetry in the flow.

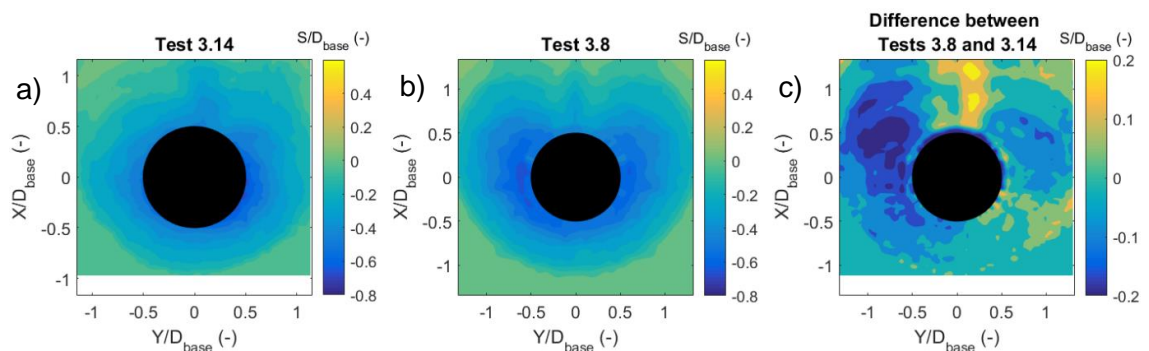


Figure 5-27: Comparison of scour contour maps between tests 3.14 and 3.8: a) Test 3.14; b) test 3.8; and c) the difference between 3.8 and 3.14.

5.3 Pressure and flow measurement

As discussed in the previous sections several aspects of the scour behaviour of the complex structures may be attributed to differences in the pressure gradient distribution around the structure. This section seeks to investigate:

- The effect the structure geometry has on the pressure distribution around the structure and the hydrodynamics.

- If potential flow theory is capable of estimating the pressure variations around the structure.

5.3.1 Test conditions

The experiments were conducted under the forcing of a unidirectional current with a logarithmic flow profile. Figure 5-28 shows the velocity profile for the present tests taken at the location of the pile before it was installed and the mean flow velocity was determined as 0.33m/s according to the trapezoidal rule described in Soulsby (1997). In the same figure the generic flow profile for the same mean flow velocity presented by Soulsby (1990) for tidal flows is also presented. The agreement of the method with the measured values show good agreement, thus confirming the present flow conditions are representative of tidal conditions.

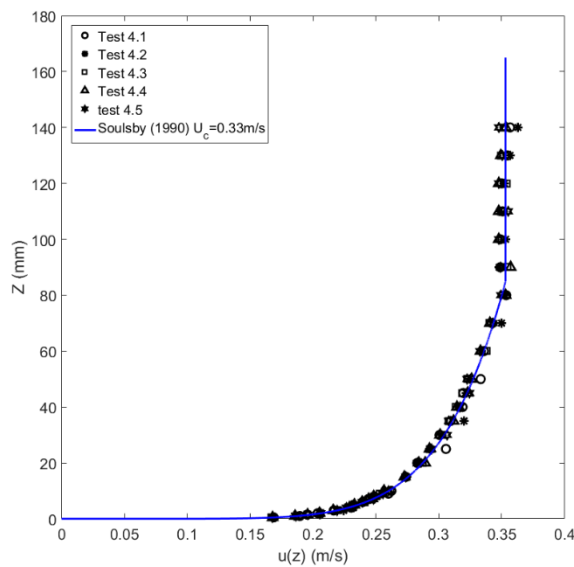


Figure 5-28: Flow profile for tests 4.1-4.5.

5.3.2 Pressure Measurements

As mentioned in section (4.5) two types of measurements were performed during this investigation. This section will present the results of the pressure measurements first and then the flow measurement will be shown to complement them

Measurements were conducted to measure the pressure field around the structure. To achieve this, specially 3D printed structures were constructed with tapping holes at

different heights along the face which led to internal tubes which were then connected to pressure sensors. This allowed the measurement of the pressure field around the periphery of the structure by simply rotating the structure.

Figure 5-29 to 3-37 present the resulting pressure measurements for all the structures. In these figures the horizontal axis represents the angle of the tapping holes on the face of the structure have relative to the flow direction. The vertical axis presents the pressure coefficient which is the non-dimensional form of the pressure measured and is defined as:

$$C_p = \frac{p - p_\infty}{\frac{1}{2}\rho u(z)^2} \quad 5-1$$

p is the pressure at the height of the tapping hole z ; p_∞ the freestream pressure at a height z and; and $u(z)$ the freestream velocity at a height z . These values were all measured during the tests.

Each figure presents the pressure distribution around the structure at different heights from the bed and the corresponding potential flow solution applied on the surface of the cylinder (which is solely a function of the of the angle relative to flow). Measurements of the pressure were conducted up to $\phi = 140^\circ$ as the quality of the measurements deteriorated after that point. The legend also presents the pile Reynolds number taken at the height of the tap which is calculated as a function of the undisturbed flow velocity and structure diameter at that height:

$$Re_D(z) = \frac{u(z)D(z)}{\nu} \quad 5-2$$

Figure 5-29 shows the result of the measurement for the cylindrical base structure. It can be seen that potential flow captures the overall trend of the pressure measurements. There is a tendency to over predict the pressure for the measurements with $Re_D(z) < 5.6e + 03$ while it underpredicts the value for the point closest to the bed which has a larger $Re_D(z)$ due to the increased size of the structure diameter at that point. In general,

potential theory shows a good agreement with the measurement for $\phi \lesssim 60^\circ$. After this point the difference between predicted and measured becomes significant.

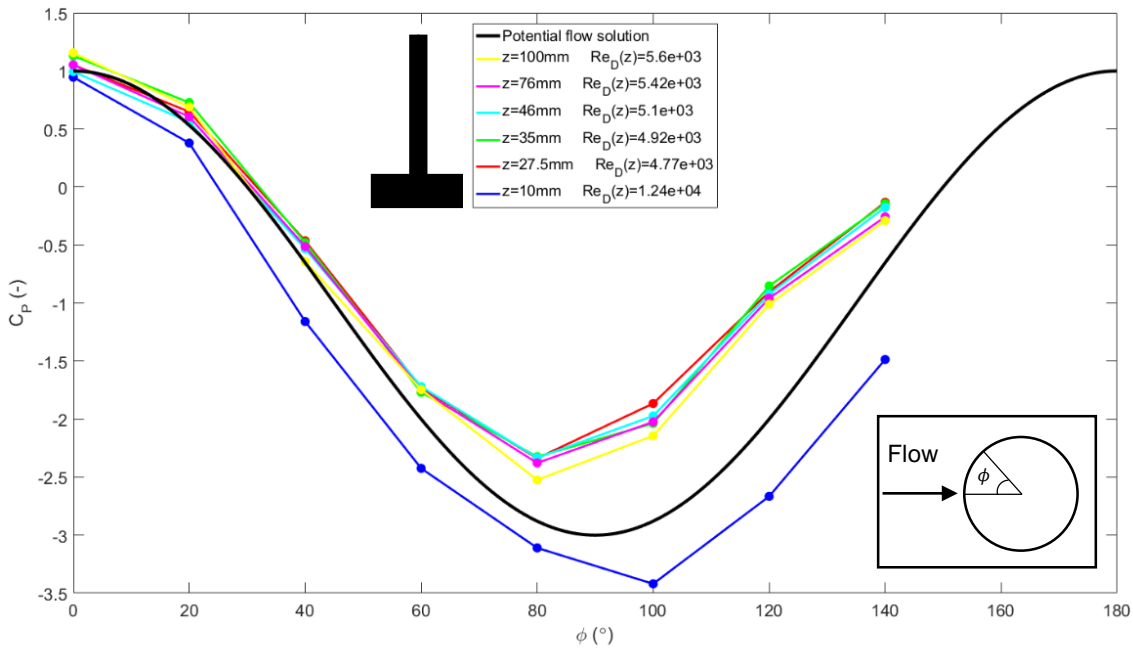


Figure 5-29: Pressure variation for the cylindrical base structure.

Figure 5-30, 3-35 and 3-36 show the results for the 45° , 60° and 75° conical base structures. Potential theory seems to predict well the pressures at the different heights for the same range of ϕ as for the cylindrical base structure. From the three diagrams it is evident that the curves describing the pressure variation as a function of ϕ do not depend on the height z but rather are dependent on $Re_D(z)$. This is because $Re_D(z)$ does not increase monotonically as the height z increases which is what we would expect for a monopile in a logarithmic flow profile where $u(z)$ increases as we move away from the bed. The behaviour of the pressure coefficient curve rather varies due to the combined change of the structure diameter and the change in the flow velocity at the specific depth and thus the $Re_D(z)$ can capture this effect. This translates in higher $Re_D(z)$ yielding larger C_p . In addition, it can be seen that the point of maximum negative pressure (which indicates the separation point) shifts further towards the lee of the structure as the pile Reynolds number increases. This translates to a delay of the flow

separation along the surface of the pile which agrees with the findings of Achenbach (1968).

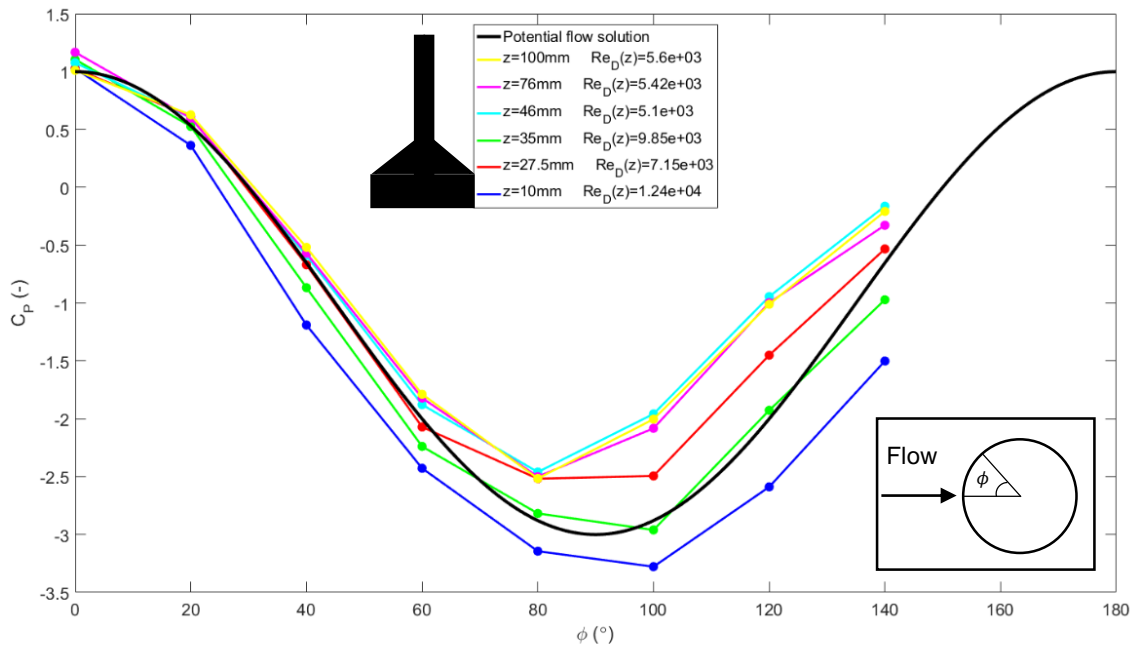


Figure 5-30: Pressure variation for the 45° conical base structure.

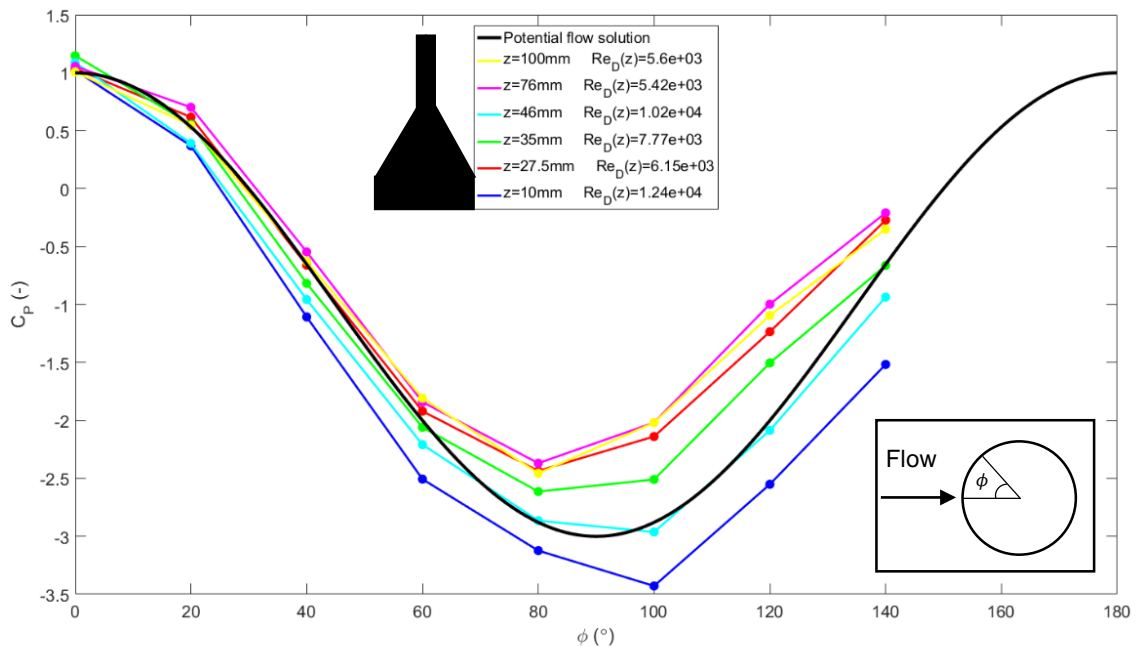


Figure 5-31: Pressure variation for the 60° conical base structure.

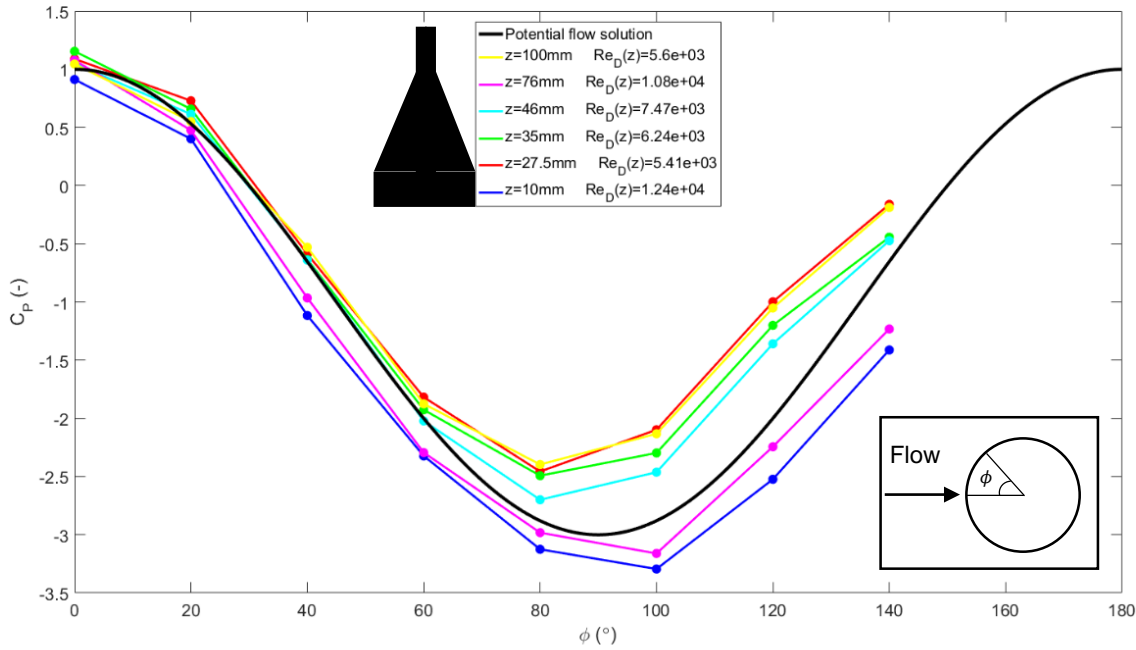


Figure 5-32: Pressure variation for the 75° conical base structure.

Finally, Figure 5-33 shows the pressure measurement for the monopile structure. There is a small tendency to under-predict the pressure coefficient throughout the entire range of ϕ but the experimental data seem to follow reasonably the potential flow solution up to $\phi = 90^\circ$. This over-prediction may be attributed to the larger Reynolds numbers expected throughout the entire height of the structure due to the larger diameter. As with the other cases the value of the pressure coefficients is monotonically dependant on the Reynolds number.

The present tests show that the pressure field around the geometries tested can be reasonably approximated using potential flow theory up to an angle ϕ of 60°-70°. The maximum negative pressure coefficient which also denotes the point of separation of the flow ranges between the 80°-100° which varies as a function of $Re_D(z)$. Larger values of the pile Reynolds number induce a delay in the separation. This can translate into variations in the vortex shedding frequency and thus a change in the behaviour of the longitudinal counter-rotating vortices which are one of the mechanisms inducing scour.

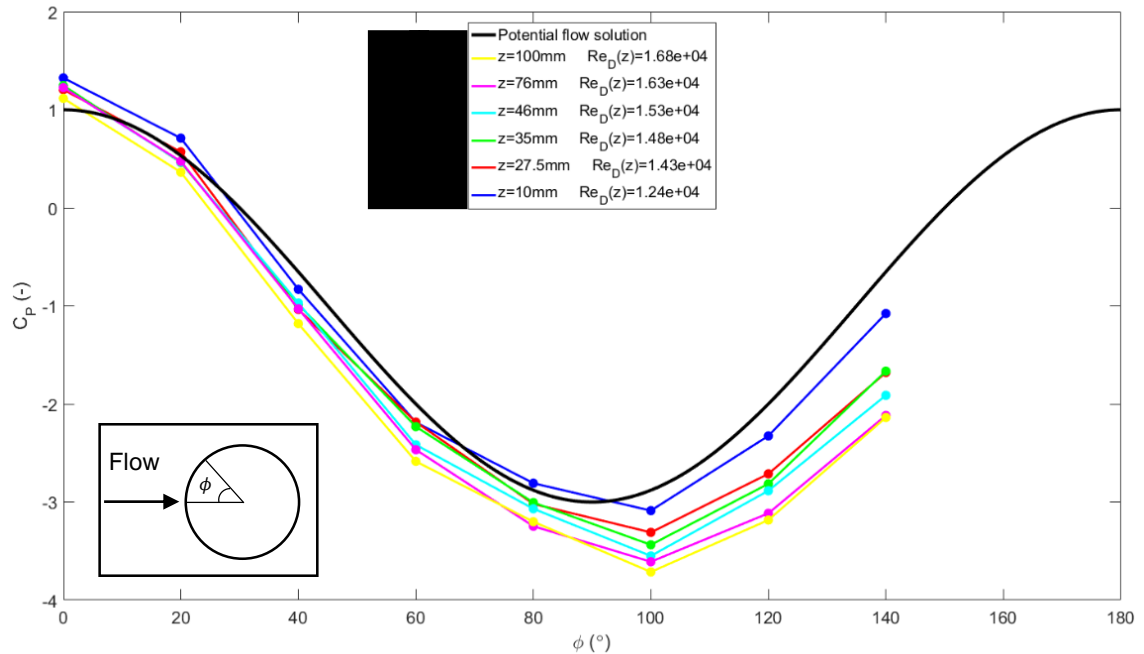


Figure 5-33: Pressure variation for the monopile structure.

5.3.3 Flow measurements

This section presents the flow measurements which were conducted using an LDV around a selection of the geometries used in the pressure measurements. The purpose of these tests is to examine the effect the geometry has on the local hydrodynamics in order to further understand the local flow phenomena that contribute towards the scour process. The following section will therefore provide a description of them for each structure.

5.3.3.1 Monopile

Figure 5-34 shows a contour plot of the vertical velocity component along with the velocity vectors. On the upstream side of the monopile the presence of a horseshoe vortex can be seen at the base of the structure with a strong clockwise circulation pattern at the base of the monopile. The position and size of the horseshoe vortex coincides with the observations of Roulund et al., 2005 who also found the width of the horseshoe vortex to be $0.5X/D$. In addition, a strong downflow at the upstream face of the structure can also be observed for $Z/h < 0.45$. At the downstream side of the pile a counter clockwise circulation pattern can be seen which starts off with downward flow near the structure

and then turns into a strong upwards flow further downstream. This upward flow ceases to exist of existence at $X/D \approx 7$. This flow pattern has also been observed by Baykal et al. (2015) and Petersen et al. (2015) who attribute it to the longitudinal counter-rotating vortices (LCRV) which are created partly by the horseshoe vortex and the variation of the shedding frequency over the height of the structure. This difference in the vortex shedding along the water column creates an upwards pressure gradient downstream of the structure which drives an upward flow.

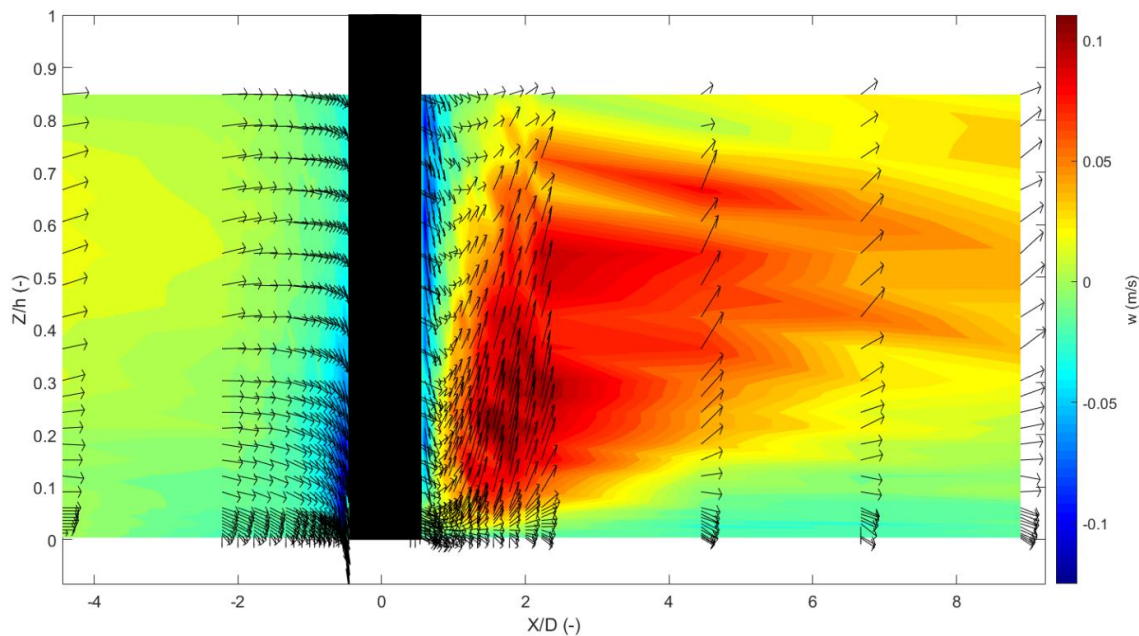


Figure 5-34: Vertical velocity component (w) distribution and $u-w$ velocity vectors along the centreline of the monopile.

To assist in the examination of the hydrodynamics around the monopile the flow around the centre of symmetry of the structure was measured at eight different heights. Figure 5-35 presents the streamwise component of the velocity while Figure 5-36 the vertical component.

The low pressure zone in front of the structure can be distinguished in Figure 5-35 where u approaches zero which agrees well with the pressure measurements presented in the previous section and also with potential flow. Moving further downstream it can be seen

that the flow accelerates along the edge of the structure and then separates at an angle approximately 90° - 100° relative to flow direction at all depths. The contour plots show that the separation point gets delayed nearer to the surface of the flow which agrees also with the pressure measurements.

Figure 5-36 shows the distribution of the vertical velocities at different heights along the structure. In the profile closest to the bed ($h/Z=0.061$) the horseshoe vortex is clearly visible, with a zone of upwards velocities followed by a zone of negative velocities closer to the pile which surround the structure up to $X/D_{base}=0.75$. The pattern of the horseshoe vortex can be observed up to height $Z/h=0.121$ even though the intensity of it weakens with an increase in Z . Directly downstream of the structure the LCRV can be observed, with strong positive (upward) velocity components which grow in strength up to height $Z/h=0.273$ after which they start reducing in intensity due to their circulating nature which is forced by the water surface boundary.

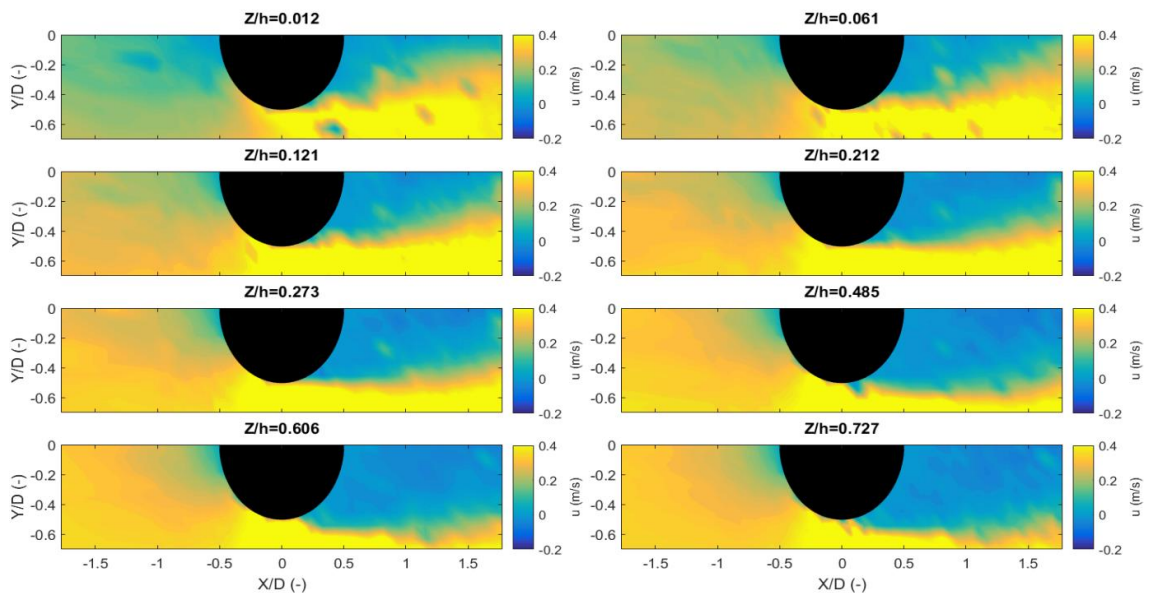


Figure 5-35: Contours of streamwise velocity component (u) around the monopile at different heights.

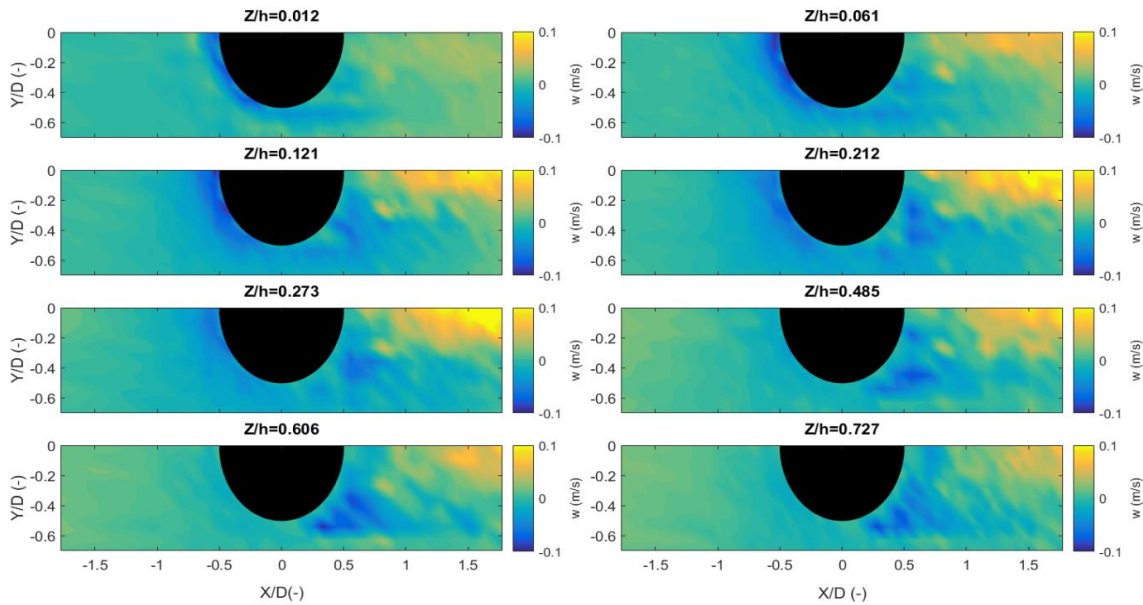


Figure 5-36: Contours of vertical velocity component (w) around the monopile at different heights.

5.3.3.2 75° conical base structure

The vector field of the u and w flow components along with the contour plot of the vertical flow component along the centreline of the 75° conical base structure is shown in Figure 5-37. The flow measurements reveal that the hydrodynamics around this geometry are significantly different compared to the monopile. At the upstream side of the structure the flow is forced to separate into an upward and downward flow at the height where the cylindrical base and the cone join. The downward component interacts with the bed and forms the horseshoe vortex while the upward flow runs along the face of the conical component up until the point where the cone meets with the top shaft. Moving downstream of the structure a zone of strong upward flow adjacent to the foundation is observed which has a width equal to the diameter of the base of the structure. This behaviour might be attributed to flow deflected of the sides of the cone which moves into the low pressure zone induced by the vortex shedding of the smaller cylindrical shaft on top which provides a route of least resistance. Furthermore, flow field shows no signs of the existence of LCRV further downstream of the structure. This is due to the interaction of the deflected flow with lee wake vortices which interrupts the upward pressure gradient induced by the variation of the vortex shedding frequency over the height of the structure.

Overall it can be seen that the hydrodynamics along the centreline of the structure differ significantly with that of a monopile.

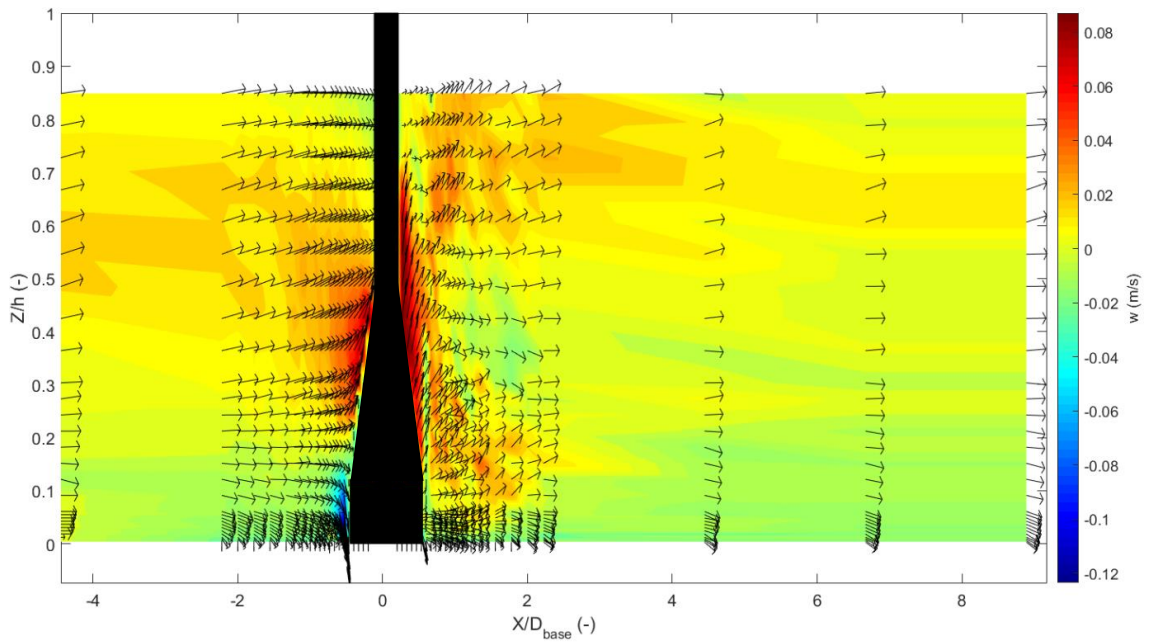


Figure 5-37: Vertical velocity component (w) distribution and u - w velocity vectors along the centreline of the 75° conical base structure.

Figure 5-38 shows the contours of the streamwise component around the structure. A strong deceleration of the flow can be observed upstream of the structure. This effect becomes smaller further away from the bed and is attributed to the reduction of the friction felt by the flow near due to the bed. The zone of low pressure (i.e. low velocities) at the upstream face of the structure is still present and the separation of the flow occurs at an angle $90^\circ \pm 10^\circ$ relative to the flow directions findings which agrees with the pressure measurements.

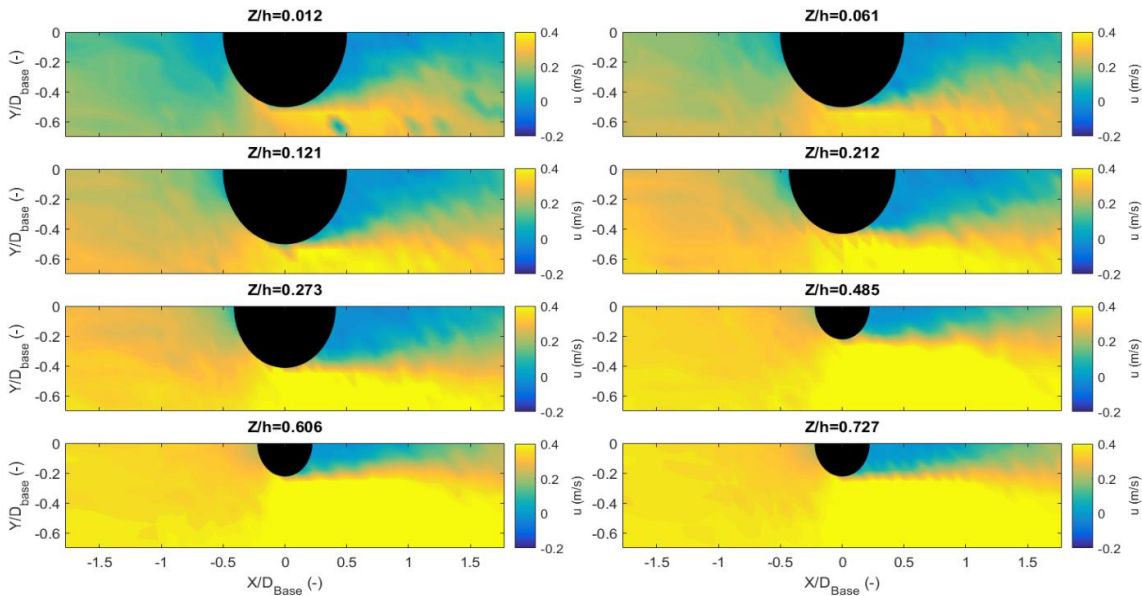


Figure 5-38: Contours of streamwise velocity component (u) around the 75° conical base structure. at different heights.

Figure 5-39 shows the vertical component (w) of the flow velocity around the structure.

As for the monopile the presence of the horseshoe vortex can be observed for $Z/h \leq 0.121$.

For $Z/h=0.061$ the vortex pattern which raps around the base of the structure can be clearly seen with a zone of positive velocities followed by a band of negative velocities.

Higher up along the leading face of the structure upward flows are observed which are attributed to the flow separation induced by the junction of the cone with the base. These decrease in intensity as z approaches water surface. On the downstream end of the structure a zone of upward flow is present adjacent to the structure. The flow starts to gain strength above the cylindrical base and reaches its peak at the junction between the conical component and the top shaft. The presence of this flow pattern in the lee of the structure disrupts the differential vortex shedding pattern as described in Baykal et al. (2015) and thus the formation of the LCRV system which is present in the case of the monopile

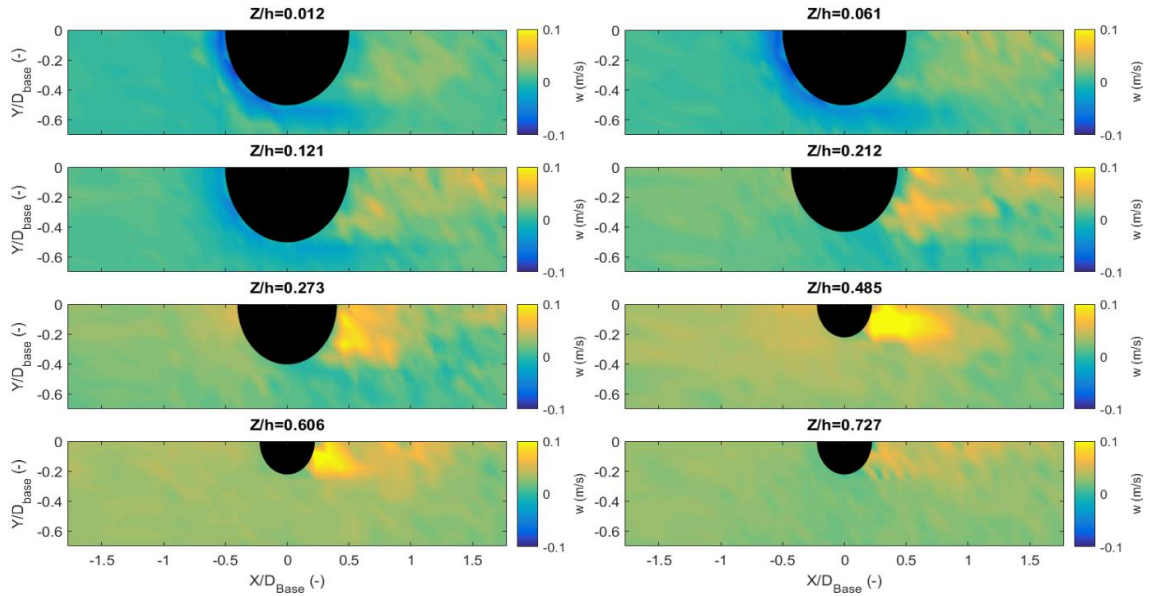


Figure 5-39: Contours of vertical velocity component (w) around the 75° conical base structure. at different heights.

5.3.3.3 60° conical base structure

Figure 5-40 presents the velocity field and the contour map of the w for the 60° conical base structure. It can be observed that the flow field resembles that of the 75° conical structure.

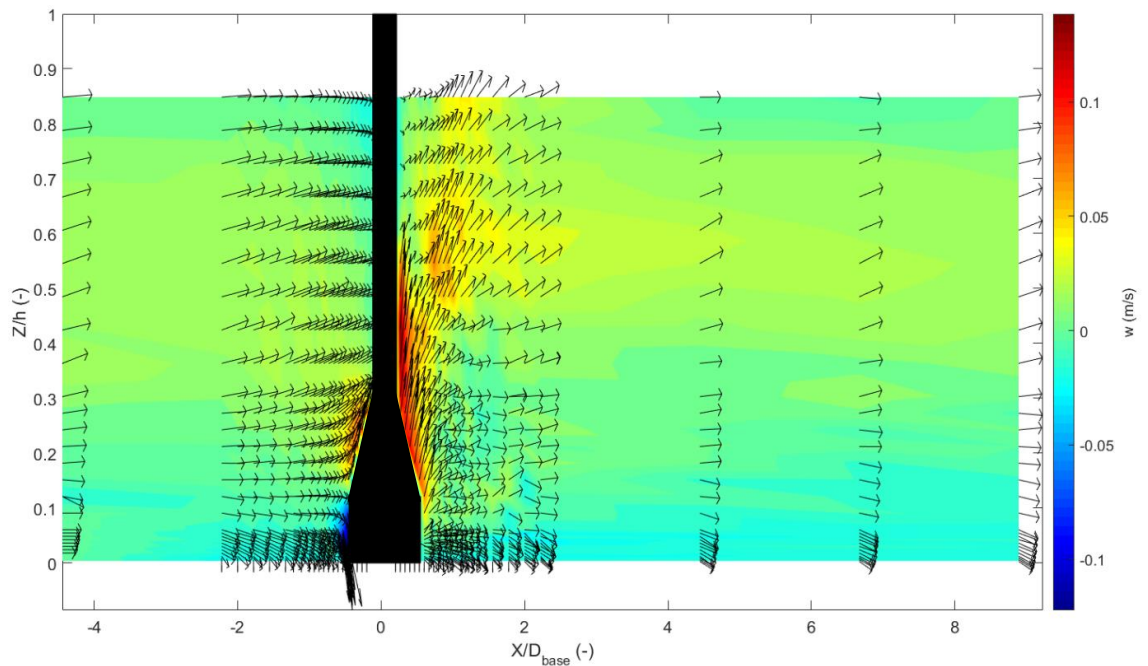


Figure 5-40: Vertical velocity component (w) distribution and $u-w$ velocity vectors along the centreline of the 60° conical base structure.

5.3.3.4 Cylindrical base

The hydrodynamics along the centreline of the cylindrical base structure show a resemblance to both the conical base structures and the monopile as Figure 5-41 shows. On the upstream side of the structure the horseshoe vortex can be distinguished at the base of the structure with a second upward flow present at the junction between the two cylinders which is a characteristic also observed at the conical based structures. There is further a second horseshoe vortex at the base of the top shaft which is smaller in size and strength compared with the one present at the base of the structure. At the downstream side of the structure the top shaft induces a LCRV system which starts at the top of the base and looks similar to that of the monopile but is smaller in area. The upwards pressure gradient creates a low pressure zone just behind the base of the structure which forms a circulation cell. This flow pattern can explain the scour pattern in Figure 5-11 which does not extend fully around the structure.

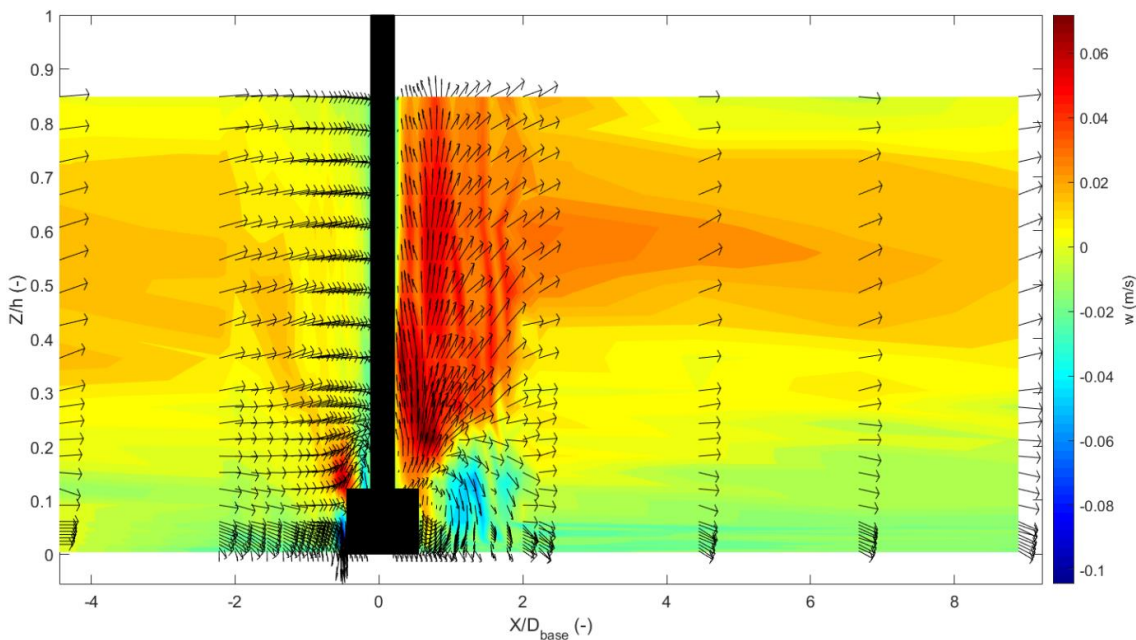


Figure 5-41: Vertical velocity component (w) distribution and u - w velocity vectors along the centreline of the cylindrical base structure.

As for the other structure the presence of the stagnation zone in front of the structure can be observed in Figure 5-42. The flow separation occurs within the same range of ϕ

as the other structures. For $Z/h=0.012-0.121$ the width of the recirculation zone can be seen immediately downstream of the structure with negative velocities present for $Y/D_{base} < 0.3$.

As for the other structures the presence of the horseshoe vortex near the bed can be seen through the bands of positive and negative velocities surrounding the leading edge of the structure in Figure 5-43. The horseshoe vortex in this case is weaker and smaller than for the monopile and 75° conical base structures which explains the smaller scour depths associated with this type of structure. The location of the flow separation at the junction between the pile cap and the shaft can be observed at $Z/h=0.121$ where a strong upward flow is present. This also explains why the horseshoe vortex is smaller compared to the other cases. At the lee of the structure the cross-flow width of the LCRV (indicated by the negative velocities) seems to be proportional to the diameter of the top shaft.

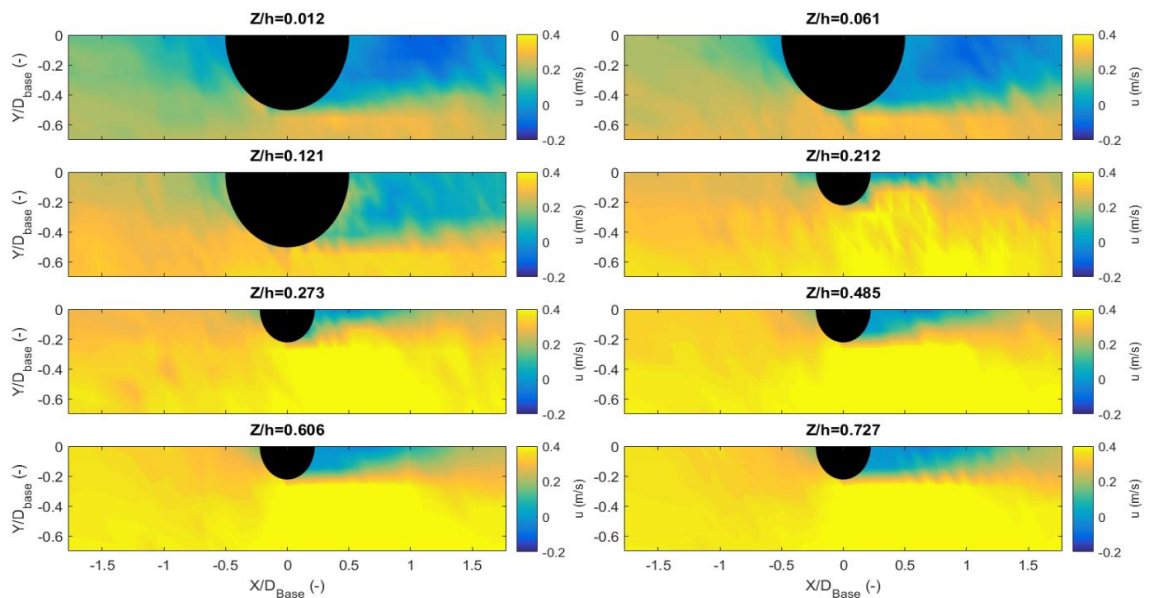


Figure 5-42: Contours of streamwise velocity component (u) around the cylindrical base structure at different heights.

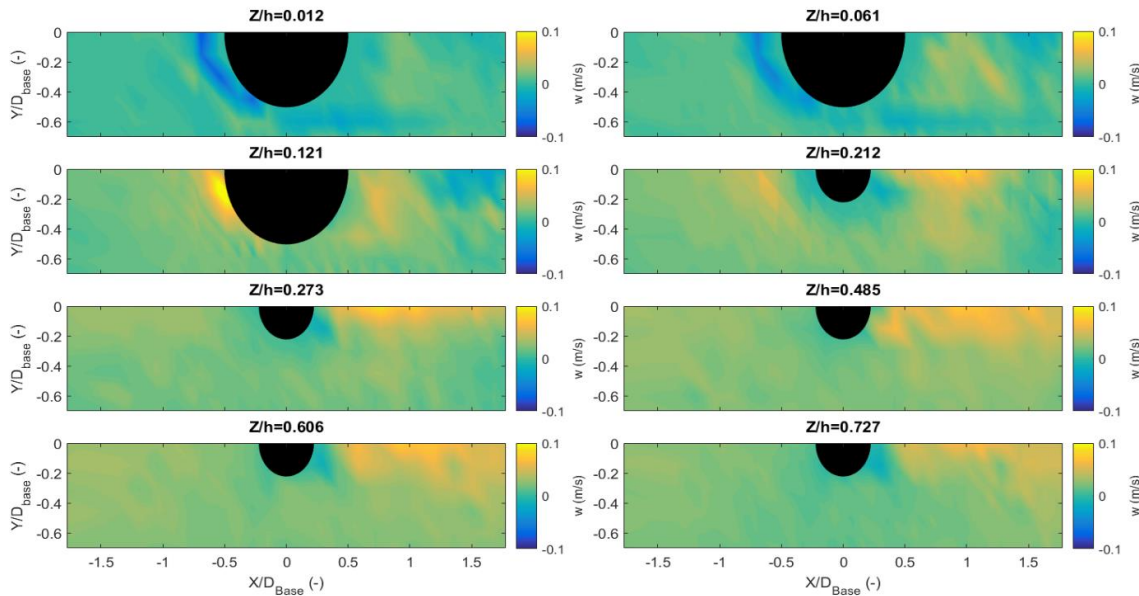


Figure 5-43: Contours of vertical velocity component (w) around the cylindrical base structure at different heights.

5.4 Summary of results

For the small scale tests the scour rate starts to increase once the scour depth around the complex structures reaches a value of $S/D_{base} = 0.2$. This suggests that this is the depth at which the horseshoe vortex starts to gain strength due to the local increase in the water depth. The tests reveal that coarser sediments slow down the scour process as it approaches the equilibrium phase. This can be attributed to the fact that the coarser grains in the sediment mixture are too heavy to be displaced out of the developed scour hole. In the case of the cylindrical base structure the clockwise circulation cell which is generated at the lee of the structure brings sediment from further downstream closer to the structure. This process can therefore explain why the scour hole does not extend fully around the structure for the small scale tests and why the scour at the lee is significantly smaller than the other structures for the large scale tests. Finally, it was shown that the equivalent diameter is not an appropriate variable for non-dimensionalising the scour depth (S).

The large scale experiments showed the scour pattern around a structure is linked to the geometry of the structure, with complex structures inducing different scour patterns from

the monopile. It was found that the structural scale has a significant effect on the equilibrium scour depth, with the larger scale experiments yielding scour depths which are up to 40% smaller than the smaller scale experiments. Given that the non-dimensional flow conditions between the large and small scale tests did not vary significantly it can therefore be concluded that the structural scale has a significant effect on the equilibrium scour depth. The time to equilibrium scour depth increased by a factor of 4 for the larger scale tests which is in accordance with the time development prediction method given by Equations (2-49) and (2-50). Even though there was a correlation between the upstream slope and the cross-sectional area of the structure for tests 3.4-3.8, there is no clear evidence that the upstream slope of the scour hole is dependent on the geometry or the incoming flow conditions for the rest of the tests. In general, the slopes in all tests ranged between 30° and 45° which correspond to the upper limit of the angle of repose for submerged sands (Miedema, 2014). The downstream slope varies from 0° to 45° and seems to depend on both the structure geometry and the hydrodynamics.

The flow measurements around the structures show that the monopile has a different hydrodynamic behaviour compared to the conical base structures, while the cylindrical base structure has similarities with both of the aforementioned structures. In the case of the monopile a distinct area of large upwards flows is found in the lee which is attributed to the LCRV. This process is interrupted by the deflected flow in the case of the conical base structures. In addition, the junction between the lower cylindrical base and the cone forces the flow to separate at that point. This creates an upward flow at the upstream face of the structure which is parallel to the side slope of the cone and a downflow which feeds into the horseshoe vortex. In the case of the cylindrical base structure two horseshoe vortex systems were found, one at the base of the structure and a second on top of the cap which is generated by the downflow from the shaft. The top of the pile cap also induces a separation in a similar manner to the conical base structure. Furthermore,

in the lee a small LCRV system is generated due the presence of the top shaft, while closer to the bed a clockwise recirculation cell is generated adjacent to the structure.

The results from the scour experiments reveal that the structural geometry has a significant effect on the scour development and the equilibrium scour depth. Structures with larger cross-sectional areas induce more rapid and deeper scour while smaller ones slower and more shallow scour holes. This behaviour can be linked to the effect the geometry has on the local change in the pressure gradient on the surrounding bed. This is because different parts of the flow interact with components of the structure that have different diameters. Results from the tests also suggest that changes of the incoming flow profiles result in changes in the scour depths. This can also be explained with the same line of logic. This statement is verified by the results of the pressure measurements which show that the pressure coefficient is dependent on $Re_D(z)$. This suggests that the pressure gradient is an important physical quantity that can explain the effect the incoming flow conditions and the geometry of a structure have on the scour process. The results from the pressure measurements show good agreement with potential flow theory. Thus this theory may be used to estimate the pressure gradient around the structure to quantify and link pressure gradient with the scour depth.

6 Prediction of equilibrium scour depth around cylindrical structures

6.1 Introduction

This chapter presents a method for predicting the equilibrium scour depth around uniform and non-uniform cylindrical structures. The method was derived using newly generated physical model results and a wide range of equilibrium scour depth data from previously published studies. The method is based on a functional relationship between the equilibrium scour depth and non-dimensional quantities that arise from a similitude analysis. These variables include the non-dimensional flow depth, sediment mobility ratio, pile Reynolds number, Froude number and Euler number. Here the Euler number is defined using the depth-averaged pressure gradient, which is a physical quantity that has never been used in the past to describe the scour process.

The structure of this chapter is as follows. Firstly, the similitude of the non-dimensional quantities that describe the scour processes are presented along with the formulation of the pressure gradient. Then, the details of the equilibrium scour database and the physical modelling tests are presented. This chapter then presents the derivation of the scour prediction formula based on the Buckingham π theorem. The results and the importance of each of the non-dimensional parameters on the equilibrium scour are then discussed.

6.2 Similitude of scour at complex geometries

The flow-structure-bed interaction around both complex and uniform cylinders can be described in terms of non-dimensionalised parameters. For a steady-state flow with an isotropic, homogeneous Newtonian fluid over a flat bed comprised of cohesionless sediment the most important variables that describe the interaction are:

$$S = f(\rho, \mu, \Delta p, D, h, g, U, U_c) \quad (6-1)$$

Here ρ is the fluid density; μ the dynamic viscosity of the fluid; Δp the change in the local pressure in the streamwise direction induced by the structure; D is the diameter of the structure in the case of a monopile, and the diameter of the base in the case of a complex structure as suggested by Yeow and Cheng (2003); h is the flow depth; g the gravitational acceleration; S is the equilibrium scour depth; U_c the depth-averaged flow velocity and U_{cr} is the critical depth-averaged velocity for bed sediment movement, which can be calculated using the Soulsby (1997) method (Equations 2-34, 2-35 and 2-38):

Further, d_{50} is the median sediment diameter, s is the ratio of sediment grain density in water, and ν kinematic viscosity of water.

By adopting a polar coordinate system, Δp in equation (6-1) can then be represented in terms of the pressure gradient by taking the derivative in the angular direction (φ) (see Figure 6-1 for definition sketch); this can be calculated using potential flow theory. This yields:

$$S = f\left(\rho, \mu, \frac{dp}{d\varphi}, D, h, g, U_c, U_{cr}\right) \quad (6-2)$$

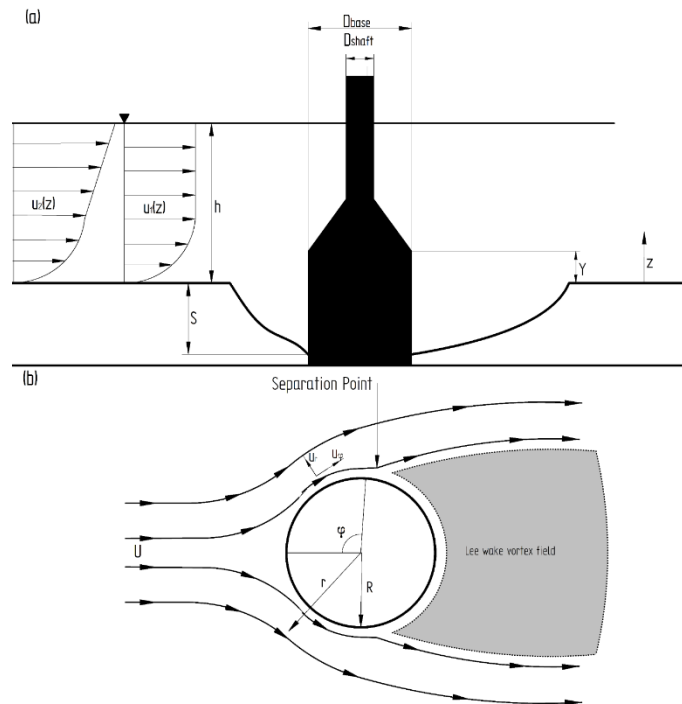


Figure 6-1: Definition sketch of main parameters: (a) side view; (b) top view.

By applying the Buckingham π theorem with normalising variables ρ, D and U the following dependence is obtained for the non-dimensional scour depth S/D :

$$\frac{S}{D} = f \left(\frac{dp}{d\phi}, \frac{U_c}{U_c^2 \rho}, \frac{U_c}{\sqrt{gh}}, \frac{U_c}{U_{cr}}, \frac{UD\rho}{\mu}, \frac{h}{D} \right) \quad (6-3)$$

This expression is equivalent to:

$$\frac{S}{D} = f \left(Eu, Fr, \frac{U_c}{U_{cr}}, Re_D, \frac{h}{D} \right) \quad (6-4)$$

This expression suggests that the pile Reynolds number ($Re_D = UD/\nu$) is the form of Re that best characterises the effect on the scour process. Indeed this is verified when considering that the flow conditions in most experimental and prototype conditions are fully developed, thus making viscous effects negligible for a channel $Re = (U_c h)/\nu > 10^4$ (Hughes, 1993). In addition, the critical grain Reynolds number is also considered implicitly in Equation (6-4) as $U_{cr} \propto \sqrt{\theta_{cr}} \propto Re_*$ which implies that the effects of hydrodynamically rough and smooth flows are also considered through the Shields parameter θ_c .

Both Re_D and Eu are of importance in the scour process. The pile Reynolds number controls two important aspects of the flow structure interaction. Firstly, the separation point of the flow along the perimeter of a cylinder shifts towards the lee of the pile for an increasing Re_D (Achenbach, 1968). This results in a narrower wake, which translates into a delay in the separation of the boundary layer, a weaker horseshoe vortex at the upstream face of the structure (Roulund et al., 2005) and a smaller equilibrium non-dimensional scour depth. Secondly, the frequency of the lee wake vortices is altered. For cylinders in the same approach flow, the vortex shedding frequency process will be influenced by any change in the structures' diameter (i.e. change in the pile Reynolds number) (Sarpkaya, 2010). This change in Re_D will result in changes in the size of the

vortices and their frequency (Melville, 2008). The importance of turbulent structures at the lee of structures with respect to scour was confirmed through a series of experiments by Ettema et al. (2006). In the study the vorticity and shedding frequency around cylinders were measured, showing that the small cylinders produce twice as much vorticity compared to the larger cylinders. According to Ettema et al., (2006) this difference is one of the mechanisms that contribute towards the general tendency of finding smaller non-dimensional scour depths in prototype conditions compared to laboratory experiments. This can partially explain the discrepancies between small scale laboratory experiments and prototype scour measurements, the latter tending to have relatively small non-dimensional scour depths (Ettema et al., 2006) whereas prototype observations of scour in the field with live-bed conditions can be large (i.e. scour depth around 1.8D; Harris and Whitehouse, 2015).

Expression (6-4) shows that both the pile Reynolds number and the Euler number are of particular importance when attempting to describe the processes involved in scour around uniform and complex structures. To the author's knowledge this form of the Euler number has not previously been used to describe the scour process. In the context of scour Eu has only been discussed in Ettema et al. (2006) who argue that, for uniform cylinders, U_c^2/gD is a form of the Euler number as it emerges from the Euler equation when applied to a water surface across an eddy. This is equivalent to describing the lee wake vorticity intensity. The formulation shown in (6-4) differs from most existing scour prediction formulae (e.g. Khalfin, 1983, for shallow foundations; Breusers et al., 1977; and Johnson, 1992, for deep foundations) that are based only on:

$$\frac{S}{D} = f\left(Fr, \frac{U_c}{U_{cr}}, \frac{h}{D}\right) \quad 6-5$$

As mentioned previously the Euler number is the non-dimensional form of the adverse pressure gradient induced by the flow-structure interaction. This pressure gradient is responsible for the formation of the horseshoe vortex and explains the flow structure

interaction outside the pile wall boundary layer and outside the lee wake region where the viscous effects are negligible. By approximating that the flow boundary layer of the structure is fully developed the pressure at the face of the structure can be determined by applying Prandtl's boundary layer theory with the familiar Bernoulli equation in polar coordinates:

$$\frac{u_{\varphi}^2 + u_r^2}{2g} + \frac{p}{\gamma} + z = C \quad (6-6)$$

where:

γ is the specific gravity of water, p is the pressure, u_{φ} is the tangential component of the velocity in polar coordinates with its origin at the centre of the structure, u_r is the radial component of the velocity in polar coordinates with its origin at the centre of the structure, z is the height above the initial bed, and C is a constant.

When combined with the equations for the velocity in the tangential and radial direction this yields equation (6-7):

$$z + \frac{p}{\gamma} + \frac{1}{2g} u(z)^2 \left(\frac{\left(\frac{D}{2}\right)^4}{r^4} - \frac{2\left(\frac{D}{2}\right)^2}{r^2} \cos(2\varphi) + 1 \right) = C \quad (6-7)$$

And by differentiating with respect to φ :

$$\frac{dp}{d\varphi} = -2\rho u(z)^2 \left(\frac{\left(\frac{D(z)}{2}\right)^2}{r^2} \right) \sin(2\varphi) \quad (6-8)$$

where:

z is the vertical distance from the bed, ρ is the density of water, φ is the angle relative to the approach flow direction, $D(z)$ is the diameter of the structure as a function of the vertical distance from the bed for complex geometries, $dp/d\varphi$ is the pressure gradient at any given location around the structure, r is the distance from the pier centre where

the pressure gradient is evaluated, and $u(z)$ is the approach velocity at any given height “z” above the initial bed.

An estimate of the effect the pressure gradient has on the bed can then be determined by calculating the depth-averaged pressure gradient ($\langle dp/d\varphi \rangle$) which leads to equation (6-9).

$$\langle \frac{dp}{d\varphi} \rangle = \frac{1}{h} \int_0^h \left(-2\rho u(z)^2 \left(\frac{\left(\frac{D(z)}{2} \right)^2}{r^2} \right) \sin(2\varphi) \right) dz \quad (6-9)$$

In equation (6-9) the integration assumes that there is no energy transfer between the fluid layers in the water column and the velocity profile can be approximated by the equations of the hydrodynamically rough velocity profile given in Einstein (1950) (i.e. equations (6-10) and (6-11)) and the Nikuradse roughness (Equation (6-12)):

$$\frac{u(z)}{U_f} = 8.6 + 2.5 \ln \left(\frac{z}{k_s} \right) \quad (6-10)$$

where:

$$U_f = \frac{U}{6.0 + 2.5 \ln \left(\frac{h}{k_s} \right)} \quad (6-11)$$

$$k_s = 2.5 d_{50} \quad (6-12)$$

d_{50} is the median sediment size; k_s is the roughness length-scale; h is the water depth and U_f is the friction velocity based on the depth-averaged velocity and median sediment diameter.

The maximum depth-averaged pressure gradient can then be determined by integrating throughout the water column at the point where the maximum tangential pressure gradient is expected (i.e. $\varphi = \pi/4$ and $r = D_{base}/2$) which leads to expression (6-13).

$$\left\langle \frac{dp}{d\varphi} \right\rangle_{max} = \left| \frac{1}{h} \int_0^h \left(-2\rho u(z)^2 \left(\frac{D(z)}{D_{base}} \right)^2 \right) dz \right| \quad (6-13)$$

where D_{base} is the diameter of the base of the structure (Figure 6-1a). Equation (6-13) implies that for the same hydrodynamic conditions the structure that has a non-uniform structure geometry such as a conical base structure of increasing diameter towards the bed will have a smaller depth-averaged pressure gradient compared to a monopile. This in turn would result in a smaller downflow on the face of the structure, a reduced amplification of the bed shear stress and thus, smaller scour depths. Evidence to support this statement is provided by Tavouktsoglou et al. (2015) who measured the amplification of the bed shear stress for the same flow conditions and structures for which the pressure gradient distribution is calculated in Figure 6-2. The pressure gradients were calculated for two of the small scale structures listed in Figure 2-2 and for a mean flow velocity of 0.39 m/s and a water depth of 0.165 m. They found that there is a significant increase in the amplification of the bed shear stress between a conical base structure and a monopile, which agrees qualitatively with the pressure gradient profiles depicted in Figure 6-2. Similarly, Equation (6-13) suggests that different vertical distributions of the incident velocities also have an effect on the pressure gradient and thus on the scour potential for a given situation. Figure 6-1 (a) shows a structure that has been subjected to two different flow conditions u_1 and u_2 with different depth profiles but the same overall flow flux (i.e. same depth-averaged velocity). Applying equation (6-13) to these two cases, the profile u_2 produces a smaller depth-averaged pressure gradient compared to that for u_1 as smaller velocities are interacting with the widest portion of the structure. This phenomenon is of particular interest in practice when considering flows in locations where large lateral wind loads are expected such as the locations where offshore wind farms are situated. In these locations the wind load effectively produces a wind driven

shear flow on top of the existing logarithmic flow creating a flow profile similar to that of u_2 in Figure 6-1 (a) (Davies and Lawrence, 1994).

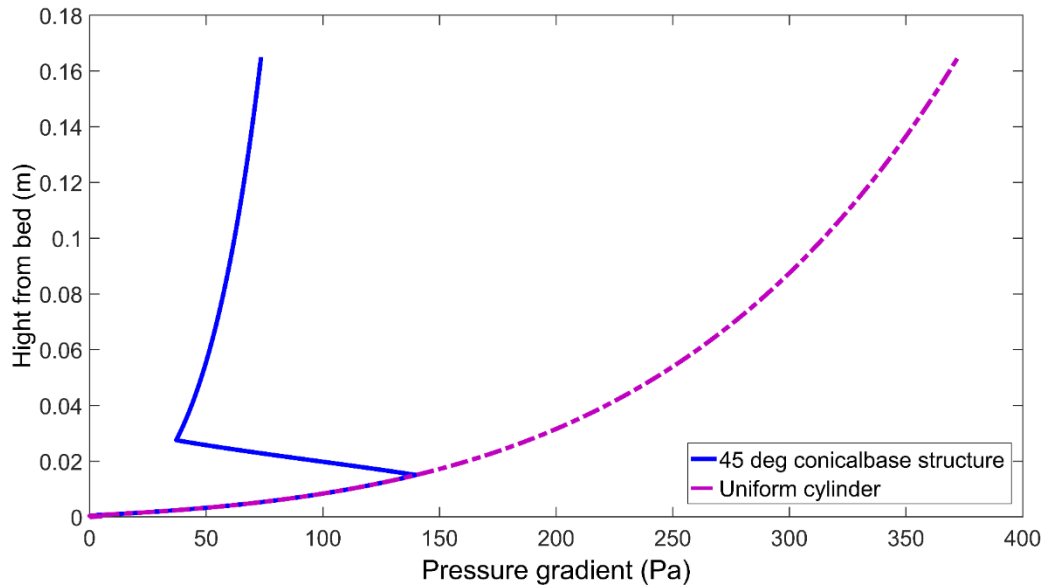


Figure 6-2: Pressure gradient distribution through the water column [calculated using Eq. (6-8)] for two different structures under the same flow conditions.

Based on equations (6-3) and (6-13) the non-dimensional form of the depth-averaged pressure gradient can now be defined as the depth-averaged Euler number, which can be written as follows:

$$\langle Eu \rangle = \frac{\langle \frac{dp}{dz} \rangle_{max}}{U_c^2 \rho} \quad (6-14)$$

For the simpler case of a logarithmic flow profile interacting with a uniform cylinder the Euler number can conservatively be assumed to take a value of 2. For all other conditions designers are recommended to:

- establish a functional relationship that describes the vertical distribution of the streamwise flow velocity ($u(z)$);
- create a function that describes the diameter of the non-cylindrical structure ($D(z)$) as a function of the distance from the bed (z); and,
- calculate the depth-averaged pressure gradient through the integration of equation (6-13) or by evaluating equation (6-13) at a minimum of 50 points

throughout the water column and substituting in expression (6-14). This process can be automated in a spreadsheet to assist in the calculation of $\langle Eu \rangle$ for different flow and structural conditions.

Equation (6-14) gives the maximum non-dimensional pressure gradient for a given set of structural parameters and flow conditions. As stated previously potential flow theory does not account for the viscous effects within the boundary layer and the lee wake region; and the vertical integration does not allow for the determination of the vertical exchange in energy across the face of the structure. For this reason $\langle Eu \rangle$ by itself is not sufficient to predict the equilibrium scour depth. The remaining parameters in equation (6-4) are required in order to determine the influence of phenomena and processes not covered by the Euler number, as will be described later.

6.3 Database Description

A significant amount of equilibrium scour data have been published in the past. In this study published data on equilibrium scour depths around both uniform and complex cylindrical structures were selected in order to create an equilibrium scour prediction equation for clearwater scour conditions. The decision to focus on the clearwater regime was made in order to avoid data that were influenced by ripple formation upstream of the structure, which would introduce additional sediment transport scale effects. A summary of the sources and quantities of scour data is given in Table 6-1 and the distribution of the most important non-dimensional parameters is given in Figure 6-3.

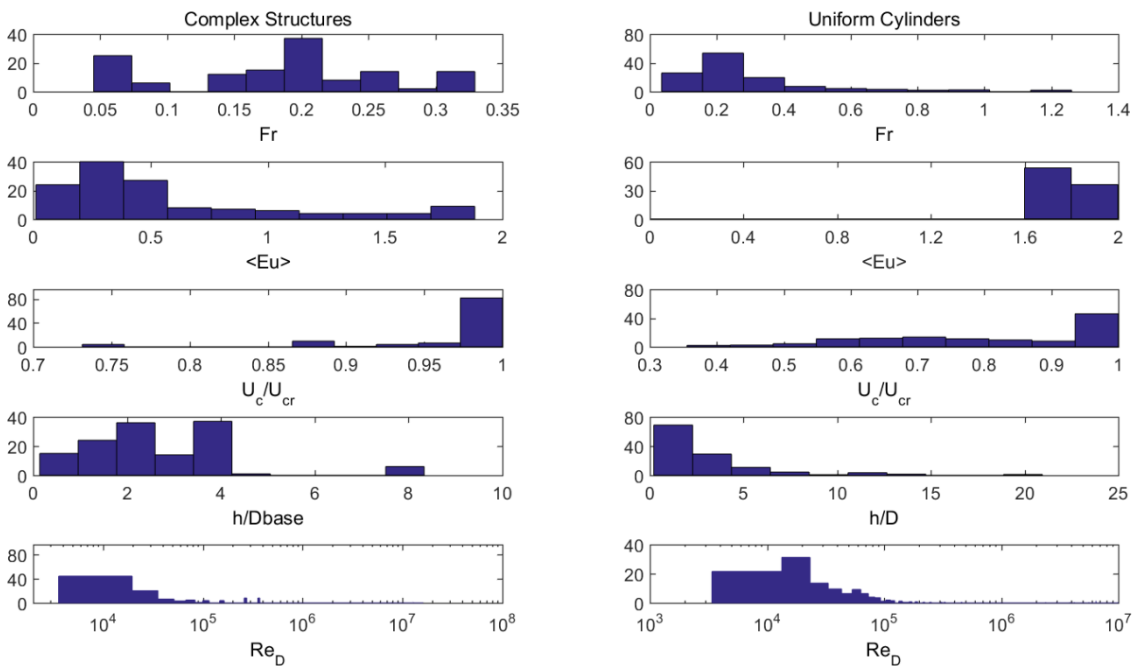


Figure 6-3: Percentage distribution of non-dimensional quantities in database

The data presented include scour tests that were conducted in the clearwater regime for cohesionless sediments only. Data were included only if all relevant parameters were presented in the publication. The aforementioned parameters include the median sediment size, average flow velocity, the sediment geometric standard deviation, water depth, structural dimensions and the time to equilibrium scour. Tests were discarded if:

- they were not run for a sufficiently long period to achieve equilibrium scour. According to Melville and Chiew (1999) this is the time required to reach a scour depth in which the scour rate does not exceed 5% of the structure diameter in 24 hours (in scaled time); and,
- the sediment geometric standard deviation (σ_g) was greater than 1.3. This was done to avoid the effects of bed armouring.

Table 6-1: Summary of sources populating the scour database.

Data Source	Number of data points
Complex geometries	
Amini et al. (2014)	6
Ataie-Ashtiani et al. (2010)	8
Ferraro et al. (2013)	10
Hoffmans and Verheij (1997)	1
Jannaty et al. (2015)	2
Melville and Raudkivi (1996)	7
Moreno et al. (2015)	8
Parola et al. (1996)	13
Present study	40
Simons et al. (2009)	4
Whitehouse et al. (2011a)	2
Total complex geometries	101
Uniform Cylinders	
Chabert and Engeldinger (1956)	85
Dey et al. (1995)	18
Ettema (1980)	70
Ettema et al. (2006)	5
Jain and Fischer (1979)	26
Melville (1997)	5
Melville and Chiew (1999)	12
Matutano et al. (2013)	10
Shen et al. (1969)	16
Sheppard and Miller (2006)	4
Sheppard et al. (2004)	4
Yanmaz and Altinbilek (1991)	14
Total uniform cylinders	269

In addition, for a limited number of structures that did not have a circular footprint the equivalent diameter was determined and used. As a consequence, only one field study is included in this dataset even though there have been a large number of field studies published. The majority of field studies were excluded for three reasons:

- field measurements tend to have time-varying flows which make it difficult to determine if a given scour hole has reached the equilibrium phase;
- in most cases, naturally occurring flows in tidal or alluvial environments are high, thus forcing scour to occur in the live bed regime for at least part of the time. The extensive bed formations developed upstream of the structure and the general

lowering of the bed would provide additional difficulty in generalising any information; and,

- in most cases it is not possible to monitor the scour development systematically and, therefore, it is not possible to determine if the scour hole is fully developed.

As Figure 6-3 shows, the majority of the data have a Froude number ranging between 0 and 0.4 which is representative of the Fr expected in most offshore locations, typically 0 to 0.2. The values of the depth-averaged Euler number are spread over the range of 0 to 1.8, showing that there is a wider distribution of complex geometries, while the distribution of $\langle Eu \rangle$ is clustered around the value of 2 for the uniform cylinders. This is explained by the higher pressure gradients expected for uniform cylinders extending to the water surface. In this dataset the majority of the data points have a mobility ratio (U_c/U_{cr}) value close to 1 for both structure categories yielding the deepest scour for the given hydrodynamic conditions. In addition, the non-dimensional flow depth is mainly below 5 for both categories, which is typical of offshore locations where structures are constructed. Finally, the majority of the data have pile Reynolds numbers smaller than 10^6 , which is due to the lack of prototype data.

6.4 Equilibrium scour depth prediction equation

On non-dimensional grounds the equilibrium scour depth for any structure and flow condition can be derived through Equation (6-4), assuming that the flow is incompressible and steady, that the soil consists of cohesionless particles with a low geometric standard deviation ($\sigma_g < 1.3$) and the scour is in the clearwater regime. The main goal of the proposed formula is to provide a tool that is able to predict the equilibrium scour depth around both complex and uniform structures reliably for unidirectional currents. This allows for the prediction of scour depths in alluvial environments accurately and in a conservative manner in offshore conditions as the action of waves reduces the effects of scour due to tidal action because of its ability to backfill the scour hole (Sumer et al., 2013).

In order to develop the new formula, the general concept presented by Breusers et al. (1977) is adopted. This describes scour as a function of the product of the governing non-dimensional parameters (f_i) identified as influencing the process. The general form reads:

$$\frac{S}{D_{base}} = F\left(\prod_1^n f_i\right) \quad (6-15)$$

For the development of the present scour prediction equation a first order rational function was selected as the fitting function which has a general form of:

$$F(x) = \frac{c_1x + c_2}{x + c_3} \quad (6-16)$$

The advantage of this formulation is its sigmoid shape which means that it is constrained by a pair of horizontal asymptotes. In practical terms this means that the scour depth described by such a function can never exceed a certain value $(S/D_{base})_{max}$. On physical grounds this is reasonable as the equilibrium scour depth around any kind of structure cannot be infinite. This statement is verified by the statistical analysis of Sumer et al. (1992) conducted on the tests of Breusers et al. (1977) which yielded that the maximum non dimensional (within one standard deviation) scour depth around a cylinder is $S/D = 2$.

The following paragraphs will present the key steps followed to develop the predictive equation. The different parameters that influence the equilibrium scour depth have been presented in equation (6-4) and will be introduced in the parameter study one after the other in order to investigate the combined influence they have on the scour depth. To get the best fit the following steps were taken:

- a) The general fit function for this study was selected (6-16).
- b) Different functional relationships were tried until the highest value of (R^2) was determined.

- c) Next non-dimensional quantity was then multiplied by the previous one and the new coefficient of determination was determined.
- d) Different functional relationships for the newly introduced variable were tested until the optimum R^2 was obtained.
- e) Steps d) and e) were then repeated until all variables listed in equation (6-4) were included.
- f) The coefficients (a, b and c) were then determined for the best fit.

One of the most important parameters that determines the magnitude of the scour depth around any cylindrical structure is the flow depth (Laursen, 1963; Breusers et al., 1977; Chee, 1982 and Raudkivi, 1986). In Figure 6-4 the non-dimensional scour depth is plotted against h/D . It can be seen that there is significant scatter in the data but there is an overall trend with an increasing flow depth resulting in an increase in the scour potential. In addition, for some flow depths (e.g. $h/D = 2$) there is a variation of the scour depth. This suggests that h/D by itself is not sufficient for describing the scour potential.

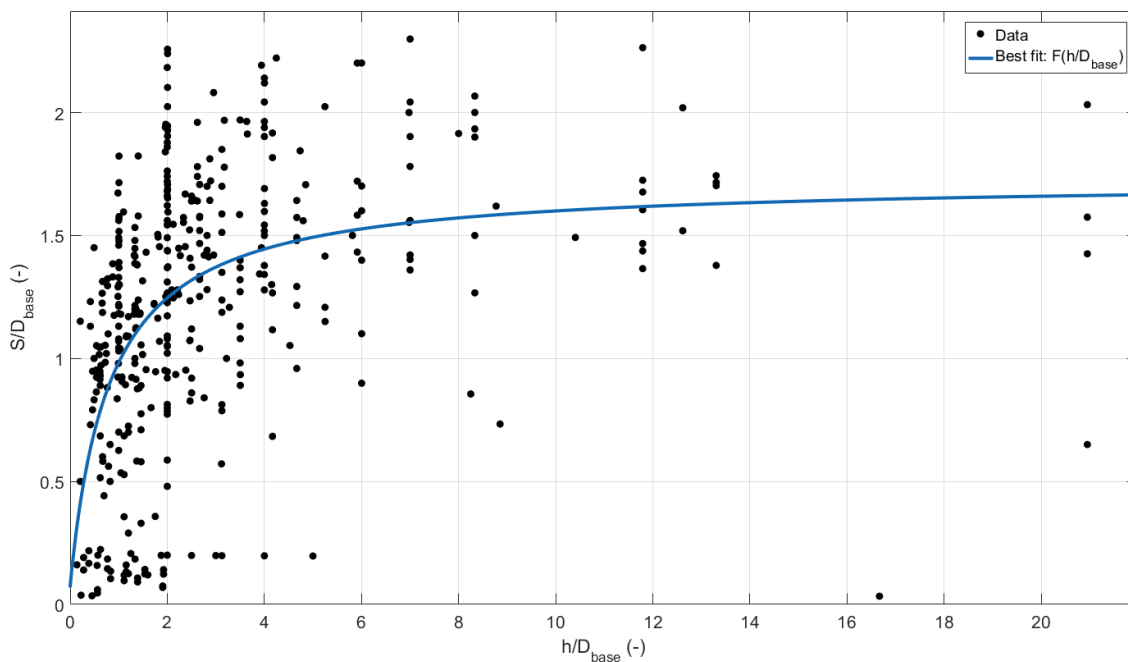


Figure 6-4: Scour depth as a function of h/D_{base} .

The combined effect of the Froude number and h/D_{base} are shown in Figure 6-5. A logarithmic scale was selected for the horizontal axis to make more visible the agreement between the proposed fit function and the data. It can be observed that the agreement

with the fit function has improved relative to the previous case. Furthermore, below the yellow line a cluster of data can be observed which corresponds to large scale tests.

In Figure 6-6, the value $h/D_{base} Fr 1/\log(Re_D)$ is plotted against the scour depth. Though at first glance there is not a big difference with Figure 6-5 the parameter $1/\log(Re_D)$ has helped to reduce the number of outliers which were data corresponding to larger scale tests and prototype data. More specifically the cluster of data lying below the yellow line in Figure 6-5 has shifted to the right. This shows the significance of the pile Reynolds number in describing scaling effects.

The combined influence of $h/D_{base} Fr 1/\log(Re_D) (U_c/U_{cr})^{0.5}$ is shown in Figure 6-7. The introduction of the factor $(U_c/U_{cr})^{0.5}$ reduces the scatter of the data. Given that 60% of the data in this database have $0.85 < U_c/U_{cr} < 1$, the influence of the equation is less pronounced but the reduction in the outliers is distinct.

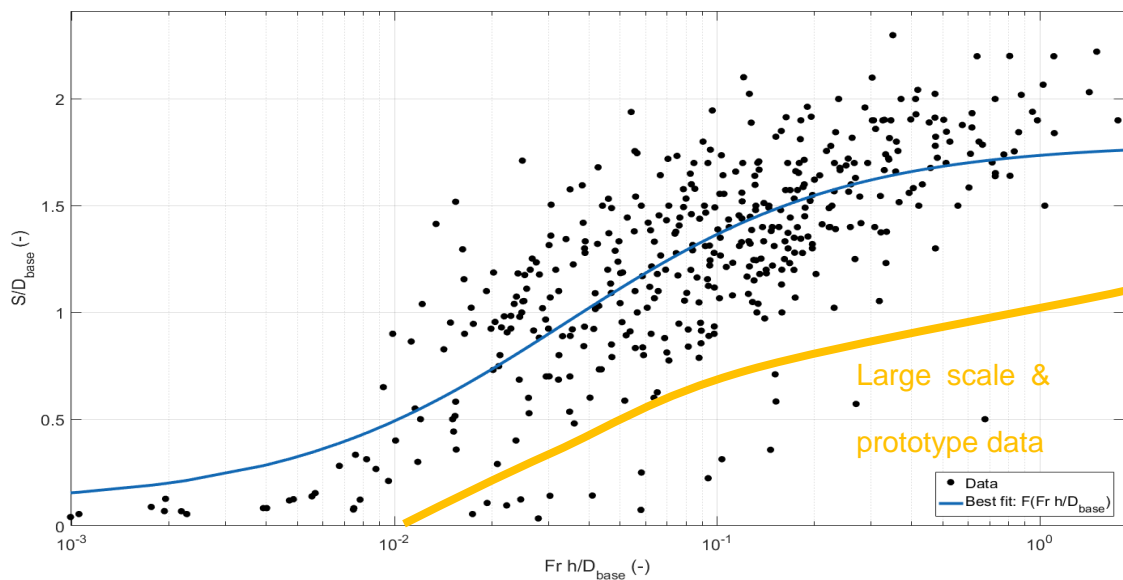


Figure 6-5: Scour depth as a function of $h/D_{base} Fr$.

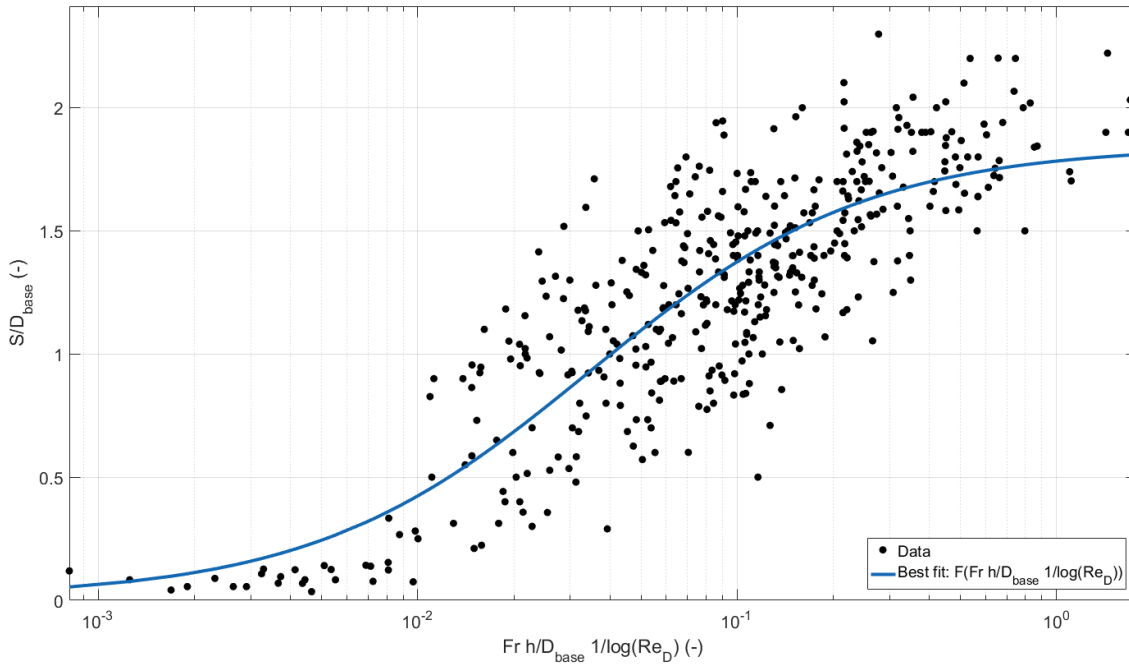


Figure 6-6: Scour depth as a function of $h/D_{base} Fr 1/\log(Re_D)$.

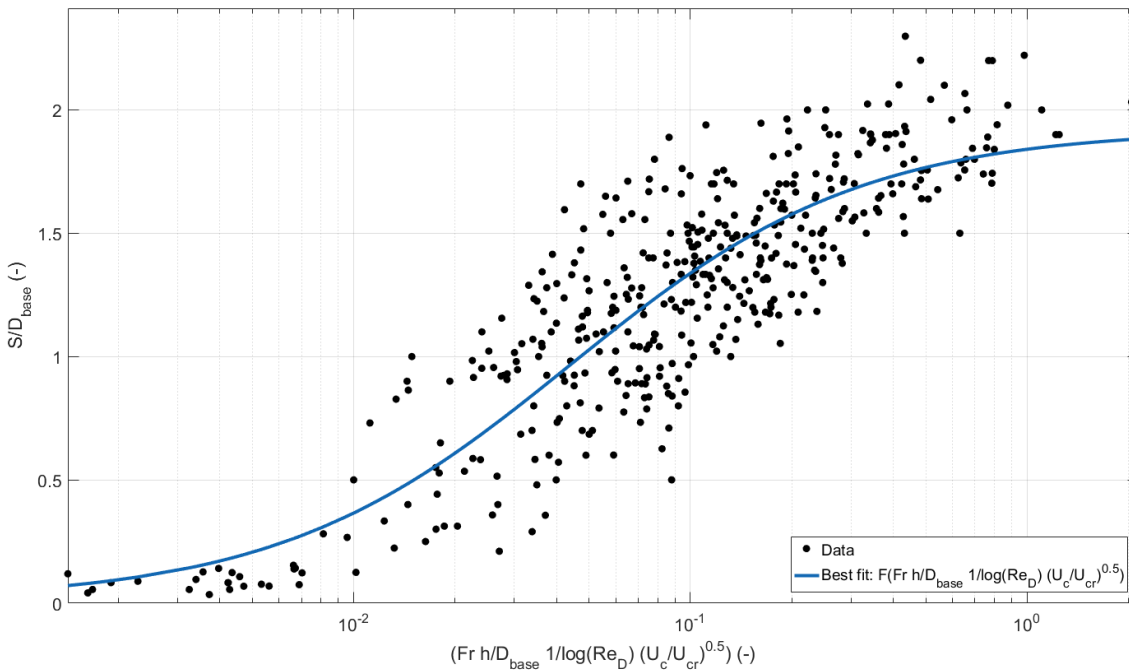


Figure 6-7: Scour depth as a function of $h/D_{base} Fr 1/\log(Re_D) (U_c/U_{cr})^{0.5}$.

After performing the parametric model study, Equation (6-17) which now includes the Euler number as well was selected as the most effective formula for predicting the non-dimensional scour depth.

$$\frac{S}{D_{base}} = \frac{c_1 \zeta + c_2}{\zeta + c_3} \quad (6-17)$$

where:

$$\zeta = \left(\frac{1}{\log(Re_D)} \right) \left(\frac{h}{D_{base}} \right) (Fr)(Eu)^{0.5} \left(\frac{U_c}{U_{cr}} \right)^{0.5} \quad (6-18)$$

c_1 , c_2 and c_3 are coefficients that were determined through parameter optimisation according to McCuen and Snyder (1986). Their values for the given data-set with the corresponding 95% confidence bounds are:

$$c_1 = 2.163 \in [2.1, 2.3];$$

$$c_2 = -0.002 \in [-0.009, 0.005]; \text{ and,}$$

$$c_3 = 0.03 \in [0.01, 0.05].$$

Figure 6-8 plots the relationship between the non-dimensional scour depth and parameter ζ . It can be observed that low values of ζ produce small equilibrium scour depths while for increasing values of ζ , S/D_{base} increases. This behaviour can be explained by the presence of D_{base} at the denominator on the right hand side of Equation (6-17), which implies that larger structures (in diameter) produce relatively shallower scour holes while smaller structures create deeper non-dimensional equilibrium scour depths. This is the behaviour reported by numerous authors such as Ettema et al. (2006). An example of such large experimental scour depths is in Chiew (1984) who measured scour depths up to $S/D = 2.7$. This high value is attributed to the effect of the pile Reynolds number according to Ettema et al. (2006), although a number of examples have been reported in the literature (e.g. Harris and Whitehouse, 2015) where prototype scour depths were comparable to those of laboratory experiments (i.e. $S/D \sim 1.8$). In addition to the effect of the pile size several physical phenomena have also been found

to contribute to the smaller scour depths in offshore locations. McGovern et al. (2014) concluded that scour in tidal flows is less than the corresponding scour induced by a unidirectional current. This conclusion was debated by Harris and Whitehouse (2015) who showed that scour depths around monopiles in offshore locations subject to tidal flows fit within the same population as scour induced around piles in unidirectional flows. This finding is also supported by Porter et al. (2015) who conducted a series of experiments and found that the scour depth for reversing and unidirectional currents does not differ. Furthermore, Sumer et al. (2012) concluded, through a series of experiments, that when the wave climate changes the equilibrium scour depth may be reduced due to a backfilling process. The previous discussion shows that there are various phenomena that may partially explain the observation of smaller scour depths at offshore monopoles in granular soils in some cases, but in general terms scour depths similar to those induced by unidirectional currents in rivers should be expected. It should be noted that additional research is required in order to understand the exact consequences of these phenomena on offshore scour.

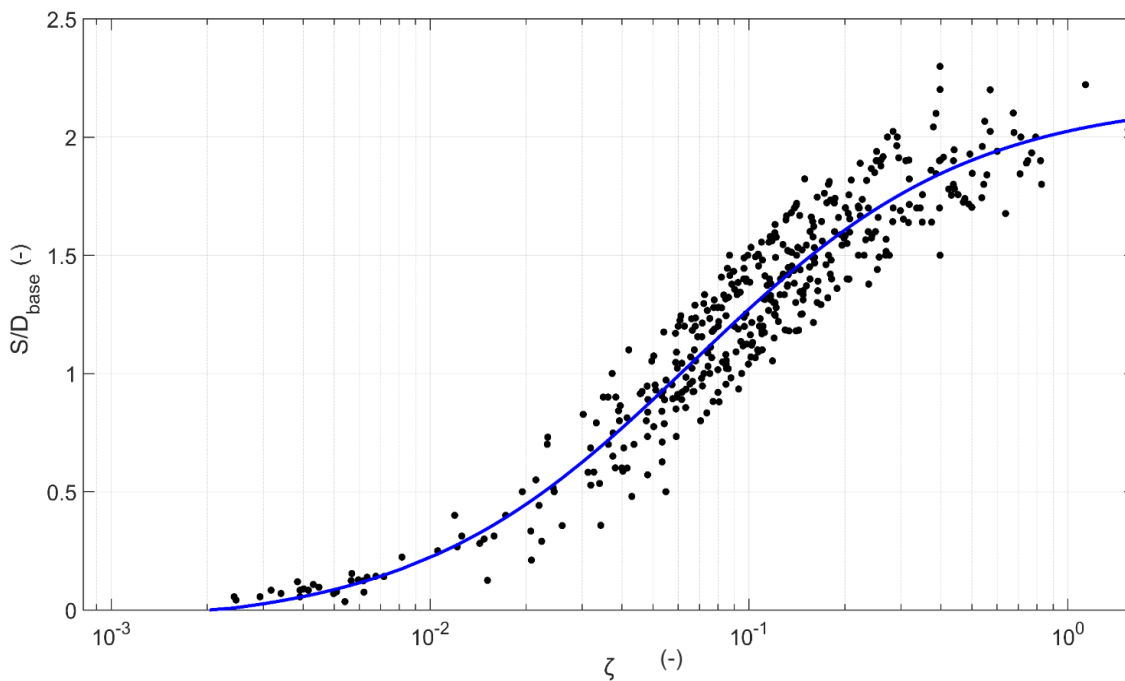


Figure 6-8: Scour depth as a function of ζ .

During the analysis of the data the velocity profile for a number of tests in the database were not known and were assumed to be logarithmic and to follow Equation (6-10). This assumption, along with the fact that laboratory experiments are prone to effects such as wall friction and non-uniform flow distribution across the width of the flume, are expected to have contributed to the scatter in Figure 6-8.

The accuracy of the present scour prediction method is evaluated through the comparison of the predicted scour depths (using equation (6-17)) to the corresponding measurements. The figure shows that a good agreement is found between the proposed method and the scour depth database compiled in this study. 55% of the predictions have an error smaller than 10% and 82% of the predictions an error smaller than 20%. The values of correlation coefficient (R^2) and RMSE (Root Mean Squared Error) were calculated as 0.91 and 0.16 respectively. It should be kept in mind that a factor contributing to this high accuracy is that the same database that was used to evaluate the accuracy of the model was also used to develop it. A limited number of scour predictors for complex structures are found in the literature. Most of them rely on shape factors to account for the different structure geometry (e.g. Breusers et al., 1977; Laursen and Toch, 1956). Scour prediction around GBFs can be calculated through the Khalfin (1983) method which may lead to the underestimation of the scour depth in some cases. This is because the method was derived for foundations with a limited skirt depth. Others provide a conservative method of estimating the equilibrium scour depth through envelope curves (i.e. FDOT, 2005) which leads to the overestimation of the scour depths in some cases. Thus the present equation may be a good solution for providing a basis for the deterministic and probabilistic assessment of scour, which cannot be done with the other prediction methods.

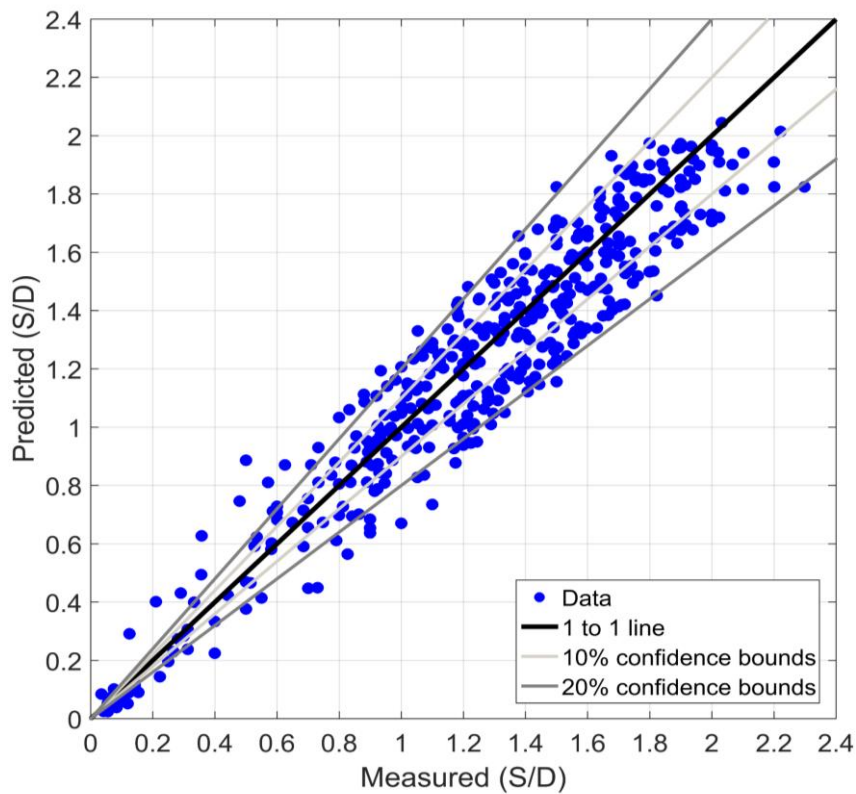


Figure 6-9: Agreement of scour-depth prediction [using Equation (6-17)] and measured scour depths with 10 and 20% confidence bounds

The predictive capacity of the proposed scour prediction equation has been validated through its comparison with a number of prototype scour measurements around offshore monopile structures published by ABPmer Ltd et al. (2010). Figure 6-10 shows the agreement between the present prediction method and the prototype measurements. As can be seen the present equation is able to predict the scour depth around the structures with good accuracy even though the scour process in most of these locations is the live bed scour regime. Exceptions to this observation are the Princess Amalia, Barrow and Kentish flats locations. In the case of the Princess Amalia site a clay layer at a depth of 2-3m ($S/D \in [0.5, 0.75]$) was discovered during the geotechnical survey. In general clays are associated with small scour depths and in many case do not allow any scour. This explains why the observed scour depths range between S/D of 0.5 and 0.8 in Figure 6-10 and why the present predictive equation over-estimates the scour depth at this location. Barrow is another location situated in an area with a mixture of fine silt and clay extending to a depth of 10m below the original bed Seacore (2004). This explains the

wide range of measured scour depths at this site, as soils mixed with clays may have variable scour response according to Whitehouse et al., 2011a.

Kentish Flats is located at an area with surficial sediment comprised of muddy sands (ABPmer Ltd et al., 2010). This also produces variable scour due to the variability in the mud's cohesive properties.

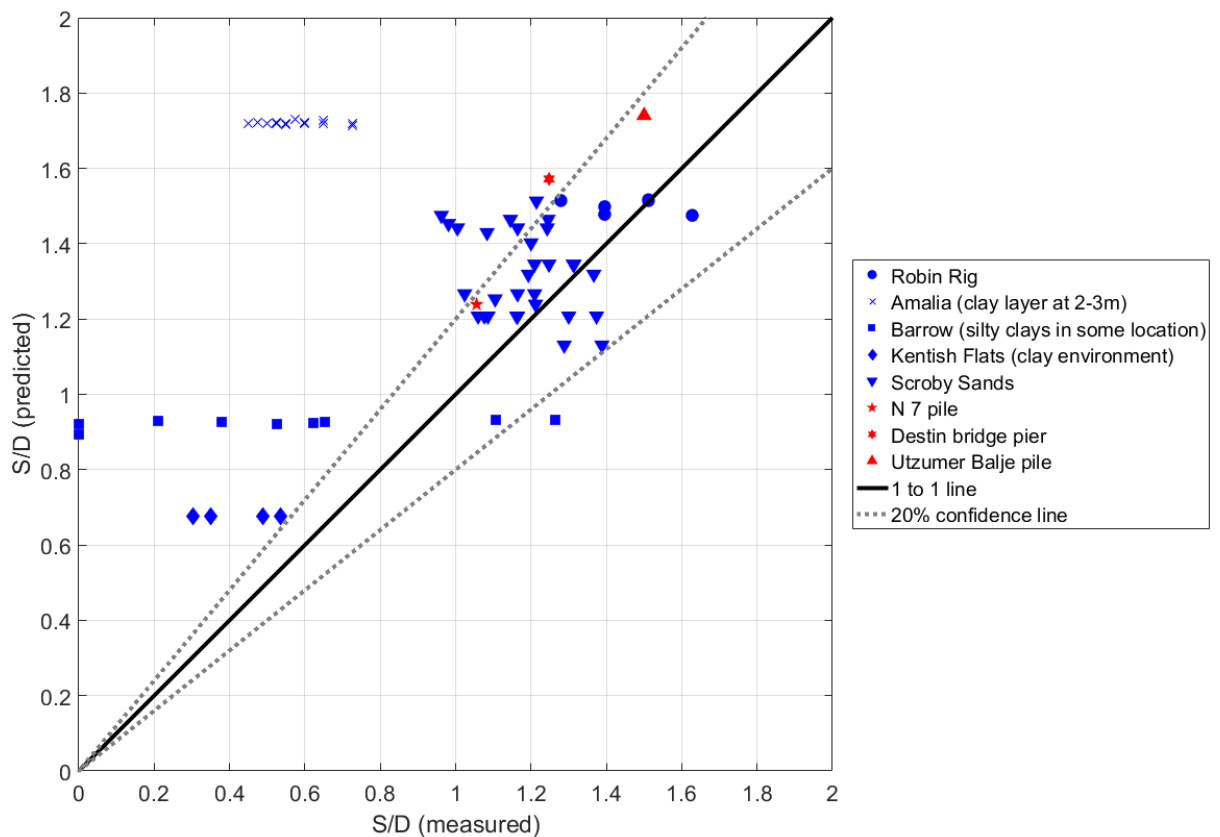


Figure 6-10: Comparison of Equation (6-17) with prototype field data.

6.5 Behaviour of scour prediction equation

Having derived the scour prediction formula, the contribution of different physical factors to its behaviour are assessed.

6.5.1 Influence of depth averaged Euler number

Given that the viscous forces in the flow-structure interaction around piers are negligible, one needs to find a non-dimensional quantity to describe the flow alteration upstream of the structure. This implies that a variable that includes the structure length scale and

some form of the kinetic energy is required. The depth-averaged pressure gradient in the form of the Euler number, described earlier in this chapter, includes both of these physical quantities, and hence it should be possible to describe the two main mechanisms driving the scour process, which are present upstream of the structure. The first of these is the horseshoe vortex and the second is the flow acceleration. Potential flow theory suggests that, given the flow conditions remain constant, an increasing blockage induced by a structure would result in a larger amplification of the adverse pressure gradient and thus an increase in the local scour potential. The experiments conducted in the current study were designed to test this hypothesis and yield results which relate the depth-averaged Euler number to the equilibrium scour depth for different structures. Figure 6-11 through 6-13 show the influence that the pressure gradient has on the equilibrium scour depth for different ranges of sediment mobility parameter, flow depth and velocity profiles. In these figures the different colours denote a different type of structure while the different symbols correspond to the different flow conditions. Figure 6-11 shows the influence of $\langle Eu \rangle$ on the equilibrium scour depth for test series 1.0 through 1.28 and the lines correspond to the prediction given by Equation (6-17) for the corresponding flow conditions. It shows that an increasing Euler number yields an increase in the equilibrium scour depth given that the remaining flow conditions are the same and it reaches an asymptotic value of S/D as $\langle Eu \rangle$ approaches 2.

Further observation of Figure 6-11 and 6-12 shows that tests conducted with different sediment sizes but having the same sediment mobility number do not differ significantly with regards to the equilibrium scour depth. In addition, a decrease in the mobility parameter (U_c/U_{cr}) or (h/D_{base}) results in the same trend described above with respect to $\langle Eu \rangle$, but with the horizontal asymptote shifting to a lower value of S/D_{base} .

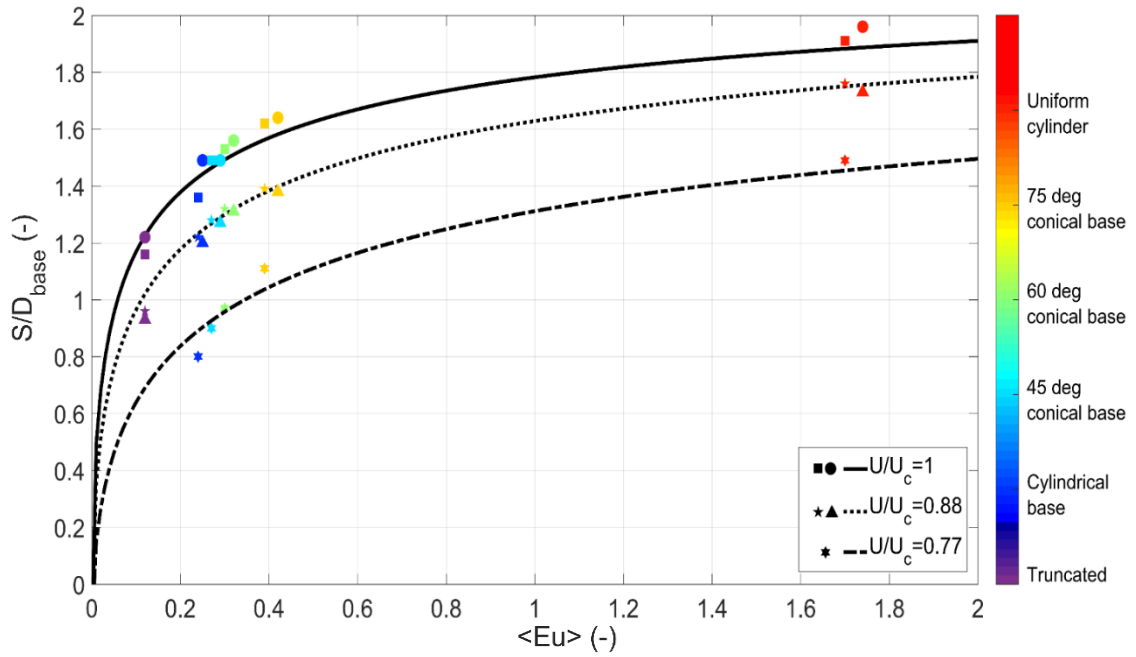


Figure 6-11: Influence of sediment mobility ratio [$U_c/U_{cr} = 0.74, 0.88$ and 1] on the variation of the equilibrium scour depth as a function of $\langle Eu \rangle$ [Note: Line shows prediction given by Equation (6-17) for each of the three sediment mobility ratios.

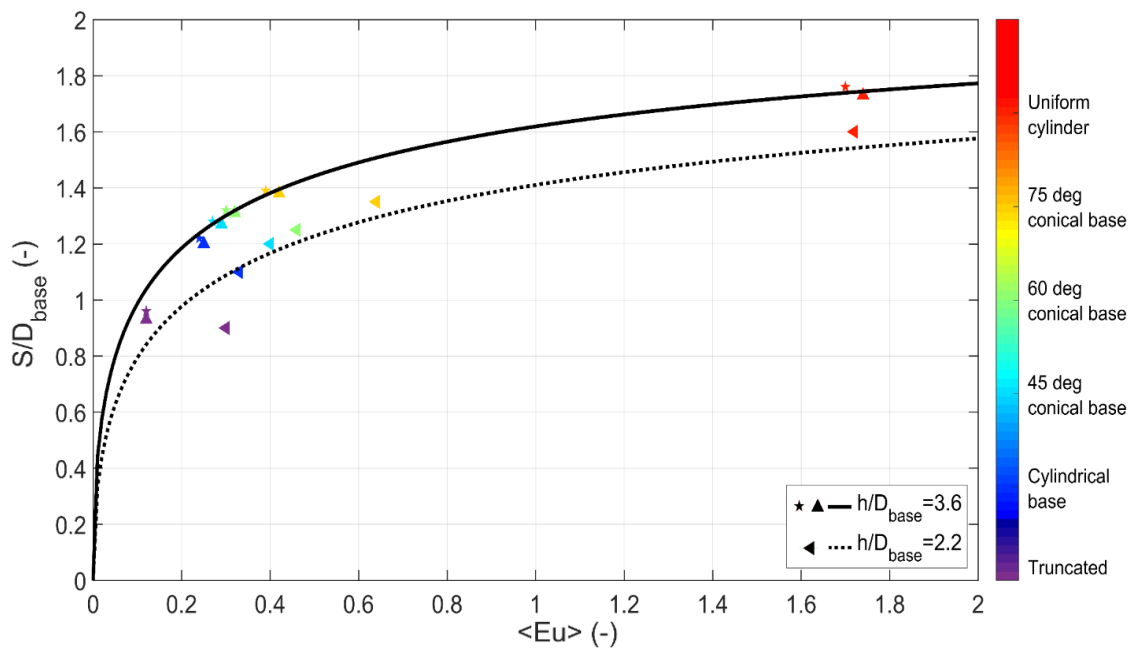


Figure 6-12: Influence of non-dimensional water depth [$h/D_{base} = 3.6$ and 2.2] on the variation of the equilibrium scour depth as a function of $\langle Eu \rangle$ [Note: Line shows prediction given by Equation (6-17) for each of the three sediment mobility ratios.

Figure 6-13 shows the results from the larger scale scour tests. It can be observed that the equilibrium scour depth increases as $\langle Eu \rangle$ increases in the same manner as for the

smaller scale tests. Furthermore, the data for complex foundation shapes corresponding to the non-logarithmic flow profile are shifted further to the left compared to the tests that were subjected to the logarithmic flow profile, while both test results fall onto the same trend line. The effect of the non-logarithmic profile on scour for the monopile is less than for the complex foundation shapes. Given that the depth-averaged flow velocity in both cases is the same, lower flow velocities are observed near the bed in the case of the non-logarithmic profile case. This translates to less kinetic energy interacting with the larger base which yields smaller $\langle Eu \rangle$ and thus smaller scour depths. In addition, given that all of the remaining non-dimensional flow parameters listed in equation (6-4) are kept constant during the two tests, it is also expected that both results fall on to the same curve defined by equation (6-17). Finally, even though the larger scale data plotted in Figure 6-13 were derived from experiments with slightly different values of the non-dimensional water depth, mobility ratio and Fr , it can be observed that an increase in the structural scale of each of the foundation models results in a significant decrease in the non-dimensional equilibrium scour depth. This effect is linked to the different pile Reynolds number for this set of tests, and will be elaborated on in the following section.

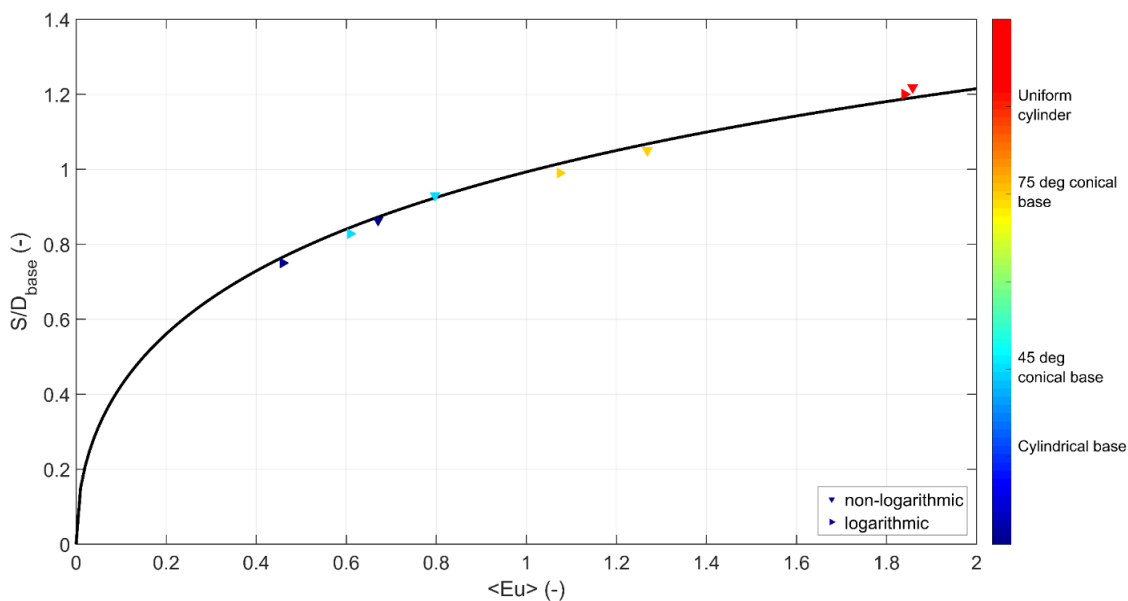


Figure 6-13: Influence of vertical flow distribution on the variation of the equilibrium scour depth as a function of $\langle Eu \rangle$ [Note: solid line shows prediction given by Equation (6-17)]

6.5.2 Influence of pile Reynolds number

During the large scale experiments two main sediment transport systems were identified:

- the sediment from the upstream region of the structure was transported and deposited at the lee of the structure at an angle 160° - 200° relative to the flow direction. This process is primarily induced by the local increase in the horseshoe vortex in front of the structure and thus described by the change in Eu , h/D and Fr ; and,
- a secondary process that suspends the previously deposited sediment at the lee of the structure into the water column. This material is then carried away from the scour hole and deposited further downstream from the structure. This process is mainly driven by the longitudinal counter-rotating vortices which are created partly by the horseshoe vortex and the variation of the shedding frequency over the height of the structure (Baykal et al., 2015; Petersen et al., 2015; Kirkil and Constantinescu, 2010). Thus this process should be characterised by the pile Reynolds number.

This finding is presented in Figure 6-14, and shows that the pile Reynolds number is an important factor controlling the scour process. According to Schlichting (1979) the size of the pile wall boundary layer is proportional to $1/\ln(Re_D)$ which means that the overall turbulence induced by the flow-structure interaction would decrease as the Reynolds number increases. In addition Achenbach (1968) showed that an increasing Re_D forces the separation point to shift further downstream around the pile, which also results in a decrease in the sediment transport capacity of the lee wake vortices and thus decrease the overall scour potential. This shows that Re_D could account for some scale effects that result in smaller non-dimensional scour depths for larger scale structures.

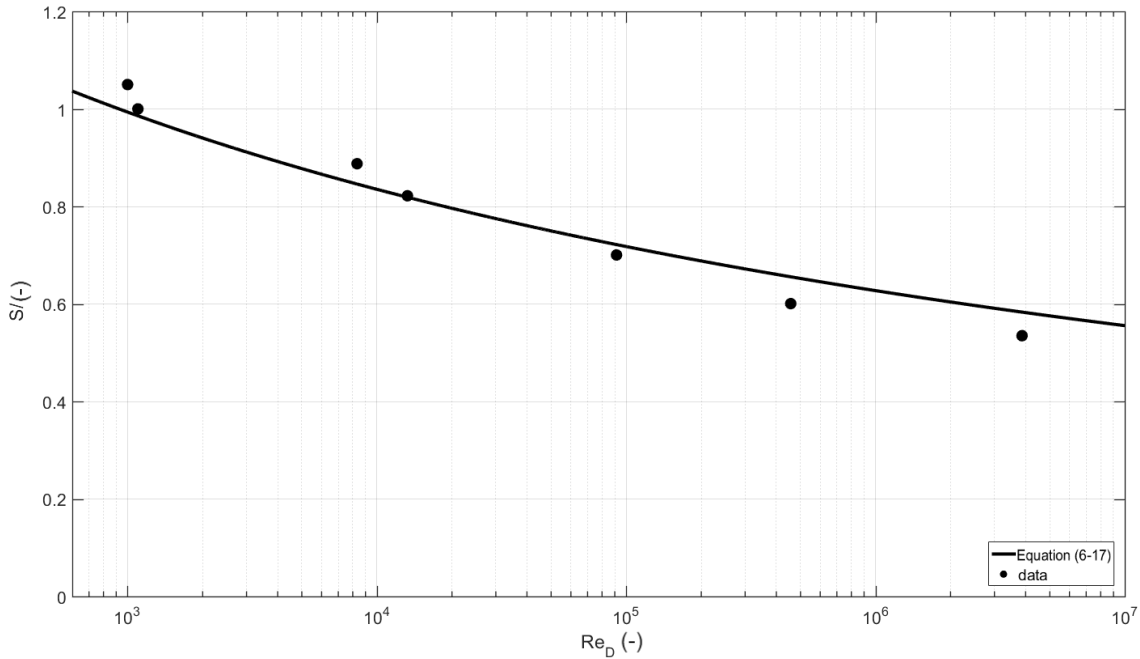


Figure 6-14: Influence of Re_D on equilibrium scour. Comparison of Equation (6-17) to scour depth data with varying Re_D and $Fr = \{0.15 - 0.20\}$, $U_c/U_{cr} = \{0.7 - 0.85\}$, $h/D = \{2 - 3\}$ and $\langle Eu \rangle = \{1.7 - 2\}$ (data from dataset collected from current study).

To demonstrate this effect Figure 6-14 shows the influence of Re_D ($10^3 \leq Re_D \leq 4 \cdot 10^6$) on the equilibrium scour depth for varying Re_D . The data points in this figure correspond to scour tests (from the dataset presented in this study) in which the remaining flow parameters did not vary significantly $Fr = \{0.15 - 0.20\}$, $U_c/U_{cr} = \{0.7 - 0.85\}$, $h/D = \{2 - 3\}$ and $\langle Eu \rangle = \{1.7 - 2\}$. As can be observed an increasing pile Reynolds number does indeed have the effect of decreasing the non-dimensional equilibrium scour depth. This trend is captured relatively well by the scour prediction equation given in (6-17) over a wide range of Re_D .

An increase in the flow velocity or the diameter of the structure would also change the other non-dimensional parameters found in equation (6-17) in addition to the pile Reynolds number. For instance, an increase in the mean flow velocity would also increase the sediment mobility number and the Froude number. The combined effect of an increase in the mean flow velocity and the pile diameter was investigated by Shen et al. (1969). In the study the influence of the pile Reynolds number was explored. The

experiments were conducted for a circular pier with diameters ranging from 0.15m to 0.9m and a median sand diameter of 0.24mm under the forcing of a unidirectional current with different flow velocities $0.3 < U/U_c < 3$. A best fit equation was then obtained by combining the test results with other published data with similar non-dimensional flow depths and pile diameters. This resulted in equation (2-54).

In Figure 6-15 a comparison of the present equation (Equation (6-17)) and equation (2-54) is shown for data compiled over a more limited range of Re_D from the midrange of the Figure 6-14. The prediction equations are plotted against the equilibrium scour depth data compiled by Breusers et al. (1977) which were obtained from Sheppard et al. (2011). In this figure only the clearwater scour data are plotted, as live bed scour is outside the scope of this study. As can be seen the two equations show a reasonable agreement with the clearwater scour data for $Re_D < 4 * 10^4$. In the same figure it can be observed that the equation in Shen et al. (1969) equation shows a tendency to give a better prediction of the Chabert and Engeldinger (1956) data, while equation (6-17) shows a better agreement with the data of Shen et al. (1969) for larger Re_D . At the lower Reynolds number range the methods tend to underpredict, and this may be related to the comment by Sheppard et al. (2011) that the Chabert and Engeldinger data in the range $U_c/U_{cr} < 0.7$ tend to feature much deeper scour than other datasets.

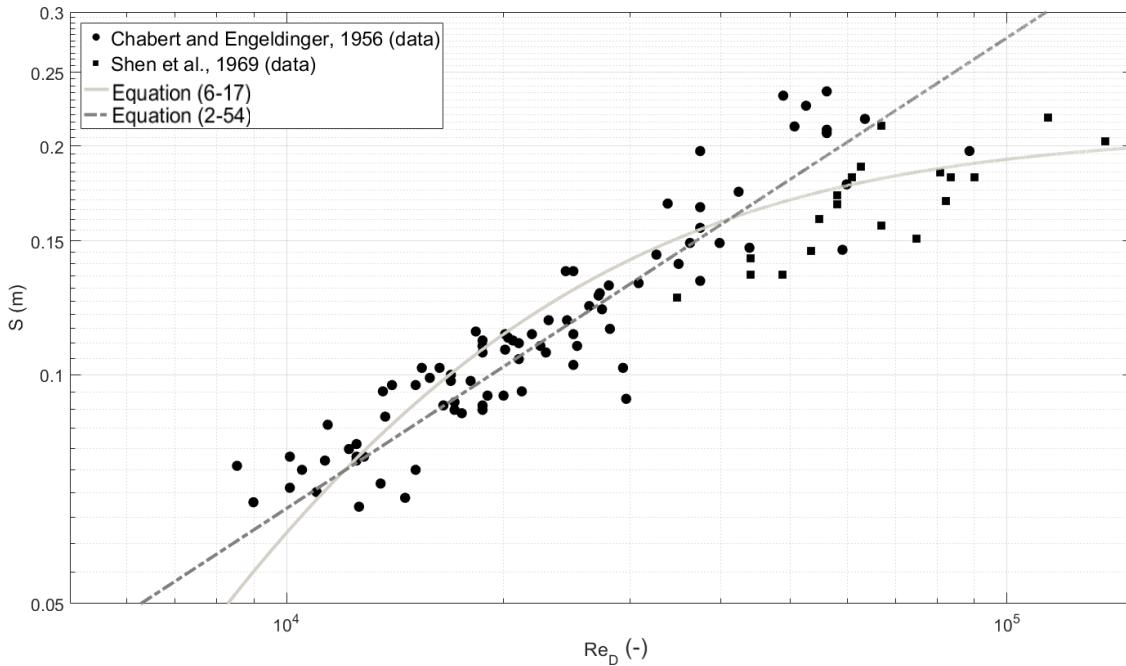


Figure 6-15: Effect of the pile Reynolds number on scour. Comparison of present equation (Equation (6-17)) and the equation of Shen et al, (1969) [Equation 2-54] to the data presented in Breusers et al. (1977) (data source: Sheppard et al., 2011).

6.5.3 Influence of Froude number

According to numerous authors (e.g. Baker, 1986; Graf and Yulistiyanto, 1998) a significant process that controls the scour process is the strength of the horseshoe vortex. On physical grounds it can be deduced that the intensity of the horseshoe vortex should be strongly influenced by the downflow at the face of the structure. Based on the Bernoulli equation and the conservation of energy it can be concluded that the downflow is dependent on both the hydrostatic component and the kinetic component of the energy. Therefore, by applying the Bernoulli equation from a location far away from the structure (where the flow field is undisturbed) to its leading face, we can obtain:

$$\frac{y}{h} \propto Fr^e \quad (6-19)$$

where y is the vertical location of the stagnation point (see Figure 6-16) along the face of the structure and e is a constant.

Figure 6-17 shows the influence of the Froude number on the equilibrium scour depth for a subset of the data presented in Table 6-1. In this figure the depicted data points

have values of the Froude number ranging from 0.11 to 0.97 while $Re_D = \{75000 - 150000\}$, $U_c/U_{cr} = \{0.8 - 1\}$, $h/D = \{2 - 3\}$ and $\langle Eu \rangle = \{1.7 - 2\}$. It can be observed that the scour depth increases following a logarithmic trend and reaches a horizontal asymptote as $Fr \rightarrow \infty$. This means that for shallow water depths the high Froude number results in a stronger kinetic component of the pressure field and, therefore, in a stagnation point which is closer to the water surface. Thus a larger portion of the flow is “captured” by the downflow which results in deeper scour depths. On the other hand, greater flow depths result in smaller Froude numbers which mean that the hydrodynamic component of the pressure force is larger, effectively creating a more evenly distributed pressure field along the face of the structure and thus leading to a vertical stagnation point closer to the bed and, therefore, smaller scour depths (Harris and Whitehouse, 2015).

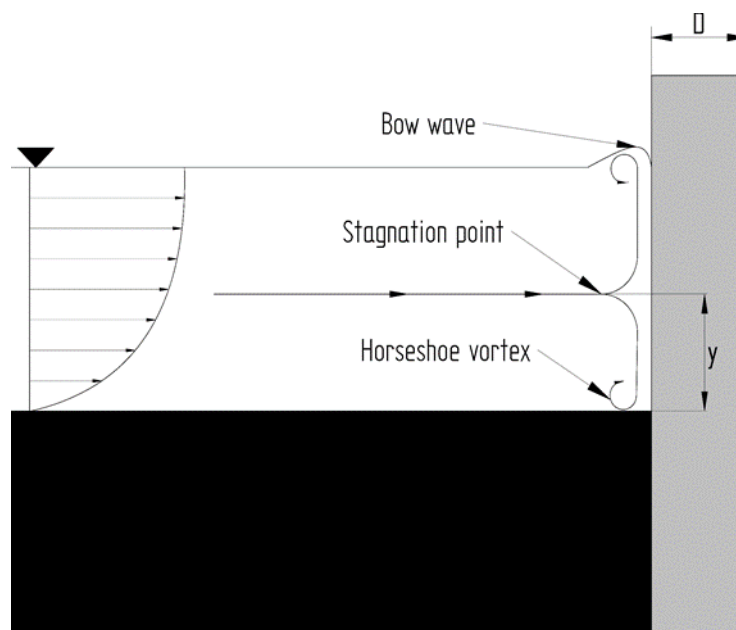


Figure 6-16: Definition diagram of the location of the vertical stagnation point.

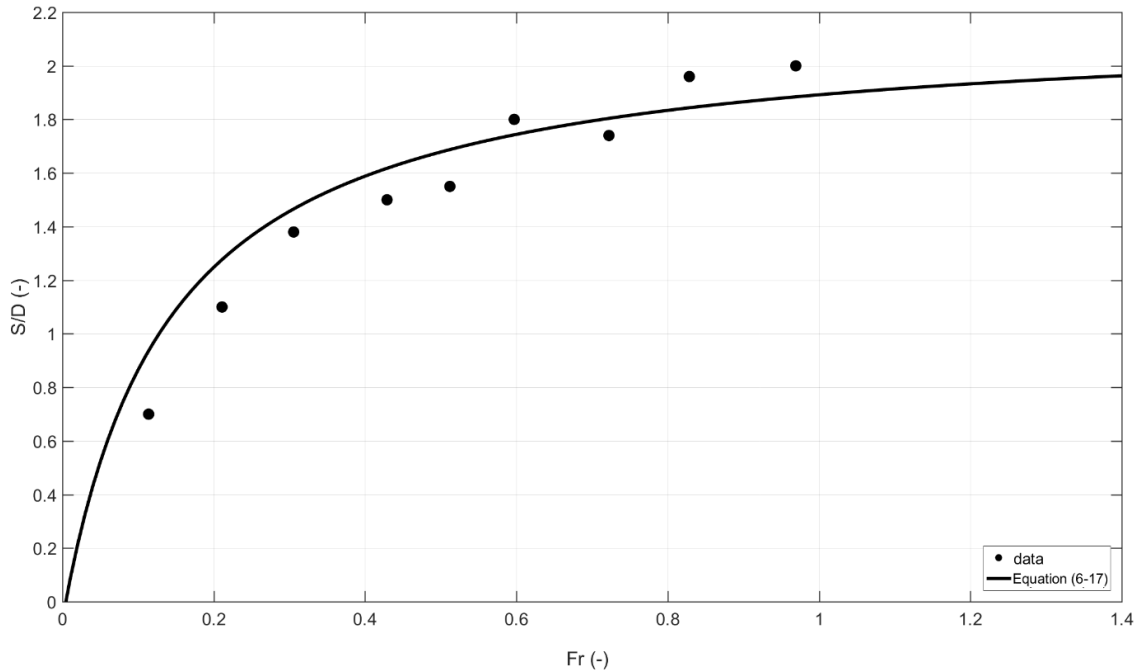


Figure 6-17: Influence of Fr on equilibrium scour. Comparison of Equation (6-17) to scour depth data with varying Fr and $Re_D = \{75000 - 150000\}$, $U_c/U_{cr} = \{0.8 - 1\}$, $h/D = \{2 - 3\}$ (Eu) = $\{1.7 - 2\}$.

6.5.4 Influence of non-dimensional flow depth

The flow depth also influences the scour depth in a way that cannot be captured by the Froude number. According to Sumer and Fredsøe (2002) the boundary layer separation at the bed will be delayed if the non-dimensional water depth is small, as a smaller h/D would result in a more uniform flow distribution. This in turn will result in a smaller horseshoe vortex and, therefore, in a smaller scour potential. Figure 6-18 shows the influence of the water depth on the non-dimensional scour depth for data where the rest of the flow conditions do not vary significantly; $Re_D = \{100000 - 300000\}$, $U_c/U_{cr} = \{0.8 - 1\}$, $Fr = \{0.1 - 0.25\}$ and $\langle Eu \rangle = \{1.7 - 2\}$.

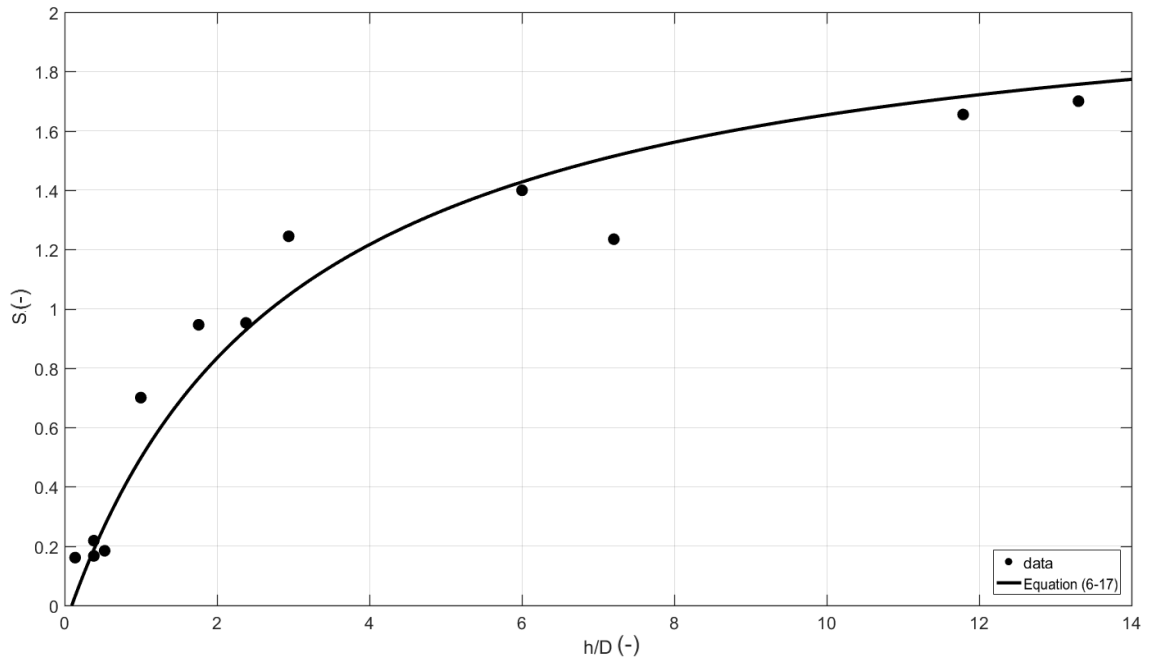


Figure 6-18: Influence of h/D on equilibrium scour. Comparison of Equation (6-17) to scour depth data with varying h/D and $Re_D = \{100000 - 300000\}$, $U_c/U_{cr} = \{0.8 - 1\}$, $Fr = \{0.1 - 0.25\}$ and $\langle Eu \rangle = \{1.7 - 2\}$.

In reality a change in the water depth (h) would affect both the Froude number and the non-dimensional flow depth (h/D). According to the discussion presented in the previous sections, an increase in the flow depth would decrease the Froude number and increase h/D . The combined effect of a change in the water depth while maintaining the values of the remaining parameters constant is demonstrated in Figure 6-19, where the clearwater equilibrium scour depth data compiled by Melville and Sutherland (1988) is also plotted. It can be observed that Equation (6-17) captures the trend of their data well, albeit with a tendency to over-predict the scour depths for $0.5 < h/D < 1.5$ and under-predict them for higher values of the non-dimensional flow depth.

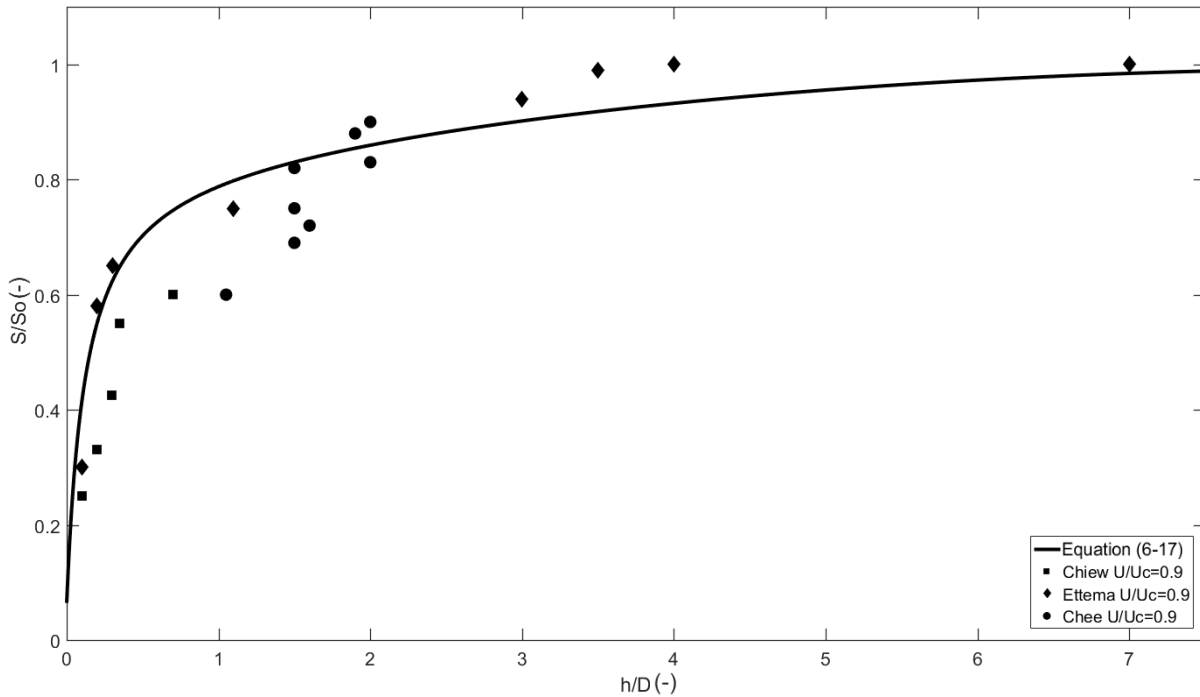


Figure 6-19: Effect of boundary layer thickness on scour. Comparison of Equation (6-17) with clearwater scour data compiled from Melville and Sutherland (1988).

6.5.5 Influence of the sediment mobility ratio

As mentioned earlier the sediment mobility ratio significantly effects the equilibrium scour depth potential for a given structure and flow conditions. In the context of the equilibrium scour Equation (6-17), U/U_c is a factor that describes the resistance of the local bed to the hydrodynamic forces that are amplified due to the presence of the structure. The importance of the sediment mobility ratio on physical grounds can be obtained by applying the 2D-Vertical continuity equation at a control volume extending from a location upstream of the scour hole to the deepest point of the scour hole and assuming that at the equilibrium phase of scour the incoming flow into the scour hole is U and the mean flow velocity at the deepest point of the scour hole is U_c , leading to Equation (6-20):

$$\frac{S}{D} = d \left(\frac{U_c}{U_{cr}} \right) \text{ for } U \leq U_c \quad (6-20)$$

in which variable d is a function of the length of the scour hole in the streamwise direction at equilibrium and the structure's diameter.

Figure (6-20) demonstrates the effect of the mobility parameter on the equilibrium scour for a set of data where U/U_c varies between 0.35 and 0.99 and $Re_D = \{50000 - 200000\}$, $h/D = \{3 - 6\}$, $Fr = \{0.1 - 0.15\}$ and $\langle Eu \rangle = \{1.7 - 2\}$. The data show reasonably good agreement with Equation (6-17) and with the observations reported by Melville and Sutherland (1988) who analysed the data of Baker (1986).

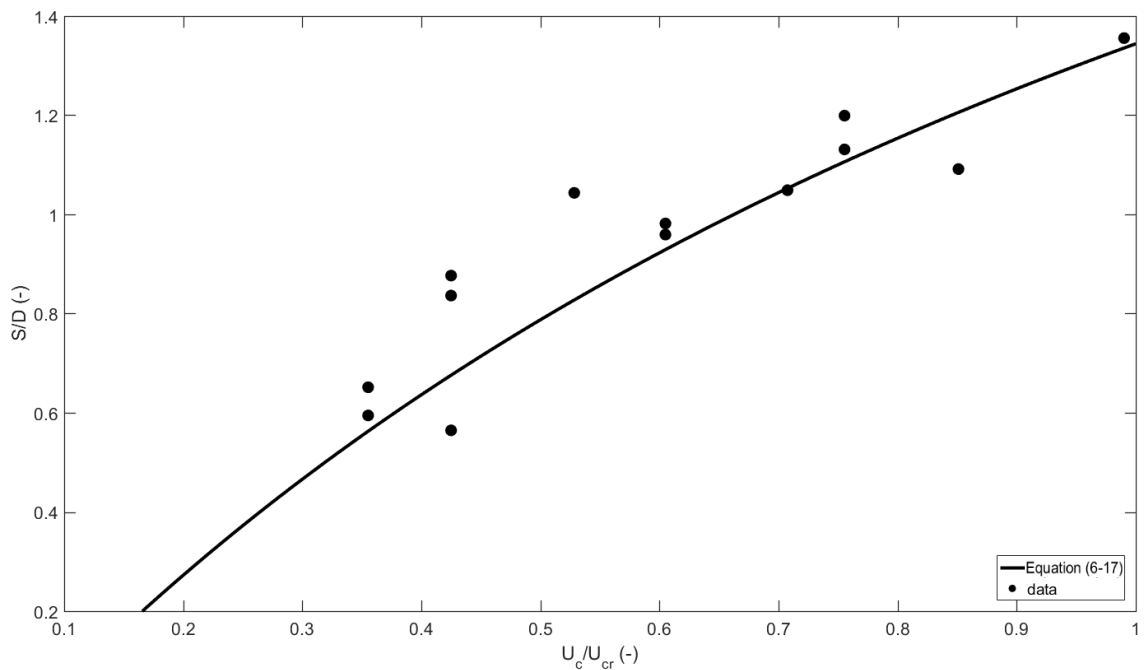


Figure 6-20: Effect of sediment mobility ratio on scour for monopiles. Comparison of Equation (6-17) to scour depth data with varying U_c/U_{cr} and $Re_D = \{50000 - 200000\}$, $h/D = \{3 - 6\}$, $Fr = \{0.1 - 0.15\}$ and $\langle Eu \rangle = \{1.7 - 2\}$.

Part III: Scour protection around complex structures

7 Methodology for scour protection stability tests

7.1 Introduction

An extensive series of tests were conducted to investigate the stability of scour protection rock (riprap) around the complex structural geometries detailed in section (4.4.1) over a range of different combinations of waves and currents. A total of 512 tests were conducted while an additional 16 tests were conducted to investigate the effect long duration design storm conditions have on the damage development. The main focus of this study was to establish the amplification of the bed shear stress required to move a stone of a certain size and density for a given set of flow conditions and structural geometries.

This chapter describes:

- The general scaling and modelling issues concerning the physical modelling of waves,
- The experiment procedures followed for the tests,
- The set-up of the experimental facilities used for these tests,
- The choice of parameters for the physical models,
- The equipment used during the tests; and
- The experimental programme for these tests.

7.2 General model and scaling considerations

In addition to the model and scaling considerations presented in section 4.2 the physical modelling of waves requires the careful consideration of the effect of wave reflection due to inadequate wave absorption. The present tests were conducted for wave periods ranging between 1s and 3s which according to Edinburgh Designs Ltd (manufacturers of wave paddles in this flume) yields negligible reflections (defined as the ratio of the incoming wave height over the reflected) which are less than 5% (see Figure 7-1).

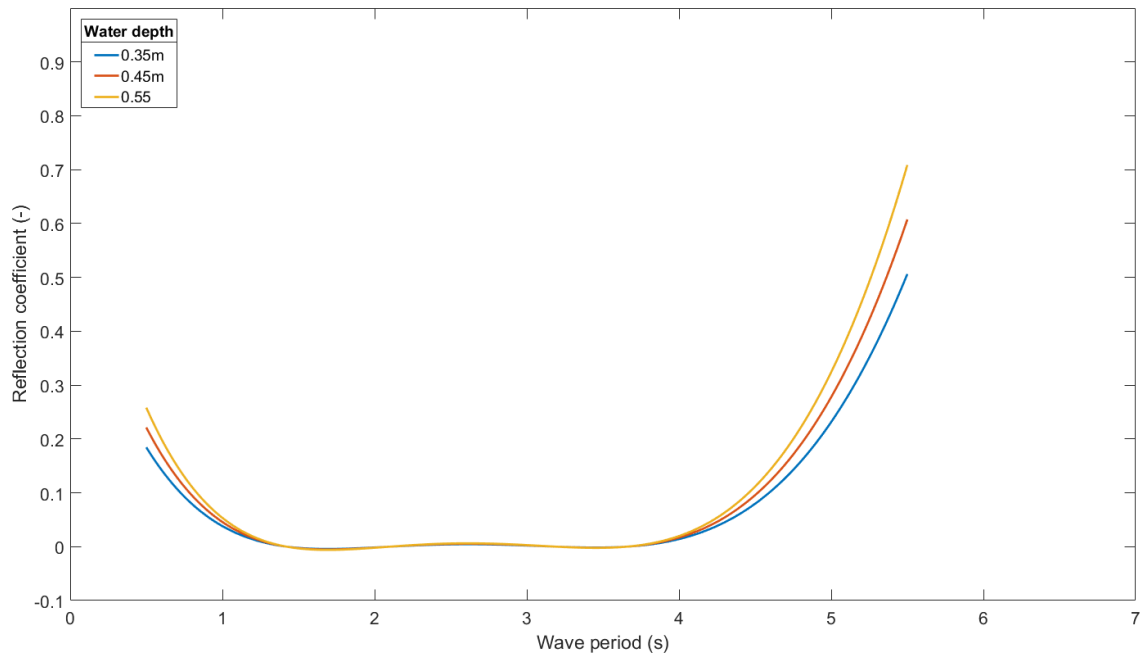


Figure 7-1: Wave absorber reflection vs incoming wave period (Figure derived from: Edinburgh Designs Ltd, 2005)

7.3 Experimental procedure

Given that measuring the amplification of the bed shear stress induced by a structure for a certain set of flow conditions over a rough bed is very difficult an indirect method for determining this amplification is followed in this study. This is explained below. Figure 7-2 presents the flow chart of the main steps followed during the tests.

Prior to initiating the experiments, the structure was installed in the middle of the flume and the scour protection was carefully laid around it. The pump was then slowly started and the flow was increased until the desired flow velocity was reached. The flow was then left for a minimum of 5min until it was stabilised. This was possible because the scour protection was large enough to withstand the bed shear stress induced by the flow.

In the case of tests which were conducted under the forcing of waves or waves and currents, regular waves were superimposed on the current. The initial waves had a certain wave period prescribed in the test programme and a wave height of 1mm. The wave height was then increased in increments of 2mm until incipient motion of the sediment was observed. It should be noted that in the context of this research moving

particles (i.e. undergoing incipient motion) are considered only if the particle is transported from its original location by more than 2 stone diameters ($\Delta x > 2D_{50}$).

In the case of the current only tests the mean current was increased by increments of $\sim 0.05\text{m/s}$ until the rock movement was initiated. After the test was completed the mean flow velocity profile was measured just upstream of the scour protection.

After the incipient motion was determined for a certain test a new structure was installed as specified in the experimental programme and the scour protection was repaired.

When a rock at a specific location just starts to move it means that the critical bed shear stress (τ_{crit}) at that location has just been reached. This means that the critical bed shear stress amplification (α_{crit}) for that structure can be determined by simply calculating the undisturbed bed shear stress (τ_{∞}) which leads to the incipient motion of the rock near the structure (i.e. exceedance of critical bed shear stress). This leads to a modified version of equation (2-39):

$$\alpha_{crit} = \frac{\tau_{crit}}{\tau_{\infty}} \quad (7-1)$$

This relation effectively shows by how much the bed shear stress of a certain set of undisturbed flow conditions gets amplified by the presence of the structure given that the rocks undergo incipient motion. The numerator in equation (7-1) can be determined using expressions (2-34) and (2-35), while the undisturbed bed shear stress can be determined using the following expressions depending on the flow conditions:

- Unidirectional current: Equation (2-5)
- Waves only: Equation (2-12)
- Combined waves and currents (2-26)

Due to the ambiguity in the definition of incipient motion and therefore critical bed shear stress (i.e. different authors define differently the criterion for which incipient motion is observed) Yalin's (1977) incipient motion criterion is adopted (Equation 2-33), which allows the quantitative definition of this condition.

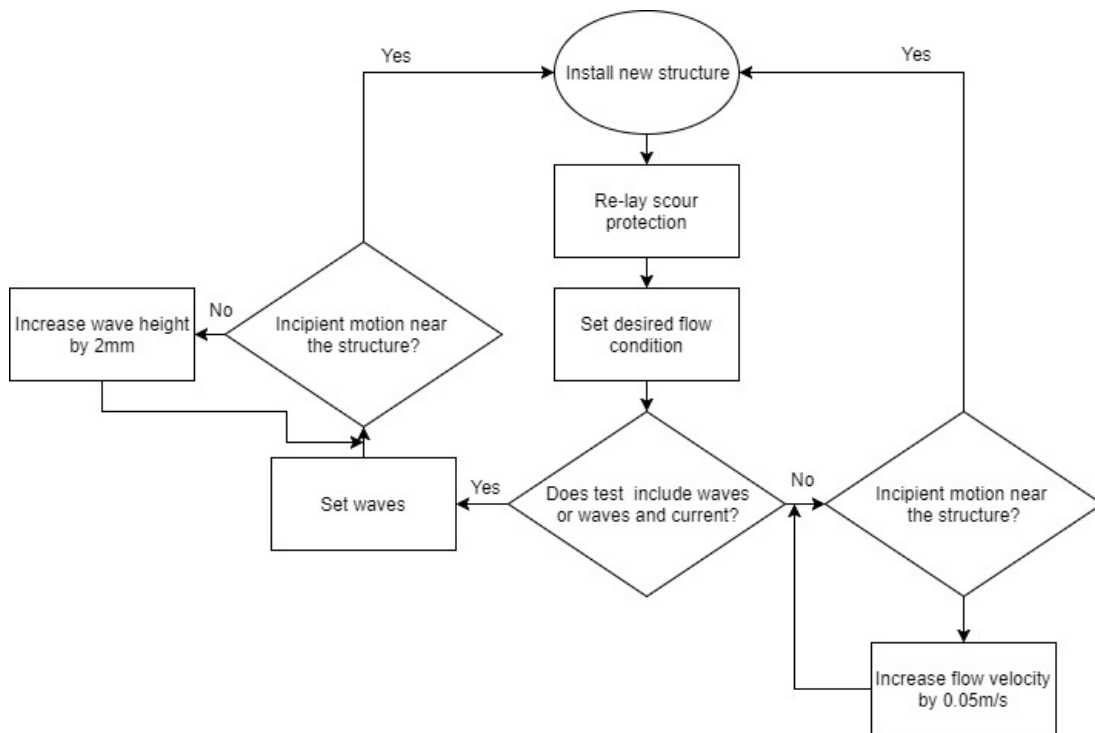


Figure 7-2: Flow chart of experimental procedure.

To investigate which flow conditions lead to the incipient motion of rocks near the structure, a set of test were conducted to examine the damage pattern induced by these conditions. This was done by continuing the tests after incipient motion was detected. The duration of the tests was approximately 10000 waves (both in the case of waves or waves and currents) or in the case of unidirectional currents 5hr as recommended by the DNV-OS-H204 manual. In the case where the scour protection at a point was completely eroded the test was stopped and the scour protection was declared “failed”. Given the long duration of these tests only a set of representative flow conditions were tested. This definition of failed scour protection was selected as GBFs cannot accommodate any scour due to their limited burial depth under the original bed.

7.4 Description of flume and the models

This section will provide an overview of the set-up of the flume and the procedures followed during the experiments.

The scour protection stability tests were conducted using the same flume and sand pit configuration as in the large scale scour tests. For a detailed description of the facility

and set up of the sand pit the reader is referred to section (4.4.1). Given that the present tests were conducted under the presence of waves and currents wave probes were installed upstream and downstream of the structure position (see Figure 7-3)

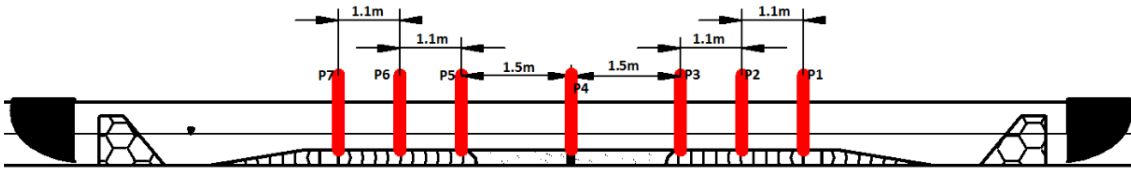


Figure 7-3: Positions of wave probes (red lines indicate position of the wave probes).

The sand pit was filled with the same fine sand used in the large scale scour tests and was smoothed flush with the top of the false bed. Two scour protection set-ups were used in this investigation. In the first case the scour protection was installed above the original bed level (Figure 7-4 a) while in the second it was installed flush with the original bed (Figure 7-4 b). It should be noted that the stickup height of the structure relative to the sand bed remained the same in both configurations. This meant the “true” stickup height in Figure 7-4 a was reduced by the thickness of the scour protection layer.

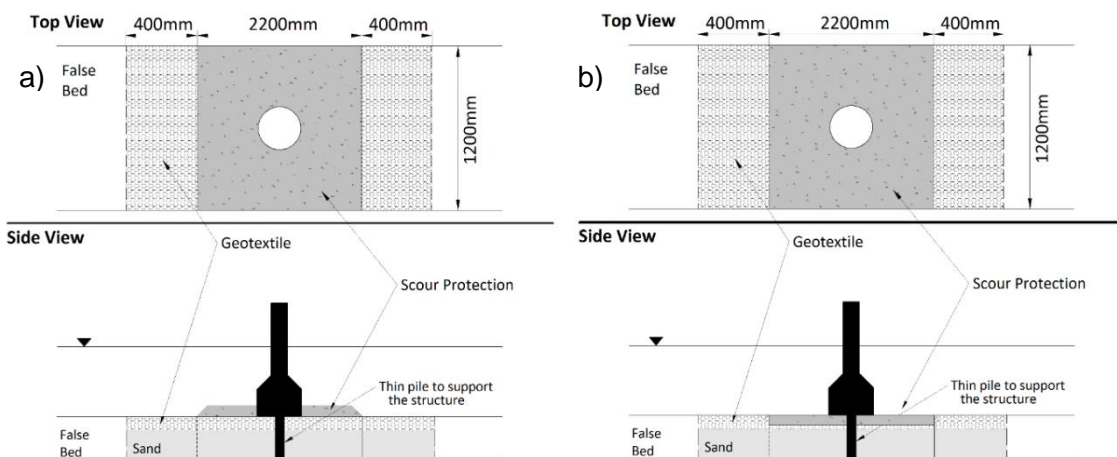


Figure 7-4: Layout of scour protection set-up for present tests.

Given that the stability tests were conducted at flow conditions that would mobilize the fine sediment the entire sand pit was covered with a geotextile with an apparent opening size of #120 (125 μ m). This contained the sediment under the cover layer while not

compromising the hydraulic conductivity of the bed. To ensure that the geotextile was fully tensioned and did not flap during the experiments it was stapled on the edges of the sand pit. In addition, U-pins were used to provide extra stability throughout the entire surface of the geotextile (see Figure 7-5). To prevent sediment from escaping the puncture holes created by the U-pins, a thin layer of silicon was used to seal potential gaps. After the geotextile was installed a small hole was opened over the point where the structure would be installed so it could be screwed into place in a similar way as for the scour experiments (section 4.3.1.2). The geotextile was then sprayed with an Nafion™ bonding agent and sprinkled with fine sand to create a roughness similar to that of the sandy bed. The advantage of the specific binding agent is that it is highly permeable to water which means the hydraulic conductivity of the sand bed would not be significantly compromised. To confirm this a constant head test was carried out with a sample of the geotextile which was laid over a sand sample. The test yielded a hydraulic conductivity of $4.53 * 10^{-3}$ cm/s which falls with the range of values expected for fine sand according to Bear (1972).



Figure 7-5: U-pins used to provide stability to the fabric.

Given that the present tests focused on the stability of the top layer of the scour protection, the scour protection layer extended across the entire width of the flume. This helped towards avoiding incipient motion of rock located at the side of the scour protection due to flow contraction between the side wall and the scour protection. The rock armour extended $5 D_{base}$ upstream and downstream of the structure. This length was selected to minimize the possibility of rock armour being destabilised by the transition between the original bed level and the scour protection. The leading and trailing slope of the scour protection had a slope of 30° to provide a smooth transition. Finally, coloured stones were placed concentrically around the structure to help identify the movement of rock armour elements. Figure 7-6 presents photographs of the scour protection layout. The scour protection material was flattened out using a scraper in a similar way described in section 4.4.1. The concentric circles with the coloured rocks were placed and flattened by hand.

A number of tests were also conducted with a scour protection set-up identical to that of Figure 7-4 (a) but without the sand pit. This was done to investigate the effect of permeability and of the ramp of the sand pit. For these tests a thin baseboard (20mm thickness) was installed centrally on the bed of the flume, the entire surface of which was roughened by gluing 0.2mm sand on it. The water depth for these tests was adjusted so that the water depth was 0.4m from the top of the base board. The structure was then screwed at its centre and the scour protection was installed around it in the same way as for the case mentioned above. Given the baseboard's limited thickness it was not possible to repeat the tests where the scour protection was flush with the bed using this apparatus. Figure 7-7 shows a sketch of this set-up.

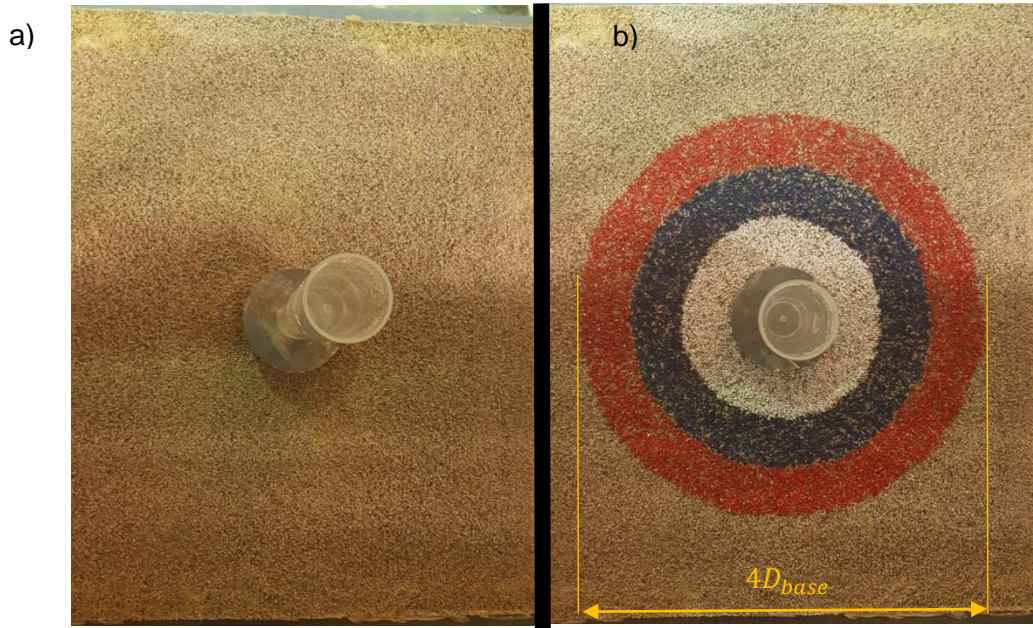


Figure 7-6: Rock armour layer set-up: a) first layer of scour protection b) final layout of scour protection with concentric circles.

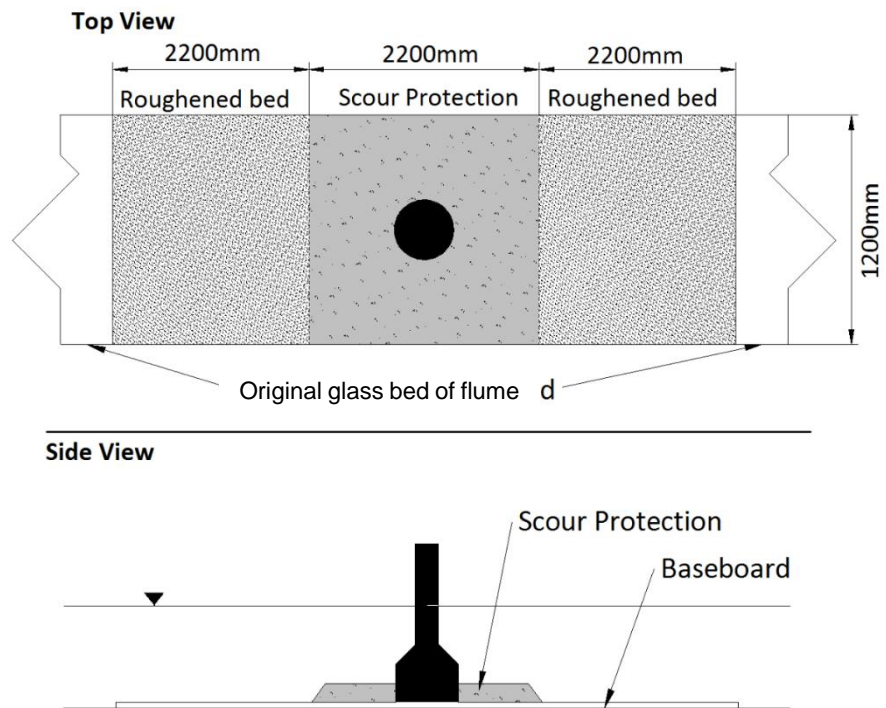


Figure 7-7: Test set-up without the sand pit.

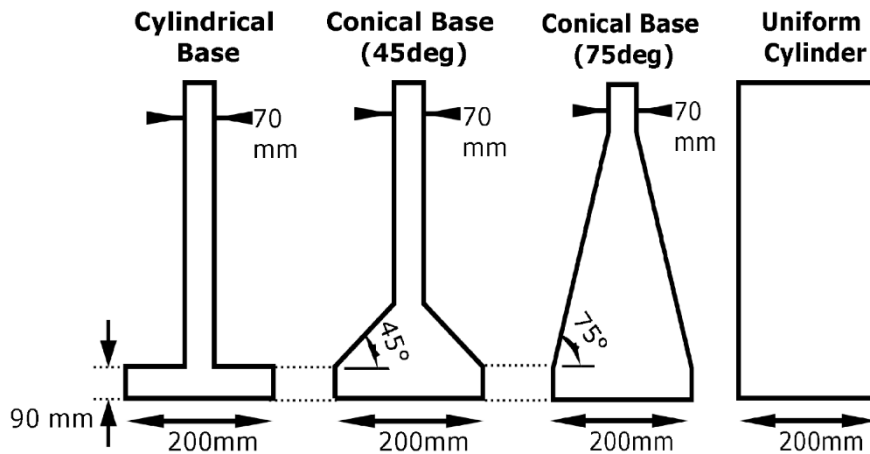


Figure 7-8: Large scale foundation geometries

7.5 Flow parameters

The range of hydraulic conditions considered in these tests is shown in Table 7-1. Regular waves were used because they tend to produce deeper scour than irregular waves and thus would provide more conservative results. This can be explained by the varying near bed oscillatory velocities which produce smaller time-averaged bed shear stresses and thus smaller scour depths (Sutherland and Whitehouse, 1998).

For this test series all current flow velocities were chosen to be in the clear water regime for the given scour protection material. The critical flow velocity for the sediments used in the tests was determined in accordance with the Soulsby (1997) method. And, prior to the scour tests, the critical Shields parameter was determined for a range of different combinations of waves and currents. This was done by setting a specific flow velocity and then gradually increasing the wave height until incipient motion was observed. The corresponding Shields parameter was determined according to the Soulsby method presented in section (2.2.4). The results of these tests are shown in Figure 7-9. It can be observed that the Shields diagram agrees well the observations with a maximum discrepancy of 10%.

Table 7-1: Summary of hydraulic conditions for scour protection stability tests

Parameter	Units	Range
H	M	0 – 0.16
T	S	1 – 3
H	M	0.4
U_c	m/s	-0.29 – 0.65
D_{50}	Mm	3.5 – 10.5

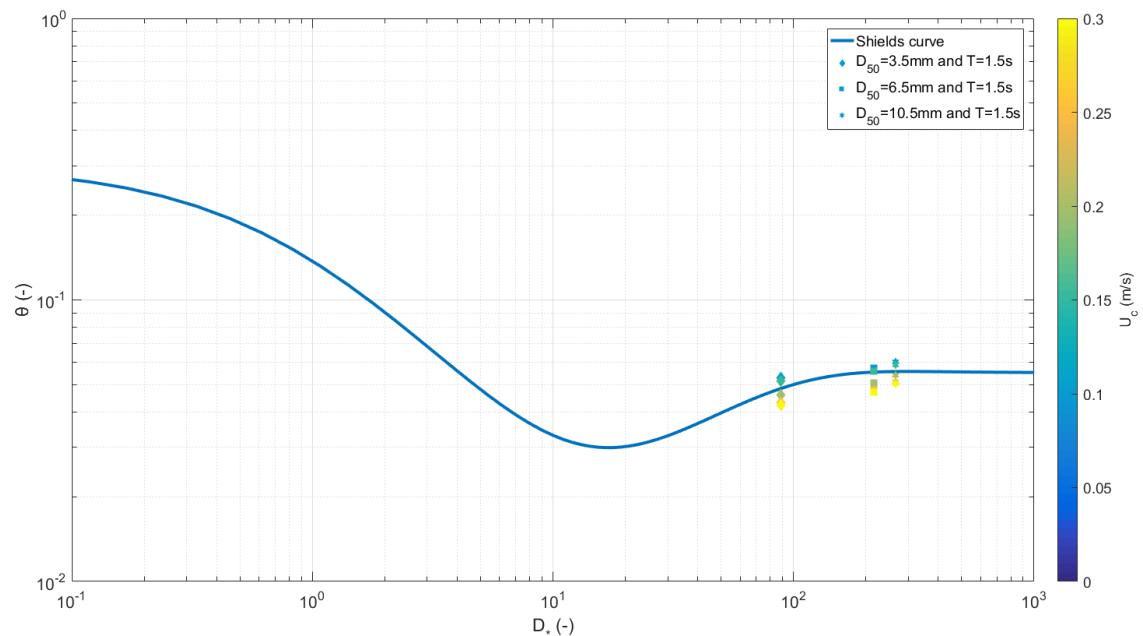


Figure 7-9: Comparison of Shields parameter with critical bed shear stress for a range of flow velocities.

All structures were tested at a water depth of 400mm (i.e. $h/D_{base}=2$) which in prototype conditions corresponds to a water depth of 35-40m. These depths are within the range in which a number of offshore wind GBFs have been built in the past (e.g. Albatros and Kårehamn offshore wind parks).

Three different stone sizes were used in the present tests. The mean stone size (D_{50}) for the aggregates was 3.5mm, 6.5mm and 10.5mm. Given that the purpose of the tests was to investigate the stability of the stones, the sediments were sieved to obtain the

narrowest grading possible. The resulting sediment distribution curves for each of the three sediments is shown in Figure 7-10. The stones for the scour protection were angular limestone of medium density. The density (ρ_s) for the 3.5mm and 6.5mm stones was 2500 kg/m³ and 2550 kg/m³ while the density for the larger 10.5mm aggregate was 2620 kg/m³.

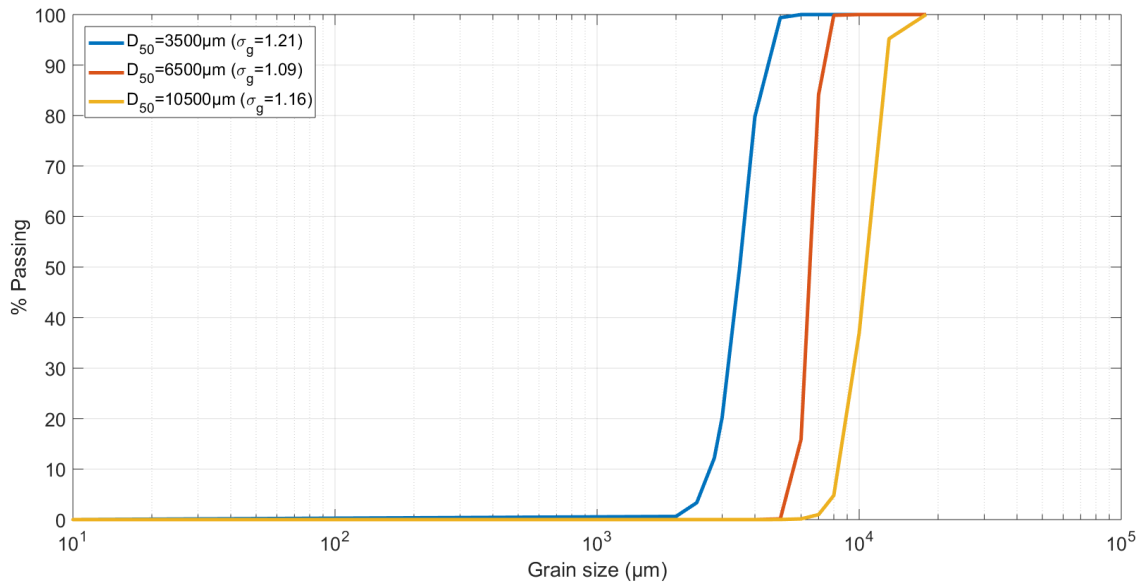


Figure 7-10: Grain size distribution for the scour protection aggregate used in the experiments.

7.6 Measuring techniques

This section provides a description of the measurement techniques used in the present experiments.

7.6.1 Detection of incipient motion for scour protection

To detect the incipient motion of the sediment two cameras were installed, one on either side of the flume at an angle of $\sim 45^\circ$ relative to the bed plane. This made it possible to monitor the full area surrounding the structure. Both cameras were connected to a PC and synchronised so that they could start and stop at the same time. After the installation of the scour protection and the structure the flow was increased with one of two ways:

- a) In the case of current only tests: by gradually increasing the undisturbed flow velocity in increments of approximately ~ 0.05 m/s.

- b) In the case of combined waves and currents or waves only: for a given set of wave period and undisturbed flow velocity the wave height was increased until the rocks started to move.

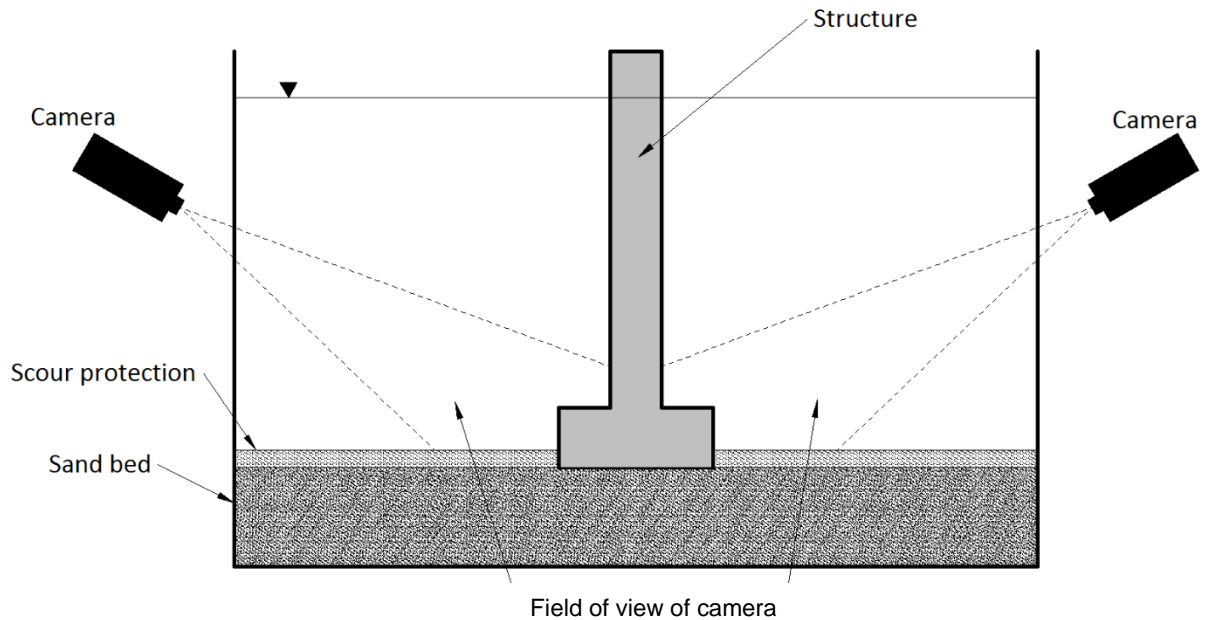


Figure 7-11: Set-up of incipient motion detection method for scour protection stability tests.

Incipient motion was then determined by subtracting two consecutive frames from the video recordings. If a rock particle had moved, then the subtraction of the two images would result in a cluster of pixels with non-zero values. Figure 7-12 presents a pair of consecutive frames from one of the tests along with the results of the subtraction of the two. As can be seen the movement of two rocks is clearly captured by this technique. By identifying the number of non-zero clusters (i.e. moving particles) recorded over a period of time (t) and area (A_D), incipient motion was able to be determined according to Yalin's criterion given in Equation (2-33). The advantage of Yalin's criterion is that it provides a quantitative criterion for defining incipient motion (ϵ). This means that for a certain set of experiments ϵ should be constant. Based on this rule, if a test was repeated with a larger rock size of the same specific gravity, then the ratio $m/(A_D t)$ should be decreased in order to maintain the same ϵ . Given that for the present tests the area of interest (A_D) was the entire scour protection surface. The values of the time interval (t) and the number

of displaced particles (m) were then chosen to yield the same value of ϵ . Table 7-2 provides the chosen values for these tests.

Table 7-2 Values used for determination of incipient motion criterion.

A_Ω (m ²)	t (s)	m (-)	D_{50} (mm)	ϵ (-)
0.502655	10	10	3.5	3.56^{-05}
0.502655	47	10	6.5	3.56^{-05}
0.502655	93	6	10.5	3.57^{-05}

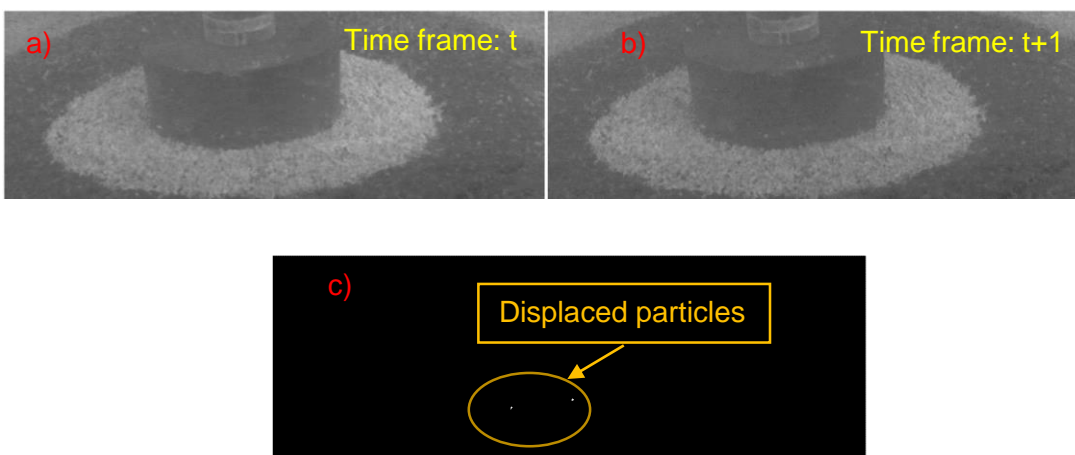


Figure 7-12: Example of particle tracking recognition: a) image at time frame t; b) image at time frame t+1; and c) result of the subtraction of the two images.

7.6.2 Flow velocity measurement

The current velocity flow profile for each flow condition was measured just upstream of the scour protection before the structure was screwed into place prior to each set of experiments. For a number of tests, the stability of the scour protection under the forcing of a unidirectional current was investigated. For these cases the flow velocity was gradually increased in increments of $\sim 0.05\text{m/s}$. Once incipient motion of the scour protection was observed the test was stopped and the full flow profile was measured 10cm upstream of the scour protection edge. All flow measurements were done using an ADV the working principle of which can be found in section 4.3.3.1

7.6.3 Measurement of scour protection damage

Stereophotogrammetry was used to measure the 3D damage pattern around the structures. The fundamental working principle of Stereophotogrammetry is triangulation. By taking photographs from a number of different positions lines of sight can be established between the camera and uniquely identifiable features of the object or terrain. The process mathematically intersects the lines of sight and produces a three-dimensional coordinate point cloud of the object. With this technique the position of an object is determined by different 2D photographs (see Figure 7-13). By taking a sufficient number of photographs this method can be used to determine the position of both the camera and the object/target at the same time. The position detection is based on targets and uniquely identifiable features located on the object (such as different color marks or rocks) which means that there is no need for a probing system. The advantage of this method is the high accuracy of the depth measurements which according to Cuypers et al. (2009) is 10^{-2} cm for a target measuring range smaller than 8×8 m. The disadvantage of this measuring technique is the long computational time required which can take up to 8hr on a conventional computer.

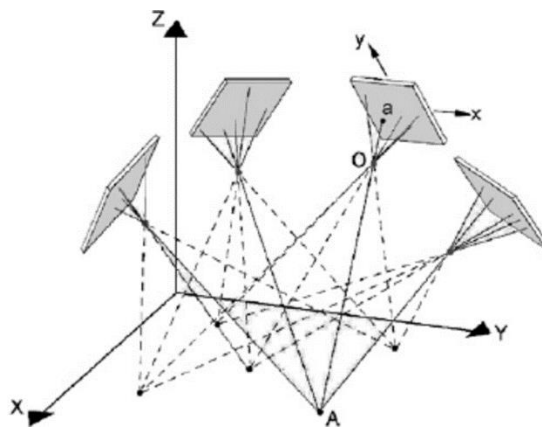


Figure 7-13: Working principle of photogrammetry [source: Cuypers et al. ,2009]

For these measurements a waterproof Canon PowerShot D20 camera was used. Photographs were taken from different heights and angles around the structure with a high overlapping ratio between them (over 80%). This enabled a robust computation of the coordinates. Given that the camera was hand-held, the experiments had to be

paused during the measurement in order to avoid disturbing the local hydrodynamics. To increase the accuracy of the method two scales were submerged into the flume prior to taking the photographs to assist in the calibration of the technique. For the analysis of the photographs Autodesk's Remake™ software was used.

7.6.4 Wave measurements

The water depth was determined in the same way as for the scour experiments. Rulers were attached externally on the side wall of the flume and the water depth was determined by averaging the water depth across all the measuring points to account for the effect of the hydraulic gradient. Given that the structure was installed in the middle of the flume the spatially averaged water depth matched the water depth recorded at the ruler closest to the structure.

The measurement of the wave heights was done using resistance type wave gauges which were calibrated every day prior to initiating the experiments. The probes were positioned along the flume at the locations indicated in Figure 7-3 and at a distance 10cm from the side wall of the flume. The positions from the structure and between them was selected to comply with the Goda and Suzuki (1976) method for the calculation of the incident and reflected wave height.

7.7 Experiment programme

Table 7-3 presents the detailed experimental programme for the scour protection stability tests. The tests are designed to look into the effects of several hydraulic parameters on the stability of the scour protection material:

- Flow direction: the direction of the flow relative to the direction of the wave propagation was changed in some cases with the waves following (positive sign) and others opposing (negative sign) the mean flow current.
- Wave period: a range of wave periods were tested to investigate the effect of the wavelength on rock stability.
- Rock size: three rock sizes were tested.
- Relative current speed: different mean flow velocities (U_{cw}) were tested.

- Scour protection configuration: the effect of the stick-up height of the scour protection was tested by using two configurations (flush with bed and above the bed).
- Bed type: the effect of bed permeability was investigated by conducted tests over a sandy bed with a geotextile on top to stabilise the sand and over a solid bed.

Table 7-3: Experimental programme for scour protection stability tests.

No	Scour protection configuration	Bed type	Structure	D_{50}	U_c	h	T
(-)	(-)	(-)	(-)	(mm)	(m/s)	(m)	(s)
5.1	Above	Geotextile	Cyl. Base	3.5	0	0.4	1.2
5.2	Above	Geotextile	45° con. Base	3.5	0	0.4	1.2
5.3	Above	Geotextile	75° con. Base	3.5	0	0.4	1.2
5.4	Above	Geotextile	Cyl. Base	3.5	0.18	0.4	1.2
5.5	Above	Geotextile	45° con. Base	3.5	0.18	0.4	1.2
5.6	Above	Geotextile	75° con. Base	3.5	0.18	0.4	1.2
5.7	Above	Geotextile	Monopile	3.5	0.18	0.4	1.2
5.8	Above	Geotextile	Cyl. Base	3.5	0.29	0.4	1.2
5.9	Above	Geotextile	45° con. Base	3.5	0.29	0.4	1.2
5.10	Above	Geotextile	75° con. Base	3.5	0.29	0.4	1.2
5.11	Above	Geotextile	Monopile	3.5	0.26	0.4	1.2
5.12	Above	Geotextile	Cyl. base	3.5	0	0.4	1.5
5.13	Above	Geotextile	45° con. base	3.5	0	0.4	1.5
5.14	Above	Geotextile	75° con. base	3.5	0	0.4	1.5
5.15	Above	Geotextile	Monopile	3.5	0	0.4	1.5
5.16	Above	Geotextile	Cyl. base	3.5	0.18	0.4	1.5
5.17	Above	Geotextile	45° con. base	3.5	0.18	0.4	1.5
5.18	Above	Geotextile	75° con. base	3.5	0.18	0.4	1.5
5.19	Above	Geotextile	Monopile	3.5	0.18	0.4	1.5
5.20	Above	Geotextile	Cyl. base	3.5	0.29	0.4	1.5
5.21	Above	Geotextile	45° con. base	3.5	0.29	0.4	1.5
5.22	Above	Geotextile	75° con. base	3.5	0.29	0.4	1.5
5.23	Above	Geotextile	Monopile	3.5	0.26	0.4	1.5
5.24	Above	Geotextile	Cyl. base	3.5	0	0.4	2
5.25	Above	Geotextile	45° con. base	3.5	0	0.4	2
5.26	Above	Geotextile	75° con. base	3.5	0	0.4	2
5.27	Above	Geotextile	Monopile	3.5	0	0.4	2
5.28	Above	Geotextile	Cyl. base	3.5	0.18	0.4	2
5.29	Above	Geotextile	45° con. base	3.5	0.18	0.4	2
5.30	Above	Geotextile	75° con. base	3.5	0.18	0.4	2
5.31	Above	Geotextile	Monopile	3.5	0.18	0.4	2
5.32	Above	Geotextile	Cyl. base	3.5	0.29	0.4	2
5.33	Above	Geotextile	45° con. base	3.5	0.29	0.4	2
5.34	Above	Geotextile	75° con. base	3.5	0.29	0.4	2
5.35	Above	Geotextile	Monopile	3.5	0.26	0.4	2

5.36	above	Geotextile	Cyl. base	6.5	0	0.4	1.2
5.37	above	Geotextile	45° con. base	6.5	0	0.4	1.2
5.38	above	Geotextile	75° con. base	6.5	0	0.4	1.2
5.39	above	Geotextile	Monopile	6.5	0	0.4	1.2
5.40	above	Geotextile	Cyl. base	6.5	0.18	0.4	1.2
5.41	above	Geotextile	45° con. base	6.5	0.18	0.4	1.2
5.42	above	Geotextile	75° con. base	6.5	0.18	0.4	1.2
5.43	above	Geotextile	Monopile	6.5	0.18	0.4	1.2
5.44	above	Geotextile	Cyl. base	6.5	-0.18	0.4	1.2
5.45	above	Geotextile	45° con. base	6.5	-0.18	0.4	1.2
5.46	above	Geotextile	75° con. base	6.5	-0.18	0.4	1.2
5.47	above	Geotextile	Monopile	6.5	-0.18	0.4	1.2
5.48	above	Geotextile	Cyl. base	6.5	0.29	0.4	1.2
5.49	above	Geotextile	45° con. base	6.5	0.29	0.4	1.2
5.50	above	Geotextile	75° con. base	6.5	0.29	0.4	1.2
5.51	above	Geotextile	Monopile	6.5	-0.29	0.4	1.2
5.52	above	Geotextile	Cyl. base	6.5	0	0.4	1.5
5.53	above	Geotextile	45° con. base	6.5	0	0.4	1.5
5.54	above	Geotextile	75° con. base	6.5	0	0.4	1.5
5.55	above	Geotextile	Monopile	6.5	0	0.4	1.5
5.56	above	Geotextile	Cyl. base	6.5	0.18	0.4	1.5
5.57	above	Geotextile	45° con. base	6.5	0.18	0.4	1.5
5.58	above	Geotextile	75° con. base	6.5	0.18	0.4	1.5
5.59	above	Geotextile	Monopile	6.5	0.18	0.4	1.5
5.60	above	Geotextile	Cyl. base	6.5	-0.18	0.4	1.5
5.61	above	Geotextile	45° con. base	6.5	-0.18	0.4	1.5
5.62	above	Geotextile	75° con. base	6.5	-0.18	0.4	1.5
5.63	above	Geotextile	Monopile	6.5	-0.18	0.4	1.5
5.64	above	Geotextile	Cyl. base	6.5	0.29	0.4	1.5
5.65	above	Geotextile	45° con. base	6.5	0.29	0.4	1.5
5.66	above	Geotextile	75° con. base	6.5	0.29	0.4	1.5
5.67	above	Geotextile	Cyl. base	6.5	-0.29	0.4	1.5
5.68	above	Geotextile	45° con. base	6.5	-0.29	0.4	1.5
5.69	above	Geotextile	75° con. base	6.5	-0.29	0.4	1.5
5.70	above	Geotextile	0	6.5	0	0.4	1.5
5.71	above	Geotextile	Cyl. base	6.5	0	0.4	2
5.72	above	Geotextile	45° con. base	6.5	0	0.4	2
5.73	above	Geotextile	75° con. base	6.5	0	0.4	2
5.74	above	Geotextile	Monopile	6.5	0	0.4	2
5.75	above	Geotextile	Cyl. base	6.5	0.18	0.4	2
5.76	above	Geotextile	45° con. base	6.5	0.18	0.4	2
5.77	above	Geotextile	75° con. base	6.5	0.18	0.4	2
5.78	above	Geotextile	Monopile	6.5	0.18	0.4	2
5.79	above	Geotextile	Cyl. base	6.5	-0.18	0.4	2
5.80	above	Geotextile	45° con. base	6.5	-0.18	0.4	2
5.81	above	Geotextile	75° con. base	6.5	-0.18	0.4	2
5.82	above	Geotextile	Monopile	6.5	-0.18	0.4	2

5.83	Above	Geotextile	Cyl. base	6.5	0.29	0.4	2
5.84	Above	Geotextile	45° con. base	6.5	0.29	0.4	2
5.85	Above	Geotextile	75° con. base	6.5	0.29	0.4	2
5.86	Above	Geotextile	Monopile	6.5	0.29	0.4	2
5.87	Above	Geotextile	Cyl. base	6.5	-0.29	0.4	2
5.88	Above	Geotextile	45° con. base	6.5	-0.29	0.4	2
5.89	Above	Geotextile	75° con. base	6.5	-0.29	0.4	2
5.90	Above	Geotextile	Monopile	6.5	-0.29	0.4	2
5.91	Above	Geotextile	Cyl. base	6.5	0.55	0.4	0
5.92	Above	Geotextile	45° con. base	6.5	0.45	0.4	0
5.93	Above	Geotextile	75° con. base	6.5	0.40	0.4	0
5.94	Above	Geotextile	Monopile	6.5	0.39	0.4	0
5.95	Above	Geotextile	Cyl. base	10.5	0	0.4	1.5
5.96	Above	Geotextile	45° con. base	10.5	0	0.4	1.5
5.97	Above	Geotextile	75° con. base	10.5	0	0.4	1.5
5.98	Above	Geotextile	Monopile	10.5	0	0.4	1.5
5.99	Above	Geotextile	Cyl. base	10.5	0.18	0.4	1.5
5.100	Above	Geotextile	45° con. base	10.5	0.18	0.4	1.5
5.101	Above	Geotextile	75° con. base	10.5	0.18	0.4	1.5
5.102	Above	Geotextile	Monopile	10.5	0.18	0.4	1.5
5.103	Above	Geotextile	Cyl. base	10.5	-0.18	0.4	1.5
5.104	Above	Geotextile	45° con. base	10.5	-0.18	0.4	1.5
5.105	Above	Geotextile	75° con. base	10.5	-0.18	0.4	1.5
5.106	Above	Geotextile	Monopile	10.5	-0.18	0.4	1.5
5.107	Above	Geotextile	Cyl. base	10.5	0.29	0.4	1.5
5.108	Above	Geotextile	45° con. base	10.5	0.29	0.4	1.5
5.109	Above	Geotextile	75° con. base	10.5	0.29	0.4	1.5
5.110	Above	Geotextile	Monopile	10.5	0.29	0.4	1.5
5.111	Above	Geotextile	Cyl. base	10.5	-0.29	0.4	1.5
5.112	Above	Geotextile	45° con. base	10.5	-0.29	0.4	1.5
5.113	Above	Geotextile	75° con. base	10.5	-0.29	0.4	1.5
5.114	Above	Geotextile	Monopile	10.5	-0.29	0.4	1.5
5.115	Above	Geotextile	Cyl. base	10.5	0	0.4	2
5.116	Above	Geotextile	45° con. base	10.5	0	0.4	2
5.117	Above	Geotextile	75° con. base	10.5	0	0.4	2
5.118	Above	Geotextile	Monopile	10.5	0	0.4	2
5.119	Above	Geotextile	Cyl. base	10.5	0.18	0.4	2
5.120	Above	Geotextile	45° con. base	10.5	0.18	0.4	2
5.121	Above	Geotextile	75° con. base	10.5	0.18	0.4	2
5.122	Above	Geotextile	Monopile	10.5	0.18	0.4	2
5.123	Above	Geotextile	Cyl. base	10.5	-0.18	0.4	2
5.124	Above	Geotextile	45° con. base	10.5	-0.18	0.4	2
5.125	Above	Geotextile	75° con. base	10.5	-0.18	0.4	2
5.126	Above	Geotextile	Monopile	10.5	-0.18	0.4	2
5.127	Above	Geotextile	Cyl. base	10.5	0.29	0.4	2
5.128	Above	Geotextile	45° con. base	10.5	0.29	0.4	2
5.129	Above	Geotextile	75° con. base	10.5	0.29	0.4	2

5.130	above	Geotextile	Monopile	10.5	0.29	0.4	2
5.131	above	Geotextile	Cyl. base	10.5	-0.29	0.4	2
5.132	above	Geotextile	45° con. base	10.5	-0.29	0.4	2
5.133	above	Geotextile	75° con. base	10.5	-0.29	0.4	2
5.134	above	Geotextile	Cyl. base	10.5	0	0.4	2.5
5.135	above	Geotextile	45° con. base	10.5	0	0.4	2.5
5.136	above	Geotextile	75° con. base	10.5	0	0.4	2.5
5.137	above	Geotextile	Monopile	10.5	0	0.4	2.5
5.138	above	Geotextile	Cyl. base	10.5	0.18	0.4	2.5
5.139	above	Geotextile	45° con. base	10.5	0.18	0.4	2.5
5.140	above	Geotextile	75° con. base	10.5	0.18	0.4	2.5
5.141	above	Geotextile	Monopile	10.5	0.18	0.4	2.5
5.142	above	Geotextile	Cyl. base	10.5	-0.18	0.4	2.5
5.143	above	Geotextile	45° con. base	10.5	-0.18	0.4	2.5
5.144	above	Geotextile	75° con. base	10.5	-0.18	0.4	2.5
5.145	above	Geotextile	Monopile	10.5	-0.18	0.4	2.5
5.146	above	Geotextile	Cyl. base	10.5	0.29	0.4	2.5
5.147	above	Geotextile	45° con. base	10.5	0.29	0.4	2.5
5.148	above	Geotextile	75° con. base	10.5	0.29	0.4	2.5
5.149	above	Geotextile	Monopile	10.5	0.29	0.4	2.5
5.150	above	Geotextile	Cyl. base	10.5	-0.29	0.4	2.5
5.151	above	Geotextile	45° con. base	10.5	-0.29	0.4	2.5
5.152	above	Geotextile	75° con. base	10.5	-0.29	0.4	2.5
5.153	above	Geotextile	Monopile	10.5	0	0.4	2.5
5.154	above	Geotextile	Cyl. base	10.5	0.65	0.4	0
5.155	above	Geotextile	45° con. base	10.5	0.56	0.4	0
5.156	above	Geotextile	75° con. base	10.5	0.50	0.4	0
5.157	above	Geotextile	Monopile	10.5	0.49	0.4	0
5.158	flush	Geotextile	75° con. base	6.5	0	0.4	1.4
5.159	flush	Geotextile	75° con. base	6.5	0	0.4	1.6
5.160	flush	Geotextile	75° con. base	6.5	0	0.4	1.8
5.161	flush	Geotextile	75° con. base	6.5	0	0.4	2
5.162	flush	Geotextile	75° con. base	6.5	0	0.4	2.2
5.163	flush	Geotextile	75° con. base	6.5	0	0.4	2.4
5.164	flush	Geotextile	75° con. base	6.5	0	0.4	2.6
5.165	flush	Geotextile	75° con. base	6.5	0	0.4	2.8
5.166	flush	Geotextile	75° con. base	6.5	0	0.4	3
5.167	flush	Geotextile	75° con. base	6.5	0.17	0.4	1.4
5.168	flush	Geotextile	75° con. base	6.5	0.17	0.4	1.6
5.169	flush	Geotextile	75° con. base	6.5	0.17	0.4	1.8
5.170	flush	Geotextile	75° con. base	6.5	0.17	0.4	2
5.171	flush	Geotextile	75° con. base	6.5	0.17	0.4	2.2
5.172	flush	Geotextile	75° con. base	6.5	0.17	0.4	2.4
5.173	flush	Geotextile	75° con. base	6.5	0.17	0.4	2.6
5.174	flush	Geotextile	75° con. base	6.5	0.17	0.4	2.8
5.175	flush	Geotextile	75° con. base	6.5	0.17	0.4	3
5.176	flush	Geotextile	75° con. base	6.5	0.22	0.4	1.4

5.177	Flush	Geotextile	75° con. base	6.5	0.22	0.4	1.6
5.178	Flush	Geotextile	75° con. base	6.5	0.22	0.4	1.8
5.179	Flush	Geotextile	75° con. base	6.5	0.22	0.4	2
5.180	Flush	Geotextile	75° con. base	6.5	0.22	0.4	2.2
5.181	Flush	Geotextile	75° con. base	6.5	0.22	0.4	2.4
5.182	Flush	Geotextile	75° con. base	6.5	0.22	0.4	2.6
5.183	Flush	Geotextile	75° con. base	6.5	0.22	0.4	2.8
5.184	Flush	Geotextile	75° con. base	6.5	0.22	0.4	3
5.185	Flush	Geotextile	75° con. base	6.5	0.27	0.4	1.4
5.186	Flush	Geotextile	75° con. base	6.5	0.27	0.4	1.6
5.187	Flush	Geotextile	75° con. base	6.5	0.27	0.4	1.8
5.188	Flush	Geotextile	75° con. base	6.5	0.27	0.4	2
5.189	Flush	Geotextile	75° con. base	6.5	0.27	0.4	2.2
5.190	Flush	Geotextile	75° con. base	6.5	0.27	0.4	2.4
5.191	Flush	Geotextile	75° con. base	6.5	0.27	0.4	2.6
5.192	Flush	Geotextile	75° con. base	6.5	0.27	0.4	2.8
5.193	Flush	Geotextile	75° con. base	6.5	0.27	0.4	3
5.194	Flush	Geotextile	75° con. base	6.5	0.32	0.4	1.4
5.195	Flush	Geotextile	75° con. base	6.5	0.32	0.4	1.6
5.196	Flush	Geotextile	75° con. base	6.5	0.32	0.4	1.8
5.197	Flush	Geotextile	75° con. base	6.5	0.32	0.4	2
5.198	Flush	Geotextile	75° con. base	6.5	0.32	0.4	2.2
5.199	Flush	Geotextile	75° con. base	6.5	0.32	0.4	2.4
5.200	Flush	Geotextile	75° con. base	6.5	0.32	0.4	2.6
5.201	Flush	Geotextile	75° con. base	6.5	0.32	0.4	2.8
5.202	Flush	Geotextile	75° con. base	6.5	0.32	0.4	3
5.203	Flush	Geotextile	75° con. base	6.5	0.4	0.4	1.4
5.204	Flush	Geotextile	75° con. base	6.5	0.4	0.4	1.6
5.205	Flush	Geotextile	75° con. base	6.5	0.4	0.4	1.8
5.206	Flush	Geotextile	75° con. base	6.5	0.4	0.4	2
5.207	Flush	Geotextile	75° con. base	6.5	0.4	0.4	2.2
5.208	Flush	Geotextile	75° con. base	6.5	0.4	0.4	2.4
5.209	Flush	Geotextile	75° con. base	6.5	0.4	0.4	2.6
5.210	Flush	Geotextile	75° con. base	6.5	0.4	0.4	2.8
5.211	Flush	Geotextile	75° con. base	6.5	0.4	0.4	3
5.212	Flush	Geotextile	75° con. base	6.5	0.08	0.4	1.4
5.213	Flush	Geotextile	75° con. base	6.5	0.08	0.4	1.6
5.214	Flush	Geotextile	75° con. base	6.5	0.08	0.4	1.8
5.215	Flush	Geotextile	75° con. base	6.5	0.08	0.4	2
5.216	Flush	Geotextile	75° con. base	6.5	0.08	0.4	2.2
5.217	Flush	Geotextile	75° con. base	6.5	0.08	0.4	2.4
5.218	Flush	Geotextile	75° con. base	6.5	0.08	0.4	2.6
5.219	Flush	Geotextile	75° con. base	6.5	0.08	0.4	2.8
5.220	Flush	Geotextile	75° con. base	6.5	0.08	0.4	3
5.221	Flush	Geotextile	75° con. base	6.5	0.12	0.4	1.4
5.222	Flush	Geotextile	75° con. base	6.5	0.12	0.4	1.6
5.223	Flush	Geotextile	75° con. base	6.5	0.12	0.4	1.8

5.224	flush	Geotextile	75° con. base	6.5	0.12	0.4	2
5.225	flush	Geotextile	75° con. base	6.5	0.12	0.4	2.2
5.226	flush	Geotextile	75° con. base	6.5	0.12	0.4	2.4
5.227	flush	Geotextile	75° con. base	6.5	0.12	0.4	2.6
5.228	flush	Geotextile	75° con. base	6.5	0.12	0.4	2.8
5.229	flush	Geotextile	75° con. base	6.5	0.12	0.4	3
5.230	flush	Geotextile	Monopile	6.5	0	0.4	1.4
5.231	flush	Geotextile	Monopile	6.5	0	0.4	1.6
5.232	flush	Geotextile	Monopile	6.5	0	0.4	1.8
5.233	flush	Geotextile	Monopile	6.5	0	0.4	2
5.234	flush	Geotextile	Monopile	6.5	0	0.4	2.2
5.235	flush	Geotextile	Monopile	6.5	0	0.4	2.4
5.236	flush	Geotextile	Monopile	6.5	0	0.4	2.6
5.237	flush	Geotextile	Monopile	6.5	0	0.4	2.8
5.238	flush	Geotextile	Monopile	6.5	0	0.4	3
5.239	flush	Geotextile	Monopile	6.5	0.17	0.4	1.4
5.240	flush	Geotextile	Monopile	6.5	0.17	0.4	1.6
5.241	flush	Geotextile	Monopile	6.5	0.17	0.4	1.8
5.242	flush	Geotextile	Monopile	6.5	0.17	0.4	2
5.243	flush	Geotextile	Monopile	6.5	0.17	0.4	2.2
5.244	flush	Geotextile	Monopile	6.5	0.17	0.4	2.4
5.245	flush	Geotextile	Monopile	6.5	0.17	0.4	2.6
5.246	flush	Geotextile	Monopile	6.5	0.17	0.4	2.8
5.247	flush	Geotextile	Monopile	6.5	0.17	0.4	3
5.248	flush	Geotextile	Monopile	6.5	0.22	0.4	1.4
5.249	flush	Geotextile	Monopile	6.5	0.22	0.4	1.6
5.250	flush	Geotextile	Monopile	6.5	0.22	0.4	1.8
5.251	flush	Geotextile	Monopile	6.5	0.22	0.4	2
5.252	flush	Geotextile	Monopile	6.5	0.22	0.4	2.2
5.253	flush	Geotextile	Monopile	6.5	0.22	0.4	2.4
5.254	flush	Geotextile	Monopile	6.5	0.22	0.4	2.6
5.255	flush	Geotextile	Monopile	6.5	0.22	0.4	2.8
5.256	flush	Geotextile	Monopile	6.5	0.22	0.4	3
5.257	flush	Geotextile	Monopile	6.5	0.27	0.4	1.4
5.258	flush	Geotextile	Monopile	6.5	0.27	0.4	1.6
5.259	flush	Geotextile	Monopile	6.5	0.27	0.4	1.8
5.260	flush	Geotextile	Monopile	6.5	0.27	0.4	2
5.261	flush	Geotextile	Monopile	6.5	0.27	0.4	2.2
5.262	flush	Geotextile	Monopile	6.5	0.27	0.4	2.4
5.263	flush	Geotextile	Monopile	6.5	0.27	0.4	2.6
5.264	flush	Geotextile	Monopile	6.5	0.27	0.4	2.8
5.265	flush	Geotextile	Monopile	6.5	0.27	0.4	3
5.266	flush	Geotextile	Monopile	6.5	0.32	0.4	1.4
5.267	flush	Geotextile	Monopile	6.5	0.32	0.4	1.6
5.268	flush	Geotextile	Monopile	6.5	0.32	0.4	1.8
5.269	flush	Geotextile	Monopile	6.5	0.32	0.4	2
5.270	flush	Geotextile	Monopile	6.5	0.32	0.4	2.2

5.271	Flush	Geotextile	Monopile	6.5	0.32	0.4	2.4
5.272	Flush	Geotextile	Monopile	6.5	0.32	0.4	2.6
5.273	Flush	Geotextile	Monopile	6.5	0.32	0.4	2.8
5.274	Flush	Geotextile	Monopile	6.5	0.32	0.4	3
5.275	Flush	Geotextile	Monopile	6.5	0.4	0.4	1.4
5.276	Flush	Geotextile	Monopile	6.5	0.4	0.4	1.6
5.277	Flush	Geotextile	Monopile	6.5	0.4	0.4	1.8
5.278	Flush	Geotextile	Monopile	6.5	0.4	0.4	2
5.279	Flush	Geotextile	Monopile	6.5	0.4	0.4	2.2
5.280	Flush	Geotextile	Monopile	6.5	0.4	0.4	2.4
5.281	Flush	Geotextile	Monopile	6.5	0.4	0.4	2.6
5.282	Flush	Geotextile	Monopile	6.5	0.4	0.4	2.8
5.283	Flush	Geotextile	Monopile	6.5	0.4	0.4	3
5.284	Flush	Geotextile	Monopile	6.5	0.08	0.4	1.4
5.285	Flush	Geotextile	Monopile	6.5	0.08	0.4	1.6
5.286	Flush	Geotextile	Monopile	6.5	0.08	0.4	1.8
5.287	Flush	Geotextile	Monopile	6.5	0.08	0.4	2
5.288	Flush	Geotextile	Monopile	6.5	0.08	0.4	2.2
5.289	Flush	Geotextile	Monopile	6.5	0.08	0.4	2.4
5.290	Flush	Geotextile	Monopile	6.5	0.08	0.4	2.6
5.291	Flush	Geotextile	Monopile	6.5	0.08	0.4	2.8
5.292	Flush	Geotextile	Monopile	6.5	0.08	0.4	3
5.293	Flush	Geotextile	Monopile	6.5	0.12	0.4	1.4
5.294	Flush	Geotextile	Monopile	6.5	0.12	0.4	1.6
5.295	Flush	Geotextile	Monopile	6.5	0.12	0.4	1.8
5.296	Flush	Geotextile	Monopile	6.5	0.12	0.4	2
5.297	Flush	Geotextile	Monopile	6.5	0.12	0.4	2.2
5.298	Flush	Geotextile	Monopile	6.5	0.12	0.4	2.4
5.299	Flush	Geotextile	Monopile	6.5	0.12	0.4	2.6
5.300	Flush	Geotextile	Monopile	6.5	0.12	0.4	2.8
5.301	Flush	Geotextile	Monopile	6.5	0.12	0.4	3
5.302	Flush	Geotextile	45° con. base	6.5	0	0.4	1.4
5.303	Flush	Geotextile	45° con. base	6.5	0	0.4	1.6
5.304	Flush	Geotextile	45° con. base	6.5	0	0.4	1.8
5.305	Flush	Geotextile	45° con. base	6.5	0	0.4	2
5.306	Flush	Geotextile	45° con. base	6.5	0	0.4	2.2
5.307	Flush	Geotextile	45° con. base	6.5	0	0.4	2.4
5.308	Flush	Geotextile	45° con. base	6.5	0	0.4	2.6
5.309	Flush	Geotextile	45° con. base	6.5	0	0.4	2.8
5.310	Flush	Geotextile	45° con. base	6.5	0	0.4	3
5.311	Flush	Geotextile	45° con. base	6.5	0.17	0.4	1.4
5.312	Flush	Geotextile	45° con. base	6.5	0.17	0.4	1.6
5.313	Flush	Geotextile	45° con. base	6.5	0.17	0.4	1.8
5.314	Flush	Geotextile	45° con. base	6.5	0.17	0.4	2
5.315	Flush	Geotextile	45° con. base	6.5	0.17	0.4	2.2
5.316	Flush	Geotextile	45° con. base	6.5	0.17	0.4	2.4
5.317	Flush	Geotextile	45° con. base	6.5	0.17	0.4	2.6

5.318	flush	Geotextile	45° con. base	6.5	0.17	0.4	2.8
5.319	flush	Geotextile	45° con. base	6.5	0.17	0.4	3
5.320	flush	Geotextile	45° con. base	6.5	0.22	0.4	1.4
5.321	flush	Geotextile	45° con. base	6.5	0.22	0.4	1.6
5.322	flush	Geotextile	45° con. base	6.5	0.22	0.4	1.8
5.323	flush	Geotextile	45° con. base	6.5	0.22	0.4	2
5.324	flush	Geotextile	45° con. base	6.5	0.22	0.4	2.2
5.325	flush	Geotextile	45° con. base	6.5	0.22	0.4	2.4
5.326	flush	Geotextile	45° con. base	6.5	0.22	0.4	2.6
5.327	flush	Geotextile	45° con. base	6.5	0.22	0.4	2.8
5.328	flush	Geotextile	45° con. base	6.5	0.22	0.4	3
5.329	flush	Geotextile	45° con. base	6.5	0.27	0.4	1.4
5.330	flush	Geotextile	45° con. base	6.5	0.27	0.4	1.6
5.331	flush	Geotextile	45° con. base	6.5	0.27	0.4	1.8
5.332	flush	Geotextile	45° con. base	6.5	0.27	0.4	2
5.333	flush	Geotextile	45° con. base	6.5	0.27	0.4	2.2
5.334	flush	Geotextile	45° con. base	6.5	0.27	0.4	2.4
5.335	flush	Geotextile	45° con. base	6.5	0.27	0.4	2.6
5.336	flush	Geotextile	45° con. base	6.5	0.27	0.4	2.8
5.337	flush	Geotextile	45° con. base	6.5	0.27	0.4	3
5.338	flush	Geotextile	45° con. base	6.5	0.32	0.4	1.4
5.339	flush	Geotextile	45° con. base	6.5	0.32	0.4	1.6
5.340	flush	Geotextile	45° con. base	6.5	0.32	0.4	1.8
5.341	flush	Geotextile	45° con. base	6.5	0.32	0.4	2
5.342	flush	Geotextile	45° con. base	6.5	0.32	0.4	2.2
5.343	flush	Geotextile	45° con. base	6.5	0.32	0.4	2.4
5.344	flush	Geotextile	45° con. base	6.5	0.32	0.4	2.6
5.345	flush	Geotextile	45° con. base	6.5	0.32	0.4	2.8
5.346	flush	Geotextile	45° con. base	6.5	0.32	0.4	3
5.347	flush	Geotextile	45° con. base	6.5	0.4	0.4	1.4
5.348	flush	Geotextile	45° con. base	6.5	0.4	0.4	1.6
5.349	flush	Geotextile	45° con. base	6.5	0.4	0.4	1.8
5.350	flush	Geotextile	45° con. base	6.5	0.4	0.4	2
5.351	flush	Geotextile	45° con. base	6.5	0.4	0.4	2.2
5.352	flush	Geotextile	45° con. base	6.5	0.4	0.4	2.4
5.353	flush	Geotextile	45° con. base	6.5	0.4	0.4	2.6
5.354	flush	Geotextile	45° con. base	6.5	0.4	0.4	2.8
5.355	flush	Geotextile	45° con. base	6.5	0.4	0.4	3
5.356	flush	Geotextile	45° con. base	6.5	0.08	0.4	1.4
5.357	flush	Geotextile	45° con. base	6.5	0.08	0.4	1.6
5.358	flush	Geotextile	45° con. base	6.5	0.08	0.4	1.8
5.359	flush	Geotextile	45° con. base	6.5	0.08	0.4	2
5.360	flush	Geotextile	45° con. base	6.5	0.08	0.4	2.2
5.361	flush	Geotextile	45° con. base	6.5	0.08	0.4	2.4
5.362	flush	Geotextile	45° con. base	6.5	0.08	0.4	2.6
5.363	flush	Geotextile	45° con. base	6.5	0.08	0.4	2.8
5.364	flush	Geotextile	45° con. base	6.5	0.08	0.4	3

5.365	Flush	Geotextile	45° con. base	6.5	0.12	0.4	1.4
5.366	Flush	Geotextile	45° con. base	6.5	0.12	0.4	1.6
5.367	Flush	Geotextile	45° con. base	6.5	0.12	0.4	1.8
5.368	Flush	Geotextile	45° con. base	6.5	0.12	0.4	2
5.369	Flush	Geotextile	45° con. base	6.5	0.12	0.4	2.2
5.370	Flush	Geotextile	45° con. base	6.5	0.12	0.4	2.4
5.371	Flush	Geotextile	45° con. base	6.5	0.12	0.4	2.6
5.372	Flush	Geotextile	45° con. base	6.5	0.12	0.4	2.8
5.373	Flush	Geotextile	45° con. base	6.5	0.12	0.4	3
5.374	Flush	Geotextile	45° con. base	6.5	0.32	0.4	1.5
5.375	Flush	Geotextile	Cyl. base	6.5	0	0.4	1.4
5.376	Flush	Geotextile	Cyl. base	6.5	0	0.4	1.6
5.377	Flush	Geotextile	Cyl. base	6.5	0	0.4	1.8
5.378	Flush	Geotextile	Cyl. base	6.5	0	0.4	2
5.379	Flush	Geotextile	Cyl. base	6.5	0	0.4	2.2
5.380	Flush	Geotextile	Cyl. base	6.5	0	0.4	2.4
5.381	Flush	Geotextile	Cyl. base	6.5	0	0.4	2.6
5.382	Flush	Geotextile	Cyl. base	6.5	0	0.4	2.8
5.383	Flush	Geotextile	Cyl. base	6.5	0	0.4	3
5.384	Flush	Geotextile	Cyl. base	6.5	0.17	0.4	1.4
5.385	Flush	Geotextile	Cyl. base	6.5	0.17	0.4	1.6
5.386	Flush	Geotextile	Cyl. base	6.5	0.17	0.4	1.8
5.387	Flush	Geotextile	Cyl. base	6.5	0.17	0.4	2
5.388	Flush	Geotextile	Cyl. base	6.5	0.17	0.4	2.2
5.389	Flush	Geotextile	Cyl. base	6.5	0.17	0.4	2.4
5.390	Flush	Geotextile	Cyl. base	6.5	0.17	0.4	2.6
5.391	Flush	Geotextile	Cyl. base	6.5	0.17	0.4	2.8
5.392	Flush	Geotextile	Cyl. base	6.5	0.17	0.4	3
5.393	Flush	Geotextile	Cyl. base	6.5	0.22	0.4	1.4
5.394	Flush	Geotextile	Cyl. base	6.5	0.22	0.4	1.6
5.395	Flush	Geotextile	Cyl. base	6.5	0.22	0.4	1.8
5.396	Flush	Geotextile	Cyl. base	6.5	0.22	0.4	2
5.397	Flush	Geotextile	Cyl. base	6.5	0.22	0.4	2.2
5.398	Flush	Geotextile	Cyl. base	6.5	0.22	0.4	2.4
5.399	Flush	Geotextile	Cyl. base	6.5	0.22	0.4	2.6
5.400	Flush	Geotextile	Cyl. base	6.5	0.22	0.4	2.8
5.401	Flush	Geotextile	Cyl. base	6.5	0.22	0.4	3
5.402	Flush	Geotextile	Cyl. base	6.5	0.27	0.4	1.4
5.403	Flush	Geotextile	Cyl. base	6.5	0.27	0.4	1.6
5.404	Flush	Geotextile	Cyl. base	6.5	0.27	0.4	1.8
5.405	Flush	Geotextile	Cyl. base	6.5	0.27	0.4	2
5.406	Flush	Geotextile	Cyl. base	6.5	0.27	0.4	2.2
5.407	Flush	Geotextile	Cyl. base	6.5	0.27	0.4	2.4
5.408	Flush	Geotextile	Cyl. base	6.5	0.27	0.4	2.6
5.409	Flush	Geotextile	Cyl. base	6.5	0.27	0.4	2.8
5.410	Flush	Geotextile	Cyl. base	6.5	0.27	0.4	3
5.411	Flush	Geotextile	Cyl. base	6.5	0.32	0.4	1.4

5.412	flush	Geotextile	Cyl. base	6.5	0.32	0.4	1.6
5.413	flush	Geotextile	Cyl. base	6.5	0.32	0.4	1.8
5.414	flush	Geotextile	Cyl. base	6.5	0.32	0.4	2
5.415	flush	Geotextile	Cyl. base	6.5	0.32	0.4	2.2
5.416	flush	Geotextile	Cyl. base	6.5	0.32	0.4	2.4
5.417	flush	Geotextile	Cyl. base	6.5	0.32	0.4	2.6
5.418	flush	Geotextile	Cyl. base	6.5	0.32	0.4	2.8
5.419	flush	Geotextile	Cyl. base	6.5	0.32	0.4	3
5.420	flush	Geotextile	Cyl. base	6.5	0.4	0.4	1.4
5.421	flush	Geotextile	Cyl. base	6.5	0.4	0.4	1.6
5.422	flush	Geotextile	Cyl. base	6.5	0.4	0.4	1.8
5.423	flush	Geotextile	Cyl. base	6.5	0.4	0.4	2
5.424	flush	Geotextile	Cyl. base	6.5	0.4	0.4	2.2
5.425	flush	Geotextile	Cyl. base	6.5	0.4	0.4	2.4
5.426	flush	Geotextile	Cyl. base	6.5	0.4	0.4	2.6
5.427	flush	Geotextile	Cyl. base	6.5	0.4	0.4	2.8
5.428	flush	Geotextile	Cyl. base	6.5	0.40	0.4	3
5.429	flush	Geotextile	Cyl. base	6.5	0.08	0.4	1.4
5.430	flush	Geotextile	Cyl. base	6.5	0.08	0.4	1.6
5.431	flush	Geotextile	Cyl. base	6.5	0.08	0.4	1.8
5.432	flush	Geotextile	Cyl. base	6.5	0.08	0.4	2
5.433	flush	Geotextile	Cyl. base	6.5	0.08	0.4	2.2
5.434	flush	Geotextile	Cyl. base	6.5	0.08	0.4	2.4
5.435	flush	Geotextile	Cyl. base	6.5	0.08	0.4	2.6
5.436	flush	Geotextile	Cyl. base	6.5	0.08	0.4	2.8
5.437	flush	Geotextile	Cyl. base	6.5	0.08	0.4	3
5.438	flush	Geotextile	Cyl. base	6.5	0.12	0.4	1.4
5.439	flush	Geotextile	Cyl. base	6.5	0.12	0.4	1.6
5.440	flush	Geotextile	Cyl. base	6.5	0.12	0.4	1.8
5.441	flush	Geotextile	Cyl. base	6.5	0.12	0.4	2
5.442	flush	Geotextile	Cyl. base	6.5	0.12	0.4	2.2
5.443	flush	Geotextile	Cyl. base	6.5	0.12	0.4	2.4
5.444	flush	Geotextile	Cyl. base	6.5	0.12	0.4	2.6
5.445	flush	Geotextile	Cyl. base	6.5	0.12	0.4	2.8
5.446	flush	Geotextile	Cyl. base	6.5	0.12	0.4	3
5.447	above	Impermeable	Monopile	10.5	0	0.4	1.5
5.448	above	Impermeable	Monopile	10.5	0.12	0.4	1.5
5.449	above	Impermeable	Monopile	10.5	0.22	0.4	1.5
5.450	above	Impermeable	Monopile	10.5	0.32	0.4	1.5
5.451	above	Impermeable	75° con. base	10.5	0	0.4	1.5
5.452	above	Impermeable	75° con. base	10.5	0.12	0.4	1.5
5.453	above	Impermeable	75° con. base	10.5	0.22	0.4	1.5
5.454	above	Impermeable	75° con. base	10.5	0.32	0.4	1.5
5.455	above	Impermeable	45° con. base	10.5	0	0.4	1.5
5.456	above	Impermeable	45° con. base	10.5	0.12	0.4	1.5
5.457	above	Impermeable	45° con. base	10.5	0.22	0.4	1.5
5.458	above	Impermeable	45° con. base	10.5	0.32	0.4	1.5

5.459	Above	Impermeable	Cyl. base	10.5	0	0.4	1.5
5.460	Above	Impermeable	Cyl. base	10.5	0.12	0.4	1.5
5.461	Above	Impermeable	Cyl. base	10.5	0.22	0.4	1.5
5.462	Above	Impermeable	Cyl. base	10.5	0.32	0.4	1.5
5.463	Above	Impermeable	Cyl. base	3.5	0	0.4	1.2
5.464	Above	Impermeable	Cyl. base	3.5	0	0.4	1.4
5.465	Above	Impermeable	Cyl. base	3.5	0	0.4	1.6
5.466	Above	Impermeable	Cyl. base	3.5	0	0.4	1.8
5.467	Above	Impermeable	Cyl. base	3.5	0	0.4	2
5.468	Above	Impermeable	Cyl. base	3.5	0	0.4	2.2
5.469	Above	Impermeable	Cyl. base	3.5	0	0.4	2.4
5.470	Above	Impermeable	Cyl. base	3.5	0	0.4	2.6
5.471	Above	Impermeable	Cyl. base	3.5	0.06	0.4	1.4
5.472	Above	Impermeable	Cyl. base	3.5	0.06	0.4	1.6
5.473	Above	Impermeable	Cyl. base	3.5	0.06	0.4	1.8
5.474	Above	Impermeable	Cyl. base	3.5	0.06	0.4	2
5.475	Above	Impermeable	Cyl. base	3.5	0.06	0.4	2.2
5.476	Above	Impermeable	Monopile	3.5	0	0.4	1.2
5.477	Above	Impermeable	Monopile	3.5	0	0.4	1.4
5.478	Above	Impermeable	Monopile	3.5	0	0.4	1.6
5.479	Above	Impermeable	Monopile	3.5	0	0.4	1.8
5.480	Above	Impermeable	Monopile	3.5	0	0.4	2
5.481	Above	Impermeable	Monopile	3.5	0	0.4	2.2
5.482	Above	Impermeable	Monopile	3.5	0	0.4	2.4
5.483	Above	Impermeable	Monopile	3.5	0	0.4	2.6
5.484	Above	Impermeable	Monopile	3.5	0.06	0.4	1.4
5.485	Above	Impermeable	Monopile	3.5	0.06	0.4	1.6
5.486	Above	Impermeable	Monopile	3.5	0.06	0.4	1.8
5.487	Above	Impermeable	Monopile	3.5	0.06	0.4	2
5.488	Above	Impermeable	Monopile	3.5	0.06	0.4	2.2
5.489	Above	Impermeable	45° con. base	3.5	0	0.4	1.2
5.490	Above	Impermeable	45° con. base	3.5	0	0.4	1.4
5.491	Above	Impermeable	45° con. base	3.5	0	0.4	1.6
5.492	Above	Impermeable	45° con. base	3.5	0	0.4	1.8
5.493	Above	Impermeable	45° con. base	3.5	0	0.4	2
5.494	Above	Impermeable	45° con. base	3.5	0	0.4	2.2
5.495	Above	Impermeable	45° con. base	3.5	0	0.4	2.4
5.496	Above	Impermeable	45° con. base	3.5	0	0.4	2.6
5.497	Above	Impermeable	45° con. base	3.5	0.06	0.4	1.4
5.498	Above	Impermeable	45° con. base	3.5	0.06	0.4	1.6
5.499	Above	Impermeable	45° con. base	3.5	0.06	0.4	1.8
5.500	Above	Impermeable	45° con. base	3.5	0.06	0.4	2
5.501	Above	Impermeable	45° con. base	3.5	0.06	0.4	2.2
5.502	Above	Impermeable	75° con. base	3.5	0	0.4	1.2
5.503	Above	Impermeable	75° con. base	3.5	0	0.4	1.4
5.504	Above	Impermeable	75° con. base	3.5	0	0.4	1.6
5.505	Above	Impermeable	75° con. base	3.5	0	0.4	1.8

5.506	above	Impermeable	75° con. base	3.5	0	0.4	2
5.507	above	Impermeable	75° con. base	3.5	0	0.4	2.2
5.508	above	Impermeable	75° con. base	3.5	0	0.4	2.4
5.509	above	Impermeable	75° con. base	3.5	0.06	0.4	2.6
5.510	above	Impermeable	75° con. base	3.5	0.06	0.4	1.4
5.511	above	Impermeable	75° con. base	3.5	0.06	0.4	1.6
5.512	above	Impermeable	75° con. base	3.5	0.06	0.4	1.8

Table 7-4 shows the programme for the tests which were conducted to examine the damage pattern induced by flow conditions which just induce incipient motion of the scour protection material. This was done by continuing the tests after incipient motion was detected. Given the long duration of these tests only a sample of representative flow conditions was tested.

Table 7-4: Summary of scour protection damage progression tests.

No	Structure	D50	U	h	T
(-)	(-)	(mm)	(m/s)	(m)	(s)
6.1	Monopile	6.5	0	0.4	1.5
6.2	Monopile	6.5	0.06	0.4	1.5
6.3	Monopile	6.5	0.36	0.4	1.5
6.4	Monopile	6.5	0.39	0.4	0
6.5	75° con. base	6.5	0	0.4	1.5
6.6	75° con. base	6.5	0.06	0.4	1.5
6.7	75° con. base	6.5	0.36	0.4	1.5
6.8	75° con. base	6.5	0.4	0.4	0
6.9	45° con. base	6.5	0	0.4	1.5
6.10	45° con. base	6.5	0.06	0.4	1.5
6.11	45° con. base	6.5	0.36	0.4	1.5
6.12	45° con. base	6.5	0.45	0.4	0
6.13	Cyl. base	6.5	0	0.4	1.5
6.14	Cyl. base	6.5	0.06	0.4	1.5
6.15	Cyl. base	6.5	0.36	0.4	1.5
6.16	Cyl. base	6.5	0.55	0.4	0

8 Results for scour protection around complex structures

This chapter will present the results of the experimental study on scour protection stability around complex foundation geometries. In this context the flow conditions for all the tests will be presented, followed by the results for the stability of the scour protection and results for the development of scour protection damage.

8.1 Flow characteristics

This section presents the measurements of the flow velocity and wave heights for the present set of experiments.

All flow measurements were undertaken over a flat bed, along the centreline of the flume and just upstream of the scour protection. The aim was to examine the effect of the scour protection configuration on the incipient motion. Given the range of different flow conditions tested in these experiments, the velocity profiles are plotted in a non-dimensional form for comparison with the Soulsby (1990) method (Figure 8-1). To distinguish the flow velocities that were opposing the waves with those that were following the waves the $u(z)$ is non-dimensionalised with the absolute value of the mean current speed ($|U_c|$). Figure 8-1 shows that there is good agreement between the flow measurements and Soulsby (1990), though there is a slight tendency for it to under-predict the velocities near the surface of the flow. In general, it can be assumed that the present flow conditions resemble these of tidal currents.

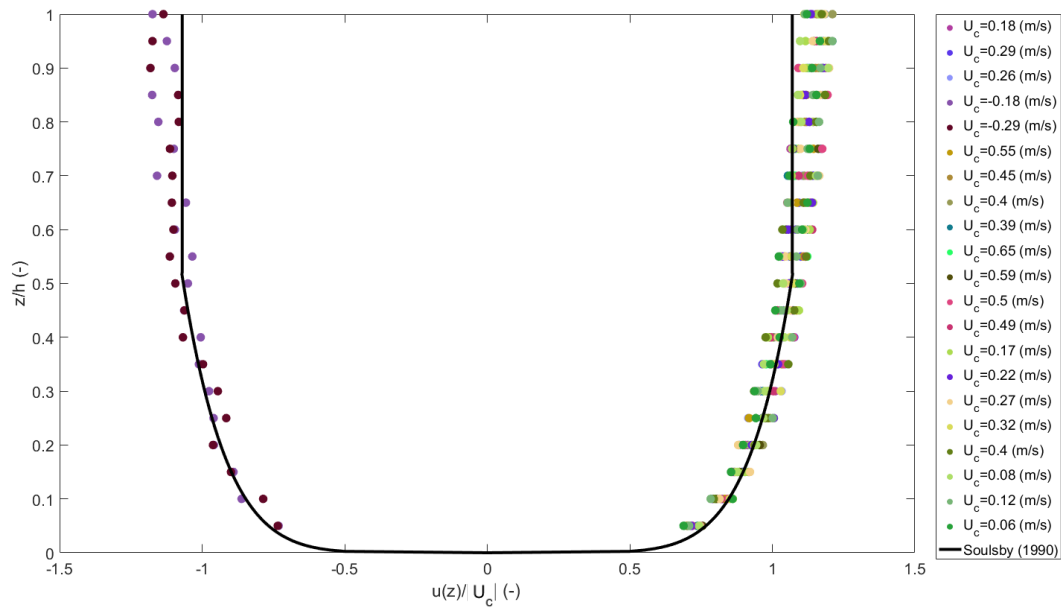


Figure 8-1: Flow profiles for scour protection stability tests (5.1-5.12 & 6.1-6.16).

Given the large number of wave records acquired during these tests it was not possible to present all of them in this thesis. For this reason typical water surface profiles for the waves used in these tests are presented in Figure 8-2. It can be seen that these waves do not follow the Airy wave theory but rather the 3rd order Stokes theory which is expected in laboratory tests according to Bosboom and Stive (2012). In addition, Dingemans, 1997 suggests that for Ursell numbers smaller than $32\pi^2/3 \approx 100$ Stokes 3rd order wave theory is the most appropriate wave theory. Figure 8-3 shows that all of the tests in this study have $Ur < 100$. For this reason, the orbital velocities for these tests are calculated using the Fenton (1985) explicit solution of the 3rd order Stokes theory.

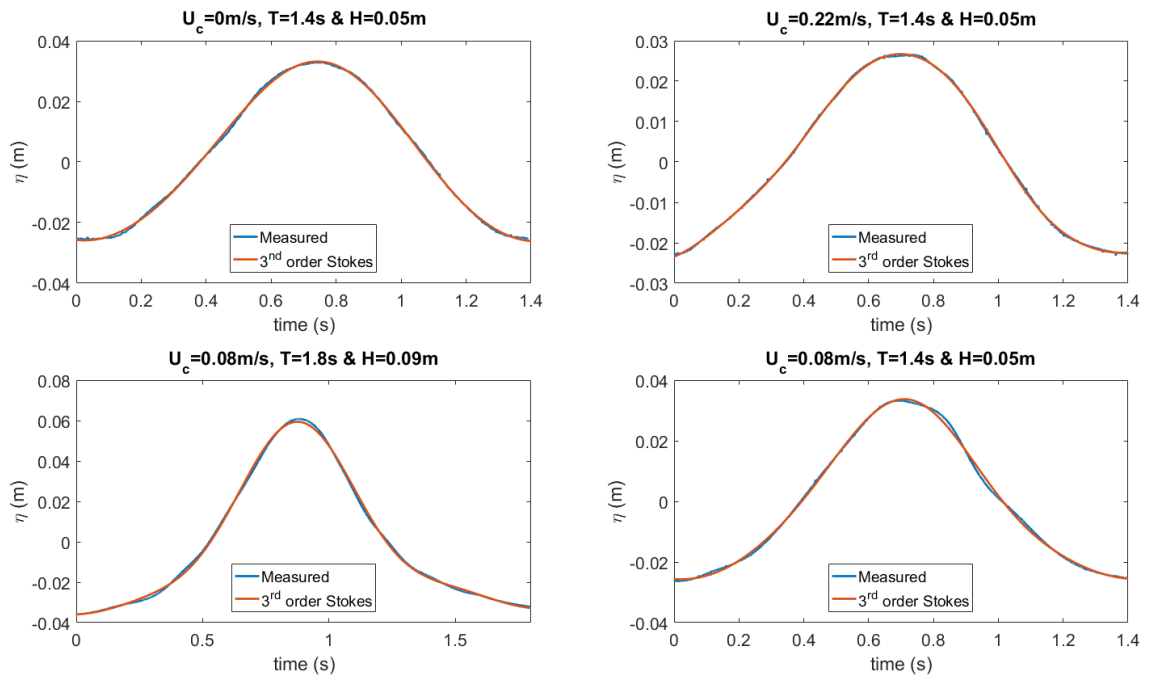


Figure 8-2: Examples of wave profiles from present tests.

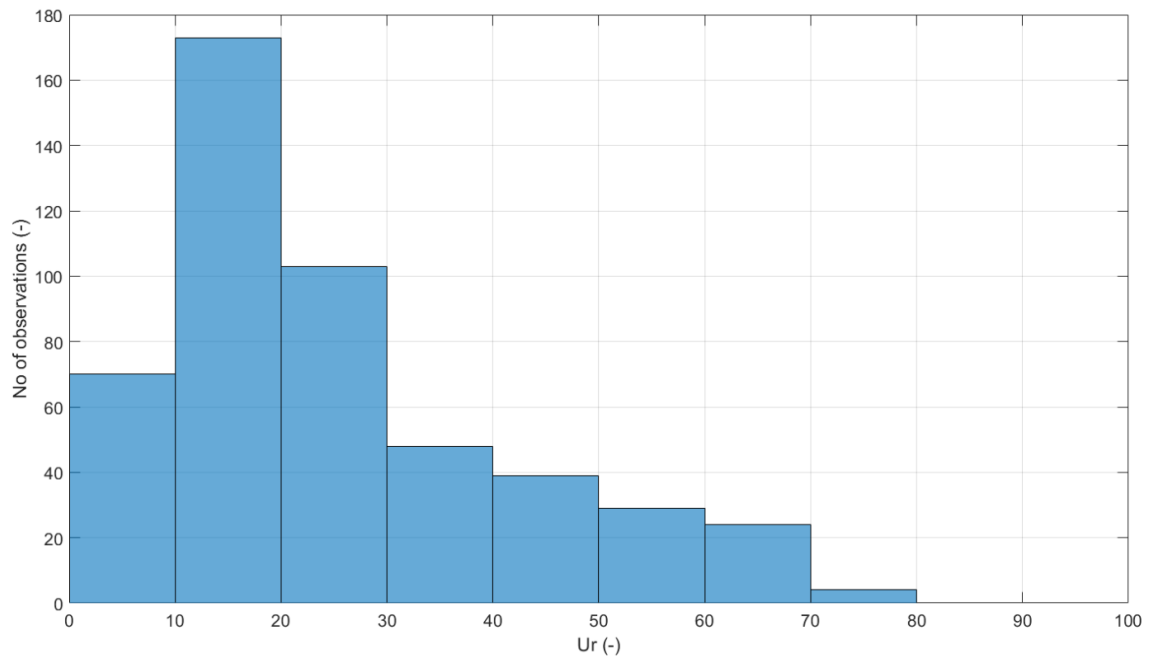


Figure 8-3: Distribution of tests as a function of the Ursell number.

8.2 Stability of scour protection

8.2.1 Choice of wave friction formula

Given that the present study aims to investigate the critical amplification of the bed shear stress around complex geometries it is important to select an appropriate method for calculating the bed shear stress induced by waves. As section 2.2.2 shows there are many methods for determining the wave friction and thus the bed shear stress.

Figure 8-4 to 8-6 show the non-dimensional bed shear stress (Shields number) as a function of the sediment size, wave height and wave period given by the different formulations. It can be observed that all of the methods show similar trends and yield similar Shields numbers within the range of parameters covered in this study.

When examining the non-dimensional shear stress as a function of the D_* (Figure 8-4) Nielsen (1992), Soulsby (1997) and Swart (1974) yield very similar results. These lie between the solutions given by Simons et al. (2001) and Myrhaug (1989).

Figure 8-5 shows the effect the wave height has on the bed shear stress based on the different formulations of the wave friction coefficient along with the range of wave heights tested during this investigation. It can be seen that again all of the formulations tend to provide similar solutions with some deviation occurring for small values of the non-dimensional wave height.

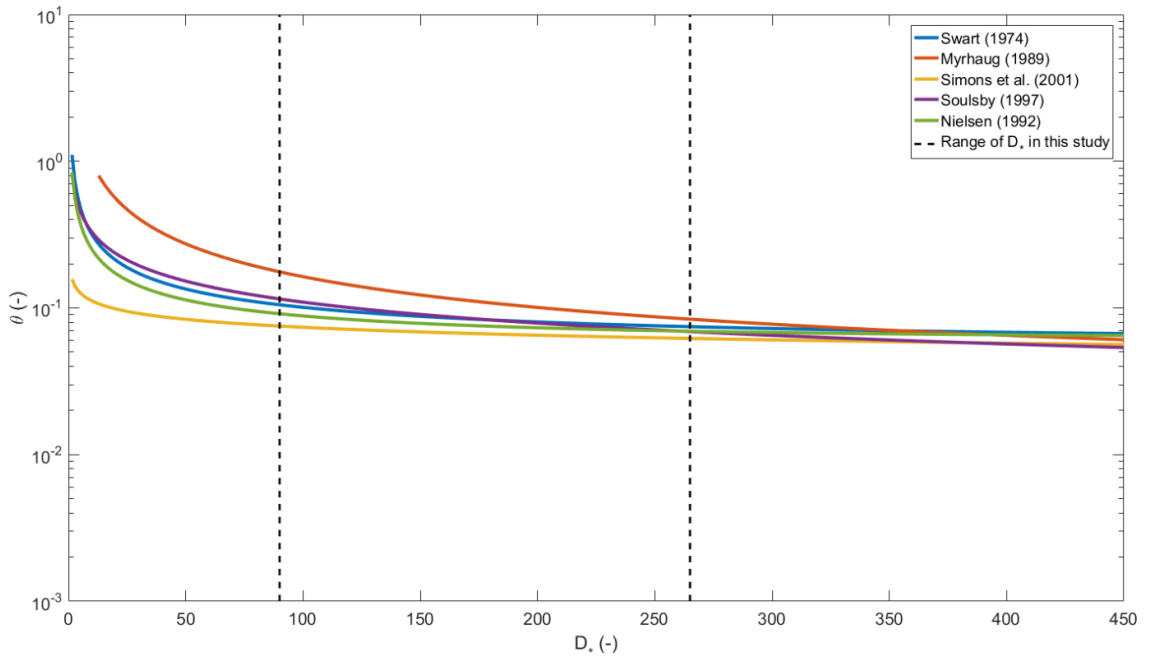


Figure 8-4: Effect different wave friction equations have on the wave induced Shields parameter (θ) presented as a function of the non-dimensional stone diameter (D_*) $T=1.5s$, $H=0.16m$.

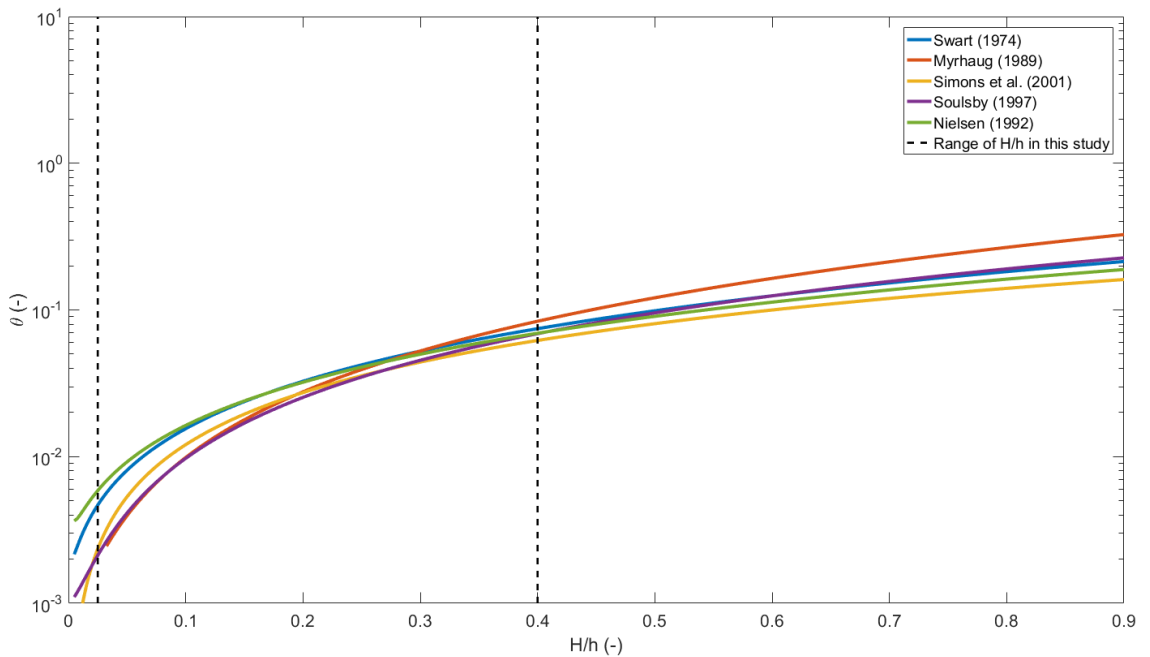


Figure 8-5: Effect different wave friction equations have on the wave induced Shields parameter (θ) presented as a function of the non-dimensional wave height (H/h): $T=1.5s$, $D=6.5mm$.

The effect of wave period on the bed shear stress predicted by the five formulations for wave friction is shown in Figure 8-6. The behaviour of the predictions is similar to that seen in Figure 8-4. Within the range of wave periods tested in this research the Swart

(1974) and Soulsby (1997) approaches yield results which lie in the middle of the solutions given by Simons et al. (2001) and Myrhaug (1989) which provide an envelope enclosing the rest of the predictions.

Based on the observations above, the undisturbed bed shear stress due to wave action will be determined using the Soulsby (1997) method. This is because it tends to provide an average estimation of the bed shear stress compared to the other methods, not only within the limits of the present test regime but also outside of it.

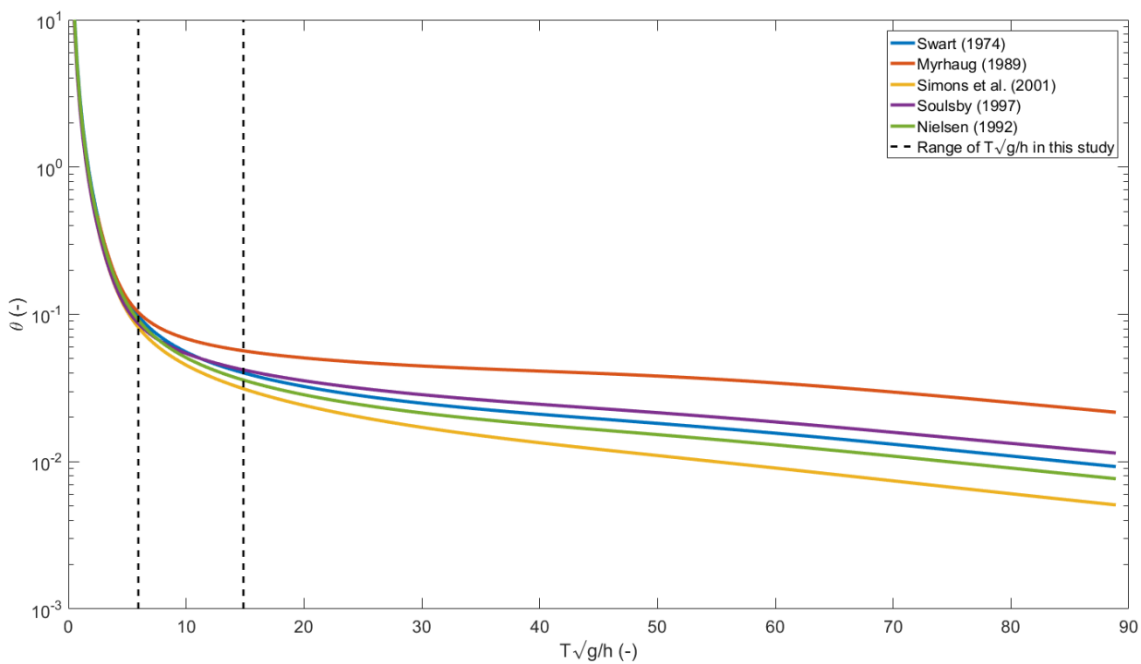


Figure 8-6: Effect different wave friction equations have on the wave induced Shields parameter (θ) presented as a function of the non-dimensional wave period ($T\sqrt{g/h}$): $H=0.16$, $D=6.5\text{mm}$.

8.3 Analysis of the results of scour protection stability tests

This section presents the results from the scour protection stability tests. The effect of the individual parameters will first be presented, then the results from all tests will be combined to derive a design graph that allow designers to select the appropriate stone size for a scour protection system.

8.3.1 Influence of main variables

In the present investigation a range of flow parameters have been tested in order to obtain a better understanding of the effects different structural and environmental parameters have on the amplification of the critical bed shear stress and thus the stability of the scour protection material. The parameter that have been tested in these experiments are summarized in table 8-1.

Table 8-1: Tested parameters

Variable	Units	Description
U_c	(m/s)	Mean flow velocity
H	(m)	Wave height
L	(m)	Wavelength
D_{50}	(m)	Median stone size
α_{dir}	(°)	Flow direction
Scour protection configuration	(-)	Scour protection flush and above original bed
Permeability of original bed	(-)	Permeable and impermeable bed
Structural geometry	(-)	Geometries listed in Figure 7-8

8.3.1.1 Influence of stone size (D_{50})

Three different stone sizes were used in the present tests, with median sizes of 3.5mm, 6.5mm and 10.5mm. Figure 8-7 shows a comparison between the critical bed shear stress amplification induced by the four different geometries as a function of the non-dimensional stone size (D_*) for three cases: a) waves only with $T=2s$, b) waves with $T=2s$ and a mean current $U_c=0.18m/s$ and c) waves with $T=2s$ and a mean current $U_c=0.29m/s$. The figure shows that there is no influence of the non-dimensional stone size on the amplification of the bed shear stress for the range of stone sizes tested in this section. This is because the effect of the roughness and therefore the stone size on

the amplification of the bed shear stress is included in α_{crit} through the critical shear stress (τ_{crit}) term in Equation 5-1. In addition, the effect of the geometry of the structure does not have a significant influence, with all the values of critical bed shear stress amplification ranging between 1-1.7 and falling within the range of bed shear stress amplification measured by Sumer et al., 1997 for monopiles.

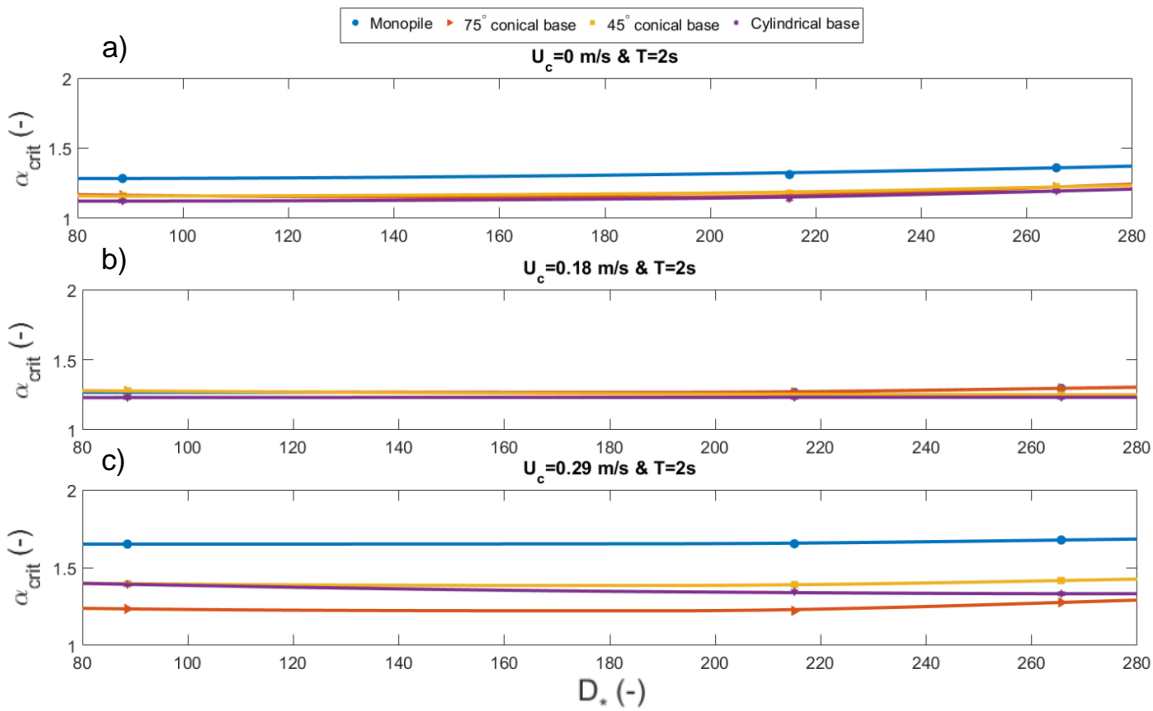


Figure 8-7: Influence of non-dimensional stone size on the amplification of the bed shear stress for different geometries (lines are linearly interpolated between points): a) waves only; b) $U_c = 0.18$ m/s and waves and c) $U_c = 0.29$ m/s and waves.

8.3.1.2 Influence of scour protection level

A number of tests were repeated with similar flow conditions over a scour protection configuration installed flush with the original bed and installed above it (see Figure 7-4). In all tests the scour protection had the same thickness and the underlying sand bed was covered with the same geotextile to provide comparable bed conditions. Figure 8-8 presents the results for waves with periods of 1.4s-1.5s and 2s which were imposed onto currents with a velocity of 0m/s to 0.29m/s. The results show that the scour protection level does not have a significant effect on the critical amplification and therefore the stability of the scour protection. This could be expected because when the scour protection is installed above the original bed the effective area of the structure is reduced

(see Figure 7-4) which compensates to a certain level for the increase in the local velocities due to the local reduction in depth. In addition, the width of the scour protection is significantly larger than the width recommended by most design guidelines. This means that the turbulence induced by the transition between the original bed and the scour protection will have more space to dissipate and therefore the effect it has on the stability of the scour protection near the structure will be less apparent.

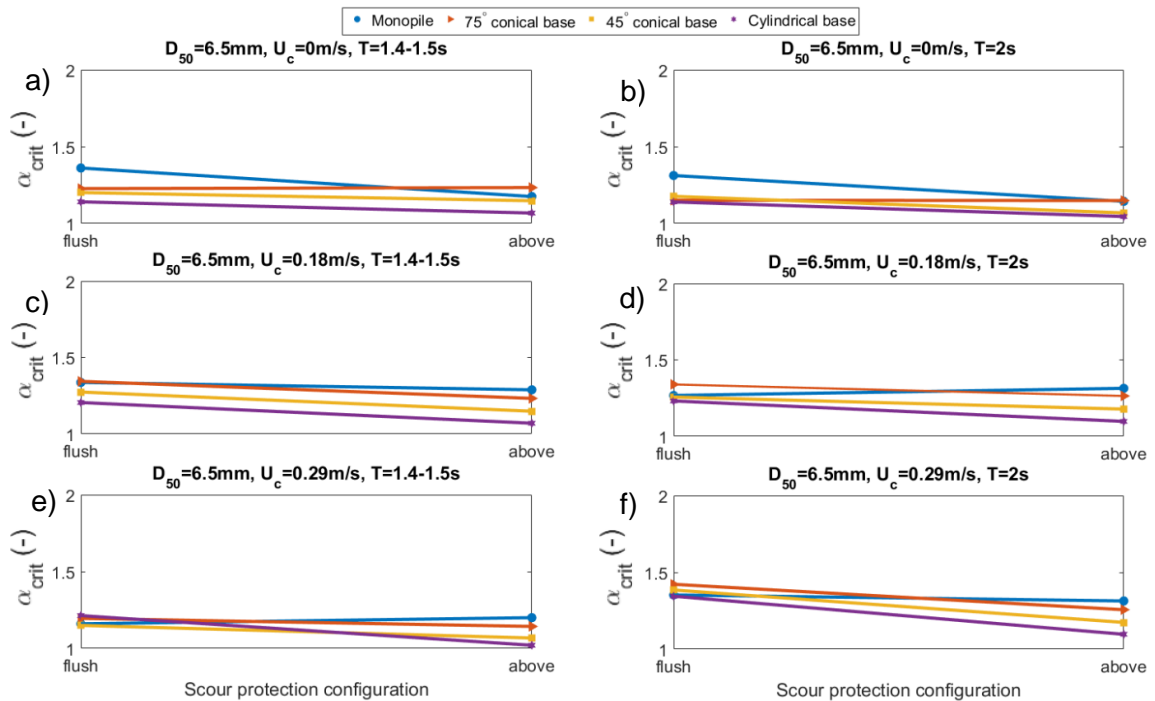


Figure 8-8: Influence of scour protection configuration on the amplification of the bed shear stress for different geometries (lines are linearly interpolated between points): a) waves only, $T=1.4-1.5$ s; b) waves only, $T=2$ s; c) $U_c = 0.18$ m/s and waves, $T=1.4-1.5$ s; d) $U_c = 0.18$ m/s and waves, $T=2$ s; e) $U_c = 0.29$ m/s waves, $T=1.4-1.5$ s; and f) $U_c = 0.29$ m/s waves, $T=2$ s.

8.3.1.3 Influence of bed permeability

The permeability of the bed may have an effect on the hydraulic flow gradients under the scour protection which may affect stability of the rock cover. Figure 8-9 shows the results for tests that were conducted under the same hydraulic conditions and scour protection configuration (scour protection above the bed level). Even though Figure 8-9 shows small increases and decreases for some cases these deviations remain well within the error margins associated with this measuring technique. Therefore, as for the other cases presented in this section the results suggest that the amplification of the bed shear stress

is not affected by the bed permeability. This is expected, as the permeability of the rock cover is $O(10)$ larger than the permeability of the bed and the geotextile. This means that the hydraulic gradient induced by the water elevation between a wave's crest and trough will be insufficient to build-up a large pressure gradient under the rocks.

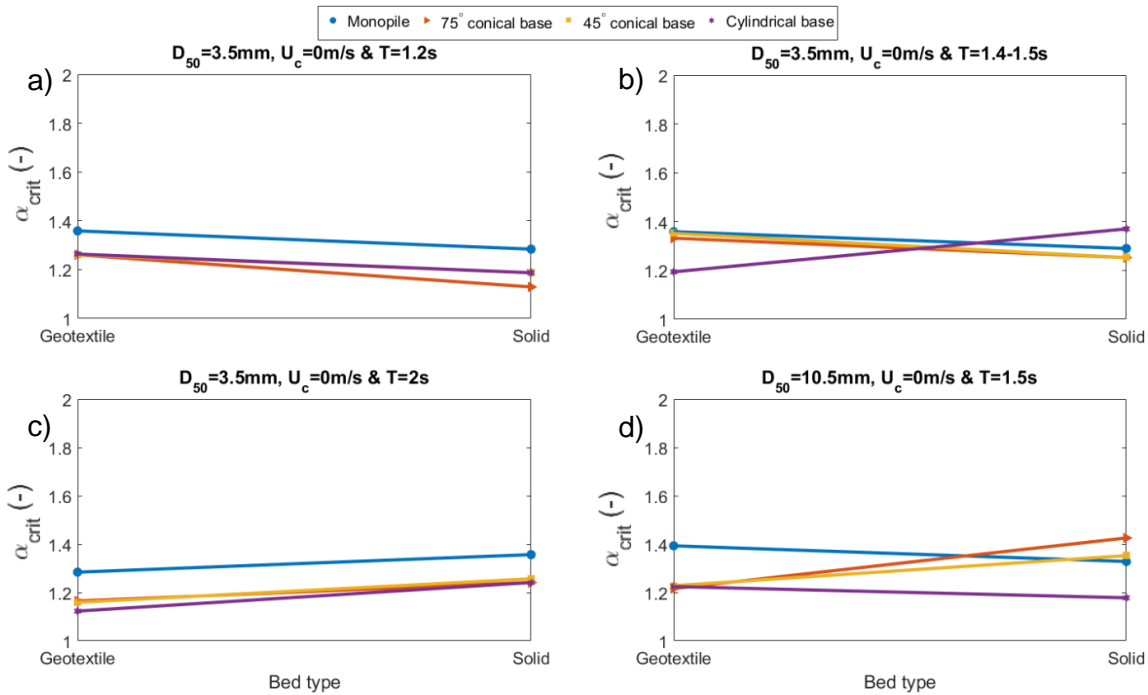


Figure 8-9: Influence of bed permeability on the amplification of the bed shear stress for different geometries: a) waves only, $T=1.2\text{s}$ and $D_{50}=3.5\text{mm}$; b) waves only, $T=1.4-1.5\text{s}$ and $D_{50}=3.5\text{mm}$; c) waves only, $T=2\text{s}$ and $D_{50}=3.5\text{mm}$; d) waves only, $T=1.5\text{s}$ and $D_{50}=10.5\text{mm}$.

8.3.1.4 Influence of flow direction

Given that the present tests were conducted in a flume, only two flow directions were tested, with the flow following (positive current velocity) and the flow opposing the waves (negative current velocity). Figure 8-10 presents the results for a number of tests which were conducted under the same conditions with flow following and opposing the waves. The results show that the amplification of the bed shear stress is not significantly affected by the flow direction. An exception to this is the behaviour of the monopile structure in the cases c and d. For these flow conditions a current following the waves induces an amplification which is approximately 30% larger than when the current is opposing the waves. This can be explained by the fact that the waves in these tests are slightly non-linear, which means that the orbital velocities under the trough are smaller than the orbital

velocities under the crest. This means that the net flow under the crest is going to be larger when a current is following the waves and thus the amplification of the bed shear stress larger. The reason why this behaviour is only observed in the case of the monopile is that this structure has the largest cross-sectional area which means that the amplification of the local pressure field will be more pronounced than for the other geometries.

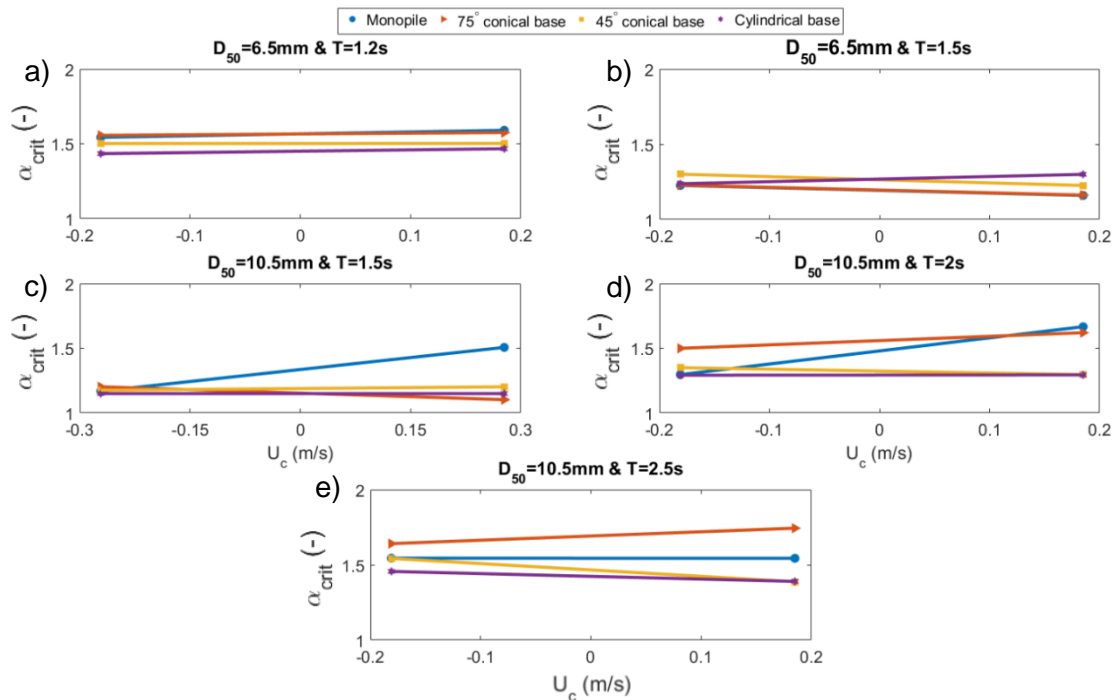


Figure 8-10: Influence of flow direction on the amplification of the bed shear stress for different geometries: a) $D_{50}=6.5\text{mm}$ and $T=1.2\text{s}$; b) $D_{50}=6.5\text{mm}$ and $T=1.5\text{s}$; c) $D_{50}=10.5\text{mm}$ and $T=1.5\text{s}$; d) $D_{50}=10.5\text{mm}$ and $T=2\text{s}$; and e) $D_{50}=10.5\text{mm}$ and $T=2.5\text{s}$.

8.3.1.5 Influence of wavelength

For a number of tests, the wave period was varied from 1.2s to 3s to investigate the effect of the wavelength on the critical bed shear stress amplification. Figure 8-11 presents the influence D_{base}/L has on α_{crit} for the four geometries examined in this study; in these tests the KC number is smaller than 2. The figure shows that α_{crit} is fairly constant for all structures when $D_{base}/L \lesssim 0.095$. After that value the amplification of the bed shear stress starts to increase and reaches a value of approximately 1.5 which corresponds to an increase of $\sim 25\%$. This increase can be explained by the phenomenon of steady streaming which was explained in section (2.4.3). According to the linear model

developed by MacCamy and Fuchs (1954) the phase resolved velocity near the structure increases as the wavelength decreases (D_{base}/L increases), which translates into a larger bed shear stress near the structure. This finding is also supported by the findings of Sumer and Fredsøe (2001) who conducted scour tests around cylinders in the steady streaming regime and found that the scour depth increased significantly when D/L was increased from 0.08 to 0.15.

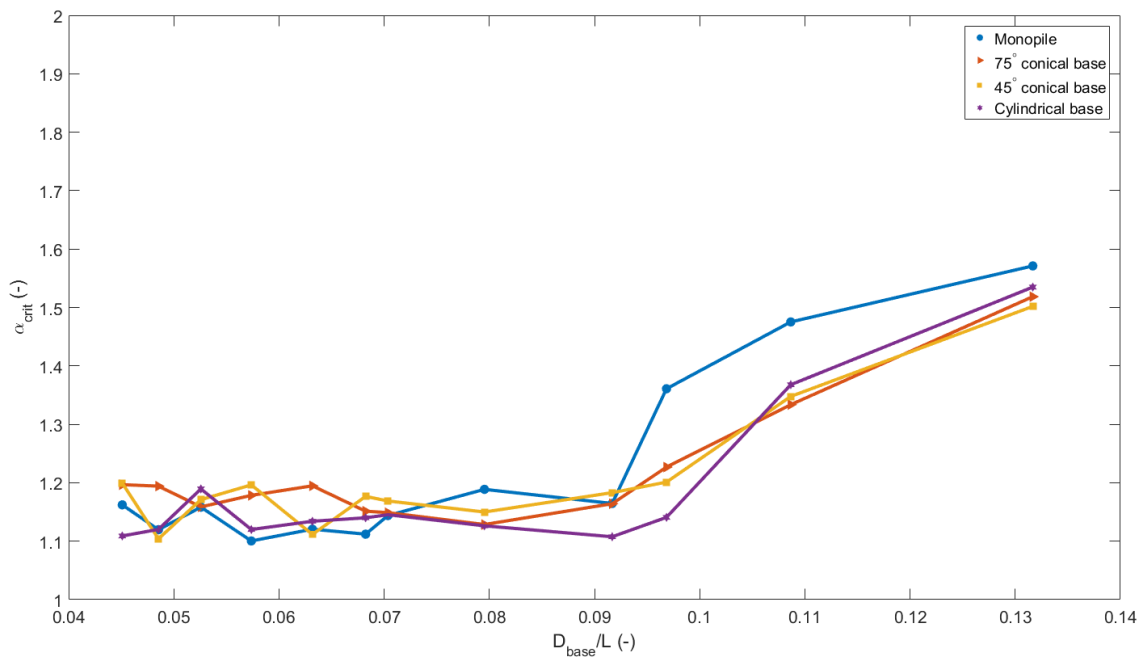


Figure 8-11: Influence of wavelength on the amplification of the bed shear stress for different geometries: $D_{50}=6.5\text{mm}$, waves only.

8.3.1.6 Influence of the velocity ratio (U_{cw})

When examining the interaction of combined waves and currents with a structure an important variable that needs to be considered is the velocity ratio between the mean current and the bed orbital velocity. Figure 8-12 shows the effect the velocity ratio has on α_{crit} . In this figure the data correspond to scour protection which has been installed flush with the original bed with $D_{50}=6.5\text{mm}$ and $1 < KC < 5$. The results show that the presence of a superimposed current does not influence significantly the amplification of the bed shear stress for $U_{cw} < 0.5 - 0.6$. This result may be attributed to the lee wake

vortex shedding induced by the current which counteracts the lee wake induced by the waves.

At higher value of the velocity ratio (i.e. $U_{cw} > 0.5$), the amplification of the bed shear stress increases significantly for all structures. This can be explained by the current which in this case is strong enough to establish a constant presence at the lee of the structure and thus generates more turbulence which in turn results in a larger α_{crit} . The presence of a strong lee wake vortex is confirmed by the observations during the tests (see Section 5.5 for a detailed discussion) which revealed that the incipient motion of the sediment occurred at the lee of the structure. This observation agrees to certain level with the finding of Sumer and Fredsøe (2001) who found that scour around cylinders becomes current-dominated when $U_{cw} \gtrsim 0.7$.

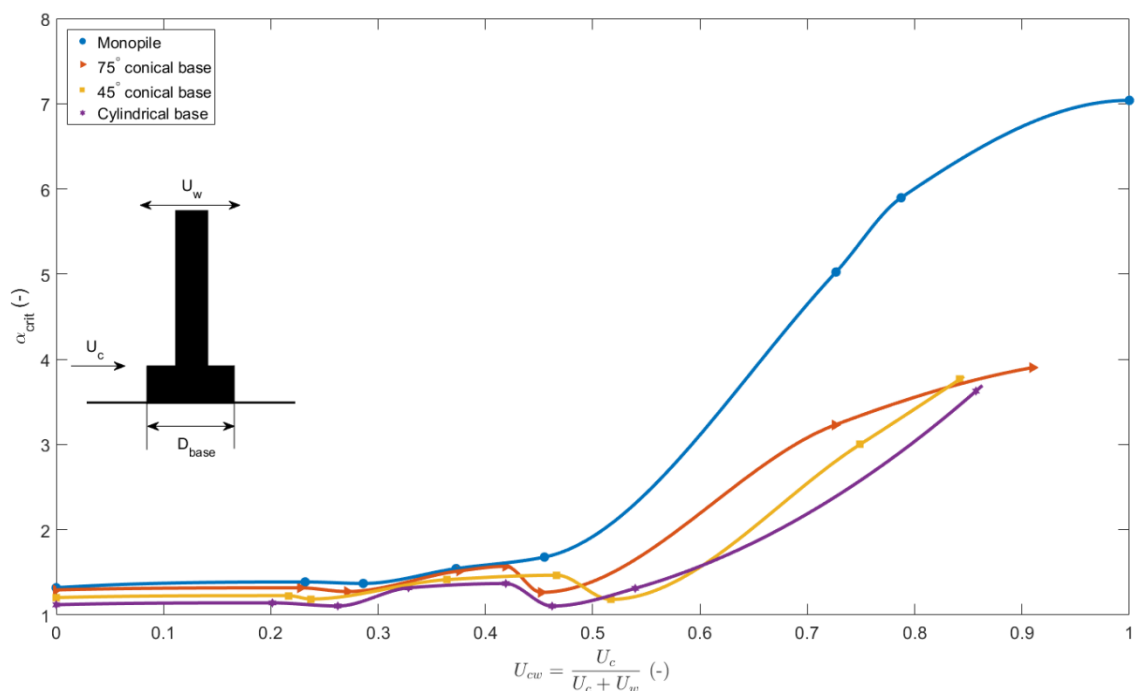


Figure 8-12: Influence of velocity ratio (U_{cw}) on the amplification of the bed shear stress for different geometries: $D_{50}=6.5\text{mm}$.

8.3.1.7 Influence of the KC number: Design diagram for rock cover size selection

Based on the findings presented in the previous sections two flow parameters have been identified that have an influence on the amplification of the bed shear stress around complex geometries. These are the wavelength which has a small effect (Figure 8-11)

and the velocity ratio which as seen in Figure 8-12 can result in an increase in α_{crit} from $O(1)$ to $O(10)$. This section will present the effect the Keulegan–Carpenter number (KC) has on α_{crit} . Through its definition KC includes the effect of the wavelength and height through the bed orbital velocity (U_w); thus the effect of the wavelength is also reflected in KC. Figure 8-13 presents all the experimental results for the four different structures. In this figure the bottom horizontal axis represents KC, while the top horizontal axis shows the corresponding amplitude of the wave orbital motion (A). It should be noted, given that the tests were conducted with structures of the same base diameter (D_{base}), that KC and A both provide a measure of the amplitude of the wave at the bed. The colour map shows the value of the velocity ratio. Each line in the figure provides a conservative estimate of the trend of the data, such that 80% of the data fall below it. Figure 8-13 shows that there are two distinct trends in the data, as described below.

In the first, a set of data between KC values of 0.5 and 5 has amplification values ranging between 1 and 2. Closer observation of this subset shows that the velocity ratio is always smaller than 0.5 which means that they correspond to wave dominated conditions. Thus the results suggest that the critical amplification of the bed shear stress in a wave dominated environment is fairly constant with a maximum value of 2.

The second cluster of data shows a large increase in α_{crit} for values of KC which are smaller than ~ 2 . The trend for each structure type then splits into four additional sets of data depending of the structure geometry and reaches its corresponding maximum value at $KC = 0$. It should be noted here that a KC of 0 corresponds to the case where no waves are present which implies that the bed orbital velocity is 0 and thus KC is also 0. This set of data has velocity ratio (U_{cw}) values ranging between 0.5 and 1 which corresponds to current dominated flow conditions.

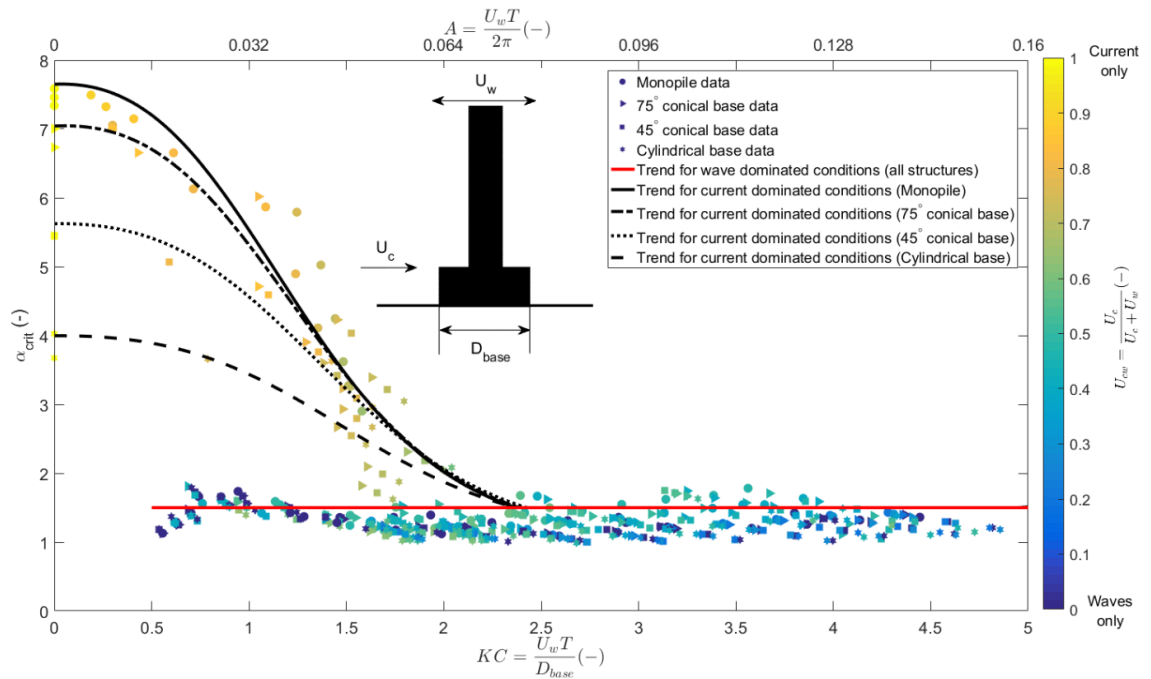


Figure 8-13: Influence of the Keulegan–Carpenter number (KC) and the amplitude of the wave orbital motion (A) on the amplification of the bed shear stress for different geometries, the colour map shows the velocity ratio and the lines a conservative estimate of the trend of the corresponding data.

A KC range 1.6-2.1 corresponds to the range values above which the first pair of lee vortices are created in the case of waves (see Figure 2-19). The formation of these vortices explains the lift-off of the data for $KC \lesssim 2$ which is seen in Figure 8-13:

- In the case of wave dominated flows ($U_{cw} < 0.5$) the current velocity is weak relative to the bed orbital velocity (U_w).
 - When $KC \gtrsim 2$ the vortices that are generated by the action of the waves interact with the lee-wake vortex system generated by the current structure interaction. Given that the spatial and temporal scales of these vortices are different their interaction breaks up the turbulent structure of the lee-wake vortex system. This means that the rock displacement in this case is mainly attributed to the horseshoe vortex (due to the wave) which is formed every half-cycle of the wave. This fact is also confirmed by the findings of Sumer et al., 1992 who found that the maximum lift force reduces significantly when a current is imposed on an oscillatory flow.
 - When $KC \lesssim 2$ no lee vortices are present which mean that the displacement of the rock is attributed to the steady streaming process.

Both the horseshoe vortex system in waves and the steady streaming are relatively weak when compared to the horseshoe vortex induced by a current.

This explains why α_{crit} is fairly constant and low throughout the range of KC values tested in this study.

- In the case of current dominated flow ($U_{cw} > 0.5$) the current is much stronger than the bed orbital velocity of the waves.
 - This means that when $KC \leq 2$ (no lee vortices present) the entire rock displacement process is driven by the horseshoe vortex and the lee-wake vortex shedding which are significantly stronger than those generated by a wave, thus inducing much larger bed shear stress amplification. The secondary split in the trend lines can be explained by the effect the structure geometry has on the amplification of the pressure field around it. structures with a smaller cross-sectional area (thus smaller amplification in the pressure field) induce smaller values of α_{crit} than larger ones (e.g. monopile).
 - Since the current intensity is strong, only a small wave (i.e. small KC) is required to initiate rock movement near the structure. This explains why there are no data with large values of KC present in the case of current dominated flows.

Figure 8-13 can also serve as a design diagram for the selection of the appropriate stone size for the cover layer of a scour protection system and can be used like the Shields diagram is used for the calculation of the critical Shields number. Figure 8-14 presents a flow chart outlining the process to be followed to determine the stone size. The first step in the calculation of the design current and wave condition for a specific site. These can then be used to calculate the corresponding KC and U_{cw} using equations (2-41) and (2-68). The undisturbed bed shear stress induced by the current (τ_0) can be calculated using Equations (2-5) through (2-8) and the corresponding bed shear stress due to waves (τ_w) using Equations (2-12) through (2-19). The combined maximum wave and current bed shear stress (τ_{max}) can then be determined using the Soulsby (1997) formulation (Equation 2-26). Having the undisturbed bed shear stress due to the combined action of waves and currents the next step is to select an stone diameter (D_{50}) and calculate the corresponding critical bed shear stress using expressions (2-34), (2-35) and (2-2) which then allows the determination of the quantity α_{crit} using Equation (7-

1). This process provides a pair of values (KC , α_{crit}) which identify a point on Figure 8-13. If that point is below the corresponding design curve, then the selected stone diameter is too small to resist the local amplified bed shear stress. This means that the designer needs to re-iterate and select a larger stone size and repeat the process until the point falls on or above the design curve. There are two types of design curve that can be selected:

- a) Wave dominated curve (red line) which should be selected if the flow conditions are wave dominated (i.e. $U_{cw} < 0.5$). This curve applies to all structure geometries.
- b) Current dominated curves (black lines) which should be selected in the case of $KC < 2.1$ and $U_{cw} > 0.5$. In this case the designer should select the curve corresponding to the structure geometry considered in their design.

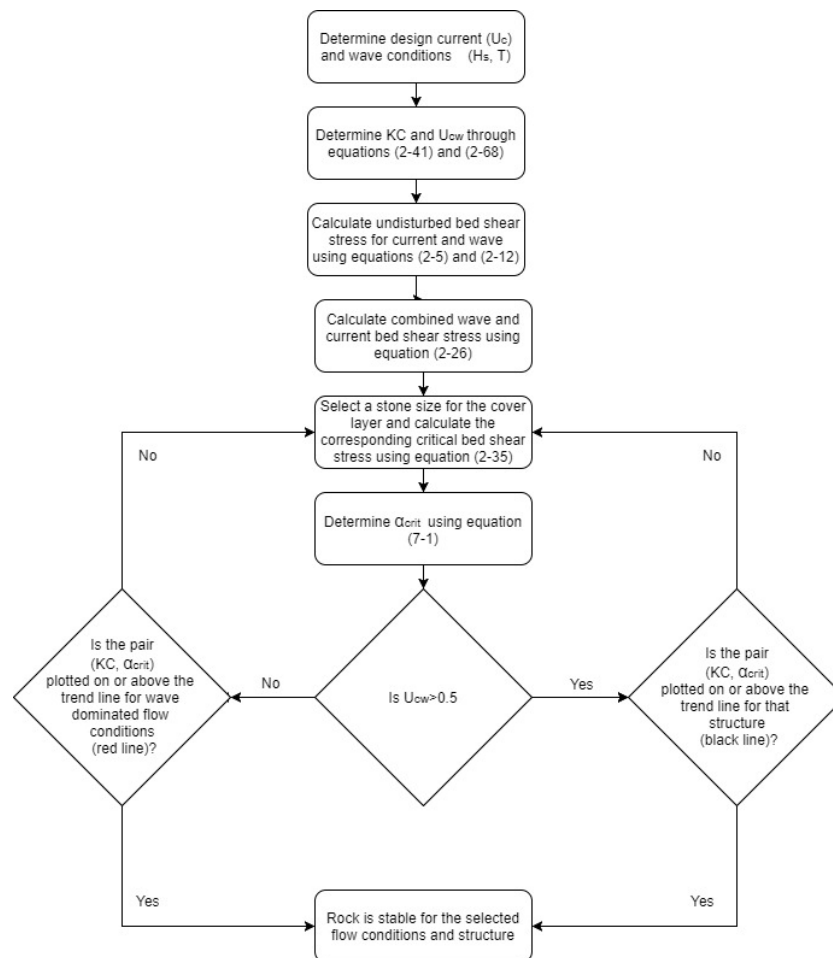


Figure 8-14: Flow chart for the calculation of the required stone size for scour protections cover layer.

8.3.2 Validation of present results

To validate the outcomes of these experiments the design curves presented in the previous section have been compared to the experimental results presented in De Vos (2008), Hjorth (1975), Sumer et al. (1994) and Baykal et al. (2016) who also determined the maximum amplification of the bed shear stress around structures. The result of the comparison is shown in Figure 8-15. The largest data set available are the results of De Vos (2008) who conducted a series of tests to develop an equation capable of calculating the required stone size for a statically stable scour protection (i.e. incipient motion of stone cover). These data show good agreement with the design curves, though there is a slight tendency for the present method to overestimate the critical amplification of the bed shear stress, especially in the case of current dominated flow conditions. This is because in the study of De Vos (2008) scour protection cover was classified as “failed” if one stone had been displaced, while in the present research the Yalin criterion has been applied which suggests that the critical bed shear stress is reached only if m particles are displaced over a certain area and time. This naturally results in an estimation α_{crit} which is higher than if only one stone is required to be displaced. An interesting finding is that the data of De Vos (2008) also suggest that in the case of low KC numbers (lower than 2) there are two trends, one with high amplification (α_{crit}) for current dominated flows and another with low amplifications for wave dominated flow conditions.

Figure 8-15 presents equivalent results from Hjorth (1975), Sumer et al. (1994) and Baykal et al. (2016) who measured (and modelled in the case of Baykal et al., 2016) the bed shear stress amplification over a smooth bed. These results are not directly comparable with the results of the present study because the tests were conducted over a smooth bed which means by definition that τ_{crit} does not exist so nor does α_{crit} . Theoretically, this means that the amplification of the bed shear stress (α) could take any value depending on the incoming flow conditions. For this reason, a second vertical axis representing the values of α is introduced on the right hand side of the figure.

Though the results of these tests tend to be significantly higher than the ones predicted by the design curve it can be seen that on a qualitative level the data obtained over a smooth bed follow the same trend with the wave dominated tests yielding α between 1.2 and 4 and in the case of current dominated conditions amplifications up to 11. One more explanation why these results yield such a high amplification is the small levels of momentum exchange between the layers of the fluid which translates into larger forces near the bed in the case of a smooth bed. In the case of a rough bed the shear stress will be smaller due to the exchange of momentum between the fluid's layers which means that more energy is diffused for the same flow conditions thus resulting in smaller bed shear stresses than in the case of a smooth bed.

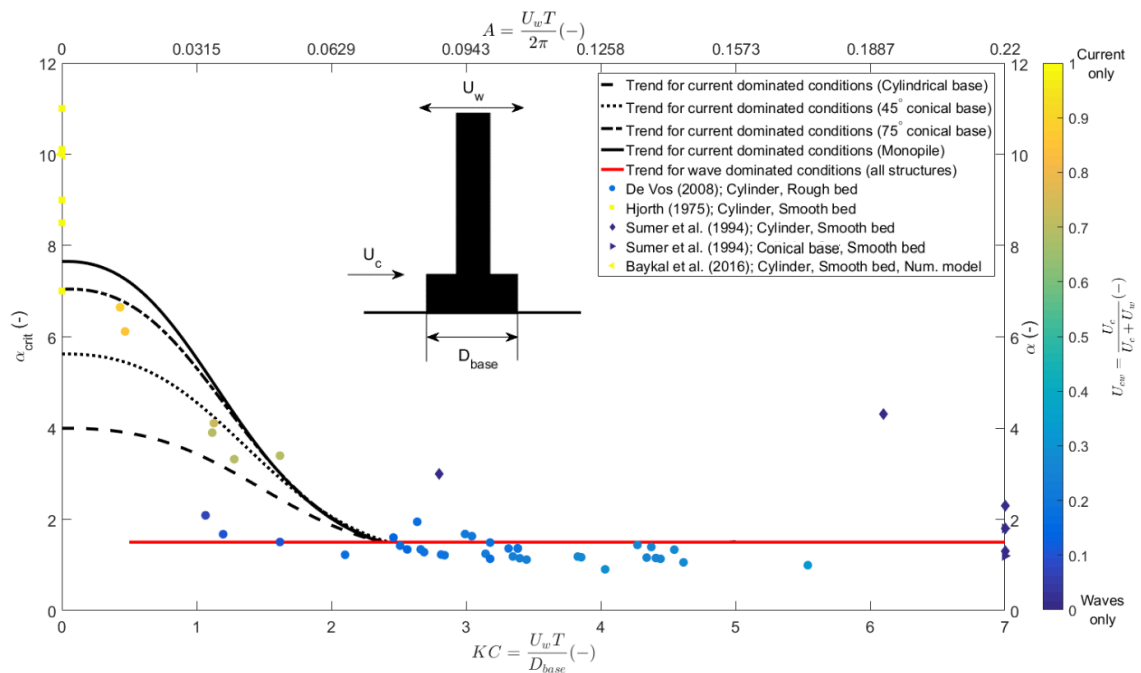


Figure 8-15: Comparison of present design curves with published experimental results.

8.4 Development of scour protection damage

This section will present the results for the experiments which investigated the damage pattern induced by flow conditions which induce incipient motion of the rock cover. The study involves the measurement of the scour protection damage profile after 500, 1000, 5000 and 10000 waves or the failed profile if it occurred prior to 10000 waves. The results

will be presented for each structure geometry separately and a discussion of the results will be presented at the end of the section.

8.4.1 Monopile damage pattern

Figure 8-16 present the damage pattern induced around the monopile under the forcing of three different flow regimes, waves only (Test 6.1), waves dominated (Test 6.2) and current dominated (Test 6.3). The figures show that after the first 1000 waves there is no significant damage pattern observed though there is some initial erosion which is less than 1 stone cover diameter (D_{50}). After 5000 waves the clear damage patterns emerge that have distinct characteristics which depend on the flow regime:

- Waves only: The damage occurs at an angle of 45° - 90° relative to the flow direction with small deposition areas observed in front and behind the structure. These locations of deposition are explained by the orbital motion of the waves near the bed which effectively erode sediment from the sides of the piles (where the amplification of the pressure is the highest) and deposit it at upstream and downstream side of the structure where the amplification is lower.
- Wave dominated: Here the erosion pattern occurs at the same location as for the wave only case but most of the deposition occurs as the lee of the structure. This is due to the current which effectively creates a net sediment transport in the direction of the mean flow.
- Current dominated: Here the presence of a strong current imposed on a small wave forces most of the damage to occur at the lee of the structure. This can be attributed to the vortex shedding induced by the stronger current.

It is also observed that though the scour protection in the first two cases has not failed after $N=5000$ the cover layer in the case of a current dominated condition failed after 3200 waves. This increased damage rate can also be explained by the higher turbulence levels associated with the lee-wake vortex shedding.

Figure 8-16 shows that the rock cover for the waves only test failed after 6100 waves and at $N \approx 7800$ in the case of a wave-dominated flow. The rate of damage in the case of a wave-dominated flow being slower than the wave only case can be explained by the skewness of the flow which may only be able to remove sediment during one half-cycle

of the wave. The location of the failure is consistent with the damage pattern observed in the previous paragraph.

Figure 8-17 present the damage pattern in the case of a current-only flow. As for the case of the current-dominated flow conditions presented in Figure 8-16 the majority of the damage occurs at the lee of the structure. In this case the two distinct scour holes are wider apart compared to the current-dominated case and can be explained by the vortex shedding induced by the current-structure interaction. In addition, it can be observed that the scour protection failed within the same time as the current dominated-case, the present tests failing after 75min and the current-dominated after 80min. This suggests that the damage pattern in these two case is mainly attributed to the lee wake vortex shedding.

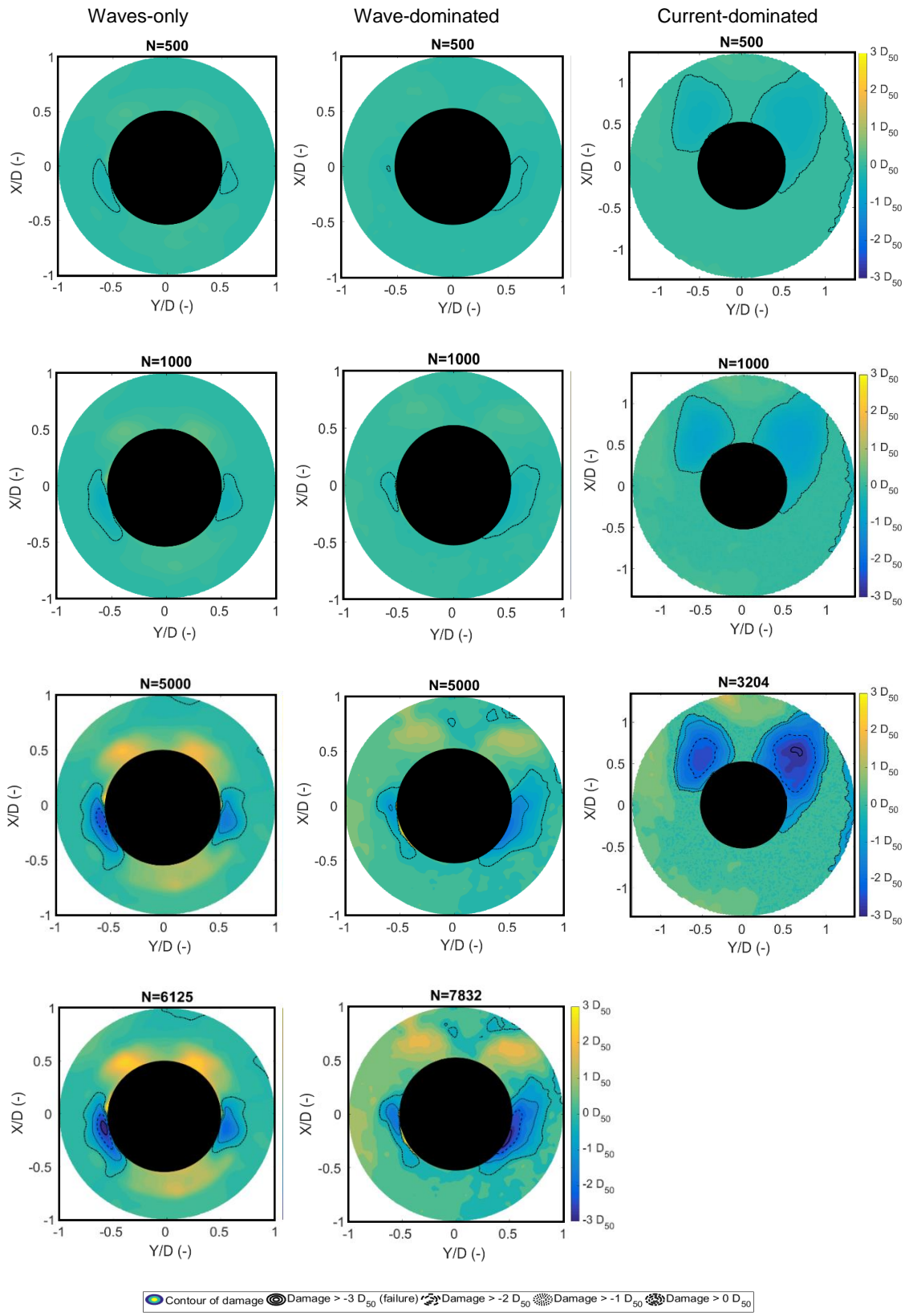


Figure 8-16: Damage induced by a cylinder in the following flow regimes: waves only; wave dominated; and current dominated after N number of waves (flow and waves in positive X-direction).

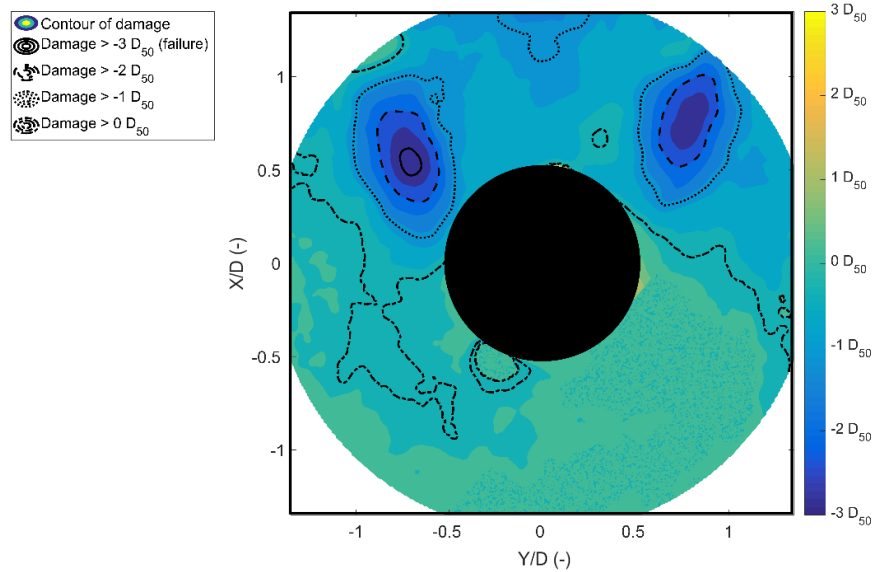


Figure 8-17: Damage induced by a cylinder in current only flow conditions after $t=1\text{hr}$ and 15min (flow in positive X -direction).

8.4.2 75° conical base

Figure 8-18 show the damage pattern for the 75° conical base for the same flow conditions as for the monopile case presented in the previous section. The results show a damage pattern with the same quantitative characteristics for the three flow conditions considered. It can be observed that there is no deposition in the wave only test. During the tests it was observed that the majority of the sediment transport occurred in the Y direction and thus the deposition patterns were not picked up by the photogrammetry measurements. In the case of the current-dominated tests (i.e. waves & strong current) the damage pattern is located further downstream of the structure. This may be a result of the flow being deflected by the slopes of the structure which transports the lee wake vortices further downstream than in the case of the monopile.

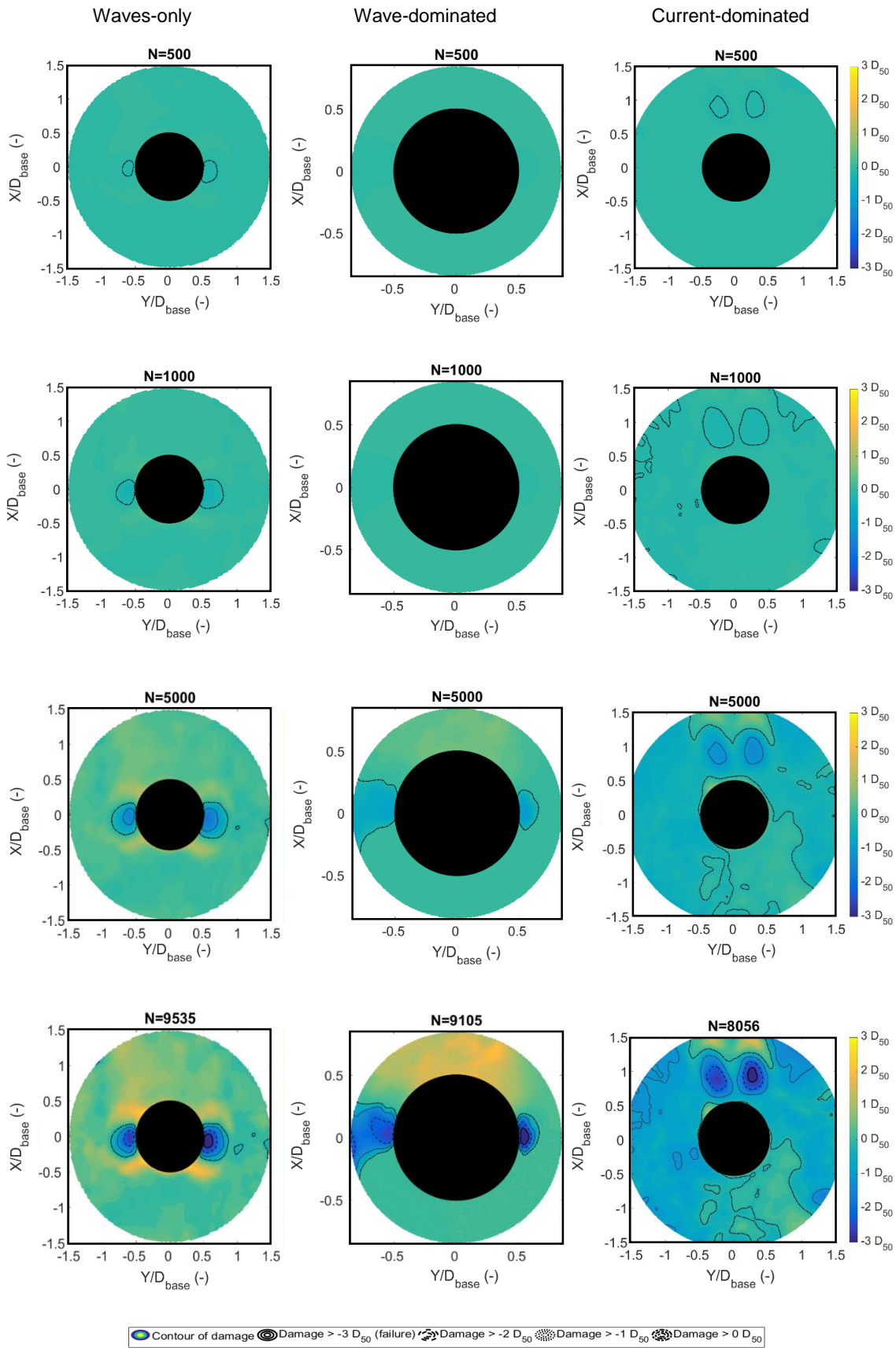


Figure 8-18: Damage induced by a 75° conical base structure in the following flow regimes: waves only; wave dominated; and current dominated after N number of waves (flow and waves in positive X-direction).

The damage profile for the 75° conical base structure under the forcing of a unidirectional current is presented in Figure 8-19. It can be observed that the damage pattern in this case is similar to that of the monopile in Figure 8-17. The difference here is that the scour holes are further to the lee of the structure which is consistent with the findings of the current dominated case. The time to failure for this test was 3hr and 1min which matches the corresponding time for the current dominated case presented in Figure 8-18 and is close to $N=7589$ (i.e. 3hr and 10 min).

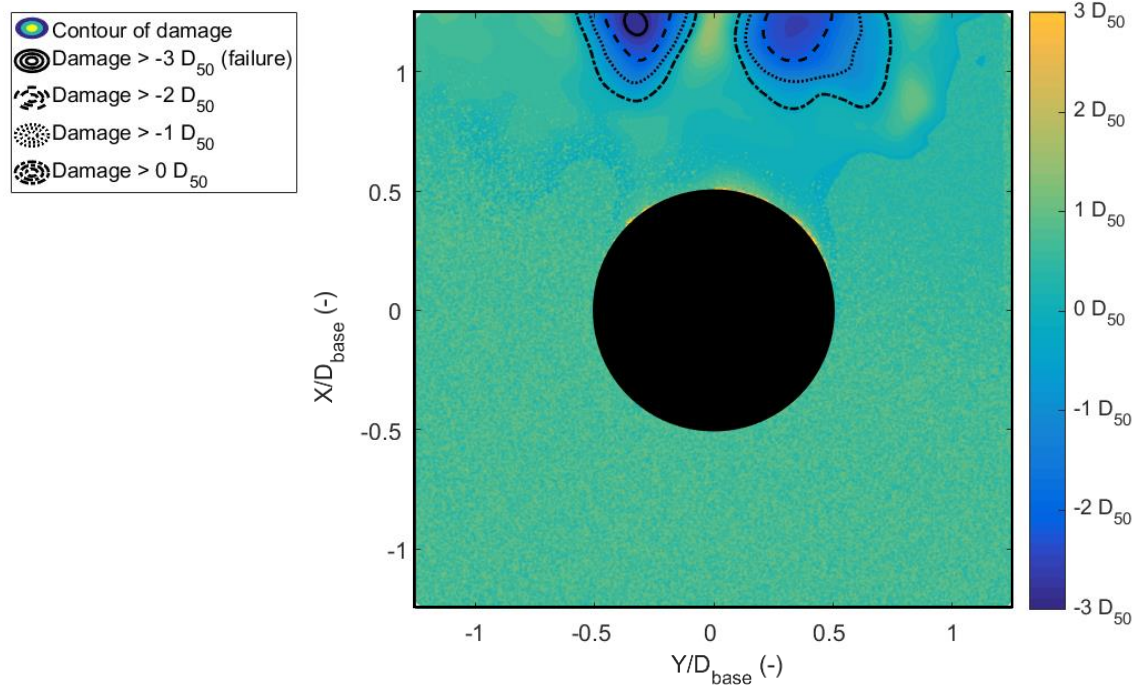


Figure 8-19: Damage induced by a 75° conical base structure in current only flow conditions after $t=3\text{hr}$ and 1min (flow in positive X-direction).

8.4.3 45° conical base

The damage pattern for the 45° conical base structure is presented in Figure 8-20. As for the two previously presented geometries the combinations of currents and waves have the same effect on damage pattern. In the waves-only case no deposition pattern is observed which was also observed in the wave dominated case of Figure 8-18. During this test the sediment was transported laterally (Y-direction) and deposited outside the photogrammetry field of view. This lateral sediment transport may be attributed to the interaction of the cone with the local hydrodynamics but further investigations need to be conducted to understand this process.

Figure 8-21 presents the damage pattern induced by a unidirectional current on a 45° conical base structure. It can be seen that the location of the damage coincides with that observed in the previous cases. In this case the footprint of the damage is smaller than the two other geometries. This is explained by the smaller shaft diameter which is interacting with the current which results in lee-wake vortices with a significantly smaller size. In addition, the location of the damage pattern in the case of the current alone (Figure 8-21) and current dominated (Figure 8-20) cases is closer to the structure compared to the 75° conical base structure which can be explained in a similar manner.

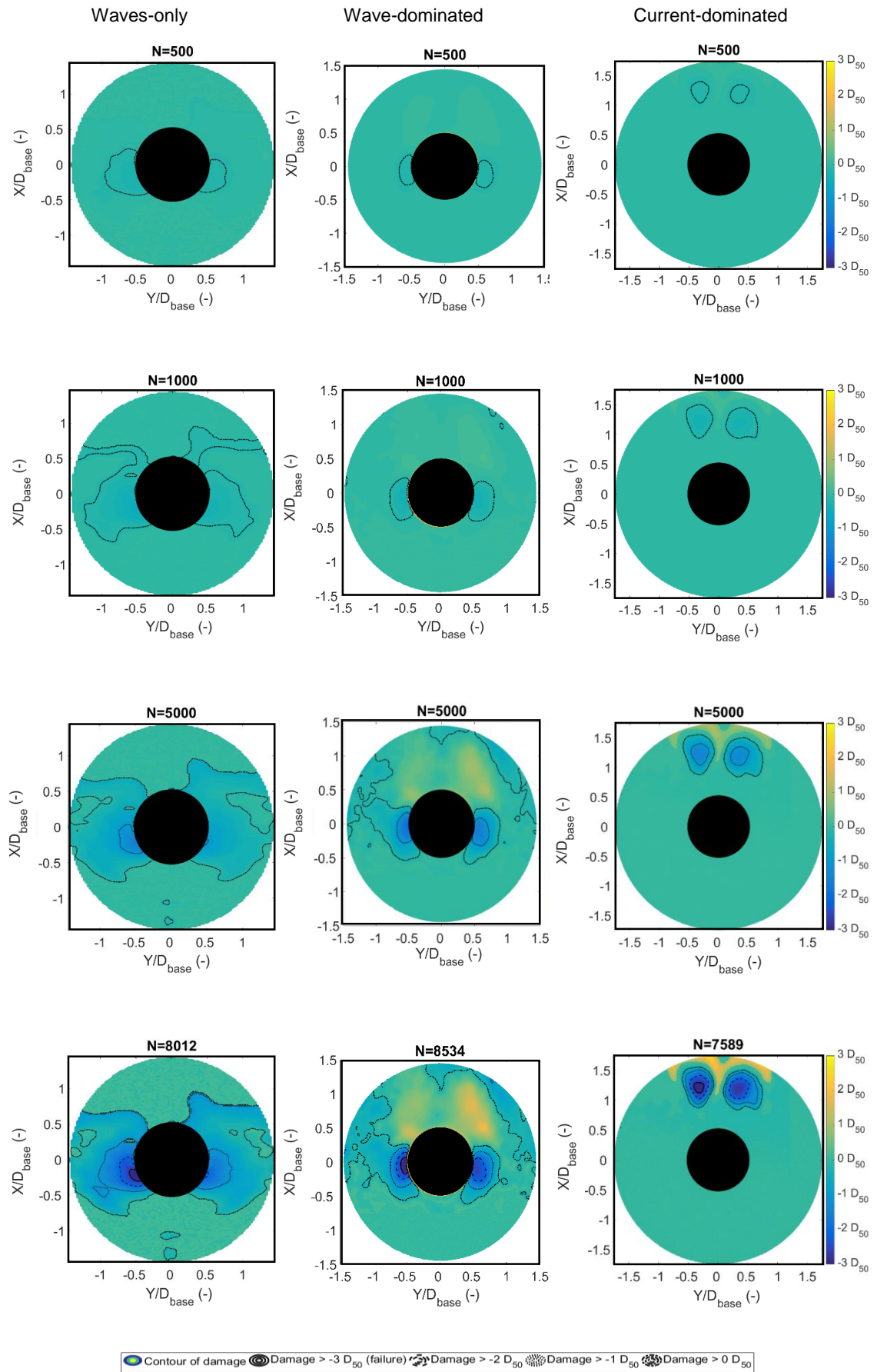


Figure 8-20 Damage induced by a 45° conical base structure in the following flow regimes: waves only; wave dominated; and current dominated after N number of waves (flow and waves in positive X-direction).

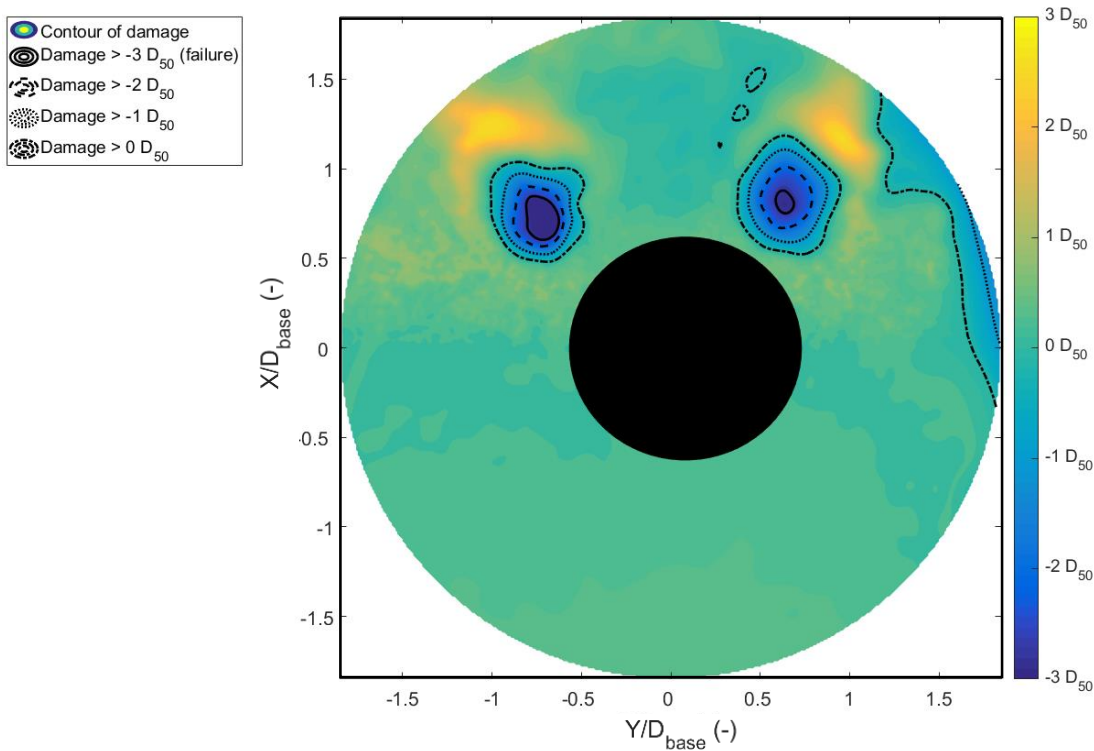


Figure 8-21: Damage induced by a 45° conical base structure in current only flow conditions after 3hr and 21min (flow in positive Y-direction).

8.4.4 Cylindrical base structure

Figure 8-22 presents the damage pattern for the cylindrical base structure under the forcing of waves only and waves and a small current.

Due to poor image capturing for the remaining two flow conditions no results were able to be obtained. The damage patterns for the two flow conditions agree with the findings of the previously presented geometries. In these tests the deposition pattern is altered slightly with most of the deposition occurring at the lee of the structure in the case of the waves-only scenario. This finding may be attributed to the non-linearity of the waves (as discussed in section 8.1) which results in smaller orbital velocities when the flow reverses. Given that the magnitude of the amplification of the pressure gradient for this structure is mainly attributed to the cylindrical cap of the structure it can be expected that under certain wave conditions the wave amplitude during one half-cycle may not be strong enough to erode sediment and therefore no deposition is required.

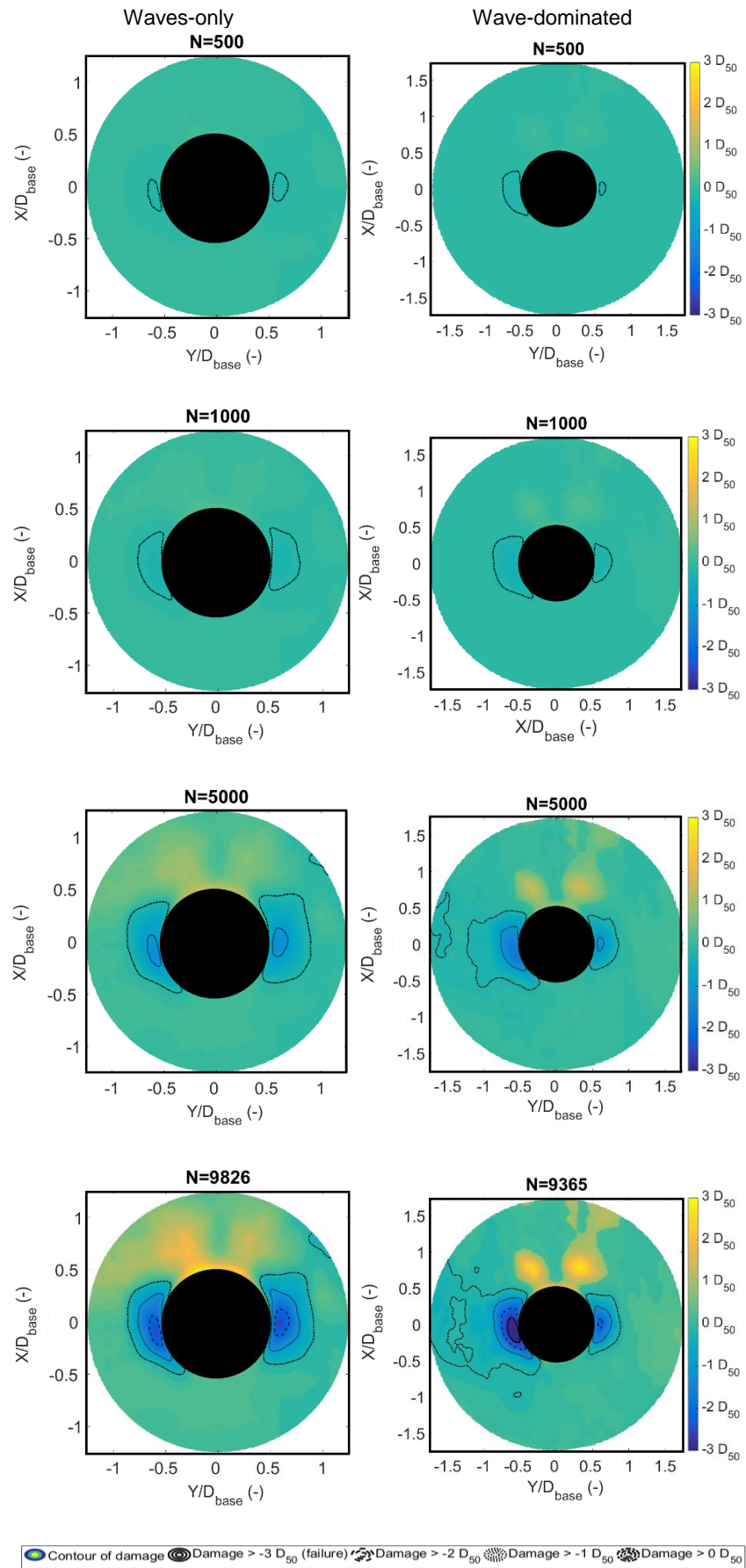


Figure 8-22: Damage induced by a cylindrical base structure in the following flow regimes: waves only; and wave dominated after N number of waves (flow in positive Y-direction and waves in Y-direction).

8.4.5 Discussion of results

Section 8.3.2 presented the findings of tests that looked into the damage pattern induced by four types of hydrodynamic conditions on four structural geometries. The results reveal that geometry does not affect the damage pattern but rather the damage pattern is influenced by the ambient flow conditions. The results showed that in the case of waves only and wave dominated conditions the damage occurs at the sides of the structure. The location of the damage under these flow conditions is attributed to the steady streaming process and the horseshoe vortex induced by the wave action. In the case of current only and current dominated flow conditions, the damage occurs at the lee of the structure due to the increased turbulence induced by the lee-wake vortex separation. The findings agree well with the findings of De Vos et al., 2008 who also found that the damage around monopiles occurs at the lee of the structure in the case of currents and at the sides in the case of waves. Furthermore, the present study showed that the scour protection will fail (i.e. a portion of the original bed will be uncovered) if flow conditions that lead to incipient motion of the rock cover persist for a sufficiently long period of time. This finding agrees with those of Vithana (2013) who found that the initial displacement of rocks leads to the destabilisation of even more rocks due to the increased roughness of the bed created by the larger protrusion of the rock. This creates additional turbulence on the layer of fluid just over the bed armour which enhances the probability of displacement of a rock element. Finally, it has been observed that the time to failure of a scour protection system is a function of two factors:

- The structure geometry: structures inducing larger depth averaged pressure gradients induce faster damage rate.
- The flow conditions: wave-dominated flow conditions induce a scour rate which is slower compared to the damage rate induced by a current dominated flow condition. This difference in the damage rate for different flow conditions is linked to the different flow structure interaction processes involved in each case.

9 Conclusions and recommendations

9.1 Conclusions

The objective of this thesis is to improve understanding of the scour process and scour protection stability around GBFs. This was achieved through an extensive laboratory test programme to examine the effects of a range of flow conditions and structural geometries. To achieve the aims and objectives outlined in chapter 3 a number of novel measuring techniques were developed and applied. This led to the development of a scour prediction equation capable of predicting the equilibrium scour depth around complex geometries and a design diagram that can be used for the selection of the appropriate static scour protection rock size.

The first part of this thesis looks into the effect the structure geometry has on the equilibrium scour depth around such structures. As part of this research a design method for the prediction of the equilibrium scour depth around uniform and non-uniform cylindrical structure geometries under clearwater scour conditions is presented. An equation is derived based on experimental and field data obtained by experiments in this study and other published work. This method is based on a new physical quantity, the depth-averaged Euler number, the influence of which is verified through experimental data collected during this research. The second part of this thesis investigated the stability of scour protection around the same geometries under the forcing of waves and currents. The study produced a design diagram that can be used to select the appropriate stone size for specific undisturbed flow conditions based on the structure geometry. The method shows good agreement with experimental data of other authors.

In addition to the methods for the calculation of the scour depth and optimum scour protection size, several conclusions have also been reached through this study:

1. The flow measurements around the structures revealed the existence of a clockwise recirculating cell at the lee of the cylindrical base structure. This

recirculation cell can explain the significant reduction of the scour depth at the lee of the specific structure.

2. The analysis of the equilibrium scour depth data showed that the equivalent pile diameter is not an appropriate length scale to normalise the scour depth. Structures with thin top shafts can lead to equivalent diameters with very low values which in turn result in values of S/D_{eq} which are unrealistically high.
3. The tests showed that the scour pattern around the structures is linked to the geometry of the structure with the complex structure inducing different scour patterns from the monopile. In addition, there is no clear evidence that the upstream scour slope is dependent on the geometry or the incoming flow conditions. In general, the slopes in all tests ranged between 30° and 45° which correspond to the upper limit of the angle of repose for submerged sands. The downstream slope varies from 0° to 45° and seems to depend both on the structure geometry and the hydrodynamics. The results also revealed that the structural geometry has a significant effect on the scour development and the equilibrium scour depth. Structures with larger cross-sectional areas induce more rapid and deeper scour while smaller ones slower and more shallow scour holes. This behaviour is linked to the effect the geometry has on the local change in the pressure gradient and on the surrounding bed. Results from the tests also suggest that changes of the incoming flow profiles result in changes in the scour depths. This can be explained with the same line of logic.
4. The flow measurements around the structures show that the monopile has a different hydrodynamic behaviour compared to the conical base structures, while the cylindrical base structure has similarities with both of the aforementioned structures. The measurements showed that the discontinuities between the different geometrical components of the structure induce flow separation.
5. The results from the pressure measurements show good agreement with potential flow theory. In addition, the equilibrium scour depth results show good agreement with the non-dimensional depth averaged pressure gradient. Based on these findings it can be concluded that potential flow theory can be used to calculate the Euler, which is an important physical quantity characterising the equilibrium scour depth.
6. Other physical quantities influencing the equilibrium scour depth have been identified as Re_D , Fr , U_c/U_{cr} , and h/D .

7. The incipient motion detection method that was developed in this study was used to determine the critical bed shear stress for different combinations of wave and currents (Figure 7-9) and was found that the results fall within 10% of the predictions of τ_{crit} given by the Soulsby (1997) method.
8. Scour protection stability tests showed that the following parameters do not have a significant influence on the critical amplification of the bed shear stress (α_{crit}) around the geometries tested in this study:
 - a. Stone size (D_{50})
 - b. Bed permeability
 - c. Flow direction
 - d. Scour protection configuration
9. It was found that for the waves tested in this study, waves opposing a current did not significantly affect the amplification of the bed shear stress around the structures.
10. The stability of the scour protection is mainly a function of the KC and U_{cw} . It was found that for wave dominated flow ($U_{cw} < 0.5$) the critical amplification of the bed shear stress is constant and does not exceed the value of 2. For current dominated flows ($U_{cw} > 0.5$) α_{crit} increases significantly as the KC value decreases and is dependent on the structure geometry.
11. The location of the damage is not dependent on the structure geometry. It rather depends on the incoming flow conditions with current dominated flows inducing damage patterns at the lee of the structure, whereas wave-dominated flow damage occurs at the sides of the structure.
12. Scour protection that undergoes incipient motion will fail as long as the flow conditions persist for a sufficiently long period.

9.2 Recommendations

The increasing computation power of modern computers and the development of new Computational Fluid Dynamics (CFD) solvers, means that the field of hydraulic engineering is increasingly reliant on the results of such programmes and less on the results of physical modelling. The outcomes of the present research and more specifically the scour prediction method can be easily coupled with CFD solvers to determine the scour depth around complex geometries in a computationally efficient manner. Such solvers require extensive validation campaigns which in turn require experimental results which are also provided in this research.

In addition, the present research has opened a number of possibilities for further research which are presented below:

- In terms of scour:
 - The scour prediction equation applicability could be expanded to include the effects of live bed scour and more complex geometries (e.g. jacket foundation, tripods and substations). Additional, experiments are required to fully evaluate these effects.
 - As only two structural scales were tested in this study, more experiments at a larger scale would complement the results and provide further insights the associated effects on scour.
 - Further research is required to understand the causes of avalanching at the edge of the scour hole that were observed during experiments 3.5-3.8.
- In terms of the scour protection stability:
 - The accuracy of the incipient motion detection method could be further increased by applying more sophisticated particle tracking algorithms and using more accurate and advanced measuring devices.
 - Additional experimental and numerical studies could provide valuable insights on the underlying physics which lead to the sudden increase in the bed shear stress amplification for $U_{cw} > 0.5$.
 - During this test the sediment was transported laterally (Y-direction) and deposited outside the photogrammetry field of view. This lateral sediment transport may be attributed to the interaction of the cone with the local

hydrodynamics but further investigations need to be conducted to understand this process.

- The application range of the design chart for the selection of the appropriate stone size for scour protection can be increased by conducting more experiments at larger KC values, varying flow depths, protection thicknesses and structure sizes. In addition, incorporating the Euler number as a variable describing the effects of the structures geometry can also lead to the application of this method to a wider range of geometries.
- The results provide valuable insights into the scour protection damage progression. More experimental data on the topic provide valuable insight and could allow the development a prediction method.
- It should be kept in mind that small scale experiments might be subject to scale and model effects. Verification of the results with large scale models and prototype measurements is indispensable.

10 References

Achenbach, E. (1968). Distribution of local pressure and skin friction around a circular cylinder in cross-flow up to $Re = 5 \times 10^6$. *Journal of Fluid Mechanics*, 34(4), 625-639.

ABPmer Ltd et al. (2010). A Further Review of Sediment Monitoring Data. Commissioned by COWRIE Ltd (project reference ScourSed-09).

Amini, A., Melville, B. W., Ali, T. M., and Ghazali, A. H. (2011). Clear-water local scour around pile groups in shallow-water flow. *Journal of Hydraulic Engineering*, 138(2), 177-185.

Ataie-Ashtiani, B., Baratian-Ghorghi, Z., and Beheshti, A. A. (2010). Experimental investigation of clear-water local scour of compound piers. *Journal of Hydraulic Engineering*, 136(6), 343-351.

Baker, C. J. (1978). Vortex flow around the bases of obstacles (Doctoral dissertation, University of Cambridge).

Baker, C. J. (1979). The laminar horseshoe vortex. *Journal of Fluid Mechanics*, 95(02), 347-367.

Baker, C. J. (1980). The turbulent horseshoe vortex. *Journal of Wind Engineering and Industrial Aerodynamics*, 6(1), 9-23.

Baker, C. J. (1985). The position of points of maximum and minimum shear stress upstream of cylinders mounted normal to flat plates. *Journal of wind engineering and industrial aerodynamics*, 18(3), 263-274.

Baker, C. J. (1991). The oscillation of horseshoe vortex systems. *Journal of Fluids Engineering*, 113(3), 489-495.

Baker, R. E. (1986). Local scour at bridge piers in non-uniform sediment. Thesis presented to the university of Auckland, New Zealand, in partial fulfilment of the requirements for the degree of Master of Philosophy.

Baykal, C., Sumer, B. M., Fuhrman, D. R., Jacobsen, N. G., and Fredsøe, J. (2015). Numerical investigation of flow and scour around a vertical circular cylinder. *Philosophical Transactions of the Royal Society of London A: Mathematical, Physical and Engineering Sciences*, 373(2033), 20140104.

Bear, J. (1972). Dynamics of fluids in porous materials. Society of Petroleum Engineers.

Bijker, E. W., and De Bruyn, C. A. (1989). Erosion around a pile due to current and breaking waves. In *Coastal Engineering 1988* (pp. 1368-1381).

Blanco, M. I. (2009). The economics of wind energy. *Renewable and Sustainable Energy Reviews*, 813(6), 1372-1382.

Blevins, R. D., and Burton, T. E. (1976). Fluid forces induced by vortex shedding. *Journal of Fluids Engineering*, 98(1), 19-24.

Bonasoundas, M. (1973). Non-stationary Hydromorphological Phenomena and Modelling of Scour Process. In *Proc. 16th IAHR Congress* (Vol. 2, pp. 9-16).

Bos, K. J., Chen, Z., Verheij, H. J., Onderwater, M., and Visser, M. (2002a). Local scour and protection of F3 offshore GBS platform. In *ASME 2002 21st International Conference on Offshore Mechanics and Arctic Engineering* (pp. 219-230). American Society of Mechanical Engineers.

Bos, K. J., Verheij, H. J., Kant, G., and Kruisbrink, A. C. H. (2002b). Scour protection around gravity based structures using small size Rock. In *First International Conference on Scour of Foundations*.

Bosboom, J., and Stive, M. J. (2012). Coastal Dynamics I: Lectures Notes CIE4305. VSSD.

Briaud, J. L. (2004). Pier and contraction scour in cohesive soils (Vol. 516). Transportation Research Board.

Breusers, H. N. C. (1965). Conformity and time scale in two-dimensional local scour. Waterloopkundig Laboratorium.

Breusers, H. N. C. (1971). Local scour near offshore structures. Publication. Delft Hydraulics Laboratory Publikatie-Waterloopkundig Laboratorium.

Breusers, H. N. C., and Raudkivi, A. J. (1991). Scouring, hydraulic structures design manual. IAHR, AA Balkema, Rotterdam, 143.

Breusers, H. N. C., Nicollet, G., and Shen, H. W. (1977). Local scour around cylindrical piers. Journal of Hydraulic Research, 15(3), 211-252.

Buffington, J.M., and Montgomery, D.R. (1997). A systematic analysis of eight decades of incipient motion studies, with special reference to gravel-bedded rivers: Water Resources Research. v. 33, p. 1993-2029.

Cardoso, A. H. and Bettess, R. (1999). Effects of time and channel geometry on scour at bridge abutments, J. Hydraul. Eng., 125:4, 388-399.

Carroll, B., Cooper, B., Dewey, N., Whitehead, P., Dolphin, T., Rees, J., Judd, A., Whitehouse, R. and Harris, J. (2010). A further review of sediment monitoring data. Cowrie ScourSed-09, Southampton, UK, 106.

Carstens, T. (1976). Seabed scour by currents near platforms. Mar. Sci. Commun., 2(1), 69-93.

Chabert, J., and Engeldinger, P. (1956). Study of scour around bridge piers. Rep. Prepared for the Laboratoire National d'Hydraulique

Chee, R. K. W. (1982). Live-bed scour at bridge piers. Publication of: Auckland University, New Zealand, (290).

Chen, H. H., Yang, R. Y., Kuo, P. C., and Hwung, H. H. (2012). Physical modeling study on scour and scour countermeasure for sea-crossing bridge piers. *Coastal engineering proceedings*, 1(33), 83.

Chiew, Y. M. (1984). Local scour at bridge piers (Doctoral dissertation, ResearchSpace@ Auckland).

Chiew, Y. M. (1995). Mechanics of riprap failure at bridge piers. *Journal of Hydraulic Engineering*, 121(9), 635-643.

Chou, J. H., and Chao, S. Y. (2000). Branching of a horseshoe vortex around surface-mounted rectangular cylinders. *Experiments in fluids*, 28(5), 394-402.

Christoffersen, J. B., and Jonsson, I. G. (1985). Bed friction and dissipation in a combined current and wave motion. *Ocean Engineering*, 12(5), 387-423.

Coleman, S. E. (2005). Clearwater local scour at complex piers. *Journal of Hydraulic Engineering*, 131(4), 330-334.

Dargahi, B. (1989). The turbulent flow field around a circular cylinder. *Experiments in Fluids*, 8(1-2), 1-12.

Davies, A. M., and Lawrence, J. (1994). Examining the influence of wind and wind wave turbulence on tidal currents, using a three-dimensional hydrodynamic model including wave–current interaction. *Journal of Physical Oceanography*, 24(12), 2441-2460.

De Vos, L., De Rouck, J., Troch, P., and Frigaard, P. (2011). Empirical design of scour protections around monopile foundations: Part 1: Static approach. *Coastal Engineering*, 58(6), 540-553.

De Vos, L., De Rouck, J., Troch, P., and Frigaard, P. (2012). Empirical design of scour protections around monopile foundations. Part 2: Dynamic approach. *Coastal Engineering*, 60, 286-298.

Den Boon, J. H., Sutherland, J., Whitehouse, R., Soulsby, R., Stam, C. J. M., Verhoeven, K., and Hald, T. (2004). Scour behaviour and scour protection for monopile foundations of offshore wind turbines. EWEC, London, UK.

Dey, S., Bose, S. K., and Sastry, G. L. (1995). Clear water scour at circular piers: a model. *Journal of Hydraulic Engineering*, 121(12), 869-876.

Dey, S., and Raikar, R. V. (2007). Characteristics of horseshoe vortex in developing scour holes at piers. *Journal of Hydraulic Engineering*, 133(4), 399-413.

Dietz, J. W. (1972). Ausbildung von Langen Pfeilern bei Schraganströmung am Beispiel der BAB-Mainbrücke Eddersheim. *Mitteilungsblatt der BAW*, 31, 79-94.

Dixen, M., Hatipoglu, F., Sumer, B. M., and Fredsøe, J. (2008). Wave boundary layer over a stone-covered bed. *Coastal Engineering*, 55(1), 1-20.

Eadie IV, R. W., and Herbich, J. B. (1986). Scour about a single, cylindrical pile due to combined random waves and a current. In *Coastal Engineering 1986* (pp. 1858-1870).

Ettema, R. (1976). Influence of bed gradation on local scour: New Zealand, University of Auckland, School of Engineering (No. 124). Report.

Ettema, R. (1980). Scour at bridge piers (No. 216 Monograph).

Ettema, R., Kirkil, G., and Muste, M. (2006). Similitude of large-scale turbulence in experiments on local scour at cylinders. *Journal of Hydraulic Engineering*, 132(1), 33-40.

Fael, C. M. S., Simarro-Grande, G., Martín-Vide, J. P., and Cardoso, A. H. (2006). Local scour at vertical-wall abutments under clear-water flow conditions. *Water resources research*, 42(10).

Florida Department of Transportation (FDOT). (2005). Bridge scour manual, Tallahassee, FL.

Fenton, J. D. (1985). A fifth-order Stokes theory for steady waves. *Journal of waterway, port, coastal, and ocean engineering*, 111(2), 216-234.

Ferraro, D., Tafarojnoruz, A., Gaudio, R., and Cardoso, A. H. (2013). "Effects of pile cap thickness on the maximum scour depth at a complex pier." *J. Hydraul. Eng.*, 10.1061/(ASCE)HY.1943-7900.0000704, 482–491.

Fredsøe, J., and Deigaard, R. (1992). *Advanced series on ocean engineering*. World Scientific, 3, 392.

Fredsøe, J., and Sumer, B. M. (1997). Scour at the round head of a rubble-mound breakwater. *Coastal engineering*, 29(3-4), 231-262.

Friedrichs, C. T., and Aubrey, D. G. (1994). Tidal propagation in strongly convergent channels. *Journal of Geophysical Research: Oceans*, 99(C2), 3321-3336.

Froehlich, D. C. (1988). Analysis of onsite measurements of scour at piers. In *Hydraulic Engineering: Proceedings of the 1988 National Conference on Hydraulic Engineering* (pp. 534-539).

Gülççe, T., Sumer, B.M. and Fredsøe, J., (1994). Scour around the head of a vertical-wall breakwater. In: *Proc. International Conf. on Hydro-Technical Engineering for Port and Harbor Construction*, Yokosuka, pp. 1097-1116.

Graf, W. H., and Yulistiyanto, B. (1998). Experiments on flow around a cylinder; the velocity and vorticity fields. *Journal of Hydraulic Research*, 36(4), 637-654.

Grune, J., Sparboom, U., Schmidt-Koppenhagen, R., Wang, Z., and Oumeraci, H. (2006). Stability tests of geotextile sand containers for monopile scour protection. In *Coastal Engineering Conference* (Vol. 30, No. 5, p. 5093). ASCE American Society of Civil Engineers.

Guo, J. (2012). Pier scour in clear water for sediment mixtures. *Journal of Hydraulic Research*, 50(1), 18-2

Hannah, C. (1980). Scour at pile groups. University of Canterbury Library.7.

Hansen, N. E. O., and Gislason, K. (2005). Movable scour protection on highly erodible sea bottom. In *International Coastal Symposium*.

Harris, J.M. and Whitehouse, R.J.S. (2015). Marine scour: Lessons from Nature's laboratory. In: *Scour and Erosion, Proc. 7th Int. Conf. on Scour and Erosion*, The University of Western Australia, 2 - 4 December, 2014, (eds.) Cheng. L., Draper, S. and An, H., CRC Press, p. 19 - 31(Keynote).

Herbich, J. B. (1984). *Seafloor scour: Design guidelines for ocean-founded structures (Vol. 4)*. Marcel Dekker Inc.

Hjorth, P. (1975). *Studies on the nature of local scour*. Department of Water Resources Engineering, Lund Institute of Technology, University of Lund, Sweden, Bull Series A 46.

Hjulstrom, F. (1939). *Transportation of detritus by moving water: Part 1. Transportation*.

Holmedal, L. E., and Myrhaug, D. (2013). Combined tidal and wind driven flows and bedload transport over a flat bottom. *Ocean modelling*, 68, 37-56.

Hoffmans, G. J. C. M. (1990). *Concentration and flow velocity measurements in a local scour hole*. TU Delft, Department of Hydraulic Engineering.

Hoffmans, G. J. (2012). *The influence of turbulence on soil erosion (Vol. 10)*. Eburon Uitgeverij BV.

Hoffmans, G. J., and Verheij, H. J. (1997). *Scour manual (Vol. 96)*. CRC Press.

Hofland, B. (2005). *Rock and roll: Turbulence-induced damage to granular bed protections*. TU Delft, Delft University of Technology.

Hughes, S. A. (1993). Physical models and laboratory techniques in coastal engineering (Vol. 7). World Scientific.

Hughes, S. (2003). Physical modelling considerations for coastal structures. In: Advances in Coastal Structure Design, Edited by Mohan, R. K., Magoon, O. and Pirrello M.

Isbash, S. V. (1935). Construction of dams by dumping stones in flowing water. U.S. Army Engr. District, Eastport, Maine.

Jain, S. C., and Fischer, E. E. (1979). "Scour around circular bridge piers at high Froude numbers." No. FHWA-RD-79-104 Final Rep., Federal Highway Administration, Washington, DC.

Jannaty, M. H., Eghbalzadeh, A., and Hosseini, S. A. (2015). "Using field data to evaluate the complex bridge piers scour methods." Can. J. Civ. Eng., 43(3), 218–225.

Johnson, P. A. (1992). Reliability-based pier scour engineering. Journal of Hydraulic engineering, 118(10), 1344-1358.

Jones, J. S., Kilgore, R. T., and Mistichelli, M. P. (1992). Effects of footing location on bridge pier scour. Journal of Hydraulic Engineering, 118(2), 280-290

Jonsson, I. G. (1966). Wave boundary layers and friction factors. Coastal Engineering Proceedings, 1(10).

Kawata, Y., and Tsuchiya, Y. (1988). Local scour around cylindrical piles due to waves and currents combined. In Coastal Engineering 1988 (pp. 1310-1322).

Kiya, M., Tamura, H., and Arie, M. (1980). Vortex shedding from a circular cylinder in moderate-Reynolds-number shear flow. Journal of Fluid Mechanics, 101(04), 721-735.

Khalfin I.S. (1983). Local scour around ice-resistant structures caused by wave and current effect. Proc. 7-th Int. Conf. on Port and Ocean Engrg. Under Arctic Conditions (POAC-83). Helsinki: Technical Research Center of Finland, ESPOO, 1983. V. 2. P. 992–1002.

Khalfin, I.S., Avdeewa, V.I., and Longinov, V.V. (1988). Local Scour of Riprap Around Ice-Resistant Cylindrical and Conical Gravity Structures Caused by Waves, Proc. of Int. Conf. on Technology for Polar Areas (POLARTECH-88), Trondheim: Tapir Publishers, vol. 1, pp. 275–285.

Khalfin, I. S. (2007). Modeling and calculation of bed score around large-diameter vertical cylinder under wave action. *Water Resources*, 34(1), 49-59.

Kobayashi, T., and Oda, K. (1995). Experimental study on developing process of local scour around a vertical cylinder. In *Coastal Engineering 1994* (pp. 1284-1297).

Lagasse, P. F., Byars, M. S., Zevenbergen, L. W., and Clopper, P. E. (2001). "Bridge scour and stream instability countermeasures, experience, selection, and design guidance." FHWA Rep. No. NHI-01-003, HEC-23, 2nd Ed., Federal Highway Administration, Arlington, Va.

Laursen, E. M., and Toch, A. (1956). Scour around bridge piers and abutments (Vol. 4). Ames, IA, USA: Iowa Highway Research Board.

Laursen, E. M. (1963). An analysis of relief bridge scour. *Journal of the Hydraulics Division*, 89(3), 93-118.

Link, O. (2006). Time scale of scour around a cylindrical pier in sand and gravel, Proc. Third Chinese-German Joint Symposium on Coastal and Ocean Eng., Tainan, Taiwan.

Lundgren, T. S. (1971). Turbulent pipe and channel flow. *Physics of Fluids* (1958-1988), 14(2), 225-230.

Kirkil, G., and Constantinescu, G. (2010). "Flow and turbulence structure around an in-stream rectangular cylinder with scour hole." *Water Resour. Res.*, 46(11), W11549.

Massey, B. S., and Ward-Smith, J. (1998). *Mechanics of Fluids (Vol. 1)*. CRC Press.

Matutano, C., Negro, V., López-Gutiérrez, J. S., and Esteban, M. D. (2013). Scour prediction and scour protections in offshore wind farms. *Renewable Energy*, 57, 358-365.

May, R. W. P., and Escarameia, M. (1992). Channel protection: Turbulence downstream of structures.

May, R. W. P., Ackers, J. C., and Kirby, A. M. (2002). *Manual on scour at bridges and other hydraulic structures (Vol. 551)*. London: Ciria.

Maynard, S. T. (1995). Gabion-mattress channel-protection design. *Journal of Hydraulic Engineering*, 121(7), 519-522.

McCuen, R. H. S., and Willard, M. (1986). *Hydrologic modeling: Statistical methods and applications (No. 627.0724 M22)*.

McGovern, D. J., Ilic, S., Folkard, A. M., McLelland, S. J., and Murphy, B. J. (2014). "Time development of scour around a cylinder in simulated tidal currents." *J. Hydraulic Engineering*, 10.1061/(ASCE)HY.1943-7900.0000857, 04014014.

Melville, B. W. (1975). *Local scour at bridge sites (Doctoral dissertation, Auckland)*.

Melville, B. W. (1984). Live-bed scour at bridge piers. *Journal of Hydraulic Engineering*, 110(9), 1234-1247.

Melville, B. W. (1997). "Pier and abutment scour: Integrated approach." *J. Hydraul. Eng.*, 10.1061/(ASCE)0733-9429(1997)123: 2(125), 125–136.

Melville, B. W., and Chiew, Y. M. (1999). Time scale for local scour at bridge piers. *Journal of Hydraulic Engineering*, 125(1), 59-65.

Melville, B. W., and Coleman, S. E. (2000). Bridge Scour. Water Resources Publication.

Melville, B. W., and Sutherland, A. J. (1988). Design method for local scour at bridge piers. *Journal of Hydraulic Engineering*, 114(10), 1210-1226.

Melville, B. W., and Raudkivi, A. J. (1996). Effects of foundation geometry on bridge pier scour. *Journal of Hydraulic Engineering*, 122(4), 203-209.

Melville, B. W., and Coleman, S. E. (2000). Bridge scour. Water Resources Publication.

Melville, B. (2008). The physics of local scour at bridge piers. In *Fourth International Conference on Scour and Erosion* (pp. 28-38).

Miedema, S. A. (2014). *The Delft sand, clay and rock cutting model*. IOS Press.

Miller, M. C., McCave, I. N., and Komar, P. (1977). Threshold of sediment motion under unidirectional currents. *Sedimentology*, 24(4), 507-527.

Moreno, M., Maia, R., and Couto, L. (2015). Effects of Relative Column Width and Pile-Cap Elevation on Local Scour Depth around Complex Piers. *Journal of Hydraulic Engineering*, 04015051.

Muzzammil, M., and Gangadhariah, T. (2003) The mean characteristics of horseshoe vortex at a cylindrical pier, *Journal of Hydraulic Research*, 41:3, 285-297.

Myrhaug, D. (1989). A rational approach to wave friction coefficients for rough, smooth and transitional turbulent flow. *Coastal Engineering*, 13(1), 11-21.

Nakagawa, H., and Suzuki, K. (1976). Local scour around bridge pier in tidal current. *Coastal Engineering in Japan*, 19.

Neil, C. R. (1968). Note on initial movement of coarse uniform material. *Journal Hydraulic Research*, 6 (2), 157–184.

Neill, C. R. (1973). Guide to bridge hydraulics, Roads and Transportation Association of Canada.

Nielsen, P. (1992). Coastal bottom boundary layers and sediment transport (Vol. 4). World scientific.

Nielsen, A. W., Sumer, B. M., Ebbe, S. S., and Fredsøe, J. (2012). Experimental study on the scour around a monopile in breaking waves. *Journal of Waterway, Port, Coastal, and Ocean Engineering*, 138(6), 501-506.

Nielsen, A. W., Liu, X., Sumer, B. M., and Fredsøe, J. (2013). Flow and bed shear stresses in scour protections around a pile in a current. *Coastal Engineering*, 72, 20-38.

Nielsen, A. W., Probst, T., Petersen, T. U., & Sumer, B. M. (2015). Sinking of armour layer around a vertical cylinder exposed to waves and current. *Coastal Engineering*, 100, 58-66.

Parola, A. C., Mahavadi, S. K., Brown, B. M., and El Khoury, A. (1996). Effects of rectangular foundation geometry on local pier scour. *Journal of Hydraulic Engineering*, 122(1), 35-40

Petersen, T. U., Sumer, B. M., and Fredsøe, J. (2012). Time scale of scour around a pile in combined waves and current. In *Proceedings of the Sixth International Conference on Scour and Erosion* (pp. 981-988).

Petersen, T. U. (2014). Scour around offshore wind turbine foundation (Doctoral thesis). Technical University of Denmark, Kgs. Lyngby, Denmark.

Petersen, T. U., Sumer, B. M., Fredsøe, J., Raaijmakers, T. C., and Schouten, J. J. (2015). Edge scour at scour protections around piles in the marine environment—Laboratory and field investigation. *Coastal Engineering*, 106, 42-72.

Porter, K., Simons, R., and Harris, J. (2014). Comparison of three techniques for scour depth measurement: photogrammetry, echosounder profiling and a calibrated pile. *Coastal engineering Proceedings*, 1(34).

Porter, K., Harris, J., and Simons, R. (2015). "Discussion of 'Time development of scour around a cylinder in simulated tidal currents' by David J. McGovern, Suzana Ilic, Andrew M. Folkard, Stuart J. McLelland, and Brendan J. Murphy." *J. Hydraul. Eng.*, 10.1061/(ASCE)HY.1943-7900.0001022, 1–2.

Porter, K. (2016). Seabed scour around marine structures in mixed and layered sediments (Doctoral thesis). University College London, London, UK.

Rance, P. J. (1980). The potential for scour around large objects. *Scour prevention techniques around offshore structures*, 41-53.

Raudkivi, A. J., and Ettema, R. (1983). Clear-water scour at cylindrical piers. *Journal of Hydraulic Engineering*, 109(3), 338-350.

Raudkivi, A. J., and Ettema, R. (1985). Scour at cylindrical bridge piers in armored beds. *Journal of Hydraulic Engineering*, 111(4), 713-731.

Raudkivi, A. J. (1986). Functional trends of scour at bridge piers. *Journal of hydraulic engineering*, 112(1), 1-13.

Raudkivi, A. J. (1991). Scour at bridge piers. *Scouring: IAHR hydraulic structures design manual*, 2, 61-98.

Richardson, E. V., and Davis, S. R. (2001). Evaluating scour at bridges: Federal Highway Administration Hydraulic Engineering Circular No. 18. Publication FHWA NHI, 01-001.

Roshko, A. (1961). Experiments on the flow past a circular cylinder at very high Reynolds number. *Journal of Fluid Mechanics*, 10(03), 345-356.

Roulund, A., Sumer, B. M., Fredsøe, J., and Michelsen, J. (2005). Numerical and experimental investigation of flow and scour around a circular pile. *Journal of Fluid Mechanics*, 534, 351-401.

Rudolph, D., and Bos, K. J. (2006). Scour around a monopile under combined wave-current conditions and low KC-numbers. In *Proceedings of the International Conference on Scour and Erosion (ICSE)*, Amsterdam.

Sarpkaya, T. (2010). *Wave forces on offshore structures*. Cambridge university press.

Schlichting, H. (1968). *Boundary-layer theory*. Springer Science and Business Media.

Schiereck, G. J. (2003). *Introduction to bed, bank and shore protection*. CRC Press.

Seacore (2004). *Factual Report C991: Geotechnical site investigation Barrow Offshore Wind Farm Project*.

Sellar, B., Harding, S., and Richmond, M. (2015). High-resolution velocimetry in energetic tidal currents using a convergent-beam acoustic Doppler profiler. *Measurement Science and Technology*, 26(8), 085801.

Shen, H. W., Schneider, V. R., and Karaki, S. (1969). Local scour around bridge piers. *Journal of the Hydraulics Division*.

Sheppard, D. M., and Glasser, T. (2004). Sediment scour at piers with complex geometries. In *Proceeding of the 2nd International Conference on Scour and Erosion (Vol. 1417)*.

Sheppard, D. M. (2003a). *Large scale and live bed local pier scour experiments. Phase 1: Large scale, clearwater scour experiments (Final Report)*.

Sheppard, D. M. (2003b). Large scale and live bed local pier scour experiments. Florida Department of Transportation. Florida.

Sheppard, D. M. (2004). Overlooked local sediment scour mechanism. Transportation Research Record: Journal of the Transportation Research Board, (1890), 107-111.

Sheppard, D. M., Melville, B., and Demir, H. (2013). Evaluation of existing equations for local scour at bridge piers. Journal of Hydraulic Engineering, 140(1), 14-23.

Sheppard, D. M., and Miller Jr, W. (2006). "Live-bed local pier scour experiments." J. Hydraul. Eng., 10.1061/(ASCE)0733-9429(2006)132: 7(635), 635–642.

Shields, A. (1936). Anwendung der Aehnlichkeitsmechanik und der Turbulenzforschung auf die Geschiebepbewegung. Preussischen Versuchsanstalt für Wasserbau.

Simons, R. R., Grass, A. J. and Kyriacou, A., 1988. The influence of currents on wave attenuation. In: B.L. Edge (Editor), International Conference on Coastal Engineering, Malaga, Spain, pp. 363-376.

Simons, R. R., Myrhaug, D., Thais, L., Chapalain, G., Holmedal, L. E., and MacIver, R. (2001). Bed friction in combined wave-current flows. In Coastal Engineering 2000: Conference Proceedings: July 16-21, 2000, Sydney, Australia (Vol. 1, p. 216). Amer Society of Civil Engineers.

Simons, R. R., Weller, J., and Whitehouse, R. J. S. (2009). "Scour development around truncated cylindrical structures." Coastal Structures 2007, Proc. of the 5th Coastal Structures Int. Conf., CSt07, World Scientific, Singapore.

Soulsby, R. L. (1990). Tidal-current boundary layers, in The Sea, vol. 9B, Ocean Engineering Science, eds B. LeMehaute and D. M. Hanes, Wiley, New York.

Soulsby, R. L., Hamm, L., Klopman, G., Myrhaug, D., Simons, R. R., and Thomas, G. P. (1993). Wave-current interaction within and outside the bottom boundary layer. *Coastal engineering*, 21(1-3), 41-69.

Soulsby, R. (1997). *Dynamics of Marine Sands: a manual for practical applications*. Thomas Telford.

Soulsby, R. L., and Whitehouse, R. J. S. (1997). Threshold of sediment motion in coastal environments. In *Pacific Coasts and Ports' 97: Proceedings of the 13th Australasian Coastal and Ocean Engineering Conference and the 6th Australasian Port and Harbour Conference; Volume 1* (p. 145). Centre for Advanced Engineering, University of Canterbury.

Soulsby, R., and Clarke, S. (2005). Bed shear stresses under combined waves and current on smooth rough beds. HR Wallingford (No. FD1905).

Sumer, B. M., Fredsøe, J., and Christiansen, N. (1992). Scour around vertical pile in waves. *Journal of Waterway, Port, Coastal, and Ocean Engineering*, 118(1), 15-31.

Sumer, B. M., Fredsøe, J., Christiansen, N., and Hansen, S. B. (1994). Bed shear stress and scour around coastal structures. In *Coastal Engineering Conference* (Vol. 2, pp. 1595-1595). ASCE.

Sumer, B. M., Kozakiewicz, A., Fredsøe, J., and Deigaard, R. (1996). Velocity and concentration profiles in sheet-flow layer of movable bed. *Journal of Hydraulic Engineering*, 122(10), 549-558.

Sumer, B. M., Christiansen, N., and Fredsøe, J. (1997). The horseshoe vortex and vortex shedding around a vertical wall-mounted cylinder exposed to waves. *Journal of Fluid Mechanics*, 332, 41-70.

Sumer, B. M., and Fredsøe, J. (1997). *Hydrodynamics around cylindrical structures* (Vol. 12). World Scientific.

Sumer, B. M., and Fredsøe, J. (2002). The mechanics of scour in the marine environment. World Scientific.

Sumer, B. M., Petersen, T. U., Locatelli, L., Fredsøe, J., Musumeci, R. E., and Foti, E. (2013). Backfilling of a scour hole around a pile in waves and current. *Journal of Waterway, Port, Coastal, and Ocean Engineering*, 139(1), 9-23.

Sutherland, J., and Whitehouse, R. J. S. (1998). Scale effects in the physical modelling of seabed scour.

Sundborg, Å. (1956). The River Klarälven: a study of fluvial processes. *Geografiska Annaler*, 125-237.

Swart, D. H. (1974). Offshore sediment transport and equilibrium beach profiles (Doctoral dissertation, TU Delft, Delft University of Technology).

Tavouktsoglou, N.S., Harris, J.M., Simons, R.R. and Whitehouse, R.J. (2015). Bed shear stress distribution around offshore gravity foundations. *Proceedings of the ASME 2015 34th International Conference on Ocean, Offshore and Arctic Engineering, OMAE2015*, St. John's Newfoundland, Canada, May 31 – June 5, Paper No. OMAE2015-41966, American Society of Mechanical Engineers, pp. V007T06A051-V007T06A051.

Teramoto, S., Yatagai, K., Murase, Y., Ninomiya, K., and Tagya, K. (1973). Study on scouring of sit-on-bottom type offshore structure. *Mitsubishi Heavy Industries Technical Review*, 10(1).

Terzaghi, K. (1939). Soil mechanics: A new chapter in engineering science. *J. Inst. of Civ. Eng. (UK)*, 12(7), 106–141.

Torum, A., and van Gent, M. (1992). Water particle velocities on a berm breakwater. *Coastal Engineering Proceedings*, 1(23).

Toue, T., Katsui, H., and Nadaoka, K. (1993). Mechanism of sediment transport around a large circular cylinder. In *Coastal Engineering 1992* (pp. 2867-2878).

Umeda, S., Yuhi, M., and Ishida, H. (2003). Numerical study of three-dimensional flow fields around the base of a vertical cylinder in oscillatory plus mean flow. In *Coastal Structures 2003* (pp. 751-763).

US Army Corps of Engineers, Hydrologic Engineering Center, (2010). HEC-RAS River analysis manual. CPD-69 CEIW.

Van der Meer, J. W. (1988). Deterministic and probabilistic design of breakwater armor layers. *Journal of Waterway, Port, Coastal, and Ocean Engineering*, 114(1), 66-80.

Van Rijn, L. C. (1984). Sediment transport, part I: bed load transport. *Journal of Hydraulic Engineering*, 110(10), 1431-1456.

Vanoni, V.A., ed. (1975). *Sedimentation Engineering: American Society of Civil Engineers, Manuals and Reports on Engineering Practice. No. 54.*

Vithana, H. P. V. (2012). The effect of stone protrusion on the incipient motion of rock armour under the action of regular waves (unpublished doctoral thesis). University College London.

Wang, C. Y. (1968). On high-frequency oscillatory viscous flows. *Journal of Fluid Mechanics*, 32(01), 55-68.

Whitehouse, R. J. S., and Hardisty, J. (1988). Experimental assessment of two theories for the effect of bedslope on the threshold of bedload transport. *Marine geology*, 79(1-2), 135-139.

Soulsby, R. L., and Whitehouse, R. J. S. (1997). Threshold of sediment motion in coastal environments. In *Pacific Coasts and Ports' 97: Proceedings of the 13th Australasian Coastal and Ocean Engineering Conference and the 6th Australasian Port*

and Harbour Conference; Volume 1 (p. 145). Centre for Advanced Engineering, University of Canterbury.

Whitehouse, R. J. (1998). Scour at marine structures: A manual for practical applications. Thomas Telford.

Whitehouse, R. J. S. (2004). Marine scour at large foundations, Proceedings of the Second International Conference on Scour and Erosion, Stallion Press, Singapore, pp. 455–463.

Whitehouse, R. J. S., Sutherland, J., and O'Brien, D. (2006). Seabed scour assessment for offshore windfarm.

Whitehouse, R. J. S., Sutherland, J., and Harris, J. (2011a). Evaluating scour at marine gravity foundations. Proceedings of the ICE-Maritime Engineering, 164(4), 143-157.

Whitehouse, R. J. S., Harris, J. M., Sutherland, J., and Rees, J. (2011b). The nature of scour development and scour protection at offshore windfarm foundations. Marine Pollution Bulletin, 62(1), 73-88.

Wörman, A. (1989). Riprap protection without filter layers. Journal of Hydraulic engineering, 115(12), 1615-1630.

Yalin, M. S. (1977). On the determination of ripple length. Journal of the Hydraulics Division, 103(4), 439-442.

Yanmaz, A. M., and Altinbilek, H. D. (1991). "Study of time-dependent local scour around bridge piers." J. Hydraul. Eng., 10.1061/(ASCE)0733-9429(1991)117:10(1247), 1247–1268.

Yeow, K., and Cheng, L. (2004). Local scour around a vertical pile with a caisson foundation. In Asian And Pacific Coasts 2003: (With CD-ROM) (pp. 1-7).

Zanke, U. (1982). Scours at piles in steady flow and under the influence of waves. Mitteilungen des Franzius-Instituts, Univ. Hannover, Heft, 54.

Zanke, U. C., Hsu, T. W., Roland, A., Link, O., and Diab, R. (2011). Equilibrium scour depths around piles in noncohesive sediments under currents and waves. Coastal Engineering, 58(10), 986-991.

11 Appendix A (correction factors for scour prediction equations)

Most scour studies focus on the prediction of the equilibrium scour depth around uniform cylinders in simplified scenarios. In reality field conditions are more complicated than in laboratory conditions and for this reason a number of correction factors have been developed to account for the differences in sediment gradation, foundation shape, pile group influence, and the orientation of the flow in case of non-cylindrical foundations. These factors are commonly known as the “K” factors which are presented below.

The product of the correction factors is given as:

$$K_i = K_\sigma K_s K_\omega K_{gr} \quad (11-1)$$

where:

K_σ is the correction factor for the sediment gradation;

K_s is the correction factor for the shape of the foundation;

K_ω is the correction factor for the orientation of the pier in the case of a non-cylindrical structure; and,

K_{gr} is the correction factor for the effect pier groups have on the equilibrium scour depth.

11.1.1 Sediment gradation (K_σ)

As discussed in section 1.4.3.3 the gradation of the sediment can result in a significant reduction of the scour depth especially in the clear water scour regime. The most common figure for determining the effect of sediment gradation on scour is given by Raudkivi and Ettema (1985) and is shown in Figure 11-1. It is recommended to use this design graph with caution for two reasons:

- This graph has been derived from a limited number of experiments and thus the effect of sediment gradation in prototype conditions may be different. The tests in Figure 11-1 were conducted in the clear water regime; and,

- Applying this correction factor to other flow conditions and especially live bed conditions with a flow intensity higher than the live bed peak would result in an overestimation of the scour depth reduction.

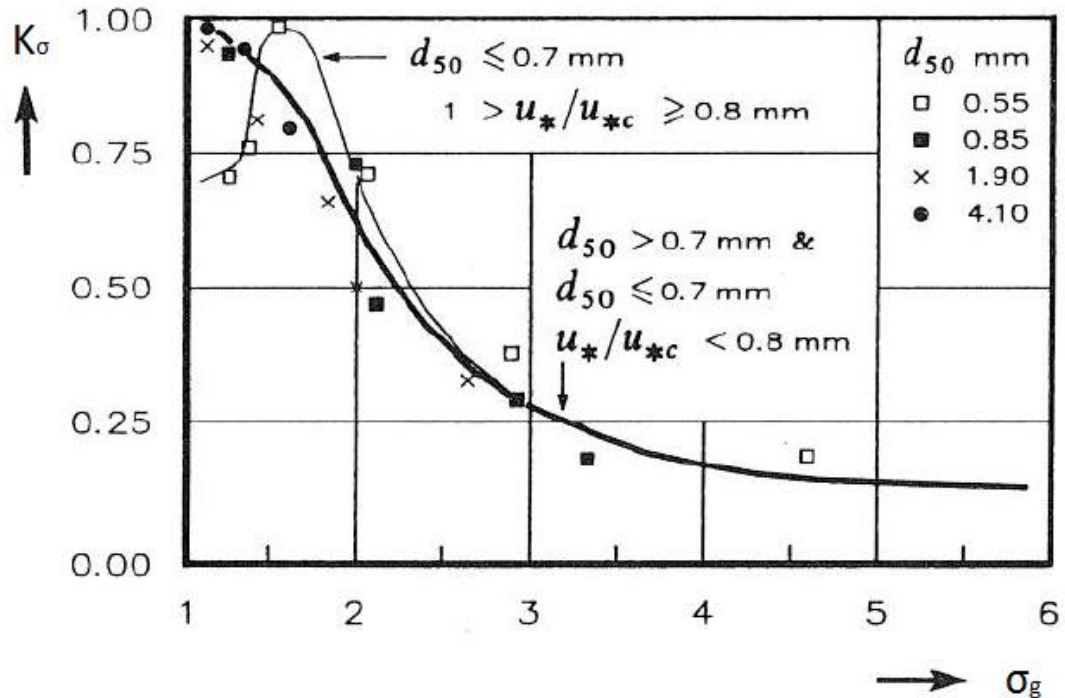


Figure 11-1: K_g as a function of σ_g (Source: Raudkivi and Ettema, 1985)

11.1.2 Foundation shape factor (K_s)

The influence of the shape of the structure on the equilibrium scour depth (in terms of shape factors) has been investigated by numerous authors (Laursen and Toch, 1956; Neill, 1973 and Dietz, 1972). For the simplest case (uniform cylinder) the shape factor can be taken as 1. Again these factors should also be used with caution as there is no information about the test conditions under which these factors have been derived. Also there are several structural geometry parameters that have not been accounted for such as the height of the structural element. The effect of structural geometries on scour is dealt with more detail in section (2.5). A summary of the main shape factors for bridge piers is presented in Table 11-1.

Table 11-1: Shape factor for different structure geometries

Cross-sectional form	Length to width ratio	Shape factor (K_s)		
		Oblong	Elliptic	Lenticular
Horizontal				
Circular	-	1	-	-
Elongated	3:2	1	-	-
Elongated	2:1	1	0.91	0.91
Elongated	3:1	1	0.83	0.76
Vertical				
Circular pile cap at base	-	0.48-0.85	-	-
Conical	-	0.76-0.89	-	-
Reversed cone (broadening upwards)	-	1.07-1.26	-	-

11.1.3 Pier orientation factor (K_ω)

The influence of the pile orientation on scour is given by the pier alignment factor (K_ω). For the simple case of a uniform cylinder, $K_\omega = 1$ due to symmetry. For the case of elongated structures Laursen and Toch (1956) give a summary of factors that account for different orientations (ω) and pile length to width ratios (L_p/b) which are limited in the number of combinations between the two parameter. The most comprehensive study on the effect of the pile orientation on scour is given by Froehlich (1988) who conducted a series of experiments and used previously published work to develop a best fit model for the orientation factor (11-2)

$$K_{\omega} = \left(\cos(\omega) + \frac{L_p}{b} \sin(\omega) \right)^{0.62} \quad (11-2)$$

11.1.4 Pier group factor (K_{gr})

The effect of pile groups on the scour around a single pile can be described in terms of the pier group factor (K_{gr}). The effect of the pier-to-pier interference has been studied by numerous authors (Breusers, 1971; Hannah, 1978; Herbich, 1984; Breusers and Raudkivi, 1991 and Sumer and Fredsøe, 2002). Scour around a single cylinder in a pier group can be described as a combination of three main two-pile group configurations (Hannah, 1978) which are shown in Figure 11-2.

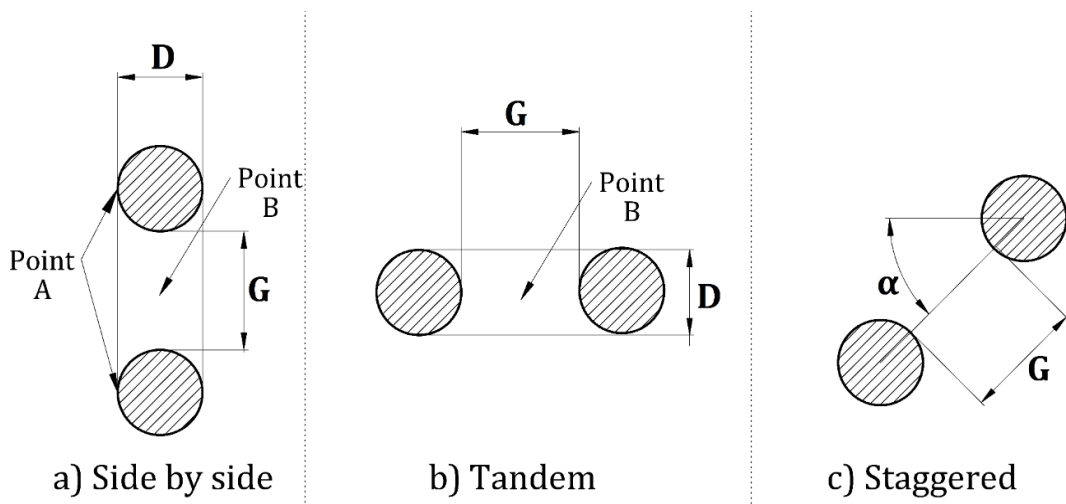


Figure 11-2: Definition sketch of pile group configurations.

According to Herbich (1984) the main parameter influencing the pile-group effect on scour is the spacing between the outer diameter of the two structures (G) (Figure 11-2). The effect the pile spacing has on the group-pile factor in a side-by-side arrangement is shown in Figure 11-3 for the scour depth in front of a pile and at the mid-point (point B in Figure 11-2) between the two structures.

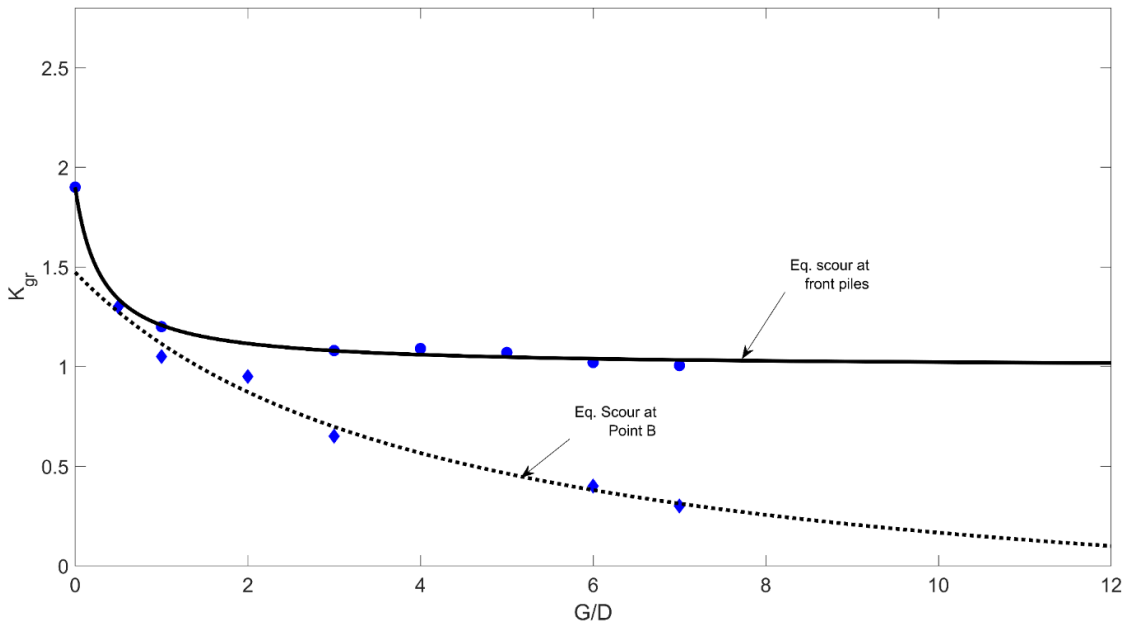


Figure 11-3: Pile-group factor for side-by-side pile configuration (configuration (a) in Figure 11-3); (Source: Hannah, 1978).

In the case of a tandem pile configuration K_{gr} is given in Figure 11-4 for three different locations (front pile, mid-point between the two cylinders and at the downstream pile).

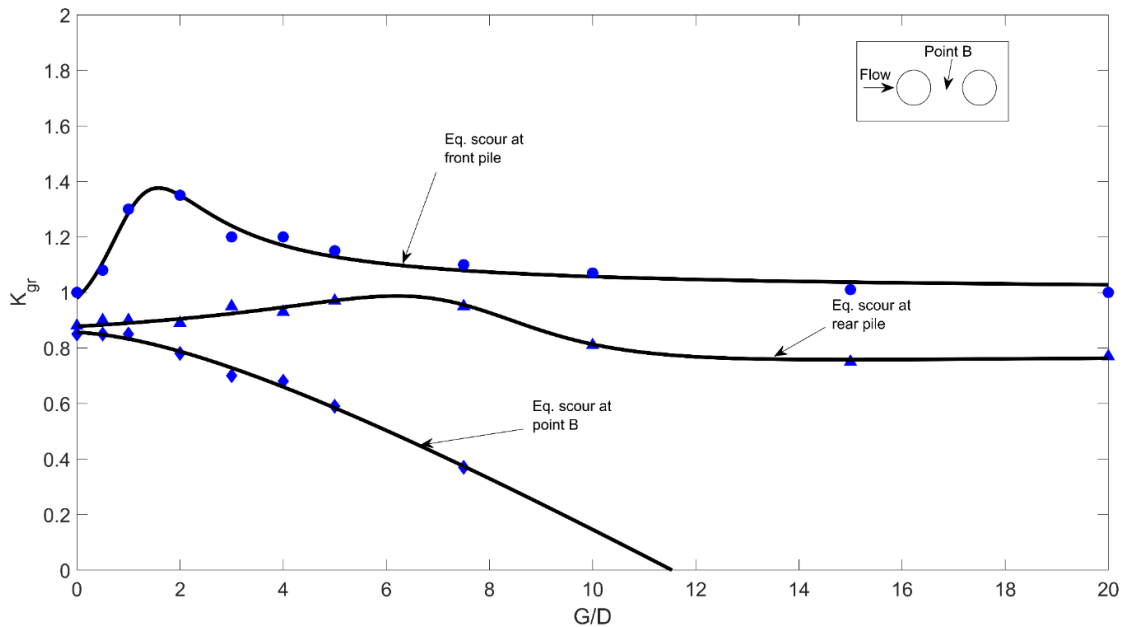


Figure 11-4: Pile-group factor for tandem pile configuration (configuration (b) in Figure 11-3); (Source: Hannah, 1978).

In the case of a staggered pile configuration the pile-group factor is a function of two parameters. The gap between the two structures and the angle between them (α) (Figure 11-2). The influence of α on K_{gr} is given in Figure 11-5 for the front and rear pile

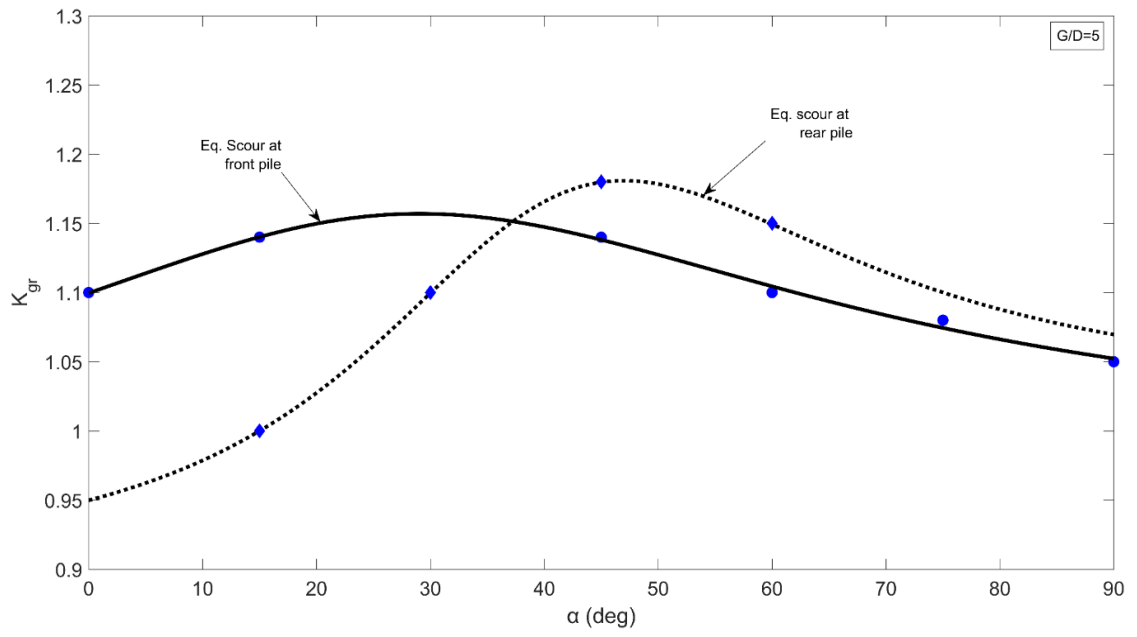


Figure 11-5: Pile-group factor for staggered pile configuration (configuration (c) in Figure 11-3); (Source: Hannah, 1978).

12 Appendix B (scour profiles along the centreline of the structures)

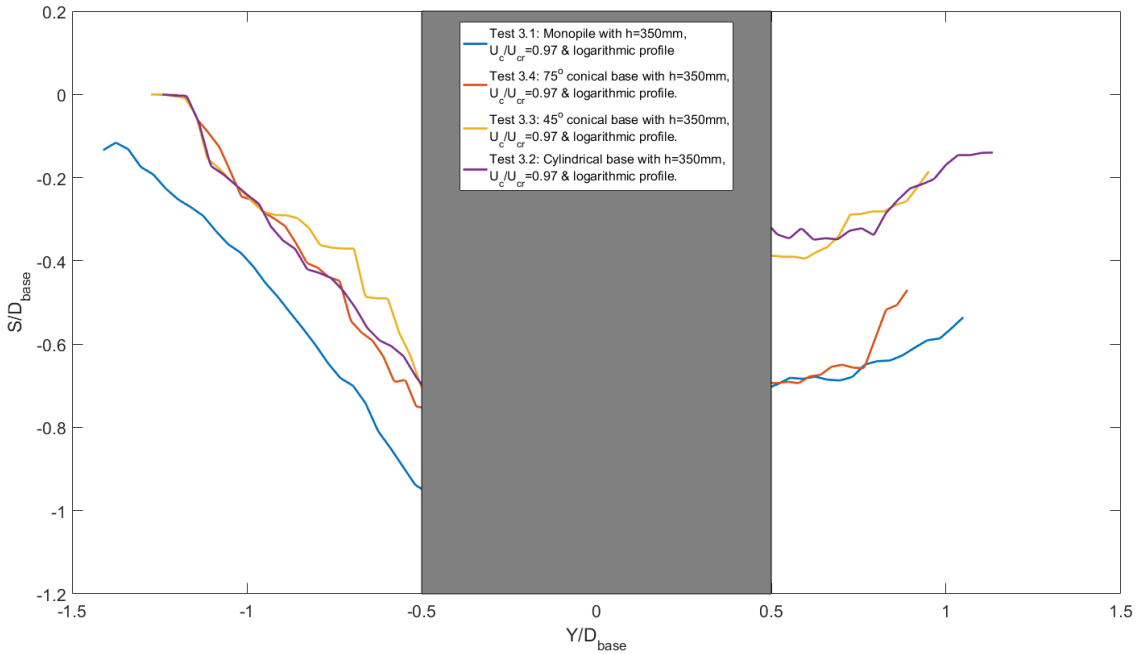


Figure 12-1: Scour profile along the plane of symmetry of the structure for Tests 3-1-3.4 (flow from left to right).

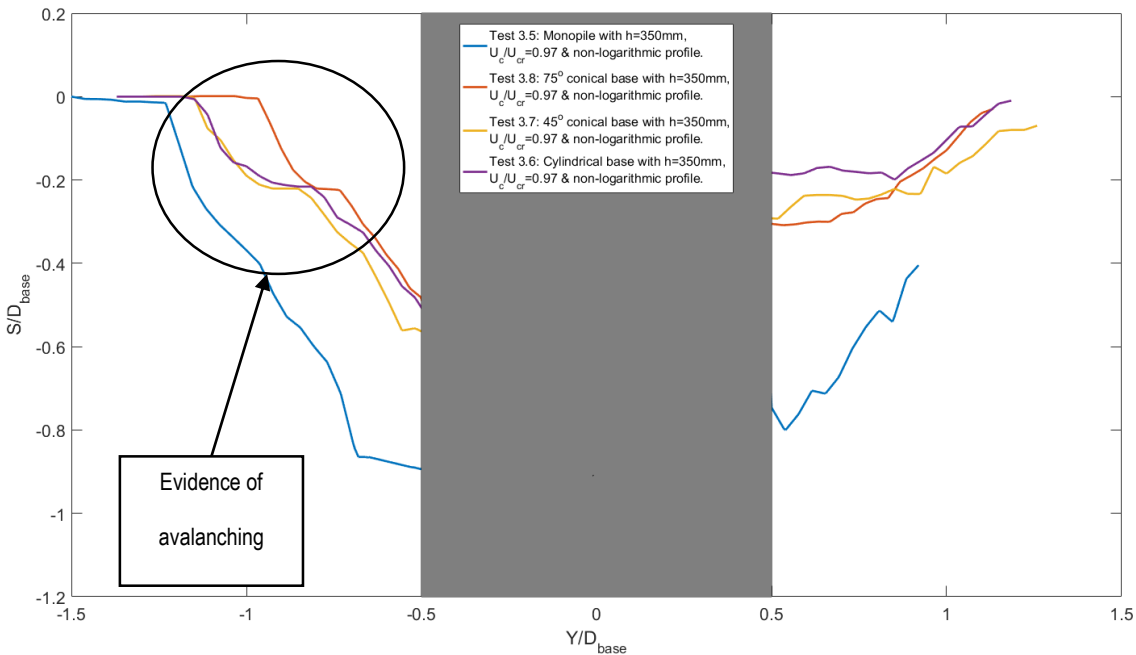


Figure 12-2: Scour profile along the plane of symmetry of the structure for Tests 3-5-3.8 (flow from left to right). The black circle highlights the avalanching at the upstream of the scour hole.

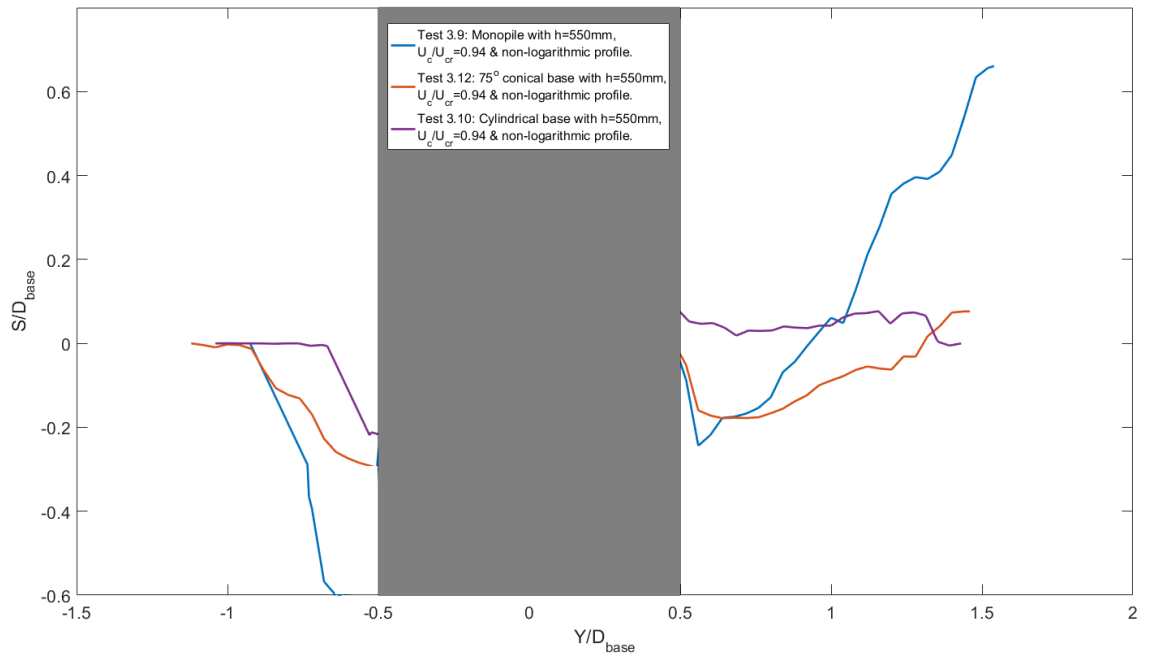


Figure 12-3: Scour profile along the plane of symmetry of the structure for Tests 3-9-3.12 (flow from left to right).

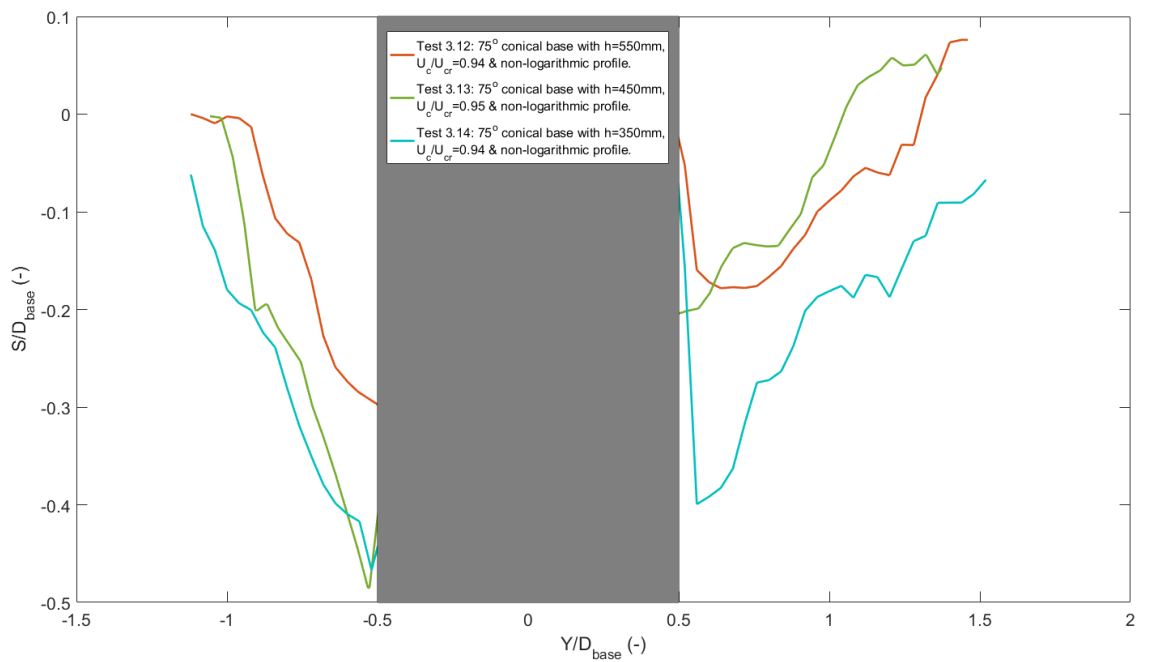


Figure 12-4: Scour profile along the plane of symmetry of the structure for Tests 3-12-3.14 (flow from left to right).